UCLA
UCLA Electronic Theses and Dissertations

Title
Attenuation of Hypersonic Second Mode Instability with Discrete Surface Roughness on Straight Blunt Cones

Permalink
https://escholarship.org/uc/item/3c85g83g

Author
Haley, Christopher

Publication Date
2021

Peer reviewed|Thesis/dissertation

eScholarship.org Powered by the California Digital Library
University of California

UNIVERSITY OF CALIFORNIA
Los Angeles

Attenuation of Hypersonic Second Mode Instability with Discrete Surface Roughness on Straight Blunt Cones

A dissertation submitted in partial satisfaction
of the requirements for the degree
Doctor of Philosophy in Aerospace Engineering

by

Christopher L. Haley

2021

© Copyright by
Christopher L. Haley
2021

ABSTRACT OF THE DISSERTATION

Attenuation of Hypersonic Second Mode Instability
with Discrete Surface Roughness on Straight Blunt Cones

by

Christopher L. Haley
Doctor of Philosophy in Aerospace Engineering
University of California, Los Angeles, 2021
Professor Xiaolin Zhong, Chair

Hypersonic boundary layer research has studied surface features, such as isolated or distributed roughness, extensively for turbulence tripping. However, there are reports of a counterintuitive phenomenon within the literature whereby surface roughness can delay the onset of laminar-turbulent transition. The reports did not attract widespread attention, leaving the phenomenon's underlying mechanism uninvestigated for several decades. A renewed interest in boundary layer control strategies motivated Fong and Zhong in 2012 to conduct an extensive numerical study on what has been termed the "roughness effect". The research found that roughness elements immersed within the boundary layer and placed at the synchronization location for a particular unstable frequency can attenuate higher unstable frequencies while amplifying lower unstable frequencies. Thus, providing a passive means to delay laminar-turbulent transition with discrete surface roughness. However, these previous numerical investigations are limited to a flat plate geometry, 2-D spanwise roughness, limited in the scope of their freestream Mach number, and focus exclusively on Mack's second mode instability. In order to advance our knowledge of the roughness effect, the objectives of this dissertation are fourfold: (1) To investigate the roughness effect on a straight blunt cone geometry, (2) To investigate the long-term downstream consequences of the roughness effect, (3) Provide experimental evidence of second mode attenuation in a flow with a growing boundary layer containing a range of unstable frequencies, and the consequences of off-design flow conditions, and (4) To investigate the appearance of the supersonic mode in

a low-enthalpy warm wall flow of the current study.

A combined approach of direct numerical simulation, body-fitted surface roughness, and linear stability theory are used to numerically investigate the roughness effect. Four cases are computed as part of the research objective. Case C.1 is a Mach 8 flow computed for the design of a passive transition-delaying roughness configuration, along with studying the roughness effect on a straight blunt cone. Case C.1-Ext is a longer cone simulation of C.1 and is computed to investigate the long-term downstream response of the roughness effect. C.2 is similar to C.1 except for a smaller nose radius and is computed for experimental validation. The last case, C.3, is a Mach 5 flow and is computed to study the roughness effect on a straight blunt cone in off-design flow conditions and for experimental validation.

The first objective to investigate the roughness effect on a straight blunt cone advances the research from a flat plate to more realistic test article geometries. Much of the experimental work done in hypersonic boundary layer stability research is done on straight cones due to the axisymmetric flows in hypersonic wind tunnels. The investigation found that the roughness effect behaves like a flat plate where unstable frequencies higher than the synchronization frequency are attenuated, and lower frequencies are amplified. The investigation also found that some flow features around the roughness elements, such as separation zones, are either smaller in size or absent in conical flow fields. The investigation also confirmed that the second mode's attenuation is a result of the element's proximity to the synchronization location and not due to its proximity with the branch I/II neutral points.

The long-term downstream effect of second mode attenuation is also investigated for a single roughness and roughness array. The numerical investigation found that the range of targeted frequencies is attenuated as expected, especially for the roughness array, which proves to be effective at attenuating unstable frequencies over a longer distance. However, the amplitudes of frequencies below the targeted range grow many times higher than they would have otherwise on a cone with no roughness. The passive transition-delaying control strategy, rather than dissipating the disturbance energy, acts to transfer the energy to lower unstable frequencies, guaranteeing eventual turbulent transition. The result demonstrates that roughness must be applied to the entire cone to have an effective control strategy.

The experimental results in this dissertation come from a joint numerical and experimental investigation of transition-delaying roughness with Dr. Katya Casper at Sandia National Laboratories. A numerical simulation is undertaken to design a surface roughness array that would attenuate Mack's second mode instability and maintain laminar flow over a Mach 8 hypersonic blunt cone. Multiple experimental runs at the Mach 8 condition with different Reynolds numbers are performed, as well as an off-design Mach 5 condition. The roughness array successfully delays transition in the Mach 8 case as intended but does not delay transition in the Mach 5 case. For validation and further analysis, numerical cases C.2 and C.3 are computed using the Mach 8 and Mach 5 experimental flow conditions. Stability analysis of case C.2 shows that the roughness array is adequately designed to attenuate the second mode. Analysis of case C.3 reveals the Mach 5 boundary layer is dominated by Mack's first mode instability and is not attenuated by the array. This investigation of multiple flow conditions combined with experimental results helps validate the numerical code and provides empirical evidence for the roughness effect.

While investigating transition delaying surface roughness, acoustic-like waves are observed emanating from the boundary layer of case C.1-Ext. The acoustic-like wave emissions are qualitatively similar to those attributed to the supersonic mode. However, the supersonic mode responsible for such emissions is often found in high-enthalpy flows with highly cooled walls, making its appearance in a flow with relatively low freestream enthalpy and a warm wall unexpected. Stability analysis on the steady-state solution reveals an unstable mode S with a subsonic phase velocity and a stable mode F whose mode F- branch takes on a supersonic phase velocity. The stable supersonic mode F is thought to be responsible for the acoustic-like wave emissions. Unsteady simulations are carried out using blowing-suction actuators at two different surface locations. Analysis of the temporal data and spectral data reveals constructive/destructive interference occurring between a primary and a satellite wave packet in the vicinity of the acoustic-like wave emissions, which has a damping effect on individual frequency growth. Based on this study's results, it is concluded that a supersonic discrete mode is not limited to high-enthalpy, cold wall flows and that it does appear in low-enthalpy, warm wall flows; however, the mode is stable.

The dissertation of Christopher L. Haley is approved.

Ann R. Karagozian

Jeffrey D. Eldredge

Mitchell Spearrin

Xiaolin Zhong, Committee Chair

University of California, Los Angeles

2021

To my parents who made this possible.

TABLE OF CONTENTS

LIST OF FIGURES

LIST OF TABLES

ACKNOWLEDGMENTS

Writing and conducting the research for this dissertation has been no small undertaking, and many people and resources have helped me along the way. First and foremost, I would like to thank my parents, Philip and Paula Haley, and my brother Thomas for their unwavering support throughout my graduate studies. I'd also like to thank Oscar and Coco, whose furry faces helped me more than they'll ever know.

I also want to express my thanks to my advisor, Professor Xiaolin Zhong, for his continued support and patience throughout my doctoral program. His guidance has been invaluable in interpreting new results. I also want to thank my committee, Professor Jeffrey Eldredge, Professor Ann Karagozian, and Professor Mitchell Spearrin, for their time, efforts, and insightful comments while serving on my committee.

I would also like to thank Dr. Katya Casper and the wind tunnel researchers at Sandia National Laboratories. Without her collaboration, the experimental results in this dissertation would not have been possible. For me personally, the results established a firm grounding for the roughness-attenuation effect as a physical phenomenon. They were a source of motivation that helped alleviate many self-doubts, and for that, I am eternally grateful.

I also want to thank my many labmates over the years—especially my friends and colleagues Ayaboe Edoh, Carleton Knisely, and Richard Abrantes. Graduate school is difficult and lonely. Our conversations over the years were an invaluable source of motivation for me to complete my studies.

I would also like to thank my friends Jillian Lawson, Patrick Long, Marie Look, Carly Stoenner, and Mollie Perlman. Your friendships made living in Los Angeles not only bearable but fun and exciting. And, of course, I can't leave out some of my oldest friends Christopher Dietrich, Robert Aiello, Lauren Hall, Miles Sebesta, and Kevin Shunta. I look forward to time spent with all of you where my mind isn't preoccupied with research.

And lastly, the research contained in this dissertation would not have been possible without various grants from the Air Force Office of Scientific Research (AFOSR) (#FA9550-15-

1-0268 and #FA9550-19-1-0206). Monitored over the years by Dr. Rengasamy Ponnappan, Dr. Ivett Leyva, and currently by Dr. Sarah H. Popkin. And by grants from the Office of Naval Research (ONR) monitored by Dr. Eric Marineau (#N00014-17-1-23-43).[1]

Special thanks to the United States Department of Defense High Performance Computing Modernization Program (DoD HPCMP), whose short queue times, large job sizes, and ample computing hours allowed me to take on some really aggressive simulations (AFOSR40702004). Additionally, special thanks to the National Science Foundation's Extreme Science and Engineering Environment (XSEDE) program, Texas Advanced Computing Center (TACC), Oak Ridge National Laboratory (ORNL), and San Diego Supercomputer Center (SDSC) for providing the necessary computational resources for my early research (#TG-ASC090076). The opportunity to interface with so many supercomputers has instilled a deep interest in high-performance computing and inspired me to re-build the lab's compute cluster.

[1]The views and conclusions contained in this dissertation are those of the authors and should not be interpreted as necessarily representing the official policies or endorsements either expressed or implied by the AFOSR, the ONR, or the U.S. Government.

VITA

2011	B.S. (Aeronautical Science and Engineering), B.S. (Mechanical Engineering), University of California Davis.
2013	M.S. (Aerospace Engineering), University of California Los Angeles.
2015–2017	Teaching Assistant/Reader, Mechanical and Aerospace Engineering Department, UCLA. Worked as a TA/Reader for MAE 150/250R, 250A, and 250D
2013-2021	Graduate Student Researcher, Mechanical and Aerospace Engineering Department, UCLA.

PUBLICATIONS

C. Haley and X. Zhong, "Supersonic Mode in Low-Enthalpy Hypersonic Flow Over a Cone and Wave Packet Interference", *Physics of Fluids*, **33**(5), 2021.

C. Haley and X. Zhong, "Mode F/S Wave Packet Interference and Acoustic-like Emissions in a Mach 8 Flow Over a Cone", AIAA paper 2020-1579, January 2020. 1-19.

C. Haley, K. Casper and X. Zhong, "Joint Numerical and Experimental Investigation of Roughness Effect on Hypersonic 2nd Mode Instability and Transition", AIAA paper 2019-0873, January 2019. 1-27.

C. Knisely, C. Haley and X. Zhong, "Impact of Conical Hypersonic Boundary Layer Transition on Skin Drag and Heating", AIAA paper 2019-1134, January 2019. 1-27.

C. Haley and X. Zhong, "Direct Numerical Simulation of Hypersonic Flow over a Blunt Cone with Axisymmetric Isolated Roughness", AIAA paper 2017-4514, June 2017. 1-27.

CHAPTER 1

Introduction

Laminar to turbulent boundary layer transition significantly impacts hypersonic vehicle design. Turbulent flow can drastically increase aerodynamic drag on the vehicle's surface, affect engine performance and operability, and adversely affect vehicle control as illustrated in Fig. 1.1, but the most detrimental consequence of turbulent flow is surface heating [Mac69, Res91, ZW12, FT11]. Turbulent hypersonic boundary layers can increase surface heating by a factor of 4 to 10 [Hol12]. In order to combat surface heating, thermal protection systems are essential to avoid overheating and failure of the vehicle's structure. Thermal protection materials, like ceramic tiles and insulation, are often heavy and add additional weight to the structure, which reduces the maximum payload. The ability to predict or even delay transition while maintaining laminar flow can result in considerable savings in aerodynamic heating, fuel economy, and vehicle weight.

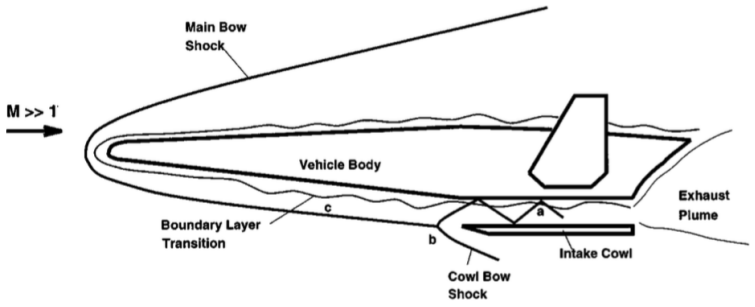

Figure 1.1: Illustration of hypersonic lifting vehicle denoting areas affected by laminar-turbulent transition. Reproduced from [Zho98].

Understanding laminar-turbulent transition is a long-standing goal of hypersonic research. In the past decades, considerable progress has been made by parsing out the problem into areas of receptivity, linear growth, and nonlinear breakdown. However, complete

knowledge of the underlying mechanisms remains elusive [Sch08]. Meanwhile, the undesired consequences of boundary layer transition persist and advocate for a means to predict and ultimately control the onset of boundary layer transition. Computational and experimental research into using 2-D finite roughness strips to delay the onset of transition has shown considerable promise [FWZ14b, FWZ15, FWH15]. As the illustration in Fig. 1.2 shows, roughness strips added to a hypersonic vehicle can decrease skin friction and heat transfer to the vehicles body. To further this research, this dissertation presents new direct numerical simulations of straight blunt cones in hypersonic flow to explore the effect of surface roughness on boundary layer instabilities.

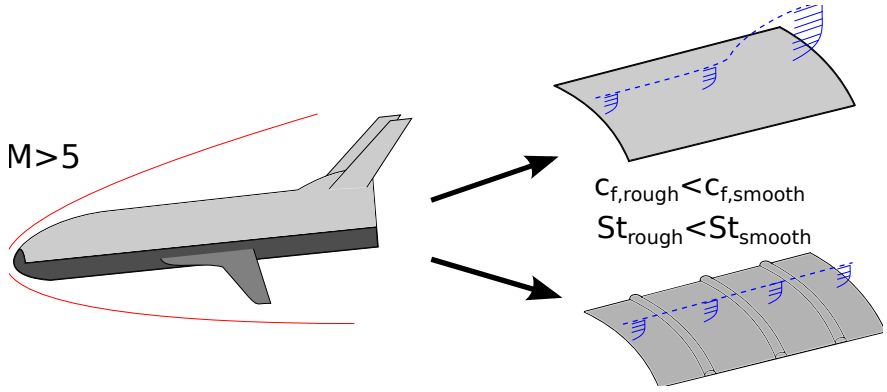

Figure 1.2: Illustration of hypersonic vehicle where the addition of 2-D finite roughness strips decreases the vehicles skin friction and heat transfer.

Ongoing research has identified several factors that affect the transition process. These factors include receptivity of freestream disturbances, nose bluntness, surface temperature, and isolated and distributed roughness. Of particular interest is the effect discrete roughness has on transition. Surface roughness is classified in terms of its height with respect to the boundary layer. Heights that expedite transition or cause immediate onset are often termed 'critical' or 'effective,' respectively. However, there are unique instances where a roughness height counterintuitively delays transition. A growing body of computational evidence supports the existence of what is known as the 'roughness effect.' The roughness effect phenomenon, as illustrated in Fig. 1.3, is where discrete roughness elements immersed within the boundary layer can attenuate certain frequencies of Mack's second mode instability based

on its surface location. The most compelling evidence for the roughness effect thus far is a collaborative effort between Fong, Zhong and Schneider [FWH15] in which a transition-delaying roughness experiment is designed and validated according to the passive laminar control strategy patented by Zhong, Fong and Wang [ZFW14]. However, more research on the roughness effect is needed. This dissertation extends the research on the roughness effect to novel conical geometries, investigates the long-term downstream implications of second mode attenuation, provides empirical evidence of second mode attenuation over a range of unstable frequencies, and examines the roughness effect in off-design flow conditions. This research also aims to develop our fundamental understanding of hypersonic boundary layer instabilities by investigating the appearance of supersonic modes in low-enthalpy warm wall flow conditions.

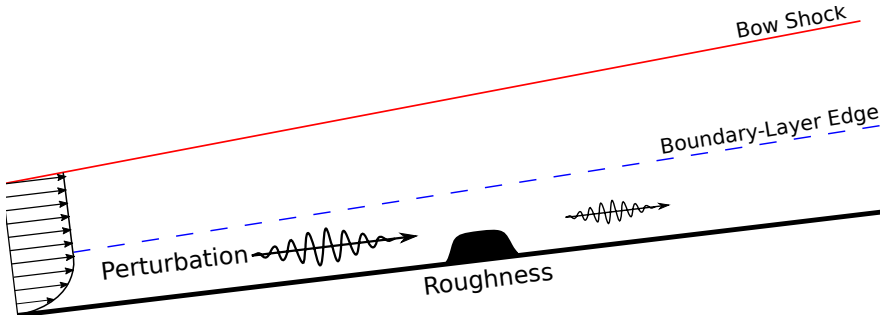

Figure 1.3: Illustration of the 'roughness effect' where a discrete roughness element is placed within the boundary layer to attenuate Mack's second mode instability.

1.1 Background

1.1.1 Overview of Hypersonic Boundary-Layer Transition

Boundary layer transition is one of the most researched and important aspects of hypersonic flow. Like wall-bounded flows in other flow regimes, a boundary layer forms on a surface due to viscous shear forces between the wall and the freestream. Typically, the boundary layer begins in a laminar state where it is stable and perturbation-free. As the bound-

ary layer grows downstream, flow perturbations introduced by environmental noise amplify and cause the boundary layer to become unstable, eventually leading to a fully turbulent boundary layer. The process that takes the boundary layer from fully laminar to fully turbulent is known as transition. Figure 1.4 reproduced from White [Whi05] illustrates an idealized transition process, where the process takes place over some length and is typified by destabilizing phenomena like compressible Tollmien-Schlichting waves (T-S waves), spanwise vorticity, 3-D vortex breakdown, turbulent spots, and edge contamination. In reality, these destabilizing phenomena may not necessarily appear together or may not appear at all before turbulent breakdown is reached. The appearance of specific phenomena depends significantly on environmental forcing. Because of this, it is difficult to predict for a general case when a laminar boundary layer starts to transition and when it will become fully turbulent. Thus, the transition process encapsulates many destabilizing phenomena and does not necessarily have a clearly defined beginning and end, making boundary layer transition a complex area of research.

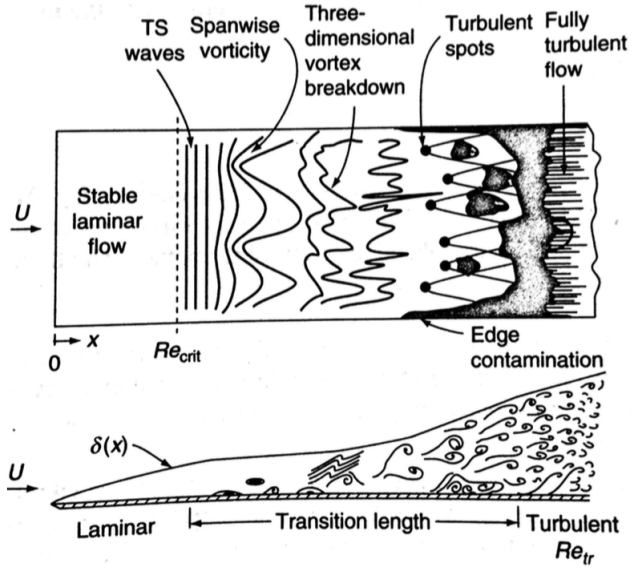

Figure 1.4: Illustration of laminar-turbulent transition on a flat plate. Reproduced from [Whi05].

For all its complexity, decades of extensive research on boundary layer transition has established a valuable framework for studying transition as a function of environmental

forcing. The framework was built by Morkovin [Mor88] and Morkovin et al. [MRH94] and views the transition process as a set of pathways from laminar to turbulent. How one navigates the pathways depends on the intensity of the initial environmental forcing and various growth mechanisms present in the boundary layer. The framework is summarized by the transition pathways diagram in Fig. 1.5. Additional mechanism research done by Reshotko [Res08b] has also improved upon the original framework.

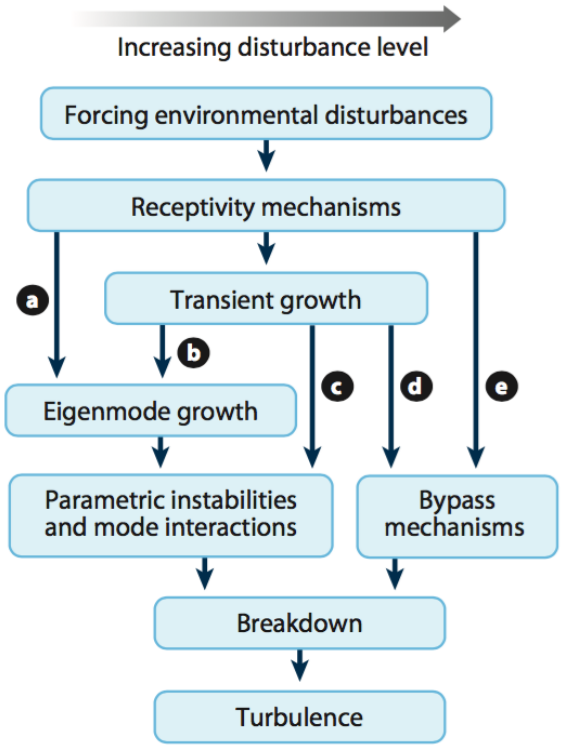

Figure 1.5: Diagram of laminar-turbulent transition pathways. Reproduced from [Fed11].

Of the five transition pathways presented in Fig. 1.5, the present research is primarily concerned with Path A. High altitude environmental noise is often minimal in real-world flight conditions, making Path A a realistic transition path [Res08a]. The pathway is typified by discrete normal modes such as the Fast and Slow modes. These discrete modes are responsible for the aforementioned T-S waves, as well as Mack's second mode instability and supersonic modes, which are unique to hypersonic boundary layers. Following Path A, the discrete normal modes are excited by low environmental disturbances entering the boundary

layer. As the modes propagate downstream, unstable modes, such as Mack's second mode, undergo linear growth. The continued growth eventually leads to modal interaction and nonlinear growth. When the growth can no longer be sustained, the laminar boundary layer breaks down and becomes fully turbulent.

Path A generally has the longest transition length from laminar to turbulent due to the linear growth of the normal modes, with the most unstable frequencies persisting far downstream. This long residency within the boundary layer is beneficial because it provides an opportunity to attenuate the unstable frequencies with surface roughness and delay transition.

The Fast mode and the Slow mode, mentioned above, are the two types of discrete normal modes induced by low environmental noise. These modes are also referred to as mode F and mode S. The Fast mode is so named because its phase speed originates near the fast acoustic spectrum, where noise propagates with a speed of $(M+1)a$. Likewise, the Slow mode originates near the slow acoustic spectrum, where noise propagates with a speed of $(M-1)a$. The acoustic spectra can be thought of as sound propagating away from a source transported in a supersonic flow.

The Fast mode and Slow mode are the discrete modes responsible for instabilities within the boundary layer [Mac84]. Depending on the flow conditions, either one of these modes will become unstable through a process of weak modal coupling [FT11]. In low Mach number flows ($M_\infty < 5$), the unstable mode is responsible for the compressible T-S wave, which is the source of boundary layer instability. The compressible analog of T-S waves are referred to as Mack's first mode instability in hypersonic stability research. As the Mach number is increased to the hypersonic regime ($M_\infty > 5$), Mack's second mode instability becomes the dominant boundary layer instability. The second mode instability has a substantial impact on hypersonic laminar-turbulent transition. It is the goal of transition-delaying surface roughness to attenuate this modal instability.

The emergence of the second mode instability, for a fixed frequency, occurs when modes F and S become weakly coupled. During the coupling, energy is exchanged between the modes,

and typically, one mode will become unstable, and the other will become more stable. The discrete unstable mode is Mack's second mode instability. During this process, the phase speeds of modes F and S will cross at a point known as the synchronization point. The synchronization point corresponds to a physical streamwise location in the flow and plays a central role in placing transition-delaying surface roughness. In all of the simulations investigated by this research, mode S is responsible for the second modal instability.

Several methods exist for simulating and analyzing these linear modal disturbances. Linear stability theory (LST) is a common approach and is used extensively in this work. The method is described in detail in Chapter 3. Parabolized stability equations (PSE) is another popular method for analyzing boundary layer stability, especially for growing boundary layers, but is not used in the present work. The last method for simulating modal disturbance is direct numerical simulation (DNS). The method is computationally demanding but for studying boundary layers with surface nonuniformities, like surface roughness, it is the only suitable method. For that reason, DNS comprises the majority of this work. A detailed description of the DNS code and its methodology is given in Chapter 2.

1.1.2 Past and Current Research on Transition-delaying Roughness

The first observation that surface roughness could delay transition was in 1959 by Carlton S. James in his paper "Boundary-Layer Transition on Hollow cylinders in Supersonic Free Flight As Affected By Mach Number and a Screwthread type of Surface Roughness" [Jam59]. The research was motivated to address conflicting wind tunnel and flight test data regarding transition Reynolds number and increasing Mach number. James' test article consisted of a fin-stabilized hollow-tube model with two-dimensional distributed surface roughness inscribed around its circumference. The hollow-tube geometry provided a shape in which the flow moved parallel to the surface—the idea being to obtain results more approximate to a flat plate than to a blunt body. The 2-D surface roughness, which resembled the threads of a bolt, varied from 100 μin to 2100 μin and extended 7.4 in over the 9 in tube. James' experiment looked at Mach numbers in the subsonic and hypersonic range. The models

were gun-launched in the NASA Ames Research Center supersonic free-flight wind tunnel. Mach numbers from 2.8 to 4.1 were obtained by firing the models through quiescent air, and Mach numbers from 4.1 to 7 were obtained by firing the models through a counter-current airstream. James considered a nominally constant freestream Reynolds number for each configuration.

The results of the experiment showed that the transition Reynolds number was found to increase with increasing Mach number at a rate dependent on both Mach number and roughness height [Jam59]. James found the laminar boundary layer could tolerate increased roughness height with increased Mach number, a result consistent with the growth of the thermal and velocity boundary layer at higher Mach number. The unexpected result that James observed—with which the present research is most interested—was that for a given Mach number an optimum height was found to give a maximum laminar downstream transition location greater than the smooth surface benchmark. This observation is the first documented result of roughness-delayed transition. James adds a caveat to his findings, however, saying the interpolation curves used to fit the roughness transition data are highly nonlinear and require more data points than were available for a better fit.

In 1964, Paul F. Holloway and James R. Sterrett were investigating the effect of discrete isolated surface roughness on boundary layer transition and heat transfer in compressible flows when they too observed roughness-delayed transition [HS64]. Their experiment was conducted on a sharp-leading-edge flat plate with discrete isolated surface roughness located 2.0 inches from the leading edge. Two roughness heights of 0.0216 and 0.036 inches were studied in Mach 4.8 and 6.0 flows. Unit Reynolds numbers ranged from 1.2×10^6 to 8.2×10^6 ft^{-1} for $M_\infty = 6.0$, and from 9.8×10^6 to 13.9×10^6 ft^{-1} for $M_\infty = 4.8$. Boundary layer transition was determined by the change in heat-rate distribution using a transient calorimetry technique. Schlieren photographs were also taken to image the boundary layer. The experiment was conducted in Langley's 20-inch Mach 6.0 Tunnel and Mach 6.2 blowdown tunnel.

The experimental results were consistent with other contemporary papers that the transition Reynolds number for natural transition increased with increasing Mach number. The report also documents that a roughness height twice the boundary-layer thickness is required

to trip the boundary layer to turbulence. However, the result most relevant to the present research is that surface roughness of height less than the boundary-layer thickness can delay transition. This result was observed in the Mach 6.0 cases for unit Reynolds numbers of 8.2×10^6 and 5.8×10^6 ft^{-1}. In the 8.2×10^6 ft^{-1} instance both roughness heights of 0.0216 and 0.036 inches delayed transition, whereas in the 5.8×10^6 ft^{-1} case only the 0.0216 inch roughness delayed transition [HS64]. Though not fully investigated, the report's explanation for this phenomenon may be because a separated flow region behind the roughness exists and that separated laminar mixing layers are more stable with increased Mach number than attached boundary layers. This hypothesis to date has not been tested.

At this point in the history of transition-delaying roughness, two independent experiments have observed the phenomenon—one with distributed roughness and the other with discrete isolated roughness. The freestream Mach number of these cases were also greater than 5.0, suggesting a purely hypersonic phenomenon. Moreover, the phenomenon only appears to manifest when the roughness is smaller than the boundary layer thickness. It would not be until 2006 that a renewed interest and in-depth investigation of this phenomenon would occur.

In 2006 Fujii performed an experiment on the effect of two-dimensional roughness on hypersonic boundary layer transition, in which transition was observed to be delayed [Fuj06]. The experiment's main objective was to investigate the response and evolution of disturbances induced by roughness. The experiment was conducted on a straight 800 mm 5° half-angle cone in JAXA's 0.5 m hypersonic wind tunnel. Test case Mach numbers varied from 7.05 to 7.13 with unit Reynolds numbers varying between 1.93×10^6 to 2.78×10^7 m^{-1}. boundary layer transition was detected by measuring heat transfer distributions using infrared thermography. The test article was also tapped with pressure transducers. Three roughness configurations were examined: a wavy wall, a line of spheres arranged circumferentially, and equally spaced wires wrapped circumferentially. All of the configurations were placed well upstream of the turbulent breakdown region.

Fujii found that when the wavelength of the wavy wall and the unstable second-mode wavelength coincided, transition onset was delayed [Fuj06]. At low stagnation temperatures,

however, the roughness configurations had no discernible effect on the transition location. Fujii postulated that the observed delay in the onset of transition could be due to the laminar separation behind the roughness—a conclusion similar to Holloway and Sterrett. The boundary layer, however, was not directly imaged in Fujii's experiment and instead relied on a numerical solution for boundary layer information.

In 2010 Duan and Zhong began studying how discrete roughness could be used to stabilize hypersonic boundary layers [DWZ10]. The study was carried out by direct numerical simulation of a 2-D flat plate. The simulation focused on a Mach 5.92 flow with a unit Reynolds number of $13.0 \times 10^6\,\mathrm{m}^{-1}$. The simulation used a half-elliptical shape roughness set flush with the plate surface and was simulated using immersed interface methods in which non-uniform-grid finite difference schemes are applied to an arbitrary surface within an otherwise uniform grid. The study considered four cases with different roughness locations. In each case the roughness was half of the local boundary layer thickness. A blowing-suction actuator on the wall upstream of the roughness imposed an unsteady pulse of 100 kHz. Linear stability analysis of the steady-state was used to determine the synchronization location—the point where the phase speeds of mode F and mode S cross—of the 100 kHz frequency. The study found that in the two cases where the roughness element is located downstream of the synchronization location, the 100 kHz pressure perturbation was attenuated. In contrast, the pressure perturbation was amplified in the two cases where the roughness element is upstream of the synchronization location.

The 100 kHz frequency of the pulse is arbitrary and does not necessarily correspond to a frequency responsible for transition. The paper does not describe what insight led to comparing the relative position of the roughness location with the synchronization location, nor does it propose a possible mechanism. However, in hypersonic stability research, it is generally known that the second mode instability leads to transition, and that the instability occurs near where modes S and F synchronize. Thus, Duan and Zhong postulate that the relationship between the roughness location and the synchronization location is responsible for the roughness-delayed transition seen in previous experiments.

Following up on Duan and Zhong's insight that the synchronization location and its prox-

imity to a roughness element is significant to amplifying or attenuating a selected frequency, Fong et al. engaged in an extensive study of the roughness effect [DWZ10, FWZ12]. One of Fong's first numerical studies was to look at cases where single 2-D roughness elements were placed upstream, downstream, and at the synchronization location of a fixed frequency and look at different roughness heights. The simulations were carried out on a hypersonic flat plate at Mach 5.92. Fong used the same immersed interface DNS code developed by Duan [DWZ10]. The stability characteristics of the base steady-state were analyzed with LST. The mode S and mode F mode shapes for a frequency of 100 kHz were imposed as unsteady disturbances near the flat plate leading-edge. LST determined a synchronization location at 0.331 m for the 100 kHz disturbance. Four cases were studied by Fong, two upstream cases, one case at the synchronization location, and one downstream location—the roughnesses were located at 0.110, 0.185, 0.331, and 0.410 m, respectively. Each case also looked at four roughness heights of 25, 37.5, 50, and 62.5% of the local boundary-layer thickness. The change in the maximum pressure perturbation as the disturbance moves downstream was used to evaluate a roughness' attenuation/amplifying effectiveness. The pressure perturbations were amplified for the upstream roughness elements, with greater amplification occurring for the roughness nearest to the synchronization location and taller roughness heights. Fong surmised that the robust amplification might lead to early boundary layer transition. The pressure perturbations were attenuated for the synchronization location and downstream roughnesses, with the tallest roughness resulting in the most robust attenuation. The attenuation effect was also most pronounced for the downstream roughness. Fong concludes that these results may explain why surface roughness had delayed transition in previous experiments instead of inducing it.

With the importance of the synchronization location firmly established for a single disturbance frequency, Fong proceeded to investigate the response of broadband disturbances to single roughness elements [FWZ14a]. This was accomplished by introducing a blowing-suction actuator with a Gaussian pulse with a continuous frequency spectrum up to 1 MHz. Since the pulse is small and linear, FFT is used to decompose the perturbation and study the evolution of different perturbation frequencies. For the same Mach 5.92 flat plate steady-

state used in the previous study, Fong placed a roughness element at 0.185 m corresponding to a synchronization location frequency of 133.26 kHz and imposed the broad spectrum pulse. It was observed that just upstream of the roughness, frequencies lower than 120 kHz were amplified and remained amplified downstream of the roughness. Meanwhile, frequencies around 133.6 kHz and higher are strongly damped downstream of the roughness.

In this study, Fong also considered using multiple roughnesses for the first time [FWZ14a]. In considering the effect of multiple 2-D roughness elements, the first element was placed at 0.185 m at 50% of the boundary-layer height, and the second element was placed at 0.231 m with the same finite height as the first element. The second location corresponds to a synchronization location frequency of 119.26 kHz. By implementing a second downstream roughness, not only were frequencies between 119.26 and 133.26 kHz attenuated but frequencies higher than 133 kHz were attenuated further. With these results, Fong surmised that successive finite 2-D surface roughnesses could attenuate unstable frequencies indefinitely and thus could be used as a way to passively control boundary layer transition.

With a renewed focus on developing a boundary layer control method, Fong et al. engaged in an extensive parametric study focusing on roughness height, width, and spacing between multiple elements to find an optimal configuration [FWZ15]. Again the study was carried out on the same Mach 5.96 flat plate simulation as the two previous studies and excited second mode instabilities with a broad spectrum pulse. The roughness shape considered is still that of a half-ellipse. Regarding the height parameter, the study found that taller roughnesses, still within the boundary layer, had the most robust attenuation and amplification effects depending on the roughness location relative to the synchronization location of the considered frequency. A much weaker amplification/attenuation response was observed for the short roughnesses. Concerning the roughness width, a wider element produced a slightly stronger amplification/attenuation response, again relative to the roughness location and frequency's synchronization location. Fong notes, however, that the effect of width is almost negligible compared with the effect of height.

Regarding the spacing parameter, six cases with spacing from five to twenty-five times the roughness width were considered, and as with the other two parameters, closely packed

and highly separated elements were found to have their advantages and disadvantages. If the spacing is too wide, a frequency amplified by the first roughness may grow to such a level as to cause transition before the second roughness can attenuate it. Likewise, if the spacing is too close, a frequency lower than the second roughness synchronization location frequency will be significantly amplified by both the first and second roughness before a hypothetical third roughness can damp it. With these trends in hand, Fong proposed a reasonable second-mode attenuation transition control design that included an array of 2-D roughness elements with a height 50% of the boundary-layer thickness, a width of two boundary layer thickness and a spacing of 10 boundary-layer thicknesses.

Fong's work on the second-mode roughness effect culminated in an experimental validation with Prof. Schneider's group at Purdue University of the proposed boundary-layer control method [FWH15]. Fong hypothesized that the onset of hypersonic boundary layer transition could be delayed by placing 2-D roughness elements downstream of the synchronization location for the disturbance frequencies deemed most likely to cause transition. The flow control was designed for a blunt nose compression cone with a 1 mm nose radius, an initial 2° half-angle, a concave compression flairing 3 m in radius, and an overall length of 0.45 m. The experiment was carried out in the Boeing/AFOSR Mach 6 quiet wind tunnel at Purdue University. The test case had a freestream Mach number of 6, a freestream unit Reynolds number of $1.026 \times 10^7\,\mathrm{m}^{-1}$ and zero angle-of-attack. This test condition was chosen because it had been previously studied experimentally without roughness. In this previous smooth surface experiment, no transition was observed, but laminar breakdown was starting to occur at the end of the cone where a maximum N-factor of 14 was reached. Before the new surface roughness experiment, a steady-state solution of the smooth cone was computed and analyzed with LST. This provided information on the boundary layer thickness and stability characteristics. However, no unsteady DNS simulation was performed to verify the roughness configuration be for the validation experiment.

Among the second mode frequencies sampled, 285 kHz was deemed to be the most amplified and likely to cause transition. An interesting feature of a compression cone is that it maintains a nearly constant boundary layer height, and since the wavelength of the second-

mode is proportional to the boundary layer thickness [Mac84], and the frequency is related to the wavelength through phase speed, it follows that the 285 kHz mode is the only frequency worth attenuating. This contrasts with flat plates and straight cones where boundary layer growth causes a range of second mode frequencies. The 285 kHz synchronization location was calculated to be at 0.25 m. With the frequency and synchronization location in hand, the transition-delaying roughness design dictated that 2-D axisymmetric elements with a height of half of the local boundary-layer and a width twice the local boundary layer and a streamwise spacing of ten times their width be placed at 0.3 meters, 5 cm downstream of the synchronization location. The design required an array of six roughness strips in total. The design was not simulated prior to the experiment.

The results of the experiment were beneficial and validated the transition-delaying roughness design. The design, only minimally altered by the Purdue group, was implemented using two layers of high-temperature tape and trimmed to meet the specified height and width dimensions. The cone was coated in temperature-sensitive paint to measure global heat-transfer and rigged with five PCB pressure transducers. Comparing the pressure data between smooth and rough surface experiments showed that the second mode peaks near 285 kHz were no longer the major disturbance and were concealed by the noise floor of the transducer. Moreover, the heating associated with the saturation and breakdown of the second mode at the end of the smooth cone were not present in the rough case showing that transition was indeed delayed. Also, it was noted that the individual elements themselves do no generate significant secondary local heating on the cone.

The Purdue group concluded that the boundary layer appeared less unstable and that second mode breakdown was not present. The experiment shows that using 2-D surface roughness to attenuate the second mode instability waves works. With experimental validation, the idea of using surface roughness as a boundary-layer control device to delay laminar-turbulent transition was patented along with the methodology of using N-factor calculations and LST to identify the frequencies likely to cause transition, and their synchronization location [ZFW14].

Following Fong et al. extensive parameterization study on the roughness effect and its

novel approach to laminar-turbulent boundary-layer transition control, a reasonable question was, "how does a real-gas airflow affect this phenomenon?" After all, the experiments that preceded and complimented Fong's work are real-gas airflows in the absolute sense (See Refs. [Jam59, HS64, Fuj06, FWH15]). More specifically, does a perfect-gas assumption over predict or under predict second mode attenuation? Mortensen and Zhong answered this question by simulating a real-gas model for airflow over a flat plate with a 2-D roughness element [MZ16]. The DNS code, adapted from Duan's immersed interface code[DWZ10], used a five species gas model for air ($N_2, O_2, NO, N,$ and O) to model chemical nonequilibrium and a two-temperature model to simulate thermal nonequilibrium. The 2-D surface roughness was simulated with immersed interface methods and a body-fitted grid roughness in different instances for comparison. Two steady-state flow conditions at Mach 10 and 15 were used to study the effects of surface roughness. Roughness heights of 25% and 37.5% of the boundary layer thickness for the Mach 10 case were considered. Results for this condition were consistent with previous research for hypersonic flows with a perfect-gas assumption. For the Mach 15 flow, both real-gas and perfect-gas were run with roughness heights of 0, 10, 20, and 30% of the boundary-layer height. Overall, the real-gas flows resulted in a 40% reduction in the maximum amplitude of the second-mode, whereas the perfect-gas flow resulted in a 34.9% reduction. The conclusion drawn from these results is that stabilization of the hypersonic boundary-layer with two-dimensional roughness extends to real-gas flow. Moreover, the study found that in high Mach number and high enthalpy flows, where perfect-gas assumptions are invalid and real-gas effects are present, real-gas flows are more effective at stabilizing the second mode. Lastly, an unforeseen result of Mortensen's research was the stabilization of Mack's third mode instability for both real-gas and perfect-gas flows. The unstable third mode plays a subordinate role to second mode dominated transition and is not extensively studied because it is often stable or weakly unstable.

With the new research on transition-delaying roughness gaining awareness, the kinds of surface features responsible for inducing the roughness effect have become relevant. This is precisely what Sescu et al. started to tackle in 2017—their numerical study focused on the response of boundary-layer disturbances to various two-dimensional surface nonunifor-

mities [SSS17]. These nonuniformities included a forward step, a backward step, a forward-backward step combination, a backward-forward step combination, a surface hump, a surface dip, and sinusoidal walls above and below the mean surface. The surface nonuniformities were applied to a flat plate in a Mach 5.92 perfect-gas flow. All surface features had a height of 0.5 mm (although not explicitly stated, this height was within the boundary layer). The simulation utilized a high-accurate solver and shock-capturing methodology. Two types of disturbances were imposed from the wall as wall normal velocities: a sinusoidal pulse over one period and a periodic oscillation over the simulation duration. The disturbances contained a single frequency of 132 kHz. These conditions appear to follow from Fong's conditions used in his numerical studies with some discrepancies, most notably the wall temperature [FWZ12, FWZ14a, FWZ15, FWH15].

Sescu et al. found that all surface feature configurations were capable of reducing the amplitude of boundary layer disturbances to a certain degree, based on their shape and localized behavior except for the dip and backward-forward step combination [SSS17]. A significant insight from this study comes from the observation of pressure gradient across the studied surface features. That is, surface features with adverse pressure gradients followed by favorable pressure gradients or a succession of adverse and favorable pressure gradients were more likely to reduce the amplitude of disturbances propagating inside the boundary layer. For all its new insight on surface feature geometries, the study acknowledges that no stability analysis of the base flow was performed and that that analysis is important for identifying the second mode, its unstable frequencies, their synchronization location and for positioning surface features to optimize suppression.

1.2 Experimental Collaboration

The simulation conditions for each of the cases featured in this dissertation are taken from experimental conditions done by Dr. Katya Casper at Sandia National Laboratories (SNL). Early on in this research, a mutual interest in collaborating was expressed, in part due to the successful validation of Fong et al. passive second mode suppression roughness design

[FWH15] and for the need of further experimental validation.

Utilizing experimental conditions from previous smooth cone experiments provides benchmark cases and provides crucial transition and turbulent breakdown data, which cannot be obtained from steady simulations (see Ref. [CBH16]). The transition location data is necessary for identifying the unstable second mode frequency responsible for transition, and thus necessary for designing a functional transition-delaying roughness array.

Two experimental runs to validate a passive transition-delaying roughness array were carried out as part of the collaboration. These are cases C.2 and C.3 in this research. The design of the passive transition-delaying roughness array is detailed by case C.1 , which uses experimental conditions from a previous experiment in the same tunnel. A description of each of the cases and their simulation conditions can be found in Section 1.4 and Chapter 4.

Initially, case C.1 was computed to design a transition-delaying array of axisymmetric roughness strips. The design used similar height, width, and spacing criteria used by Fong et al. [FWH15]. The linear stability analysis of the steady-state solution identified the second mode frequency most likely to cause transition and it synchronization location. The finished design was then implemented by Casper on the test article. In the course of the experiment, however, a nose radius of 0.05 mm instead of the 0.5 mm prescribed by C.1 was used, which lead to the case C.2 and stability analysis of its steady-state solution to verify the feasibility of the applied roughness array.

Concurrent with the first experiment, the option of running a Mach 5 case was also available; this lead to case C.3. The height and width of the original roughness design were scaled down by the square root of the ratio of the freestream Mach numbers ($\sqrt{M_{\infty,C.3}/M_{\infty,C.2}} = \sqrt{5/8}$) while maintaining the same surface placement. The scaling was done to ensure the roughness strips remained within the boundary layer and would attenuate the second mode. This case offers the opportunity to explore off-design flow conditions on transition-delaying roughness.

All of the experiments were carried out in Sandia National Laboratories' Hypersonic Wind Tunnel (HWT). The tunnel is a blowdown to vacuum tunnel and can achieve freestream

Mach numbers of 5, 8 and 14 with freestream unit Reynolds numbers varying from 0.2 to $10 \times 10^6 \text{ft}^{-1}$. The tunnel can reach stagnation temperatures of 2500 °R. Run times are approximately 45 seconds at 45 minute intervals. The tunnel uses air at Mach 5 and nitrogen at Mach 8 and 14. The test section is 18" in diameter and can accommodate a model 4" to 5" in diameter.

1.3 Supersonic Mode in Low-Enthalpy Warm Wall Flow

While performing an unsteady simulation of case C.1-Ext without surface roughness, the acoustic-like waves seen in Fig. 1.6 were observed emitting from the boundary layer. These acoustic-like waves are qualitatively similar to those seen by Chuvakhov and Fedorov[CF16], and Knisely and Zhong[KZ19a, KZ19b, KZ19c, KZ20] in their direct numerical simulation (DNS) investigation of supersonic modes. Despite the similarities between the observed phenomena, the simulation conditions are very different. The supersonic mode reliably appears in flows with cooled walls, which makes the appearance of similar acoustic-like waves in a flow with a warm wall unexpected. In addition to transition-delaying surface roughness, this thesis also investigates acoustic-like emissions from the boundary layer of a low-enthalpy flow with a warm wall condition. Moreover, it also investigates an associated wave packet interference pattern between primary and satellite waves.

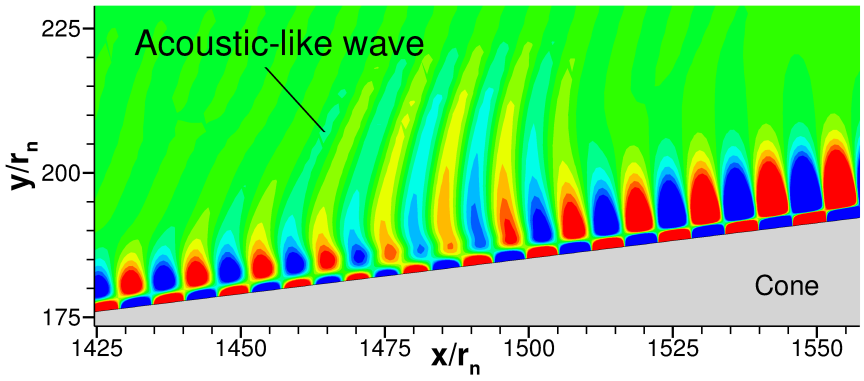

Figure 1.6: Weak acoustic-like waves emitting from the boundary layer. The waves are similar in appearance to those emitted by the supersonic mode.

As mentioned previously, the transition process has multiple pathways leading to turbulence [MRH94]. The research in this thesis is concerned with the pathway associated with low environmental forcing. This pathway is typified by discrete normal modes such as the Fast and Slow modes (modes F and S). These discrete modes are responsible for the well-known Tollmien-Schlichting waves and Mack's second mode instability, and most recently, by a renewed interest in supersonic modes. Recent research into supersonic modes has shown that unstable supersonic modes can contribute to Mack's second mode and increase the boundary layer's overall stability [Mor18, KZ19b, KZ19c]. For this reason, it is important to know under what physical conditions supersonic modes appear and their underlying physical mechanism, which is not currently well understood.

Supersonic modes were first described from Mack's numerical investigations in 1984 [Mac84], 1987 [Mac87], and 1990 [Mac90], and by Reshotko in 1991 citeReshotko1991. Mack showed there exists discrete neutral waves whose phase velocity caused the wave to propagate supersonically relative to the flow at the boundary layer edge. Such as when the discrete wave's phase velocity, c, is less than the propagation speed of a slow acoustic wave, $u - a$. In terms of relative Mach number, this relationship is given by,

$$\overline{M}(y) = \frac{\overline{u}(y) - c}{\overline{a}(y)} > 1, \tag{1.1}$$

where $\overline{M}(y)$, is the relative Mach number, $\overline{u}(y)$ is the steady boundary layer velocity, $c = \omega/\alpha$ is the disturbance phase velocity defined by circular frequency ω and streamwise wavenumber α, and $\overline{a}(y)$ is the local steady flow speed of sound.

Mack also showed that supersonic modes transfer energy away from the wall. In unsteady simulations this property is exhibited as acoustic-like emissions from the boundary layer into the flow behind the bow shock. In Mack's 1987[Mac87] numerical investigation, he found unstable supersonic waves—the instability however, was much weaker than the second mode instability and was thus considered less consequential.

Recently, there has been a renewed interest in supersonic modes. Their presence in high-enthalpy impulse facilities motivated Bitter and Shepard [BS15] to numerically investigate unstable supersonic modes over cold walls with LST. They found that decreasing the wall-to-

edge temperature ratio leads to unstable supersonic modes appearing over a broader range of frequencies. Their work also characterized an unstable discrete mode (like Mack's second mode instability) is likely to become supersonically unstable when the complex phase speed has to cross the slow acoustic continuous spectrum.

Shortly thereafter, Chuvakhov and Fedorov performed theoretical and DNS research on unstable supersonic modes where they studied highly cooled plates, with particular attention to the "spontaneous radiation of sound" [CF16]. Their theoretical work showed that Mack's second mode instability radiates acoustic-like waves out of the boundary layer when synchronized with the slow acoustic continuous spectrum when on a sufficiently cool plate. Tumin also studied the same flow conditions and concluded that the acoustic-like waves are not the result of nonlinear interactions due to nonparallel flow effects and that the boundary layer does have a mechanism for redistributing energy to the inviscid layer [Tum20].

The effect of nose bluntness on supersonic modes was recently studied by Mortensen [Mor18]. Mortensen's findings show that increasing the nose radius promotes supersonic mode instability and increases the severity of the instability, eventually dominating over the traditional second mode instability. Knisely and Zhong [KZ19b, KZ19c] also did an extensive LST and DNS study of supersonic modes in high-enthalpy flows on slender blunt cones with warm and cold walls. A notable result of theirs is that, while they could detect unstable supersonic modes with DNS in both hot and cold wall cases, LST analysis could only detect the supersonic mode in the cold wall case and not the other. They reasoned that this was due to modal interaction and suggested a combined LST and DNS approach to study the supersonic mode. Zanus et al. [ZKM20] revisited the case of Knisely and Zhong using a combination of LST, linear parabolized stability equations, and DNS. In one warmer wall case, they found the sound radiation came from a stable supersonic mode interacting with the slow acoustic.

Additional theoretical work in the area of supersonic mode instabilities has been done by Wu [Wu05] and, Wu and Zhang [WZ19], who studied the radiation of supersonic beams emanating from wavetrains. The result is qualitatively similar to the acoustic-like waves seen in unsteady supersonic mode simulations.

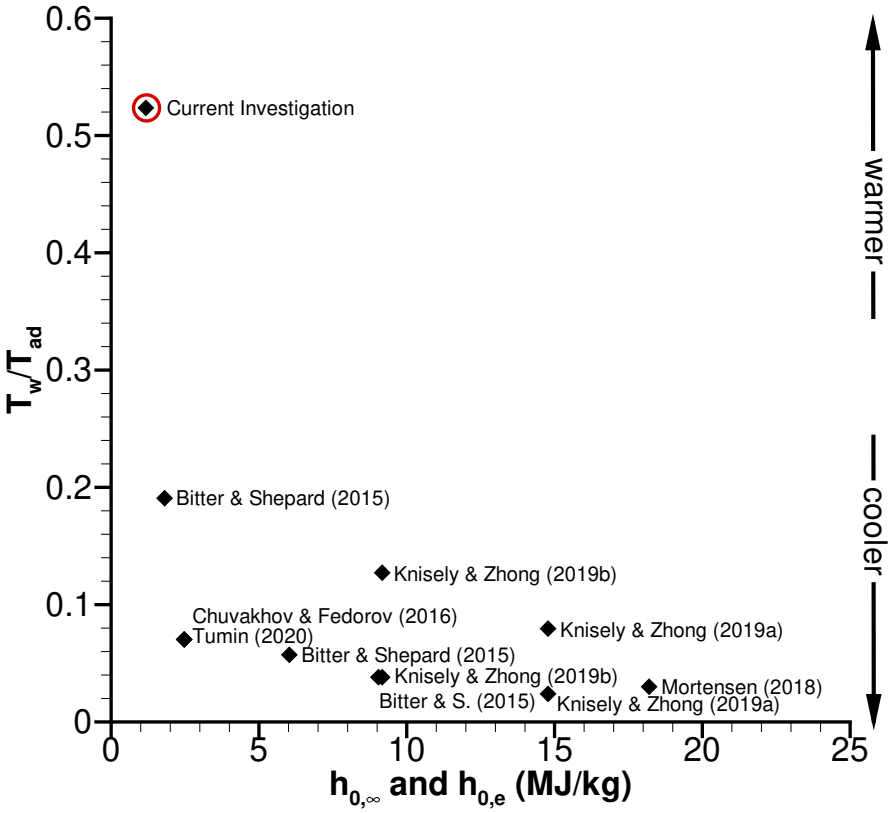

Figure 1.7: Comparison of recent supersonic mode investigations and the present investigation by freestream enthalpy and recovery temperature ratio.

The present paper shares some commonalities with the literature already discussed but differs significantly in wall temperature and flow enthalpy. To gain a better idea of where the current case lies in the space of supersonic mode investigations, Fig. 1.7 compares the total freestream enthalpy and wall-to-recovery temperature ratio of recent investigations with the present investigation. In some instances, the freestream enthalpy and temperature ratios had to be calculated from available parameters. The general trend in Fig. 1.7 shows that the most recent investigations are highly cooled flows over a range of enthalpies. This is because unstable supersonic modes are reliably known to exist in cooled flows, as Bitter and Shepard[BS15] put forth. Figure 1.7 also shows that the unstable supersonic mode is not highly dependent on the freestream stagnation enthalpy. Low-enthalpy cases with warmer wall conditions were included in the studies done by Chuvakhov and Fedorov[CF16], and

Mortensen[Mor18]. However, in both instances, no supersonic mode behavior was observed associated with the unstable second mode, and no other modes appear to have been investigated.

The current investigation is far removed from the general trend in Fig. 1.7, making this thesis's in-depth analysis of a low-enthalpy flow with warm wall condition unique in the literature. Amongst the recent supersonic mode investigations, the case parameters in this paper occupy an unexamined space that has been otherwise dismissed because the unstable mode did not have supersonic mode attributes, leaving stable modes unexplored. The current investigation seeks to understand an unexpected numerical result and to shed light on the supersonic mode in low freestream enthalpy flows with a warm wall condition.

1.4 Research Motivation & Simulations

This research aims to advance the understanding of the roughness effect from an idealized two-dimensional setting into a more realistic setting, such as investigating new conical geometries, studying the downstream effects of second mode attenuation, providing experimental evidence of second mode attenuation over a range of unstable frequencies, and exploring the passive roughness control strategy in off-design flow conditions. This research also aims to advance our fundamental understanding of hypersonic boundary layer instabilities by investigating the appearance of supersonic modes in low-enthalpy warm wall flow conditions. This dissertation makes inroads into all five of these objectives in the following ways:

1. **Straight blunt cone geometry:** Previous computational work on the roughness effect focused solely on flat plates. While this is a common test article geometry, especially for comparison with theoretical work, it is not a geometry often used by hypersonic experimentalists, whose cylindrical shock tubes and blow-down tunnels are better suited for axisymmetric geometries like straight blunt cones. Although Fong et al.'s experimental validation case was done on a compression cone, no unsteady simulation of the roughness design was undertaken [FWH15]. Instead, the flat plate observations of the roughness effect were presumed to yield similar attenuation results on the com-

pression cone. Conical flow fields are notably different from flat plate flow fields owing, among other things, to their prominent bow shock, entropy layer swallowing, conical surface, and flow relief angle. For all these differences, it is necessary to study the roughness effect on straight blunt cones.

2. **Downstream effect of second-mode attenuation:** Work on the roughness effect has already established that frequencies higher than the roughness element's synchronization frequency are attenuated while lower frequencies are amplified. This is the case whether a single element or an array of elements are implemented. Previous investigations did not adequately address the downstream behavior of the lower amplified frequencies. It is unknown whether they grow downstream normally or with an increased growth rate, and if the growth rate is enough to cause transition. In order to investigate the downstream behavior of un-attenuated frequencies, a transition-delaying roughness array is applied to the middle of a one-meter long cone, providing enough length for unattenuated frequencies to grow downstream.

3. **Experimental investigation of roughness effect in growing boundary layer:** A notable commonality of flat plates and straight blunt cones is their growing boundary layers. A growing boundary layer is significant because the second mode's wavenumber is proportional to the boundary layer thickness, meaning that a range of unstable frequencies are present. In flows with a near-constant boundary layer thickness, like the compression cone in Fong et al.'s experimental validation [FWH15], only a single dominant unstable frequency is present. To test the ability of the roughness effect to attenuate a wide range of frequencies, the design and analysis of a Mach 8 transition-delaying roughness array is presented and applied to a straight blunt cone test article. The joint Mach 8 experiment provides validation that the passive boundary layer control strategy can attenuate the second mode instability in a boundary layer containing a broad range of unstable frequencies.

4. **Experimental investigation of off-design flow conditions:** A common concern about transition-delaying surface roughness is how well will it perform in off-design

flow conditions, and how will it respond to flow instabilities other than the second mode. These concerns are investigated by subjecting the Mach 8 designed roughness array to Mach 5 flow conditions. Not only are the flow conditions drastically different, but the flow is dominated by Mack's first mode instability.

5. **Investigate the supersonic mode in a low-enthalpy warm-wall flow:** While investigating transition-delaying surface roughness, acoustic-like waves are observed emanating from the boundary layer of case C.1-Ext. The acoustic-like wave emissions are qualitatively similar to those attributed to the supersonic mode. However, the supersonic mode responsible for such emissions is often found in high-enthalpy flows with highly cooled walls, making its appearance in a flow with relatively low freestream enthalpy and a warm wall unexpected. The current investigation seeks to understand a new numerical result and shed light on the supersonic mode in atypical flow conditions.

Four cases have been computed to investigate these research objectives. The cases differ primarily in their freestream Mach number, blunt nose radius, r_n, and overall length, l. The freestream flow conditions, such as density, pressure, temperature, stagnation enthalpy, etc., for each case are tabulated in Chapter 4.

Case C.1: $M_\infty = 8$, $r_n = 0.5$ mm, $l = 0.517$ m.

- Steady and unsteady simulations of single roughness strip with planer disturbance wave. This simulation introduces a simple transition-delaying roughness on the new straight cone geometry and can be easily compared to flat plate 2-D roughness simulations. The results of this simulation are featured in [HZ17].
- The linear stability results from this case are used to design the roughness array used in the Mach 8 and Mach 5 experimental validation cases.

Case C.1-Extended: $M_\infty = 8$, $r_n = 0.5$mm, $l = 1.0$m.

- A more extensive LST analysis of C.1 on a longer cone. The longer cone analysis extends the range of lower unstable second mode frequencies. And reveals other discrete modes such as F2, and F3.

- The case is used to study the downstream growth of unstable frequencies un-attenuated by a single roughness strip.
- The transition-delaying roughness array designed in C.1 is applied to the cone to study attenuation provided by the array, as well as study the downstream growth of un-attenuated unstable frequencies.
- Unsteady simulations of the cone with no surface roughness featuring acoustic-like waves emanating from the boundary layer are analyzed for the supersonic mode.

Case C.2: $M_\infty = 7.84$, $r_n = 0.05$mm, $l = 0.517$m.

- Replicate and analyze the Mach 8 experiment flow conditions and compare with the roughness array design. This ensures that the changes in sharp cone geometry did not hamper the roughness array's ability to attenuated the second mode.

Case C.3: $M_\infty = 4.96$, $r_n = 0.5$mm, $l = 0.517$m.

- Replicate the Mach 5 experiment flow conditions.
- Analyze the steady-state with LST for 2-D and oblique waves. This analysis contributes to first mode/second mode interaction research.

With these research objectives in mind, this dissertation contributes significantly to the study of transition-delaying surface roughness and the fundamental understanding of stable supersonic modes. This dissertation begins with an overview of the governing equations and numerical methods in Chapter 2, followed by an overview of Linear Stability Theory and the stability analysis used in this research in Chapter 3. Chapter 4 provides a detailed description of the cone geometry and freestream conditions, and a description of Sandia's Hypersonic wind tunnel facilities and model instrumentation. Chapter 5 presents the analysis of case C.1 and the design of the transistion-delaying surface roughness. The results of the extended cone, case C.1-Ext, and the downstream behavior of unattenuated unstable frequencies are presented in Chapter 6. The Mach 8 and Mach 5 experimental validation cases are provided in Chapter 7. The results on the supersonic mode in a low-enthalpy flow investigation are presented in Chapter 8. Lastly, the summary and conclusion of the research are presented in Chapter 9.

CHAPTER 2

Governing Equations & Numerical Methods

This dissertations computational fluid dynamic (CFD) results were obtained using a high-order shock-fitting code. These CFD results include steady-state solutions and unsteady simulations. The steady-state solutions provide insight into the flow field and provide the boundary layer profiles used in stability analysis. They are also used as the base flow in unsteady simulations, in which a blowing-suction actuator introduces a propagating disturbance. This chapter contains a detailed description of the numerical methods and simulation approaches used to obtain the CFD results presented in the following chapters. The contents include the governing equations solved by the shock-fitting code. A description of the shock-fitting method and its curvilinear grid transformation implementation. The high-order finite difference schemes and how they are used to discretize the governing equations. The analytical functions for discrete surface roughness and how they are adapted to work with a body-fitted grid. A description of the unsteady DNS pulse and its implementation. And lastly, the simulation steps taken with the shock-fitting code to obtain the results presented in this dissertation.

2.1 Governing Equations

This dissertation uses direct numerical simulation (DNS) of the Navier-Stokes equations to obtain steady and unsteady solutions of hypersonic flow over a blunt cone. The simulation code utilizes a unique shock-fitting approach combined with high-order finite difference schemes to solve for the location of the bow shock and flow field over conical geometries. Specifically, the code solves the conservation-law form of the three-dimensional Navier-Stokes

equations assuming a calorically perfect gas. Written in vector form without body forces or external heat addition, the governing equations are,

$$\frac{\partial U}{\partial t} + \frac{\partial F_j}{\partial x_j} + \frac{\partial G_j}{\partial x_j} = 0, \tag{2.1}$$

in which U is the state vector of conserved quantities, F_j is the inviscid flux, and G_j is the viscous flux in the j^{th} spatial direction. The state and flux vectors are defined as,

$$U = \{\rho,\ \rho u_1,\ \rho u_2,\ \rho u_3,\ e\}^T, \tag{2.2}$$

$$F_j = \{\rho u_j,\ \rho u_1 u_j + p\delta_{1j},\ \rho u_2 u_j + p\delta_{2j},\ \rho u_3 u_j + p\delta_{3j},\ (e+p)u_j\}^T, \tag{2.3}$$

and

$$G_j = \{0,\ \tau_{1j},\ \tau_{2j},\ \tau_{3j},\ \tau_{jk}u_k - q_j\}^T, \tag{2.4}$$

where ρ is density, u_i is the velocity vector, e is internal energy, p is pressure, τ_{ij} is the viscous stress tensor, q_j is the heat flux vector, and δ_{ij} is the Kronecker delta. The internal energy, viscous stress tensor, and heat flux are defined as follows,

$$e = \rho\left(c_v T + \frac{u_k u_k}{2}\right), \tag{2.5}$$

$$\tau_{ij} = \mu\left(\frac{\partial u_i}{\partial x_j} + \frac{\partial u_j}{\partial x_i}\right) + \delta_{ij}\lambda\frac{\partial u_k}{\partial x_k}, \tag{2.6}$$

and

$$q_j = -\kappa\frac{\partial T}{\partial x_j}, \tag{2.7}$$

where T is temperature, μ is dynamic viscosity, λ is the bulk viscosity equal to $-2/3$, and κ is the thermal conductivity. Assuming a calorically perfect gas, Eq. (2.1) is closed with the ideal gas law,

$$p = \rho R T, \tag{2.8}$$

which is a reasonable assumption for low-enthalpy hypersonic flows. For the simulations featured in this dissertation, gases of nitrogen and air are used. Their properties are implemented through their specific gas constant: $R_{N_2} = 296.8 J/kgK$ and $R_{air} = 287.0 J/kgK$. The specific heats c_p and c_v are held constant with a specific heats ratio of $\gamma = 1.4$. Moreover, the dynamic viscosity is calculated using Sutherland's law [Sut93],

$$\mu = \mu_r\left(\frac{T}{T_o}\right)^{3/2}\frac{T_o + T_s}{T + T_s}, \tag{2.9}$$

where $\mu_r = 1.7894 \times 10^{-5}$ N·s/m^2, $T_o = 288.0$K, and $T_s = 110.33$K. Lastly, the thermal conductivity κ is computed as,

$$\kappa = \frac{c_p \mu}{Pr} \tag{2.10}$$

using a constant Prandtl number of 0.72. In general, the conservative-law form of the Navier-Stokes equation constitutes the governing equations solved by the simulation code.

The simulation code makes use of a body-fitted grid in order to accurately compute the bow shock's location and movement. This requires that Eq. (2.1) be solved in curvilinear coordinates that follow the underlying conical geometry and shock shape, as illustrated in Fig. 2.1. This is done by transforming the Cartesian coordinates system (x, y, z, t) into the generalized nonorthogonal curvilinear coordinate system (ξ, η, ζ, τ) using the transform:

$$\begin{cases} \xi = \xi(x,y,z) \\ \eta = \eta(x,y,z,t) \\ \zeta = \zeta(x,y,z) \\ \tau = t \end{cases} \Leftrightarrow \begin{cases} x = x(\xi,\eta,\zeta,\tau) \\ y = y(\xi,\eta,\zeta,\tau) \\ z = z(\xi,\eta,\zeta,\tau) \\ t = \tau \end{cases}, \tag{2.11}$$

where ξ is in the direction tangent to the cone surface, η is normal to the cone surface, ζ is in the azimuthal direction, and τ is time. After taking the necessary derivatives of Eq. (2.11) and applying the transformation to Eq. (2.1) the governing equations become,

$$\frac{1}{J}\frac{\partial U}{\partial \tau} + \frac{\partial E'}{\partial \xi} + \frac{\partial F'}{\partial \eta} + \frac{\partial G'}{\partial \zeta} + \frac{\partial E'_v}{\partial \xi} + \frac{\partial F'_v}{\partial \eta} + \frac{\partial G'_v}{\partial \zeta} + U\frac{\partial (1/J)}{\partial \tau} = 0 \tag{2.12}$$

where J is the Jacobian of the coordinate transformation and

$$E' = \frac{F_1\xi_x + F_2\xi_y + F_3\xi_z}{J} \tag{2.13}$$

$$F' = \frac{F_1\eta_x + F_2\eta_y + F_3\eta_z}{J} \tag{2.14}$$

$$G' = \frac{F_1\zeta_x + F_2\zeta_y + F_3\zeta_z}{J} \tag{2.15}$$

$$E'_v = \frac{F_1\xi_x + F_2\xi_y + F_3\xi_z}{J} \tag{2.16}$$

$$F'_v = \frac{F_1\eta_x + F_2\eta_y + F_3\eta_z}{J} \tag{2.17}$$

$$G'_v = \frac{F_1\zeta_x + F_2\zeta_y + F_3\zeta_z}{J}. \tag{2.18}$$

At its core, the code is solving Eq. (2.12). The code was originally developed and implemented by Zhong[Zho98]. The same base code was used by Fong and Zhong [FWZ14b], Huang and Zhong [HZ14], and Lei and Zhong [LZ12] for simulating perfect gas hypersonic flow.

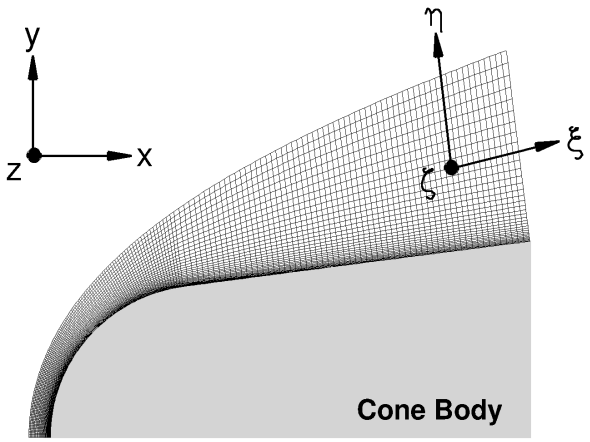

Figure 2.1: Illustration of the relationship between the curvilinear coordinate system to the Cartesian coordinate system near the blunt nose tip.

Within this text, the CFD code is occasionally referred to as a DNS code. However, within the literature, DNS typically implies that the simulation has been resolved to turbulent scales. Since the research in this dissertation is primarily concerned with the linear growth of boundary layer instabilities and not turbulence, it is not computationally advantageous to resolve turbulent scales. In general, however, the conservative form of the Navier-Stokes equation implemented by the code makes no simplifying assumptions about the underlying flow physics and is thus capable of direct numerical simulation with adequate scale resolution. The only limiting physical assumption that goes into solving Eq. (2.1) is its use of a calorically perfect gas model, which limits the application of the code to low-enthalpy hypersonic flows.

2.2 Shock-fitting Method & Simulation Domain

The code used in this dissertation uses a shock-fitting approach to solve for the bow shock over a hypersonic cone. Shock-fitting methods incorporate the shock discontinuity into the

flow field solution by treating the shock as a computational boundary and using shock relations to solve for the shock's position. In doing so, shock-fitting methods avoid shock smearing and non-physical oscillations introduced by other shock techniques. The end result is a defined shock front and an accurate flow field behind the shock. Thus, shock-fitting methods are ideally suited to the physical problem of simulating hypersonic flow over a cone.

Going into more detail, the shock-fitting algorithm seeks to solve for the shock position, $H(x, y, z, t)$. As such, H and it's speed, H_t, must be solved as independent flow variables. This is accomplished by taking the Rankine-Hugonoit relations, which provide the flow boundary conditions behind the shock, as a function of the freestream velocity, U_∞, and the shock front velocity, v_n. The shock front velocity is determined by a characteristic compatibility equation at the grid point immediately behind the shock. The resulting ODE for the shock position is then solved alongside the governing equations.

The shock-fitting algorithm's solution procedure is relatively simple. The algorithm assumes an unsteady shock front and an initial arbitrary shock position. The algorithm converges when the shock speed reaches zero, and the shock position reaches a steady state.

The shock-fitting method also pairs well with the body-fitted curvilinear grid transformation introduced by Eq. (2.11). Since the method treats the bow shock as a domain boundary, the shock is the transformed surface:

$$\eta(x, y, z, t) = \eta_{max} = constant. \tag{2.19}$$

Accordingly, the functions for the shock position and speed take the form $H(\xi, \zeta, \tau)$ and $H_\tau(\xi, \zeta, \tau)$, and are solved alongside the transformed governing equations, Eq. (2.12). Moreover, since the shock surface undergoes transient movements, η is the only coordinate in the transformed domain that is also a function of t. In contrast, surfaces of constant ξ and ζ are fixed. Additional details on the shock fitting algorithm can be found in Ref. [Zho98].

2.3 Finite Difference Schemes

An explicit 5^{th}-order upwind scheme and an explicit 6^{th}-order central finite-difference scheme are used to discretize the inviscid and viscous terms of Eq. (2.12) in the ξ and η-directions. A seven point stencil is used in both instances:

$$\frac{df_i}{dx} = \frac{1}{hb_i}\sum_{k=-3}^{3} a_{i+k}f_{i+k} - \frac{A}{6!b_i}h^5\left(\frac{\partial f^6}{\partial^6 x}\right) \tag{2.20}$$

where the stencil coefficients are,

$$a_i = -\frac{5}{3}A, \quad a_{i\pm1} = \pm 45 + \frac{5}{4}A, \quad a_{i\pm2} = \mp 9 - \frac{1}{12}A, \quad a_{i\pm3} = \pm 1 + \frac{1}{12}A, \quad b_i = 60, \tag{2.21}$$

and h is the step size. A dissipation scaling coefficient of $A = -6$ is used to achieve a low dissipation upwind scheme for the inviscid terms, and $A = 0$ is used to obtain a central scheme for the viscous terms. Second order derivatives are obtained by applying Eq. (2.20) twice. Fourier collocation is used for derivatives in the ζ-direction for axisymmetric cases and finite-difference is used in non-axisymmetric cases.

Lastly, Lax-Friedrichs flux-splitting is used for the inviscid flux terms resulting in

$$F' = F'^{+} + F'^{-} \quad \text{where} \quad F'^{\pm} = \frac{1}{2}\left(F' \pm \Lambda U\right), \tag{2.22}$$

and Λ is a diagonal matrix that ensures F'^{+} and F'^{-} contain only positive and negative eigenvalues, respectively. A low storage 3rd-order Runge-Kutta method[Wil80] is used to converge the steady-state as well as to advance the unsteady solutions.

2.4 Discrete Body-fitted Roughness

The discrete surface roughness elements in this work are implemented by mapping the function of an analytical shape to a cone frustum. In order to be mapped, the analytical function must be compatible with the grid transformation described by Eq. (2.11). The transforms grid metrics require that the shape have continuous derivatives throughout the domain. Consequently, sharp-edged geometries such as diamonds, squares, or channels are not suitable roughness shapes. Such geometries can be implemented using a finite volume or immersed

interface method approach but at the cost of losing high-order accuracy around the roughness element. By limiting the geometry to analytical shapes, the high-order accuracy of the solution is maintained. In this work, the roughness shape is defined as the difference of two hyperbolic tangents,

$$y'(x', z') = \frac{1}{2}h\left\{\tanh\left[q\left(x' + \frac{w}{2}\right)\right] - \tanh\left[q\left(x' - \frac{w}{2}\right)\right]\right\} \tag{2.23}$$

where x', y', and z' are Cartesian coordinates prior to being mapped to the cone surface. The parameters h and w control the height and width of the roughness, and q is a parameter that controls the edge steepness. Equation (2.23) is mapped to the cone's frustum using the following system of rotations and translations:

$$\begin{aligned} x &= cos(\theta_{\frac{1}{2}})x' - sin(\theta_{\frac{1}{2}})y' + x_c \\ y &= [sin(\theta_{\frac{1}{2}})x' + cos(\theta_{\frac{1}{2}})y' + y_c]cos(\phi) \\ z &= [sin(\theta_{\frac{1}{2}})x' + cos(\theta_{\frac{1}{2}})y' + y_c]sin(\phi) \end{aligned} \tag{2.24}$$

in which x, y, and z are the Cartesian coordinates in the physical domain, $\theta_{\frac{1}{2}}$ is the cone half-angle, ϕ is the angle in the cone's azimuthal direction about the cone, and x_c and y_c is the surface location of the roughness center at $\phi = 0°$.

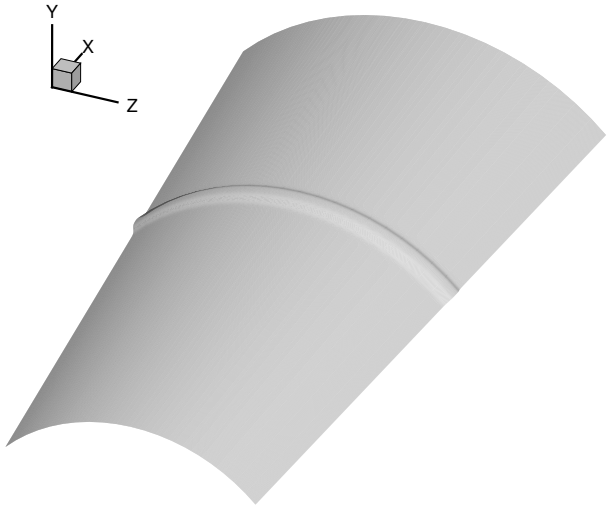

Figure 2.2: Roughness shape generated by Eq. (2.23) for $q = 1500$ after being mapped to a cone surface.

Figure 2.2 plots Eq. (2.23) as it would appear on a cone frustum. The figure shows that applying Eq. (2.24) produces a circumferential roughness strip. Parametric investigations of the roughness damping effect, thus far, have only investigated the importance of an elements overall height and width, with little attention paid to the physical shape (e.g., elliptical strips vs. square strips). Experiments and simulations with comparable results but slightly different shapes suggest that the physical geometry has little bearing on the roughness's ability to attenuate boundary layer disturbances [FWH15, FWZ15]. The more important parameter appears to be the roughness elements height.

Also central to the roughness transition-delaying flow control strategy is using an array of roughness elements to target a wide range of unstable frequencies. Simulating an array of roughness elements is done by expressing the surface roughness function as the sum of multiple individual roughness elements offset from one another. The resulting roughness array function is,

$$y'(x', z') = \frac{1}{2}\sum_{i=1}^{N} h_i \left\{ \tanh\left[q\left((x' - l_i) + \frac{w_i}{2} \right) \right] - \tanh\left[q\left((x' - l_i) - \frac{w_i}{2} \right) \right] \right\} \tag{2.25}$$

where i is the index of the roughness element, and l_i is the distance between the i^{th} element and the first element in the array; the remaining variables are the same as Eq. (2.23). Equation (2.25) is subject to the same grid transform metric constraints as Eq. (2.23) and is also mapped to the cone's surface using Eq. (2.24). Figure 2.3 diagrams Eq. (2.25) as it would appear mapped to a cone for an array of six roughness strips. The roughness configuration in Fig. 2.3 is the same one used for the multi-roughness array cases featured in this research.

2.5 Direct Numerical Simulation of Disturbances

To simulate unsteady disturbances, a circumferential blowing-suction actuator is used to introduce a pulse into a resolved steady-state flow. The circumferential slot extends azimuthally around the cone and produces a two-dimensional disturbance in the streamwise direction. The actuator is placed upstream of the roughness element or roughness array. The pulse is sinusoidal in space and its amplitude has a Gaussian amplitude in time. The

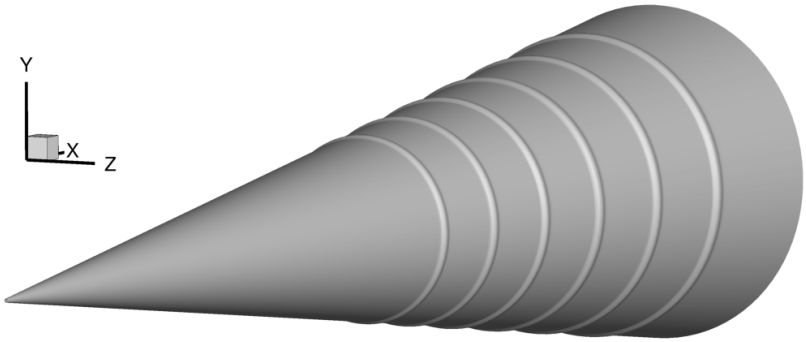

Figure 2.3: Roughness array generated by Eq. (2.25) for six strips with $q = 2000$. This arrangement of the same configuration used in the C.1-ext, C.2, and C.3 multi-roughness simulations

sinusoid prevents the introduction of additional mass into the simulation, which could change the flows underlying stability characteristics. The Gaussian term makes it possible to introduce a broadband pulse into the flow. The frequency spectrum of the pulse is chosen to be broad enough as to include the most unstable mode frequencies for the given flow conditions. Downstream of the actuator, each frequency is examined for amplification or attenuation based on the frequency spectrum of a temporal Fourier decomposition (FFT). This technique of using a Gaussian pulse to examine mode amplification/attenuation was previously implemented by Fong and Zhong[FWZ12] and Knisely and Zhong[KZ19b, KZ19c].

The mass flux of the blowing-suction actuator follows the equation,

$$\dot{m}_p(s,t) = \varepsilon(\rho U)_\infty \exp\left(-\frac{(t-\mu)^2}{2\sigma^2}\right) \sin\left(2\pi \frac{s-s_c}{l}\right) \tag{2.26}$$

for $s_c < s < s_c + l_a$ and $t > 0$. In which μ is the mean, σ is the standard deviation, s_c is the starting location for the actuator on the cone surface, and l_a is the length of the actuator. The mass flux is scaled as $\varepsilon(\rho U_\infty)$, where imposing a weak ε keeps the flow field's response linear and prevents perturbation of different frequencies from interacting with one another. In this way the pulse can be decomposed by FFT and each frequency can be studied independently. The mean of the pulse, μ, is defined in terms of a minimum mass flux, $(\rho v)_{min}$, which is the initial mass flux at $t = 0$. Naturally, $(\rho v)_{min}$ is very small, preferably close to zero, however not too small that an appreciable amount of computational time passes before the pulse is

fully developed. The equation for μ is given as,

$$\mu = \sqrt{-2\sigma^2 ln\left(\frac{(\rho v)_{min}}{\varepsilon(\rho U)_\infty}\right)}. \tag{2.27}$$

By defining it in this way, μ can be fixed with a reasonable $(\rho v)_{min}$ regardless of the simulation conditions. Thus, by design, the only remaining free parameter in Eq. (2.26) is σ which permits direct control over the frequency content of the pulse. Hence, when designing the pulse for a particular case, only the standard deviation needs to be modified. The pulse parameters used in this work are given in Table 2.1, and the time history of Eq. (2.26) and its corresponding FFT are given in Fig. 2.4. Figure 2.4b shows that the spectrum of the pulse contains nominal frequencies greater than 1MHz, which is sufficient for the range of unstable mode frequencies found in the unsteady simulation.

Table 2.1: Gaussian pulse parameters for DNS

Parameter	ε	$(\rho v)_{min}$ [kg m/s]	σ [μs]	μ [μs]	s_c [m]	l [mm]
Value	10^{-3}	10^{-10}	0.3	2.0398	0.1025	1.9703

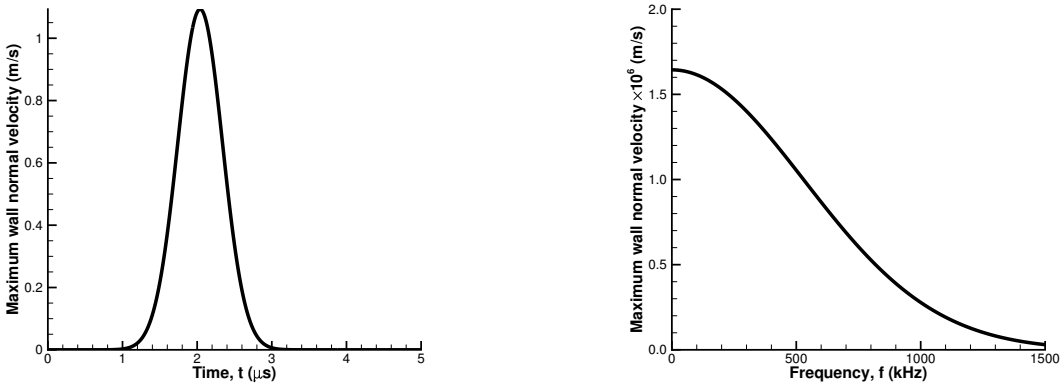

(a) (b)

Figure 2.4: (a) Time history of the maximum wall normal velocity. (b) FFT of maximum wall normal velocity in (a).

2.6 Simulation Approach

Studying the effect of surface roughness on hypersonic boundary layer instabilities is a multi-step process that requires several steady-state solutions and separate unsteady simulations. Broadly speaking, in order to study any surface roughness configuration, a steady-state solution containing the configuration and a smooth surface solution are needed. These steady-states then serve as the base flow for unsteady simulations. The smooth surface solution serves as a benchmark for evaluating the roughness configuration.

The process starts with computing the steady-state flow for the smooth surface case with the shock-fitting code described in this chapter. Once converged, this baseline flow guides the surface roughness design process. Initially, LST analysis of the flow field establishes the range of unstable frequencies that a roughness configuration may want to attenuate. Next, synchronization location results obtained from the LST analysis dictate the placement of roughness elements. Lastly, the local boundary layer profiles from the steady-state solution determine the element's physical dimensions.

After the roughness configuration under study is designed, the smooth surface steady-state solution is duplicated, and the roughness configuration is added to the surface. The altered simulation is then re-converged. This approach saves computational time by using the smooth surface solution as an initial guess.

Next, a blowing-suction actuator is added to both converged steady-state solutions. The pulse's standard deviation is chosen to include the entire range of unstable frequencies present in the flow. The simulation is then run, and the time history of the disturbance is recorded. The simulation is complete when the pulse has propagated throughout the entire domain. The time history of both simulations is decomposed with FFT analysis, and the results are compared.

In the case of the supersonic mode study presented in Chapter 8, where no surface roughness was studied, only a smooth surface steady-state solution and its unsteady DNS were required.

2.7 Grid Independence and Convergence

Grid independence and convergence studies were performed for each of the cases. The results in this section look specifically and the convergence of case C.1-Ext. The grid independence study looks at two grid distributions along the cone frustum: a coarse grid of 3602x121 points and a finer grid of 7202x181 points. Both grid solutions were converged to a relative pressure error of $\mathcal{O}(\varepsilon_p) = 10^{-9}$. Figure 2.5a plots the velocity boundary layer at $s/r_n = 500$ for 121 and 181 points in the wall-normal direction. The location was chosen based on its proximity to the blowing-suction actuators used in the unsteady simulation. The ability to achieve a grid independent steady-state solution is highly dependent on the number of points in the wall-normal direction due to the steeper gradients in the boundary layer. The profiles are in good agreement for both grid point distributions, indicating an independent solution. The largest errors are confined to the region along the bow shock, where the wall-normal grid stretching is coarsest, and far away from the boundary layer.

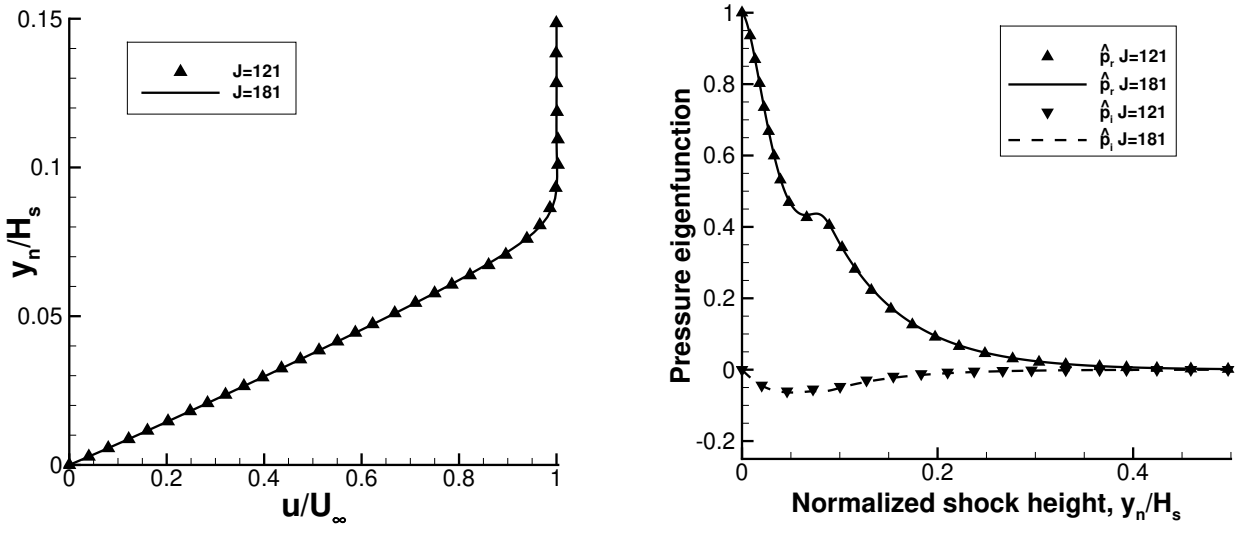

(a) (b)

Figure 2.5: Steady-state grid independence study of (a) the velocity boundary layer, and (b) the complex pressure perturbation eigenfunction at $s/r_n = 500$ for wall-normal grid distributions J=121 and 181.

The accuracy of the stability calculations obtained from LST is also very sensitive to the wall-normal grid distribution of the steady-state, as LST makes use of numerical derivatives obtained from the steady state solution. Therefore, as a double check, the eigenfunctions of each wall-normal grid distribution can also be compared to check for steady state grid independence. As such, Fig. 2.5b plots the real and imaginary parts of the pressure eigenfunction at $s/r_n = 500$ and 160 kHz. Again there is good agreement between the two grid point distributions of the steady state.

Unlike the gradients in the wall-normal direction, the gradients in the streamwise direction are less steep and thus require fewer points to obtain a grid independent solution: $I = 3602$ points provided and average of 1.8 pts/unit and $I = 7202$ points provided and average of 3.6 pts/unit. As can be seen from the contour comparison in Fig. 2.6, doubling the number of points in the streamwise direction had very little effect on the solution. In summary, there were no significant differences in the steady flow profiles or the LST calculations based on them.

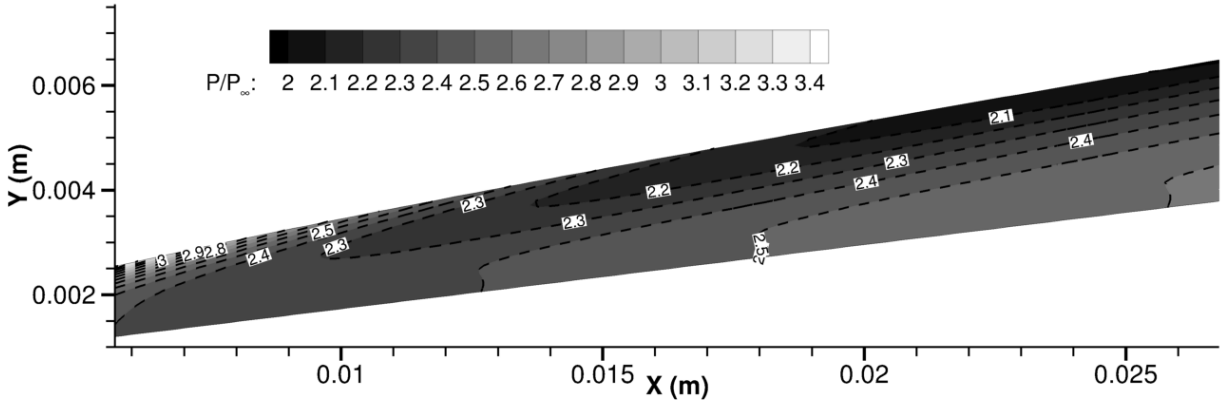

Figure 2.6: Comparison of steady state pressure contours for two different grid densities of 3602x121(dashed contour) and 7202x181 (shaded contour)

CHAPTER 3

Linear Stability Theory & Analysis

The boundary layer stability analysis performed in this work is based on compressible linear stability theory (LST). The theory is primarily concerned with finding normal mode solutions to the perturbed Navier-Stokes equations. These normal mode solutions are seen as instability wave propagating within the boundary layer, and LST provides insight into the linear growth and decay of these instability waves. The theory's linear framework prescribes that the instabilities' amplitudes remain small relative to the steady-state flow; otherwise, non-linear processes will take over and lead to saturation and turbulent breakdown[MRH94]. Since this research is primarily concerned with the attenuation of such instabilities before reaching turbulent transition, LST is the proper tool for analyzing the boundary layer's stability characteristics.

Specifically, LST is used to determine a steady-state flow's stability characteristics prior to unsteady simulations and to design the transition-delaying surface roughness. The analysis provides the data needed to construct a flows neutral stability curve, modal phase speed and growth rate plots, transition N-factors, and mode shapes. However, before going into further detail on stability analysis, it is prudent to describe the derivation and solution of the compressible LST equations.

The derivation of the compressible linear stability equations starts with the Navier-Stokes equations for a viscous compressible ideal gas, Eq. (2.1). Perturbation theory is applied to the equations wherein an instantaneous solution comprised of a steady term and a fluctuating term is assumed. Thus, each flow variable is represented as the sum of a steady quantity and a fluctuating quantity,

$$q(x, y, z, t) = \bar{Q}(x, y, z) + \tilde{q}(x, y, z, t) \tag{3.1}$$

where q represents the flow variables of velocity, temperature, and pressure. It should be noted that the variables in Eq. (3.1) and the variables throughout this chapter are nondimensional unless specified otherwise. The instantaneous variable forms are then substituted into Eq. (2.1). Wholly steady terms that satisfy Eq. (2.1) are subtracted from the substitution, and higher-order fluctuating terms are assumed small and linearized. The result is the linearized perturbation equations, which can be found in full detail in Ref. [Mal90].

Next, the stability of a locally parallel compressible boundary layer flow is considered. The 'locally parallel flow' assumption assumes the remaining steady quantities are a function of y only:

$$U = U(y), \quad V = 0, \quad W = W(y), \quad T = T(y), \quad \rho = \rho(y), \tag{3.2}$$

with a constant pressure across boundary layer. In this work the steady-state quantities are provided by the steady-state solutions obtained by the shock-fitting simulation code. Strictly speaking, a steady conical flow is not a parallel flow, but taken on a local basis it can be approximated as such. After some manipulation of the perturbation quantities, a coupled set of five ordinary differential equations is obtained.

From this set of coupled ordinary differential equations, a normal mode solution is assumed for the fluctuation variables of the form:

$$\tilde{q}(x, y, z, t) = \hat{q}(y) \exp[i(\alpha x + \beta z - \omega t)], \tag{3.3}$$

where $\tilde{q}$ is the vector of the fluctuating variables, $\{\tilde{u}, \tilde{v}, \tilde{p}, \tilde{T}, \tilde{w}\}^T$, $\hat{q}(y)$ is the vector of their complex eigenfunctions, α and β are the wavenumbers, and ω is the circular frequency. Substituting the normal mode solution into the system for the fluctuating terms results in a system of ODE's for the linear disturbances in the form of

$$\left(\mathbf{A} \frac{d^2}{dy^2} + \mathbf{B} \frac{d}{dy} + \mathbf{C} \right) \hat{q}(y) = 0, \tag{3.4}$$

where $\hat{q}$ is a vector defined by $\{\hat{u}, \hat{v}, \hat{p}, \hat{T}, \hat{w}\}^T$ and $\mathbf{A}$, $\mathbf{B}$, and $\mathbf{C}$ are complex square matrices whose entries can be found in Ref. [Mal90]. Equation (3.4) constitutes a eigenvalue problem, wherein Dirichlet boundary conditions are applied at the surface and in the far field,

$$\hat{q}(y) = 0 \text{ at } y = 0 \text{ and } y \to \infty. \tag{3.5}$$

Strictly speaking, the far field boundary conditions do not take into consideration the presence of the bow shock, which is present in the steady state shock-fitting simulation. However, for the purposes of this research the shock, is considered to be sufficiently far away from the boundary layer as to not have a significant effect on the stability calculations. Solving the resulting eigenvalue problem yields the complex dispersion relation $\omega = \Omega(\alpha, \beta)$ for the flow field.

The determination of the dispersion relation is a two-step process. Initially, an approximate value of the eigenvalue is obtained from using a global method and refined using a local method. Specifically, the global method is a standard QZ algorithm used to solve the generalized eigenvalue problem. The method produces numerous eigenvalues, many of which produce spurious numerical eigenfunctions. Nevertheless, among the spurious values are eigenvalues that relate to the Fast and Slow modes (Mode F and S), which produce physical mode shapes (eigenfunctions). Work done by Ma and Zhong provides a means to identify these physical modes by plotting the eigenvalues as a spectrum and picking the eigenvalues that emerge from the fast and slow acoustic continuous spectrums[MZ03]. These eigenvalues, however, are only approximate because the QZ algorithm must linearize nonlinear wavenumber terms in Eq. (3.4) in order to be evaluated. As such, the eigenvalues obtained by the global method provide the local method with an initial guess upon which to iterate.

The local method is based on Malik's multi-domain-spectral-collocation (MDSP) method described in Ref. [Mal90]. Of the numerical methods available to solve the eigenvalue problem, the MDSP method provides the most accurate eigenvalues (wavenumbers) and eigenfunctions (mode shapes) with the fewest number of boundary layer profile points compared to available finite-difference scheme approaches. The multi-domain approach is also well suited for the high Mach flows seen in hypersonics research, as using several domains can help maintain grid resolution throughout the boundary-layer profile and the resulting eigenfunction. The MDSP utilized in this work uses three domains with sinusoidal grid stretching to cluster points at the domain boundaries. Ultimately, the local MDSP method solves the dispersion relation and provides the mode shapes necessary to describe the flow field's

stability characteristics.

The objective of LST analysis is to solve the dispersion relation, Ω. The dispersion relation describes the relationship between a wave's frequency, ω, and its wavenumbers, α and β, within a dispersive medium such as the boundary layer. There are two approaches to solving Ω: temporal and spatial. Temporal stability analysis presumes a stationary wave that is either growing or decaying with time. In temporal analysis, α and β are fixed, and Ω is solved for a complex ω. Conversely, spatial stability analysis presumes a traveling wave that is either growing or decaying downstream. In spatial analysis, ω is fixed, and Ω is solved for complex α or β. Specifically, this dissertation uses the spatial approach in its LST analysis because it compares well with DNS results, which simulates a disturbance propagating downstream. The analysis assumes a 2-D planar wave, which removes the solution's dependency on β. In the instance of an oblique wave analysis, β is a non-zero complex wavenumber. Next, a reasonable real value for ω is taken and Eq. (3.4) is solved for a complex α. The result is a solution to the dispersion relation: $\alpha = \Omega(\omega)$. With the solution to the dispersion relation in hand, ω and α can be used to provide insightful stability analysis.

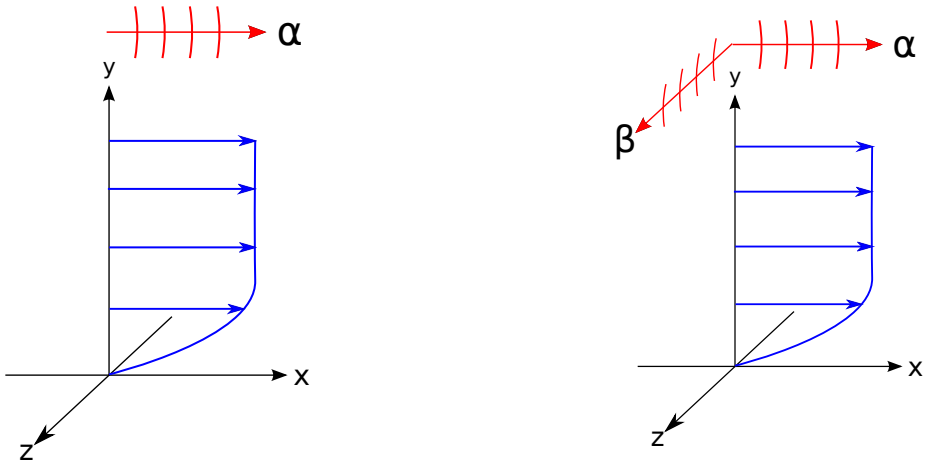

Figure 3.1: Diagram of laminar boundary layer and the respective wavenumber directions for (a) planar waves and (b) oblique waves.

In this work, LST analysis is used extensively to obtain the neutral stability curves,

growth rates, phase speeds, and N-factors for the discrete boundary layer modes present in hypersonic boundary layers. The neutral stability curve for instance demarks regions of stable and unstable growth within the domain as a function of frequency. The curve is obtained by solving the dispersion relation throughout the domain for all frequencies at which the imaginary part of the wavenumber, α_i, is zero. This is because α_i is directly linked to the growth and decay of Eq. (3.3) through the dimensional growth rate $-\alpha_i/L^*$. The growth rate is an important quantity in stability studies because it defines when modes are stable or unstable. Specifically, there are three cases to consider,

$$\begin{aligned} -\alpha_i/L^* < 0 \quad &\text{stable wave,} \\ -\alpha_i/L^* = 0 \quad &\text{neutral wave,} \\ -\alpha_i/L^* > 0 \quad &\text{unstable wave.} \end{aligned} \tag{3.6}$$

Understandably, a stable growth rate causes the wave's amplitude to decay downsteam, while an unstable growth rate causes it to grow. The growth rate alone tells us a great deal about the stability characteristics of the flow field but it is not the only useful metric.

The phase speed of the discrete modes is also computed from LST results. The nondimensional phase speed is defined as:

$$c_r = \frac{\omega}{\alpha_r}, \tag{3.7}$$

where α_r is the real part of the nondimensional wave number. Normally, the modal phase speed described the speed at which a wave is propagating. However, in hypersonic stability research, knowing a discrete mode's phase speed throughout the flowfield can provide insight into the mode's behavior. For example, when a mode bifurcates, undergoes a branch cut, or coalesces with a continuous spectrum. Moreover, a mode is identified by where it originates in the phase speed diagram, with mode S originating near slow acoustic speeds and mode F originating near fast acoustic speeds. Also relevant to roughness-attenuation research is when mode S and mode F become synchronized, as indicated by an intersection of their phase speeds. The synchronization location tells the researcher where to place their surface element to attenuate their desired frequency.

In addition to the wave's growth rate and phase speed, LST analysis can be used to compute the N-factor for each unstable frequency present in the flow field. The N-factor

comes from the e^N method of transition prediction, which attempts to correlate transition with experimentally obtained thresholds of N. The N-factor calculation itself tries to quantify how unstable a frequency becomes by integrating $-\alpha_i$ over its unstable region. This is done by setting $-\alpha_i$ equal to the spatial amplification rate of some arbitrary fluctuation variable with maximum amplitude A,

$$\frac{1}{A}\frac{\mathrm{d}A}{\mathrm{d}x} = -\alpha_i. \tag{3.8}$$

Rearranging Eq. (3.8) and integrating over the unstable range of $-\alpha_i$ with a fixed ω, the integral

$$\ln\left(\frac{A}{A_o}\right) = -\int_{x_o}^{x} \alpha_i \,\mathrm{d}x \tag{3.9}$$

is obtained, where x_o is the location where $-\alpha_i$ first becomes unstable and A_o is the initial amplitude. The term $\ln(A/A_o)$ evaluates to N. The N-factor is computed over a range of frequencies and compared with experimentally obtained values to estimate transition location.

In studies of boundary-layer instability, a collection of nondimensional parameters are commonly used. For instance the local Reynolds number, R, is used. This Reynolds number is defined as,

$$R = \frac{\rho_\infty U_\infty L^*}{\mu_\infty} \tag{3.10}$$

where ρ_∞, U_∞, and μ_∞ are the freestream density, velocity and viscosity respectively. L^* is the local boundary-layer length scale defined as,

$$L^* = \left(\frac{\mu_\infty s}{\rho_\infty U_\infty}\right)^{1/2}. \tag{3.11}$$

where s is the surface location where L^* is being evaluated. This local length scale is also used here to nondimensionalize the growth rate. The frequency of a boundary-layer mode is also commonly nondimensionalized to obtain,

$$F = \frac{2\pi f \mu_\infty}{\rho_\infty U_\infty^2} \tag{3.12}$$

where f is the dimensional frequency in Hertz. Also the frequency may be nondimensionalized with a spatial component resulting in,

$$\omega = \frac{2\pi L^* f}{U_\infty} = RF \tag{3.13}$$

Both nondimensionalizations for frequency are used in the analysis of LST and DNS results.

Before concluding this Chapter, a discussion on discrete mode terminology is in order. In general, this paper follows the modal naming conventions put forth by Fedorov and Tumin [FT11]. In this paper, mode F describes the discrete modes that originate from the fast acoustic spectrum where $c_r = 1 + 1/M_\infty$, and mode S describes the discrete mode that originates from the slow acoustic spectrum where $c_r = 1 - 1/M_\infty$. If more than one discrete mode appears from either acoustic spectrum the modes are numbered in order of appearance by increasing ω. For example, mode F1 and mode F2 are two discrete modes originating from the fast acoustic spectrum, however, mode F1 will have appeared first at a lower ω than mode F2. Occasionally, a discrete mode may undergo a branch cut or bifurcation when crossing one of the continuous spectra, such as the entropy/vorticity spectrum ($c_r = 1$). In such a case, as ω is increased, the mode approaching the branch cut is given a "+" to its name, and the mode departing the branch cut is given a "-". In the cases explored by this dissertation, mode F undergoes a branch cut when crossing the entropy/vorticity spectrum. Lastly, Mack's second mode instability, which is the instability most likely to cause transition in a hypersonic boundary layer, is ascribed to whichever discrete mode becomes unstable when modes F and S become weakly coupled. This weak coupling is referred to as mode synchronization in roughness-attenuation research. In each of the cases explored by this research, mode S is responsible for Mack's second mode instability.

CHAPTER 4

Freestream and Simulation Conditions

This chapter contains a detailed description of the cone geometries and freestream parameters for the computational cases and a description of the experimental setup and running of the experimental validation cases. Each of the computational cases investigated by this dissertation has very similar cones that vary only slightly in one aspect of their geometry. Similarly, the cases also have comparable freestream parameters but are tailored to match previous wind tunnel experiments and the experimental validation runs. Concerning the experimental validation runs featured in this research, the runs were performed at Sandia National Laboratories (SNL) in their hypersonic wind tunnel facilities. A description of the tunnel capabilities is provided in this chapter as well as a description of the test article, its instrumentation, and the experimental runs performed.

4.1 Cone Geometry

The three cases examined by this thesis are based on similar straight blunt cone geometries with slight variations in their nose radii, r_n, cone length, l, and freestream conditions. The cones in each case have a 7° half-angle and no angle-of-attack. In case C.1, the cone geometry is based on the experimental test article dimensions used in Ref. [CBH16]. The test article used in that reference has exchangeable nose tips and a maximum length of 0.517 meters measured from a virtual sharp cone tip. Case C.1-Ext has the same blunt nose radius as C.1 but is 1 meter long. Cases C.2 and C.3 are based on the cone geometries used in the joint computational and experimental investigation with Dr. Katya Casper at SNL [HCZ19]. Case C.3 has the same cone geometry as C.1 but different freestream conditions. Case C.2 has a

blunt nose radius ten times smaller than the other cases at 0.05 mm. The cone dimensions for each case are listed in Table 4.1.

Table 4.1: Cone Dimensions

Dimension	C.1	C.1-ext	C.2	C.3	Unit
r_n	0.5	0.5	0.05	0.5	mm
l	0.517	1.0	0.517	0.517	m

4.2 Physical Parameters

The freestream conditions and physical parameters used to define each CFD case are presented in this section. The conditions for cases C.1 and C.1-Ext are taken from experimental conditions featured in Ref. [CBH16]. The conditions for cases C.2 and C.3 come from the transition-delaying roughness validation experiments performed by Dr. Casper and SNL[HCZ19]. The simulation conditions between cases C.1 and C.2 are ostensibly the same, with freestream Mach numbers around 8.0 and stagnation enthalpies around 1.2 MJ/kg. The main difference between these two cases is their blunt nose radii. Case C.3 has a freestream Mach number of 4.96 and a stagnation enthalpy of 0.829 MJ/kg. The freestream conditions and other relevant parameters for each case are listed in Table 4.2. Lastly, since all of the case conditions come from previous experimental conditions, none of the simulations investigate unrealistic flow conditions.

Table 4.2: Simulation Parameters

Parameter	C.1 & C.1-ext	C.2	C.3	Unit
M_∞	8.0	7.84	4.96	-
h_o	1.155	1.277	0.829	MJ/kg
ρ_∞	0.024803	0.022455	0.055751	kg/m^3
p_∞	330.743	344.442	1297.27	Pa
T_∞	44.9	51.7	81.1	K
T_o	619.6	687.3	480.1	K
T_w	297.0	297.0	297.0	K
μ_∞	2.7148×10^{-6}	3.2141×10^{-6}	5.5639×10^{-6}	Pa·s
Re_∞/l	9986576	8026662	8970243	m^{-1}
Gas	N_2	N_2	*Air*	-

In order to close Eq. (2.1), the ideal-gas law is invoked. Thus, the gases used in this work are assumed to be calorically perfect and conform to the ideal-gas law. The molar mass of the gases used by the code are given below in Table 4.3.

Table 4.3: Molar Mass of Gases Used

Gas	M (g/mol)
Air	28.97
N_2	28.0134

Initially, the experimental basis for case C.2 was planned to validate the transition-delaying roughness array designed using C.1 flow conditions. However, at the time of the experiment, a smaller nose radius was installed on the test article, setting up case C.2 to be a semi-independent case. The experimental case that serves as the basis of case C.3 was run to investigate how the roughness array performed at off-design flow conditions.

4.3 Sandia Hypersonic Wind Tunnel

The Sandia Hypersonic Wind Tunnel (HWT) was used to perform the roughness array validation experiments. The tunnel is a blowdown-to-vacuum facility. Interchangeable nozzle and heater sections allow the tunnel to be run at Mach 5, 8 or 14. The validation experiments were carried out at Mach 5 and Mach 8 with an average run time of 30 seconds. HWT-5 uses air as the driver gas and has a P_0 range of 345–1380 kPa and a T_0 range of 330–890 K. The tunnels unit Reynolds number ranges from 3.3 to 26×10^6 m^{-1}. Tunnel noise levels vary from 1–2%[Cas09]. HWT-8 uses 689 MPa nitrogen supplied from a bottle farm. It has a P_0 range of 1720–6890 kPa and a T_0 range of 500–890 K. The tunnels unit Reynolds number can be varied from 3.3 to 20×10^6 m^{-1}. Noise levels vary from 3–5% [Cas09]. The run conditions for the validation cases are presented in Table 4.4.

Table 4.4: Experimental Run Conditions

Case	Re $\times 10^6$ (m^{-1})	M_∞	P_o (kPa)	T_o (K)	Roughness
1	7.0	7.8	2924	697	No
2	7.2	7.8	2950	687	Yes
3	8.6	7.9	3189	644	No
4	9.0	7.9	3230	630	Yes
5	8.8	5.0	655	480	Yes
6	9.4	5.0	683	472	No

4.4 Model and Instrumentation

The test article is a 0.517 m long 7° half-angle stainless-steel cone that accepts exchangeable nose tips of different radii. The test article installed in the wind tunnel with roughness array can be seen in Fig. 4.1. The test article is also plumbed with an assortment of high frequency pressure transducers. The boundary layer state is characterized by PCB132 pressure sensors at x = 0.422 and 0.497 m measured from a virtual sharp nosetip. These sensors are very high

frequency piezoelectric time-of-arrival sensors that are used to measure pressure fluctuations between 11 kHz and 1 MHz. This high frequency response allows a study of instability breakdown to transition on the cone (typically near 200 kHz) and is a useful indicator of transition on the model. The PCB132 sensor signals connect to a PCB 482A22 signal conditioner that provides constant-current excitation to the built-in sensor amplifier. The output from the signal conditioner is fed through a Krohn-Hite Model 3944 Filter with a 1.25 MHz low-pass anti-aliasing Bessel filter. This filter has four poles and offers 24 dB of attenuation per octave. The sampling frequency for the PCB132 signals is 2.5 MHz. Pressure sensor data was recorded using a National Instruments PXI-1042 chassis with 14-bit PXI-6133 modules (10 MHz bandwidth).

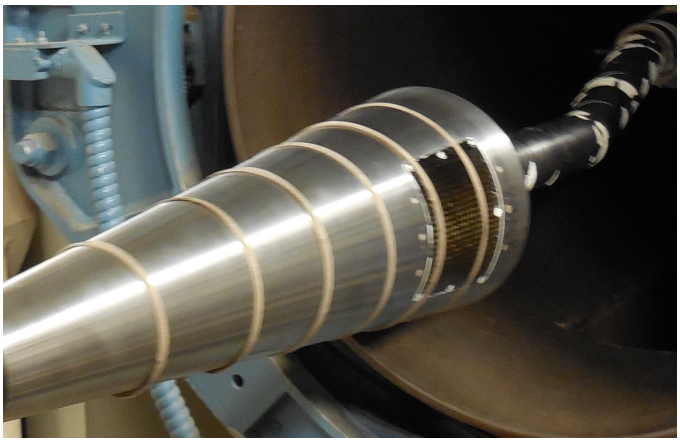

Figure 4.1: Wind-tunnel test article with roughness strips in the Sandia Hypersonic Wind Tunnel. Image reproduced from Ref. [HCZ19].

A high-speed schlieren system was also used to take movies at 200 kHz of the boundary layer between x = 0.422 and 0.497 m while also being able to resolve the detailed structure of the boundary-layer disturbances. The design and implementation of this system is discussed in detail in Ref. [CBH16]. Fig. 4.2 shows a simple schematic of the system. A Cavilux Smart Laser was used as the light source, in place of the Flashpoint II Monolight that had been used in previous setups. The light from the source was passed through a slit to increase sensitivity. Two 101.6-mm diameter convex lenses with a 1-m focal length were then used to collimate the remaining light, pass it through the test section, and focus the light on a knife edge. The lenses were equally spaced on either side of the tunnel centerline. Most of

the light was cut off at the knife edge to increase the sensitivity of the schlieren system. The remaining light was then captured by a Phantom v12.1 digital camera. The slit, knife edge, and camera were all tilted 7° from horizontal to align with the cone surface.

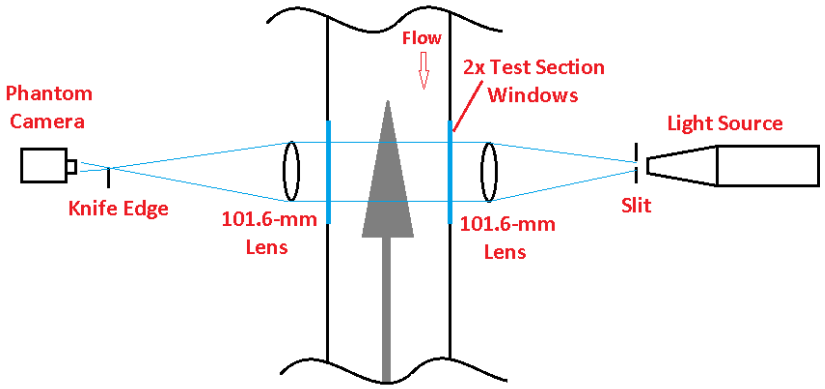

Figure 4.2: Schematic of the high-speed schlieren system for the Sandia Hypersonic Wind Tunnel. Diagram reproduced from Ref. [CBH16].

CHAPTER 5

C.1 Results: Design of Transition-delaying Roughness

This Chapter focuses on the design of transition-delaying surface roughness for a straight blunt cone in a Mach 8 flow. The specific flow conditions are listed in Table 4.2 under case C.1. The design process begins with simulating the steady-state flow for a cone with no roughness. From this result, a stability analysis is performed with LST to determine the stability characteristics of the flow. The results, in turn, determine the dimensions of the transition-delaying roughness strip and its location on the cone. A new steady-state containing the single circumferential roughness strip is computed. Next, the two steady-states with and without roughness are used as the base flows for unsteady simulations. A blowing-suction actuator on the cone surface produces a broadband disturbance that propagates downstream. Fourier decomposition of the unsteady results provides insight into which individual frequencies are growing and which are attenuated by the roughness strip. Lastly, the single roughness strip design is extended to a roughness array using Zhong and Fong's passive laminar flow control strategy [ZFW14].

5.1 Smooth Cone Steady-state Results

The pressure and density contours from the steady-state simulation for case C.1 with no surface roughness are featured in Figs. 5.1 and 5.2. Since the simulation is axisymmetric, a streamwise slice of the domain is presented. The computational domain is bounded at the top by the bow shock and below by the cone surface. The pressure contours in Fig. 5.1 are typical of blunt cone results. There is an increase in pressure across the shock with a significant increase near the stagnation point and a moderate pressure increase across the

shock along the frustum. Likewise, the density contours in Fig. 5.2 are also typical of blunt cone results. The density increases across the shock from the freestream as expected, with the highest contour values localized near the stagnation point. The other flow quantities, such as temperature and velocity are also typical of blunt cone results.

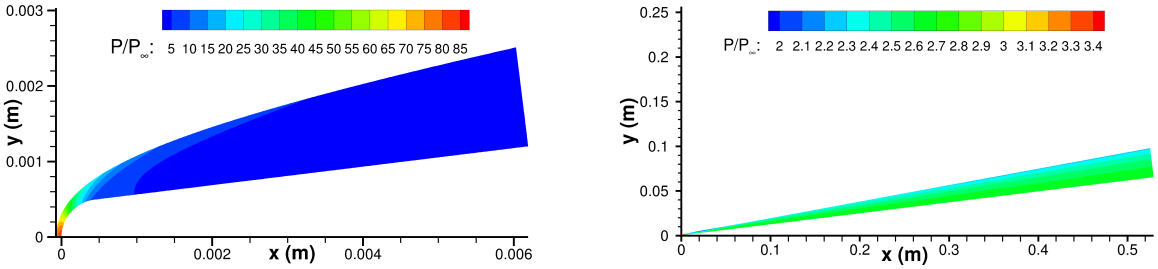

(a) (b)

Figure 5.1: Pressure contour behind bow shock over (a) the blunt nose and (b) cone frustum.

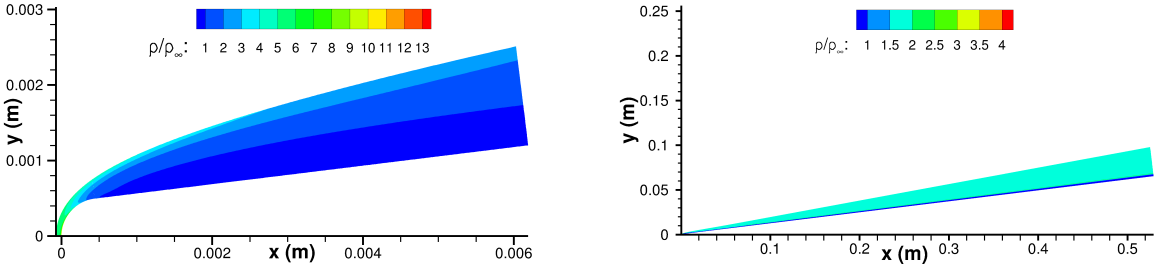

(a) (b)

Figure 5.2: Density contour behind bow shock over (a) the blunt nose and (b) cone frustum.

5.2 Stability Analysis of Steady-state at 240 kHz

Using boundary layer profiles from the smooth cone steady-state data, an N-factor plot for mode S is computed. Using the empirical e^N method, disturbances in the boundary layer are measured by integrating the modal growth rate at a fixed frequency as the disturbance propagates downstream. The modal growth rate is obtained from LST. The N-factor results are

then compared to experimental intermittent turbulence results to determine the frequency responsible for transition.

The N-factor plot in Fig. 5.3 below contains a frequency range from 200 to 420 kHz. Based on a previous experiment by [CBH16], the intermittent turbulence results for the same cone geometry with the same Mach number and similar unit Reynolds number indicated that at 0.340 m, the instability wave intermittency began to drop as turbulent intermittency picked up. Comparing this 0.340 m location on Fig. 5.3 below, the location corresponds to an N-factor of 5.7 for a frequency of 240 kHz.

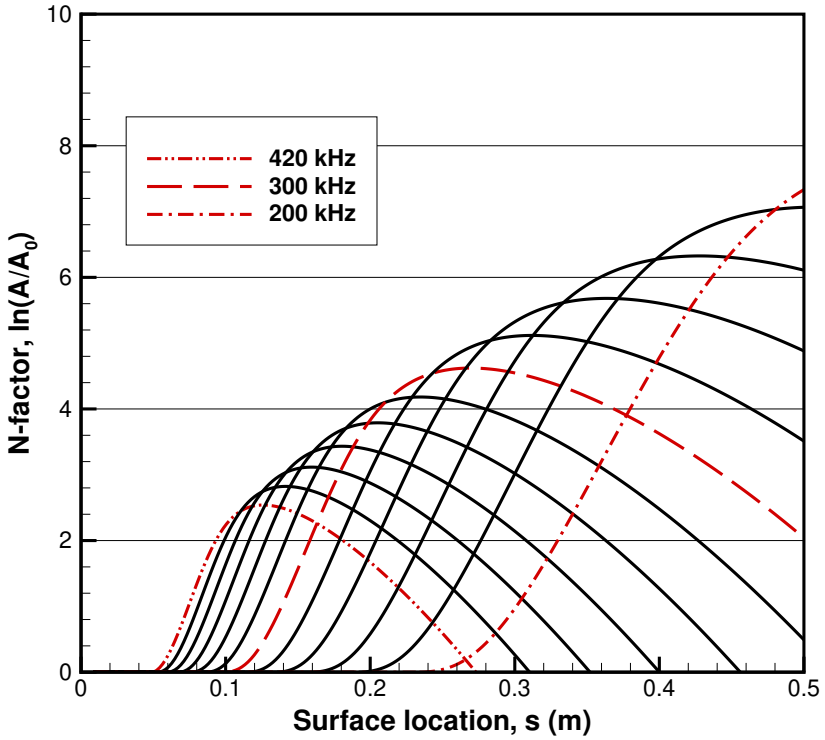

Figure 5.3: N-factor values for Mack's second mode instability on mode S. Fixed frequencies go from 200 to 420 kHz in increments of $\Delta f = 20kHz$.

Taking 240 kHz as the second mode frequency most likely to cause turbulent transition, it can be targeted and attenuated using transition-delay roughness strips. This is done by locating the synchronization location—the point where the phase velocity of mode F and mode S cross—and placing a roughness strip at that location or downstream of it. This approach of identifying the target frequency's synchronization location is the main idea

behind Zhong and Fong's patented passive laminar flow control method [ZFW14].

The phase velocity plot for the target frequency is given in Fig. 5.4 below and provides a synchronization location of $s = 0.223$ m along the cone surface was determined. Along with the phase velocity, the growth rate for mode F and mode S at the target frequency is also determined. Figure 5.4 shows that mode S is unstable form most of the cone. The 240 kHz instability becomes unstable at $s = 0.1589$ m and only stabilizes at $s = 0.488$ m. Meanwhile, mode F is entirely stable at the target frequency.

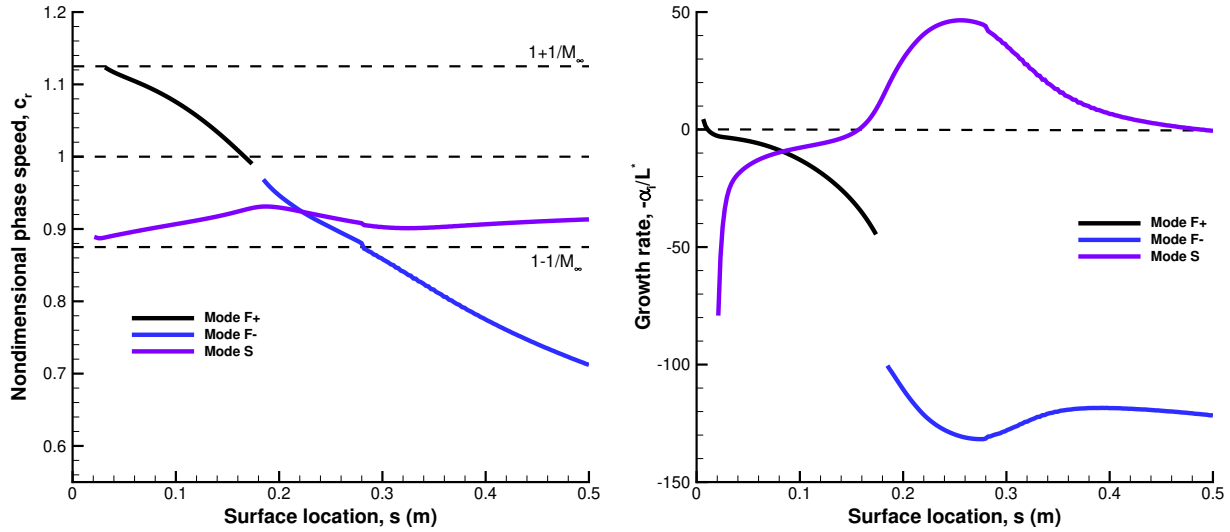

(a) (b)

Figure 5.4: (a) Phase velocity and (b) growth rate for mode F and mode S at 240 kHz.

It is well known that Mack's second mode is the dominant acoustic instability wave in hypersonic boundary layers [Mac84], and clearly is the instability present on mode S in Fig. 5.4. The presence of the second mode can be confirmed by examining the mode shape at these locations. Figure 5.5, contains the pressure and temperature eigenfunctions for two locations: the synchronization location ($s = 0.223$ m) and the experimental location where Casper et. al.[CBH16] determined the turbulent intermittency begin to dominate ($s = 0.340$ m). The pressure eigenfunction for both locations are indicative of the second mode—comprising of one peak and one valley [MZ03]. Moreover, the eigenfunctions have a

positive growth rate and are consequently unstable.

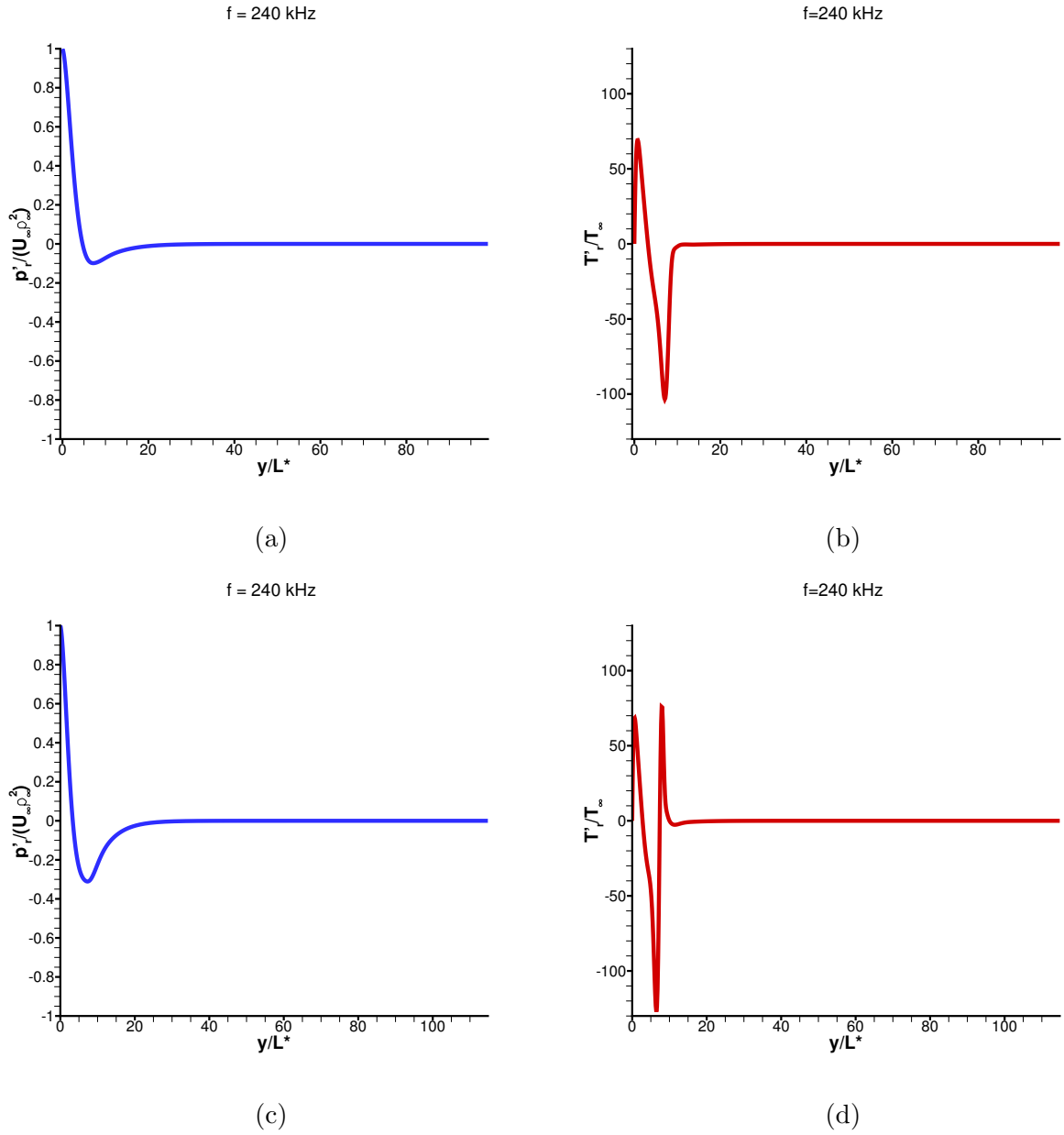

Figure 5.5: (a) Pressure and (b) temperature mode shapes at $s = 0.340$ m. And (c) pressure and (d) temperature mode shapes at $s = 0.223$ m.

In addition to the N-factor analysis, a growth rate map of mode S for the majority of the smooth steady-state over a range of frequencies was constructed. From the map given in Fig. 5.6, the neutral curve can be viewed alongside the peak unsteady growth rate. Within the confines of the neutral curve, the growth rates are unstable and those outside are stable. The

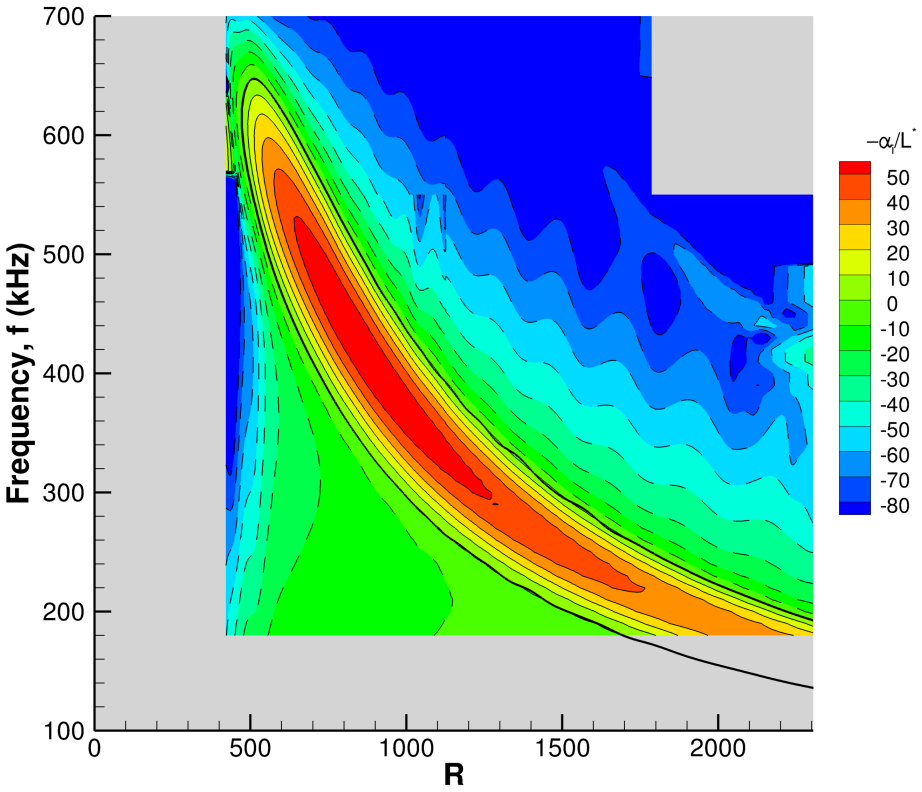

Figure 5.6: Growth rate map of mode S overlain with the neutral stability curve (━). Solid contours (—) denote unstable growth rates, dashed contours (- - -) denote stable growth rates.

peak unstable growth rate occurs around a frequency of 417 kHz, while the target frequency of 240 kHz and the frequencies most likely to lead to transition are quite lower. This is because the width of the neutral curve, for a given frequency, is wider for lower frequencies. As can be inferred from Eq. (3.9), one means of obtaining a large N-factor is for a given frequency to remain spatially unstable longer. Frequencies higher than 400 kHz are not considered in the the N-factor analysis, as they only produce smaller and smaller values of N and are not likely to lead to transition. The neutral stability curve also provides the range of relevant unstable second mode frequencies. Any unsteady broadband disturbance should contain the range of unstable second mode frequencies between 180 and 650 kHz. As seen in Fig. 2.4b, the pulse FFT nominally contains frequency content up to 1 MHz, which is sufficient for covering the unsteady frequencies.

5.3 Transition-delaying Roughness Strip Design

Moving on to the design of the transition-delay roughness Strip; the location, height, and width of the element must be determined. In a previous computational/experimental collaboration, [FWH15] the roughness strip was placed 5 cm downstream of the target frequency's synchronization location. This was to guarantee the attenuation of the target frequency. A parametric study by Fong and Zhong [FWZ15] found that placing the roughness element at the synchronization location, attenuated frequencies higher than the target frequency while amplifying lower frequencies. Thus, by placing the element further downstream, at the synchronization location of a lower frequency, attenuation of the target frequency was guaranteed. Moreover, in the aforementioned computational/experiment collaboration, the height and width of the element were set at half the local boundary layer thickness in height, and is twice the local boundary-layer thickness in width.

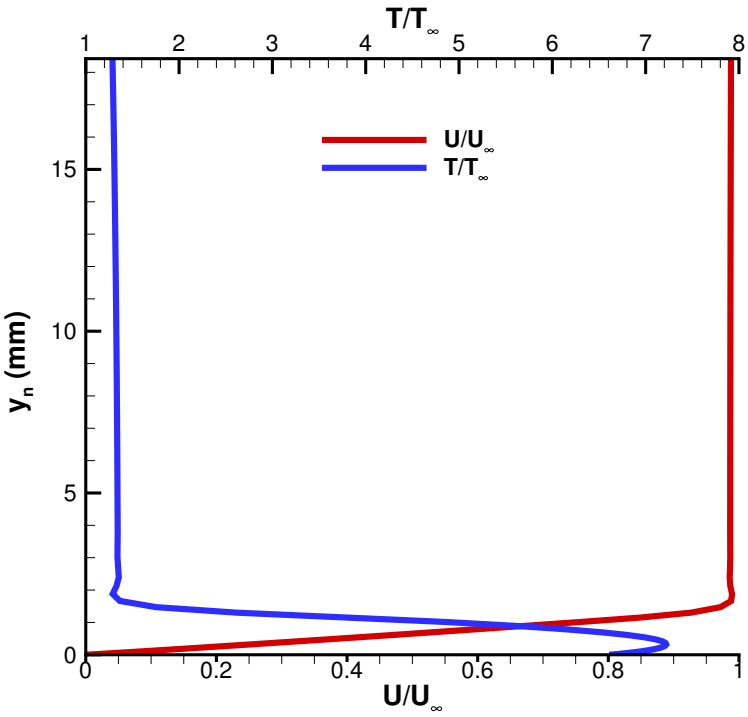

Figure 5.7: Velocity boundary layer and thermal boundary layer at $s = 0.2936$

Following the convention set by Fong and Zhong [FWH15], the roughness strip is placed 7 cm downstream of the synchronization location at $s = 0.293$ m. Figure 5.7 contains the boundary-layer profile at $s = 0.293$ m extracted from the steady-state data. The δ_{99} measure of the profile is used as the boundary layer thickness. The roughness strips height and width based this thickness are listed in Table 5.1.

Table 5.1: Roughness Parameters

Parameter	s [m]	δ_{99} [mm]	h [mm]	w [mm]
Value	0.2936	1.627	0.8135	3.254

5.4 Stability Analysis at 208 kHz

Since the roughness strip's physical location is placed further downstream at $s = 0.2936$ it is prudent to analyze the boundary layer's stability at this location. As mentioned previously, placing the roughness strip downstream guarantees the attenuation of the target frequency by essentially placing the element at the synchronization location of a lower frequency. Thus, we wish to determine the frequency whose synchronization location corresponds to $s = 0.2936$ m. After searching through a range of frequencies, 208 kHz provides a synchronization location closest to the roughness location. Figure 5.8 contains the phase velocity and growth rate plots for this frequency. The passive laminar flow control strategy predicts that frequencies lower than 208 kHz will be attenuated by the roughness strip while higher frequencies will be amplified.

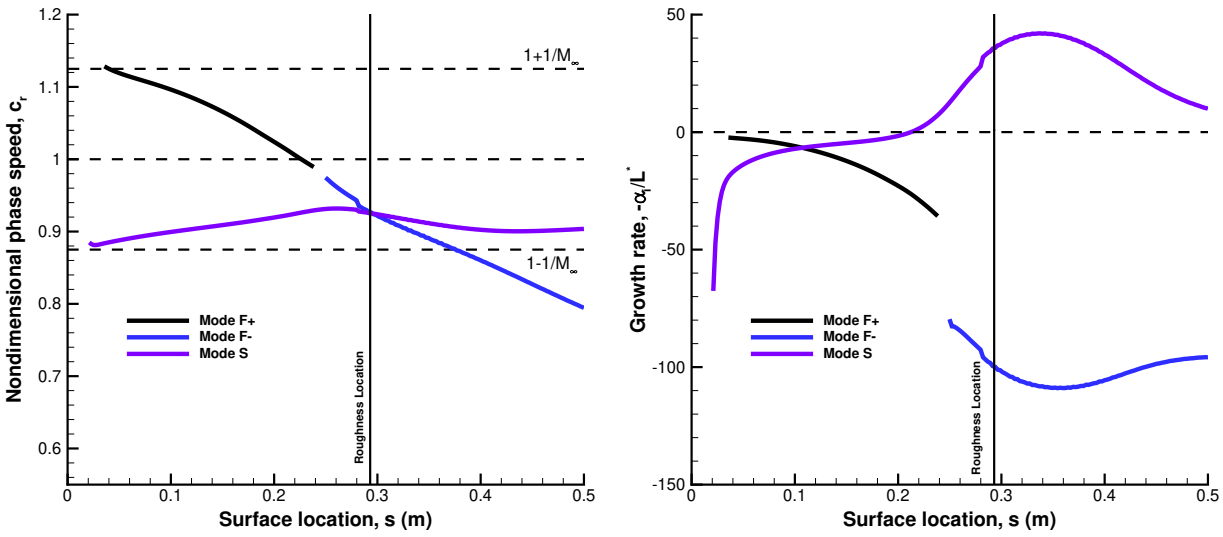

(a) (b)

Figure 5.8: (a) Phase velocity and (b) growth rate for mode F and mode S at 208 kHz.

5.5 Rough Cone Steady-state Results

With the element dimensions defined, the rough case steady-state can be computed. Figures 5.9 and 5.10 provide an overall view of the steady-state pressure contour for the surface and the flow cross-section. Since the roughness strip introduces significant non-parallel flow in the vicinity of the roughness, it is not possible to perform a stability analysis with. Thus, phase speed and growth rate plots cannot be constructed. In spite of this the roughness steady-state is full of significant features.

The steady-state pressure contour plot nearest the roughness strip in Fig. 5.11 shows a Mach wave on the strips upstream edge with an expansion fan on the downstream edge. From this figure it can been seen that the presence of the roughness influences the upstream pressure field significantly by at least four roughness widths while the downstream pressure field shows less influence. This is a notable departure from flat plate simulations in which the influence of the element was felt nearly equally upstream and downstream [FWZ14b].

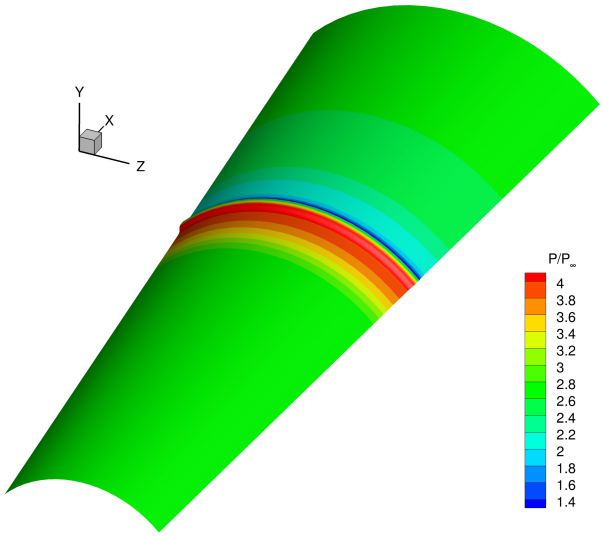

Figure 5.9: Steady-state pressure contours on cone surface.

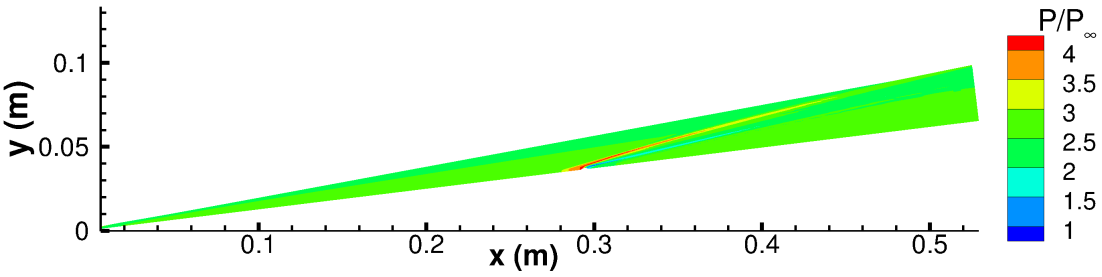

Figure 5.10: Streamwise cross-section of steady-state pressure contours.

The reason for the decreased downstream influence can be seen in the streamtrace plot in Fig. 5.12. The downstream flow separation zone is not only smaller than in flat plate cases but is nearly nonexistent when compared to the extent of the upstream flow separation zone.

The existence of the diminutive downstream separation region is an interesting result, as it has been proposed by Tang et. al. [TZC15] that it is this separation region that is responsible for the second mode attenuation via an application of Miles' Theory, in which the second mode undergoes amplitude reduction by reflecting off the region. As will be seen later, despite the downstream separation region's diminutive size, the roughness element is more than capable of attenuating its target frequency.

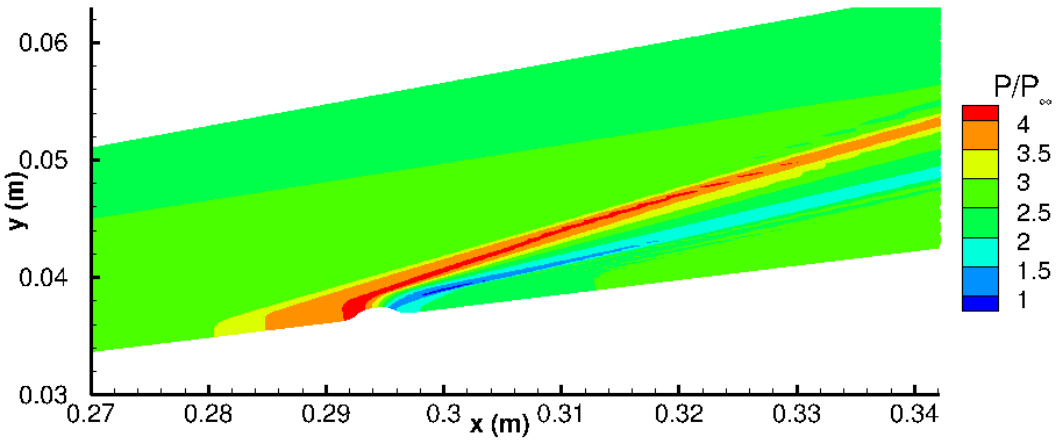

Figure 5.11: Steady-state pressure contours around roughness element.

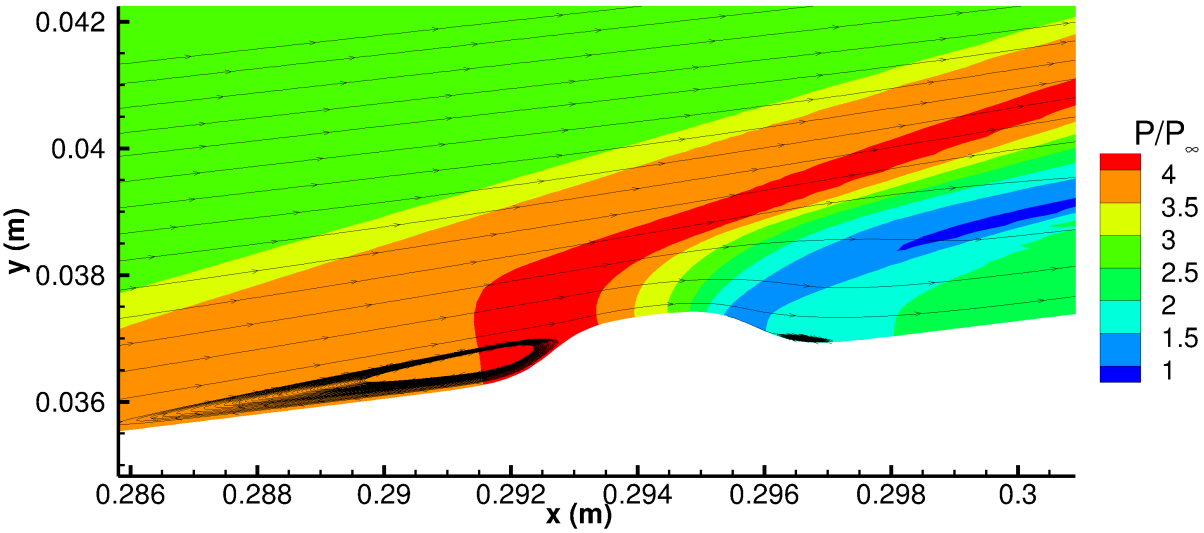

Figure 5.12: Streamtrace around roughness element.

5.6 Unsteady Results on a Smooth Cone

Moving on to the unsteady DNS simulations, a blowing-suction actuator is added to the smooth cone steady-state simulation and the pulse defined by Eq. (2.26) and Table 2.1 is imposed on the flow field. Figures 5.13 and 5.14 show the second mode wave packet as it propagates downstream. As illustrated by Fig. 5.13, the unsteady results are axisymmetric. The blowing-suction actuator wraps circumferentially around the cone and thus produces a

2-D instability wave. Figure 5.14 shows the cross-sectional view of the instability wave.

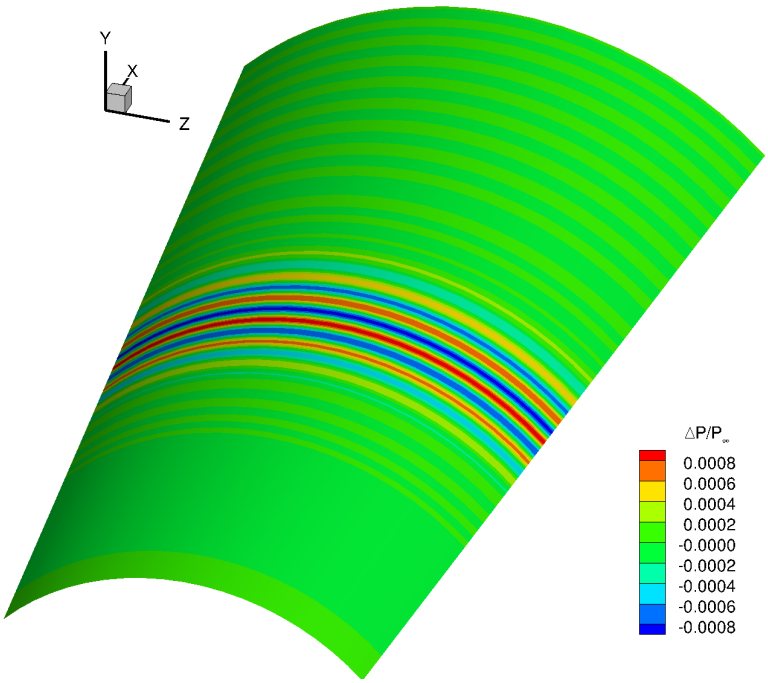

Figure 5.13: Surface view of second mode surface pressure perturbation on a section of cone frustum. The blowing suction actuator is located out of view at $s = 0.198$ m

In addition to the instantaneous view of the pressure perturbations provided in Fig. 5.14, the time history of the surface pressure perturbation can be extracted from the unsteady simulation. Figure 5.15plots the instability wave for the smooth case at five separate locations over the same time period and the same pressure perturbation range. The figure highlights the instability waves constant wave speed and amplitude growth as it propagates downstream. The wave speed is calculated to be 1039 m/s, which is below the 1093 m/s of U_∞ but also above the 956 m/s of $U_\infty - a_\infty$, putting the wave speed in the slow acoustic range. Moreover, the waves amplitude grows 4.54 times over 8.1 cm, indicative of the unstable growth rate.

Fourier decomposition of the time histories in Fig. 5.15 can provide insight into the amplitude growth of specific frequencies. Applying the transform to the entire surface produces the non-dimensional frequency spectrum map in Fig. 5.16. From the shape of the maps

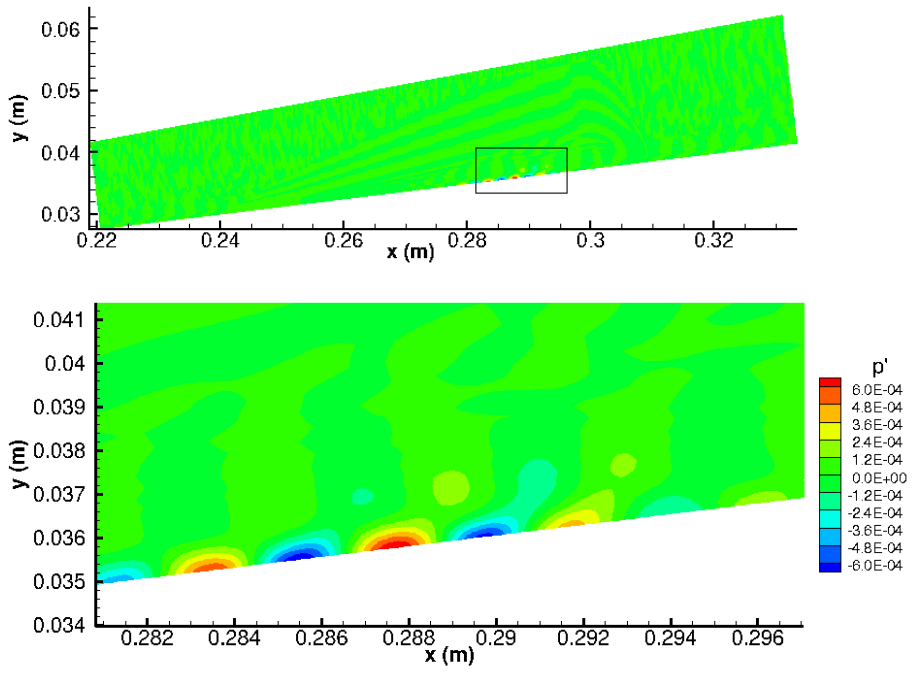

Figure 5.14: Pressure perturbation, $\Delta p/P_\infty$, of the second mode instability wave on a smooth cone.

contours, it is clear that the instability waves frequency content changes as it propagates. Higher frequencies grow and then dampen out while lower frequencies, which initially have a background amplitude, eventually begin to grow at downstream locations. This brings to light that at any one location, only a narrow band of frequencies make up the instability, with the frequency content shifting to lower frequencies downstream.

Overlaying the frequency spectrum in Fig. 5.16 are two sets of curves: the neutral curve and the synchronization location curve. The neutral curve is the same curve from Fig. 5.6. As expected the instability grows downstream of the first branch of the neutral curve. And close examination of the contour lines for a fixed frequency show that the pressure perturbation begins to dampen after crossing the second neutral curve branch as expected. The synchronization location curve depicts a handful of synchronization locations at fixed frequencies. An interesting result is how well the curve follows the contour of the frequency spectrum. This would suggest that it is the interaction of the second mode with mode F that kick starts the growth of the instability wave.

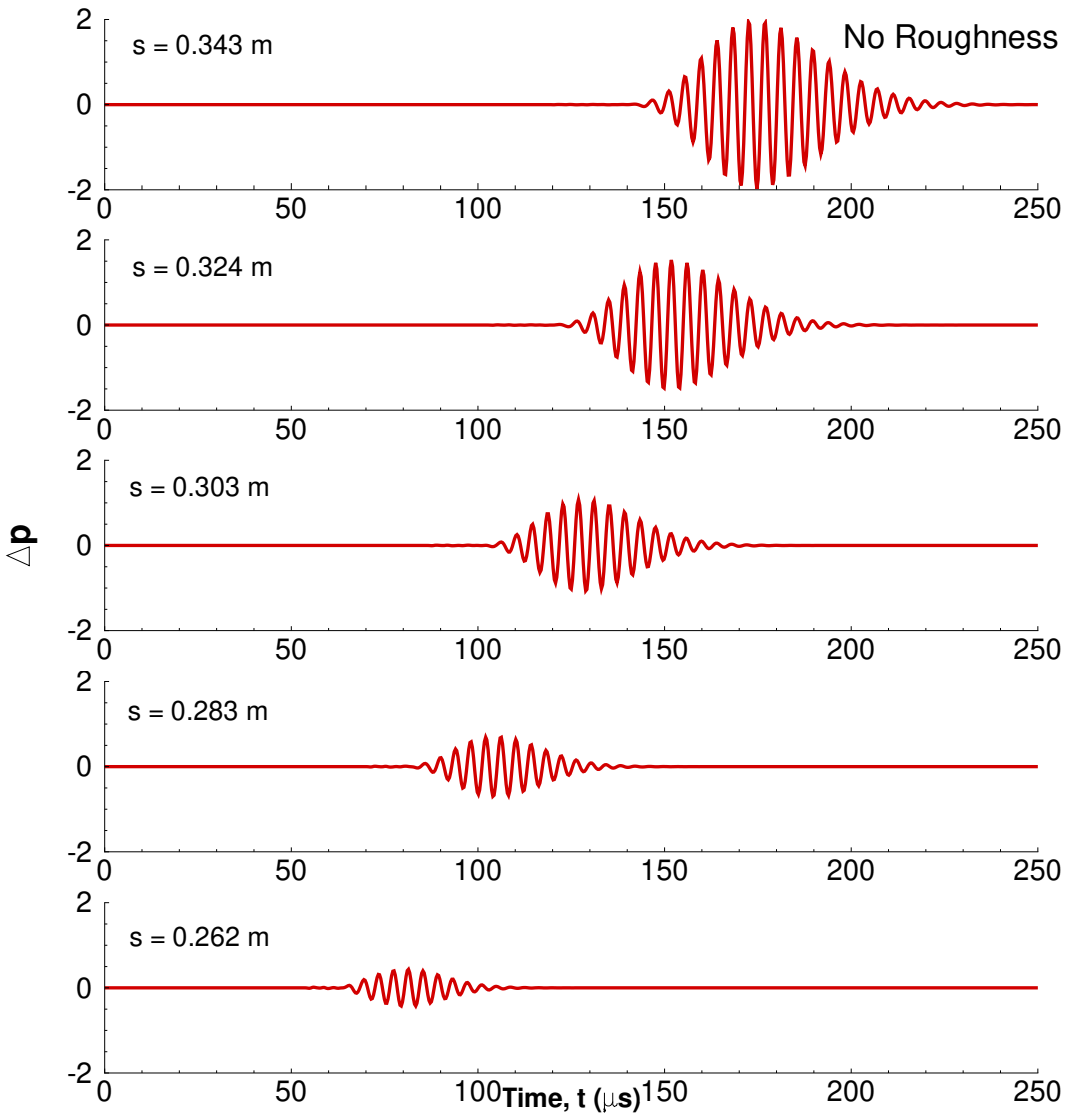

Figure 5.15: Time history of pressure perturbation at several surface locations on a smooth cone.

Lastly, Figs. 5.17a and 5.17b contain select FFT results for fixed frequency and fixed location from the frequency spectrum. For fixed frequency, Fig. 5.17a looks at a range that covers the instability including the target frequency of 240 kHz. As already noted, the higher frequencies tend to grow and then dampen out, this can be seen for the frequencies of 270, 260, 250 and 240 kHz. Moreover, the lower frequencies, such as 210, 220 and 230 kHz, start low and eventually grow at downstream locations. Notably, the location where the spatial evolution reaches its maximum corresponds to the second branch of the neutral stability

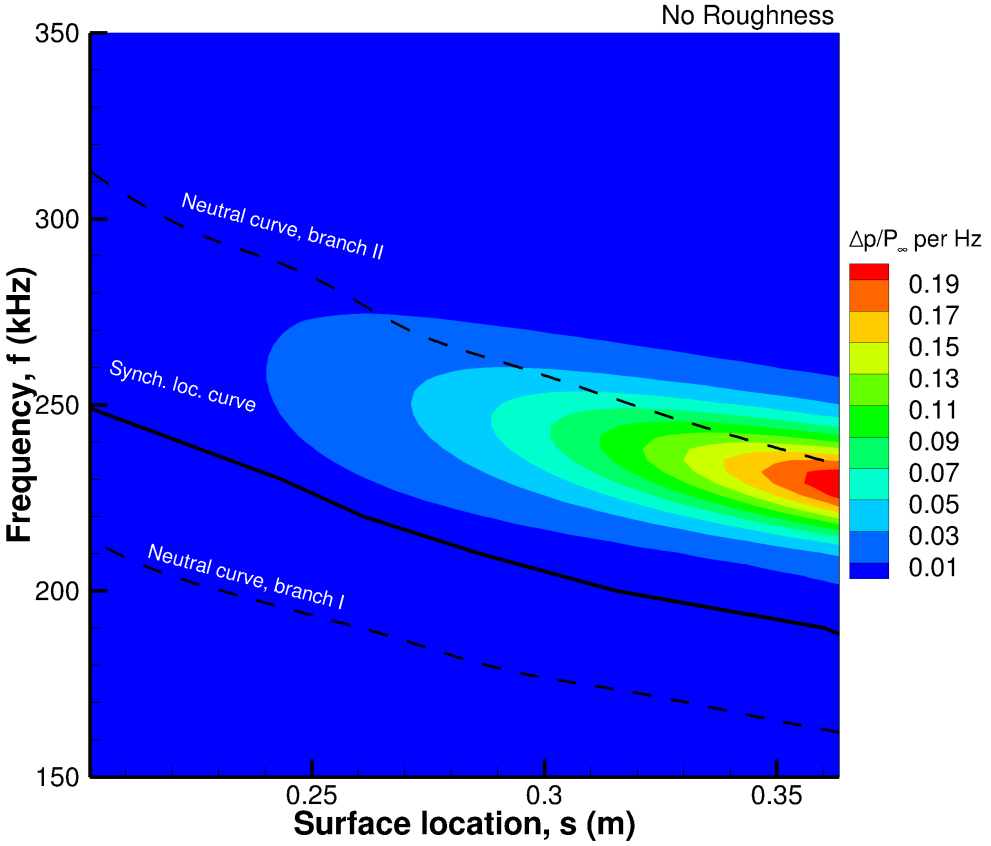

Figure 5.16: Non-dimensional frequency spectra of surface pressure perturbation along a smooth cone.

curve.

Figure 5.17b looks at four fixed locations: the synchronization location for the target frequency (0.223 m), 0.268 m, the roughness location (0.293 m) and where the experimental turbulent intermittency begins to dominate (0.340 m). As noted previously, for any given location, the prevailing instability frequencies consist of a narrow band. Moreover, the peak amplitude of this narrow band increases downstream. More subtly, however, the frequency of the peak decreases moving downstream.

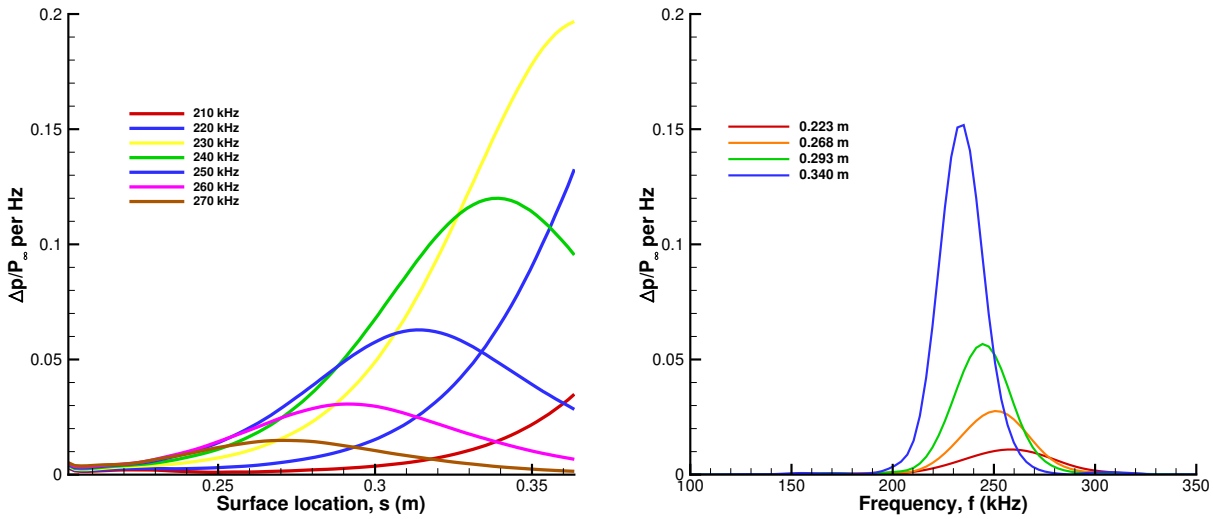

(a) (b)

Figure 5.17: (a) Spatial evolution of fixed frequency FFT results for smooth case, and (b) fixed location frequency spectrum for smooth case.

5.7 Unsteady Results on a Rough Cone

Just as with the smooth cone steady-state, a blowing-suction actuator is added to the rough cone steady-state and a pulse is imposed on the flow field. Figure 5.18 shows an overview of the second mode as it propagates downstream toward the roughness element.

Figure 5.19 features the second mode pressure perturbations at several instances: once when the disturbance is upstream of the element, another when it is passing over the element, and lastly when it is downstream of the element. Comparing Fig. 5.19b with Fig. 5.14 shows a much stronger disturbance in the rough case than in the smooth case. This is consistent with previous flat plate simulations in which the trend is to amplify the disturbance frequency band immediately upstream of the element before attenuating the desired range [FWZ15]. In Fig. 5.19c, the disturbance is stretched and deformed as it passes over the roughness. On close examination the weaker pressure perturbation seen above the main perturbation would appear to grow in amplitude as the wave packet negotiates the slope of the roughness. These newly amplified perturbations dampen out quickly; disappearing just as they pass over the element. They should not be confused with the strong off-the-wall perturbations seen in

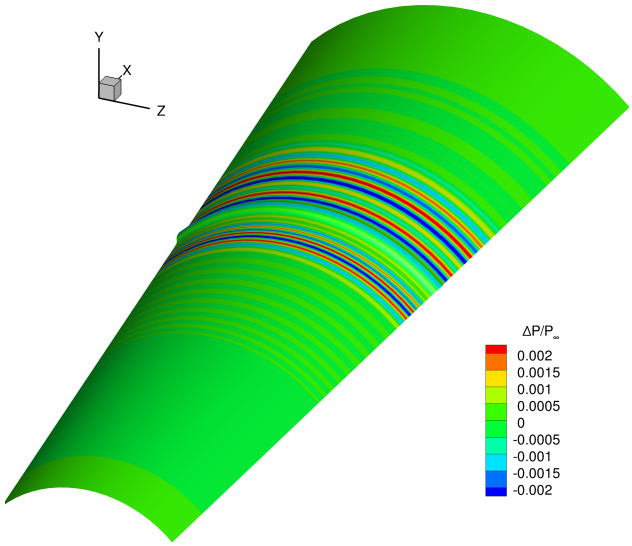

Figure 5.18: Surface view of second mode surface pressure perturbation on a section of cone frustum. The blowing suction actuator is located out of view at $s = 0.198$ m.

Fig. 5.19d, which are 'shed' from the main disturbance as it passes down the backside of the element and carried away in the expansion fan. These 'shed' features notwithstanding, the most important feature of Fig. 5.19d is the significant attenuation of the second mode on the wall when compared to the incoming second mode in Fig. 5.19b.

Just as in the smooth case results, the time history of the surface pressure perturbation can be extracted from the unsteady simulation. Figure 5.20 plots the time history at five separate locations. For comparison, the plots share the same domain and range as the plots in Fig. 5.15. The figure shows that the disturbance grows considerably between the first two locations, dampens after passing the roughness location ($s = 0.2936$ m), and then proceeds to grow again. Examined more closely, between $s = 0.262$ m and $s = 0.283$ m the perturbation amplitude grows 139% over 2.1 cm. Between $s = 0.283$ m and $s = 0.303$ m, the disturbance passes over the roughness element which in turn attenuates the packets amplitude by 57%. From this new state, the perturbation amplitude grows 150% between $s = 0.303$ m and $s = 0.343$ m. This amounts in a total amplitude growth of 159% over the span of 8.1 cm.

Comparing the last location ($s = 0.343$ m) between Figs. 5.15 and 5.20, the disturbance

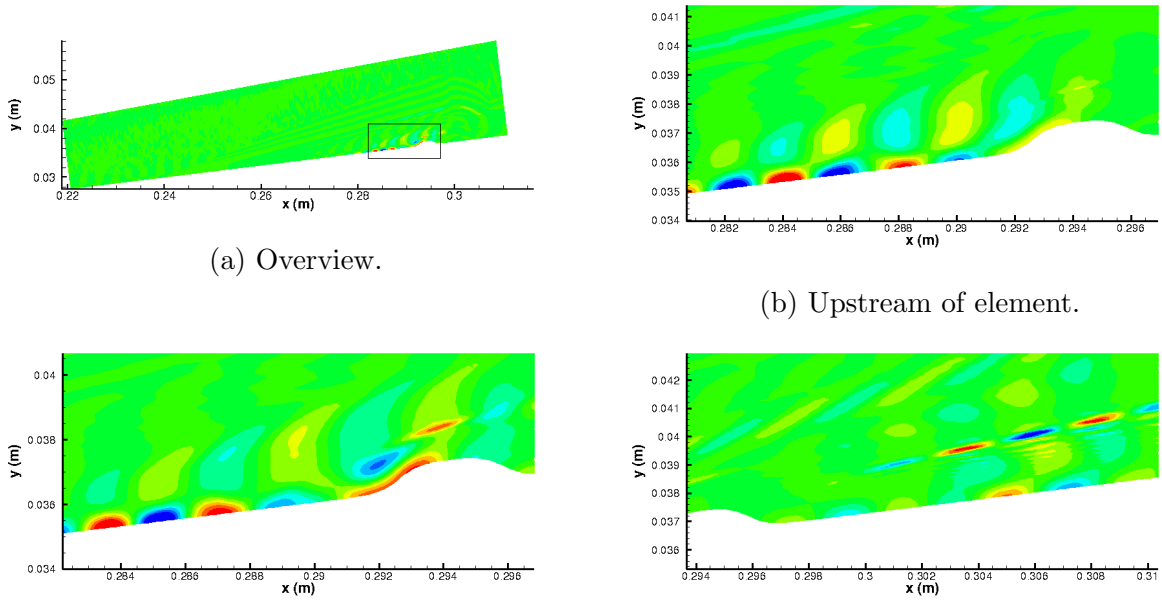

(a) Overview.

(b) Upstream of element.

(c) Traveling over element.

(d) Downstream of element.

Figure 5.19: Rough case cross-sectional view of second mode pressure perturbation.

packet in the rough case is 39% smaller than in the smooth case. The same reduction in magnitude can also be noted for the $s = 0.303$ m and 0.324 m locations as well. Comparison of the time histories between the two cases illustrates quite clearly the surface elements ability to dampen the second-mode. It should be noted, however, that the roughness strip does not, in actuality, stabilize the boundary layer. For all intents and purposes the second mode's growth rate remains unstable, as seen by its amplification before and downstream of the roughness. It is only in the vicinity of the element that its amplitude is reduced. Previous discourse on this topic has left the impression that surface elements stabilize the flow downstream of the element. This is why in the experimental undertakings of this topic, successive roughness strips are employed to delay transition.

Moving on to the Fourier analysis of the time histories, Fig. 5.21 is the non-dimensional frequency spectrum map of the rough case. As in the smooth case, the map is overlaid with the neutral curve and synchronization location curve. These curves come from the stability analysis done on the smooth cone. Due to the non-parallel flow in the vicinity of

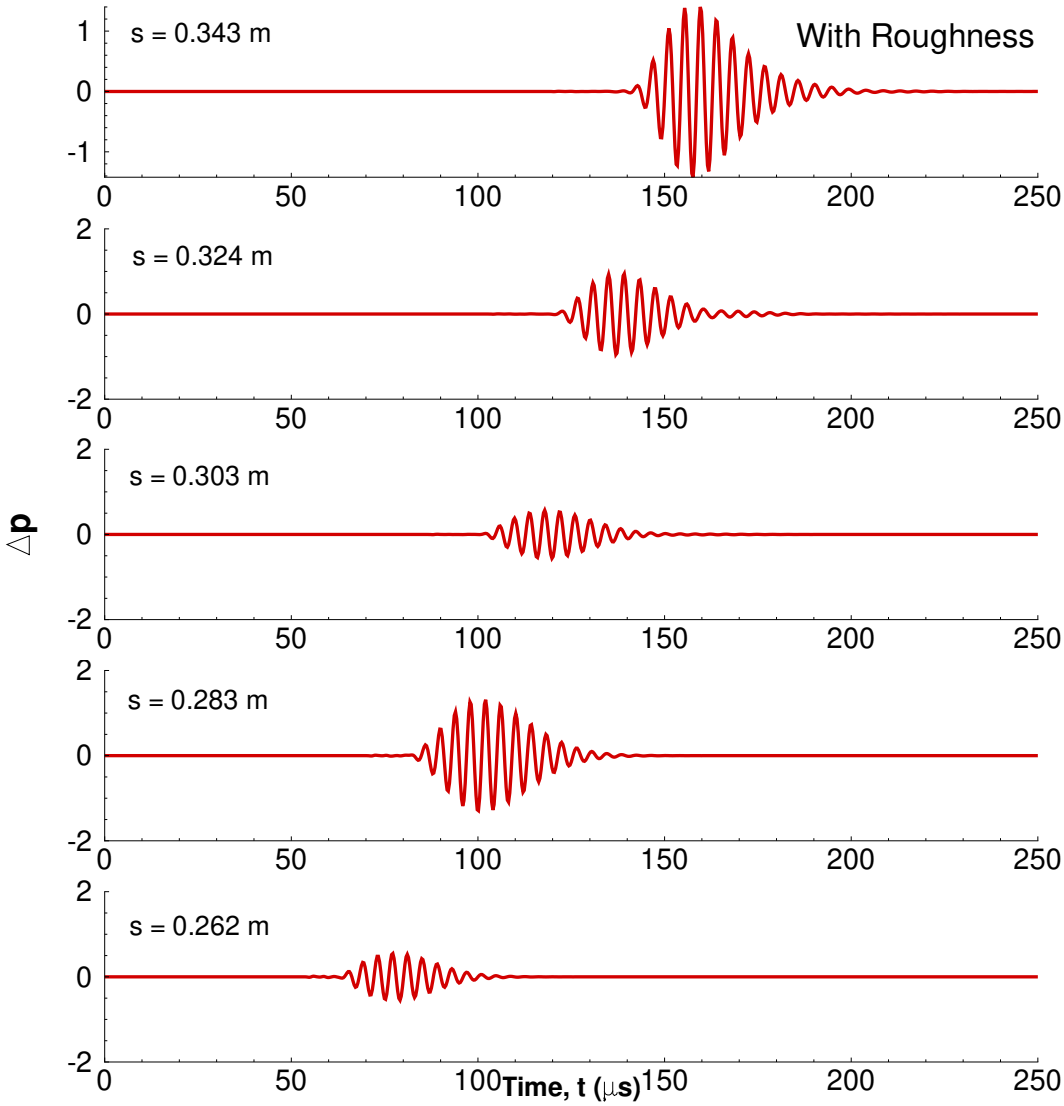

Figure 5.20: Time trace of pressure perturbation at several surface locations on a cone with a finite roughness element.

the roughness, stability analysis using LST is not valid. Thus, the curves serve to compare how the unsteady flow with roughness differs from the nominal case. The most notable feature of the spectrum are the contour oscillations in the vicinity of the roughness element denoted by the red line. It would appear the surface perturbation enters an irregular state in which the perturbation spreads and contracts to higher and lower frequencies, all the while undergoing an overall reduction. Aside from this prominent feature, the general shape of the contours is reminiscent of the smooth case with some distinct differences. The first is

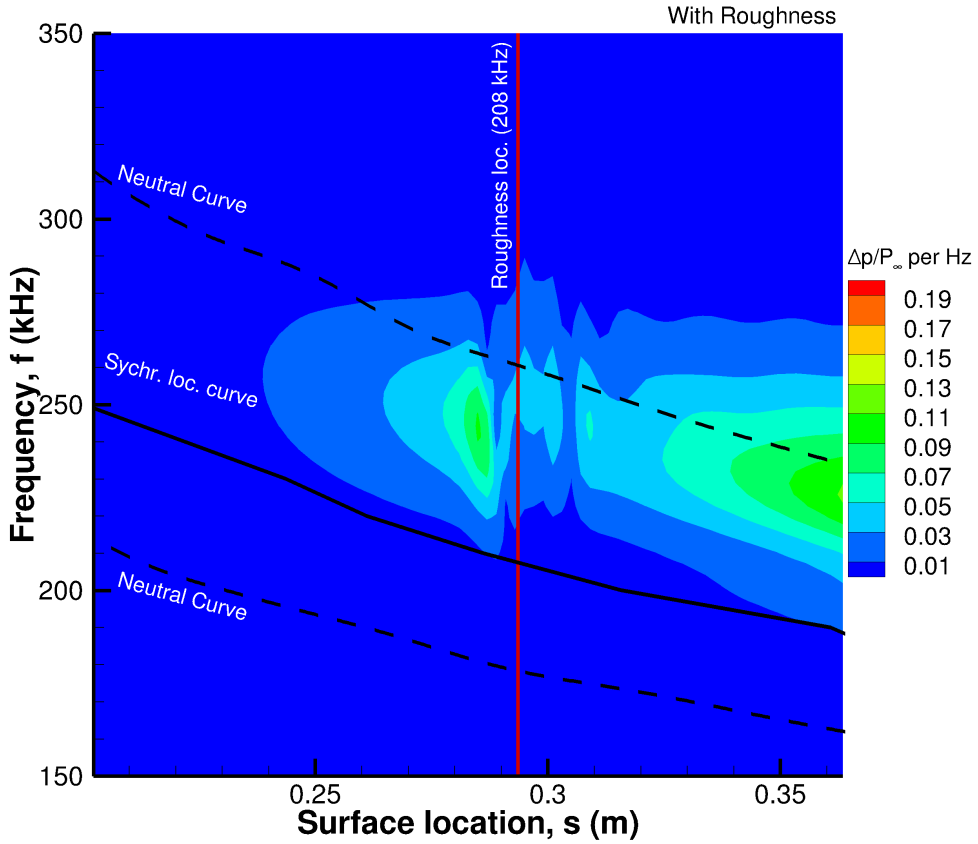

Figure 5.21: FFT map with neutral curve and the synchronization location of multiple frequencies.

the magnitude of the contours; both Figs. 5.21 and 5.16 share the same contour scaling. Notably, the case with roughness is less amplified, never reaching the same peak amplitude. More downstream results are needed to support this speculation however and to determine its significance.

In addition to Fig. 5.21, Fig. 5.22 is the same contour plot but with lines denoting features important to this research. The first is the vertical line denoting the synchronization location for the target frequency of 240 kHz. As the N-factor and LST analysis showed, 240 kHz was determined to be the leading frequency responsible for causing transition. As expected the dashed line denoting 240 kHz intersects the vertical line on the synchronization curve. Further down this horizontal line we see an overall attenuation of the 240 kHz frequency, which is very apparent in Fig. 5.23a and is the desired outcome of the roughness design.

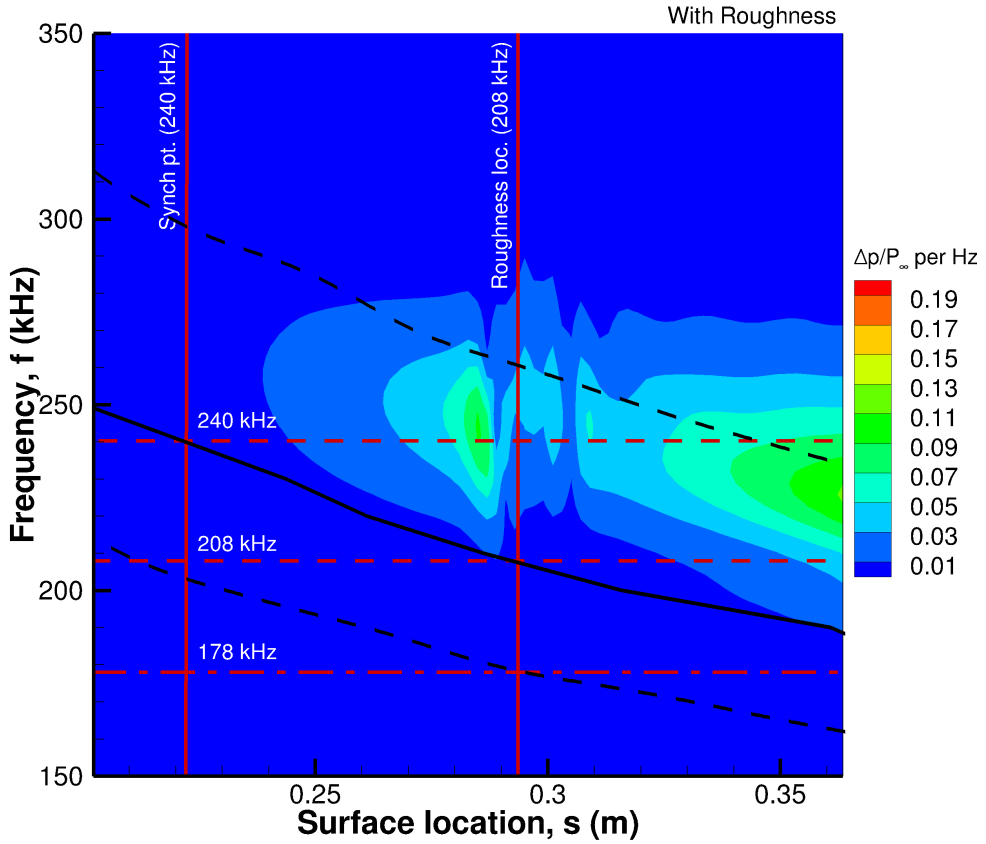

Figure 5.22: FFT map with neutral curve and the synchronization location of multiple frequencies. Vertical lines demarcate the synchronization location for 240 kHz and the roughness location with a synchronization frequency of 208 kHz.

Moreover, there is no frequency growth below the synchronization curve. All frequency growth occurs to the right of the roughness location between the 208 kHz cut-off frequency and the synchronization curve. Also featured in Fig. 5.22 is the roughness location and its synchronization frequency. For this frequency of 208 kHz there is marginal attenuation but more importantly frequencies lower than it start to amplify downstream. The last horizontal line in the figure is the dash-dot line at 178 kHz, which denotes the first neutral point at the roughness location. There is some debate that it is the neutral point with respect to the roughness location that determines which frequencies are attenuated or amplified. But as the frequency spectrum shows, there is both growth and attenuation at frequencies greater

than the neutral point frequency. And as seen in the figure, the first branch of the neutral curve is generally far removed from the observed frequency response.

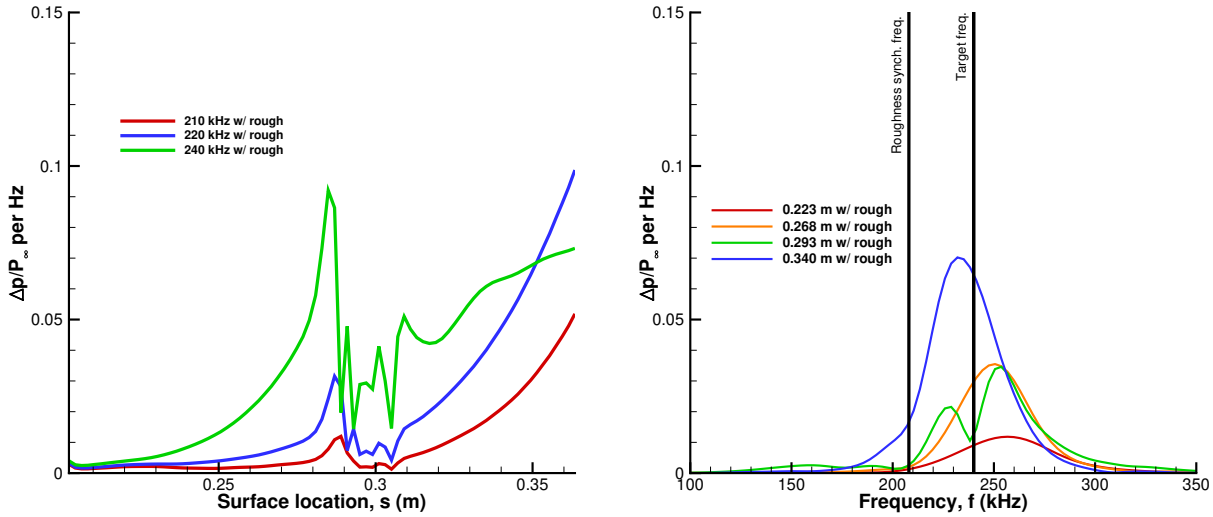

(a) (b)

Figure 5.23: (a) Spatial evolution of wall pressure perturbation at fixed frequency FFT results, and (b) fixed location frequency spectrum results for a cone with roughness.

Lastly, Figs. 5.23a and 5.23b contain FFT results for fixed frequency and fixed location. For fixed frequency, Fig. 5.23a looks at the same range considered in the smooth case plotted over the same range and domain. But unlike the smooth case there is obvious attenuation especially for 240 kHz and higher and moderate attenuation for 230 and 220 kHz. There is, however, some growth for 210 kHz not seen in the smooth case. This growth is expected as the frequency is near the roughness synchronization location frequency of 208 kHz. If the unsteady simulation were extended downstream, as it is in case C.1-Ext we would expect to see more growth of frequencies below 208 kHz. Also evident is the disturbance amplification upstream of the roughness element, which is consistent with flat plate simulations.

Figure 5.23b also looks at the same four fixed location considered in the smooth case. Here, again the attenuation of the narrow band of frequencies is obvious. There is some amplification of the 0.268 m band but not so much as to dominate the already attenuated

bands. In the next section the rough and smooth cases will be compared and contrasted more closely with more definitive conclusions on the effect of roughness on this cone.

5.8 Comparison of Smooth and Rough FFT Results

For a clearer understanding of the effect of transition-delaying roughness, the frequency spectrum results for both the smooth and rough cases are reproduced here side-by-side. Figure 5.24 contains both frequency spectrum maps with letters in different region denoting important features. The first region is A, which denotes an area upstream of the roughness in which the frequency is higher than the local synchronization frequency. Between the smooth cone contour on the left and rough contour on the right, there is a mild overall amplification of all frequencies before reaching the roughness. Moving downstream, region B is entered. This region denotes an area where frequencies are attenuated significantly. It is this behavior which promotes surface roughness as an approach to passive transition-delay. Moving into the region below the synchronization frequency, region C sees some amplification between the smooth and rough case. The amplification, however, is bounded from below by the synchronization curve. This behavior can be detrimental to the passive transition-delay strategy as these amplified frequencies can lead to transition on their own, but can be mitigated by using successive roughness strips as will be seen in Chapter 6 [FWH15].

Lastly, the results for fixed frequency and fixed location are compared together. Figure 5.25a compares several fixed frequencies in which the chosen frequencies are the target frequency (240 kHz), a frequency below the target frequency (220 kHz) but above the roughness synchronization frequency, and a frequency near the roughness synchronization frequency (210 kHz). For 240 kHz the instability is significantly attenuated by the roughness. For 220 kHz the instability is mildly attenuated by the roughness, which is to be expected since the frequency is only slightly higher than the roughness synchronization location frequency. And lastly, for 210 kHz the instability is slightly amplified by the roughness since its frequency is near the roughness synchronization location frequency.

Moreover, Fig. 5.25b compares several fixed locations of the frequency spectrum. At

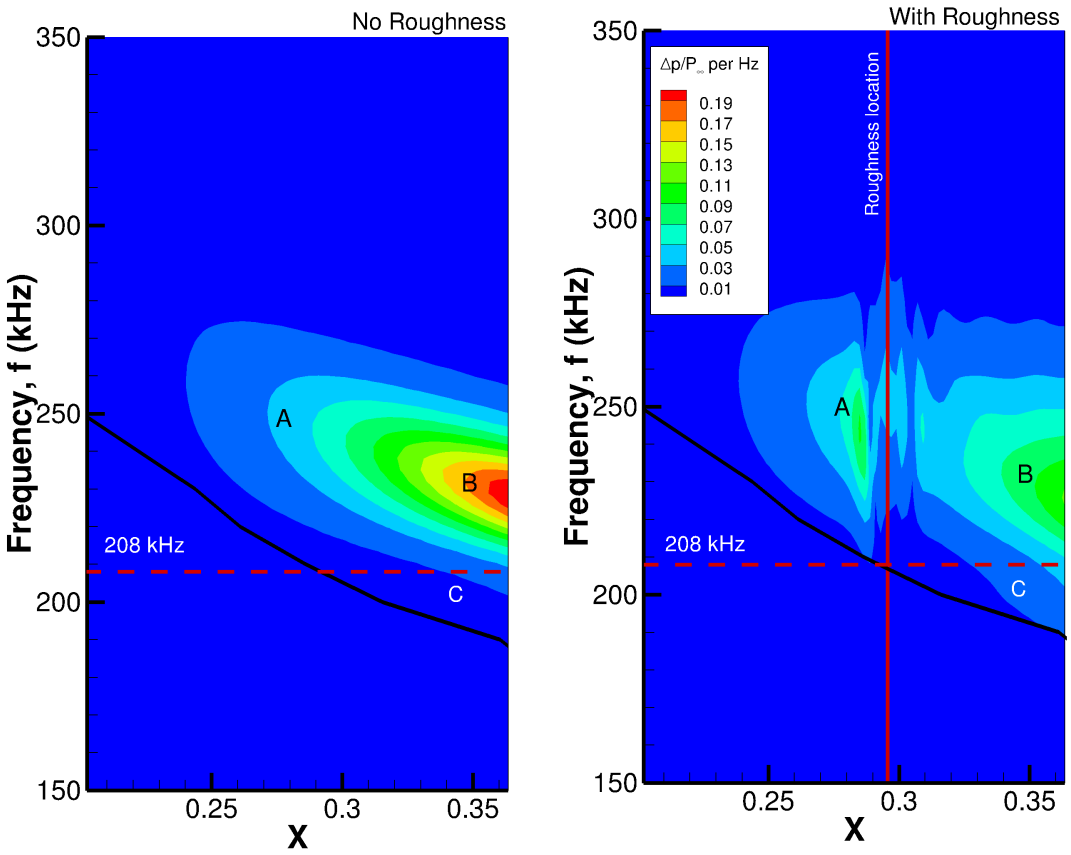

Figure 5.24: Comparison of FFT maps for both instances of the smooth and rough cases.

$s = 0.243$ m, there is only the slightest amplification across the entire band. This is not surprising since the location is upstream of the roughness element. The next location at $s = 0.268$ m is also upstream of the roughness and here too the frequency band is amplified. From peak to peak the amplification is 28%. The next location at $s = 0.293$ m is at the roughness location, here there is clear attenuation and some modulation of the band. From peak-to-peak, the attenuation here is nearly 40%. And lastly at $s = 0.340$ m, the experimental location where turbulent intermittency begins to dominate, there is a peak-to-peak attenuation of 54%. An interesting observation of this comparison plot is slight growth of frequencies greater than 260 kHz for $s = 0.293$ m. This higher frequency growth is not apparent at $s = 0.340$ m in which the amplified frequencies are below 215 kHz. This growth above 260 kHz at $s = 0.293$ m may be due to the proximity of the roughness strip.

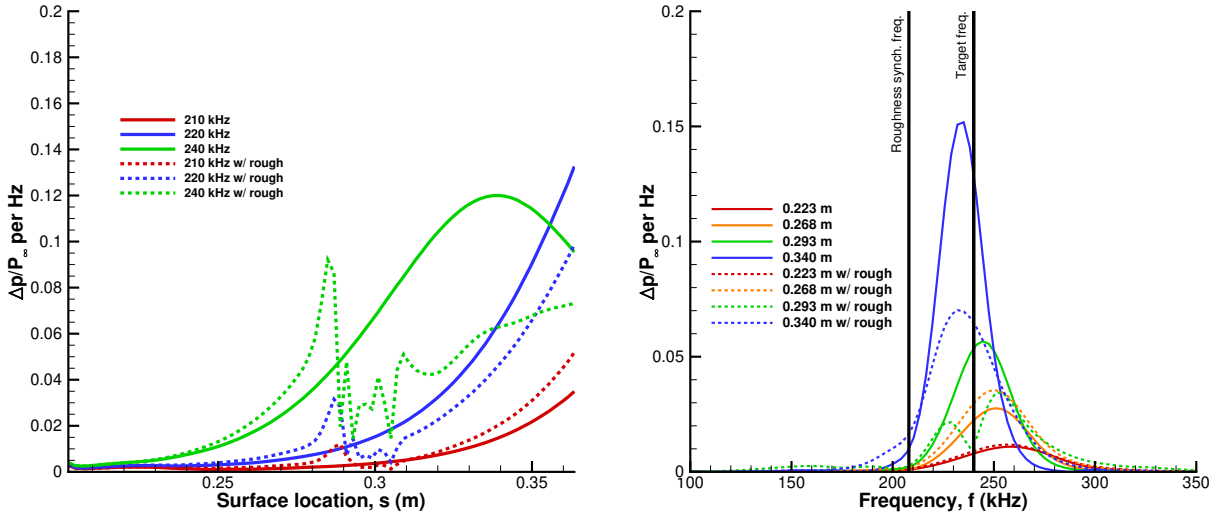

(a) (b)

Figure 5.25: Comparison of FFT results for smooth and rough cases

CHAPTER 6

C.1-Extended: Downstream Behavior

The purpose of the extended C.1 case is to a gain more complete stability analysis and understanding of second mode attenuation for a cone that is not limited by the physical length of an experimental test article. In the scope of the stability analysis, higher N-factors are calculated, and lower unstable second mode frequencies become relevant. Moreover, the longer cone makes it possible to investigate the re-growth of attenuated second mode frequencies and the growth of amplified frequencies downstream, which is important for the practical application of transition-delaying roughness.

6.1 Smooth Cone Steady-state Results

The steady-state pressure and temperature results for the extended C.1 frustum are featured in Fig. 6.1. Overall, the results are consistent with the steady-state results in Chapter 5. The pressure results on the top half of the cone show a moderate pressure ratio, relative to the freestream pressure, along the majority of the cone. The temperature ratio in the bottom half is also consistent with previous steady-state results. The contours show a high thermal gradient between the boundary layer and the flow behind the shock, which extends over the length of the frustum. This is to be expected as the simulation assumes a constant wall temperature, which is considerably higher than the freestream temperature.

The cone's blunt nose tip is featured in Fig. 6.2. The pressure contours show a maximum pressure ratio at the very tip of the cone followed by a favorable pressure gradient moving downstream. It is also apparent that the moderate pressure ratios seen on the frustum are reached within approximately eight nose radii of the tip. The temperature contours too show

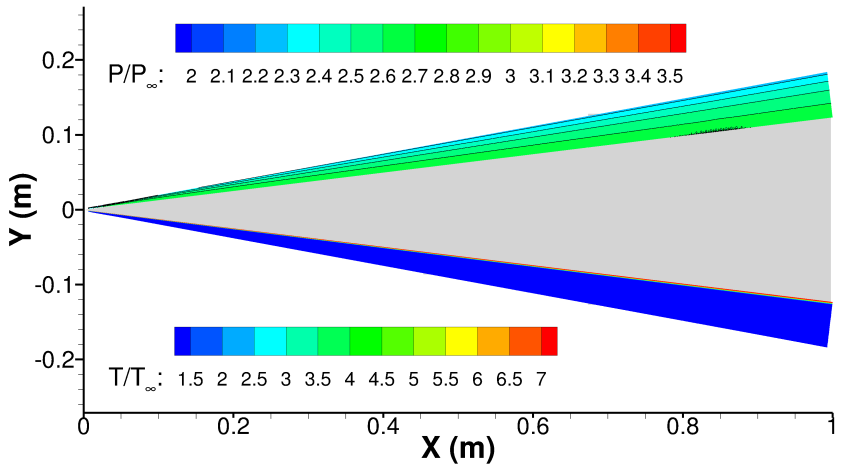

Figure 6.1: Pressure & temperature contours along the cone frustum. The figure is split with pressure plotted on the top half of the cone and temperature plotted on the bottom half.

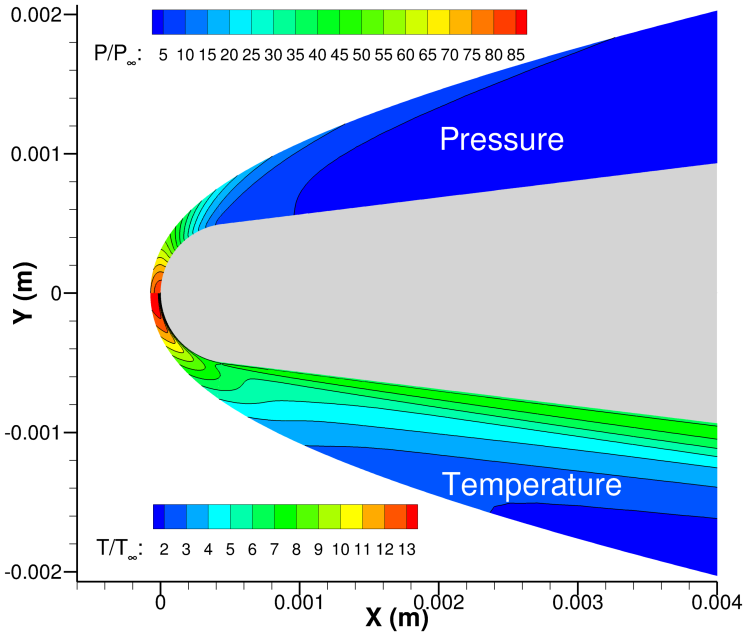

Figure 6.2: Pressure & temperature contours at the blunt nose tip. The figure is split with pressure plotted on the top half of the cone and temperature plotted on the bottom half.

a maximum temperature ratio at the cone tip. The maximum however is offset from the cone surface. This offset is due to the constant wall temperature boundary condition, which does not consider surface heating. Moving downstream, the temperature ratios seen along the cone frustum are reached within six nose radii.

6.1.1 Design of Roughness Array

Moving to the design of the transition-delay roughness array: the location, height, and width of each strip must be determined. In Chapter 5, the singular roughness strip was scaled to measure half the local boundary layer thickness in height and twice the boundary layer thickness in width; these same ratios are used here for each of the strips in the array. As in case C.1 the first roughness strip is located at $s = 0.293\ m$—seven centimeters downstream of the synchronization location for the 240 kHz second mode instability. In order to attenuate the second mode over a wider frequency range, multiple strips are placed downstream of the first roughness. The downstream spacing of the strips is measured as twenty times the boundary layer thickness of the previous strip location. Since the boundary layer thickness increases downstream, the physical dimensions of each roughness strip changes but the proportions are kept the same as described above. The dimensions for the complete roughness array designed for the simulation are listed in Table 6.1. The locations of the strips are calculated based on the surface length, s. For convenience, the x-locations for each array is also given, where x=0 is measured from the tip of a corresponding sharp cone with the same half-angle.

6.2 Stability Analysis of Extended Steady State

This section is a brief overview of the stability analysis for case C.1-Ext. The neutral curve, N-factor, phase speed, and growth rate results for the first 0.5 meters of the cone surface are the same as case C.1 as expected. However, the extended frustum increases the range of unstable frequencies present in the boundary layer, increases the maximum obtainable N-factor value, and reveals an additional discrete mode.

The neutral curve in Fig. 6.3 is similar to the neutral curve featured in Fig. 5.6 alongside

Table 6.1: Dimension and location of each strip in the roughness array

Strip	Surface, s (m)	x-location, x (m)	Height, h (mm)	Width, w (mm)
1	0.2936	0.2943	0.813	3.254
2	0.3261	0.3265	0.864	3.457
3	0.3607	0.3609	0.916	3.663
4	0.3973	0.3972	0.955	3.819
5	0.4355	0.4351	1.001	4.006
6	0.4756	0.4749	1.053	4.211

the growth rate map for case C.1 with the exception that the present neutral curve extends to one meter and contains additional lower unstable frequencies. The neutral curve is composed of two branches that enclose an area of unstable growth rates. The area outside of the curve contains stable growth rates. The curve itself is where the growth rate is zero, and the frequency is neither growing nor decaying. Branch I and branch II of the neutral curve are the points where a given frequency will become unstable and then stabilize again, respectively.

The target frequency for the onset of intermittent turbulence is still 240 kHz, just as in case C.1; however, the extended cone provides the ability to investigate lower unstable frequencies. Lower frequencies are likely to lead to transition because the neutral curve is the widest for a given frequency. The farther apart the branches of the neutral stability curve are, the more distance an unstable frequency has to grow. With the additional 0.5-meter cone length, unstable frequencies between 101 and 139 kHz are now present within the flow field.

Starting at $s = 0.5$ m on branch I and going downstream, the unstable frequency lower bound is extended from 139 to 101 kHz. The entire unstable frequency range now extends from 101 to 647 kHz. Moreover, the extended simulation allows frequencies between 139 and 200 kHz to stabilize along branch II of the neutral curve. The range of new unstable frequencies between 101 and 139 kHz may be narrow, only 38 kHz, but can reach very high N-factor values. For these reasons, it is important to be aware of the lower unstable frequencies

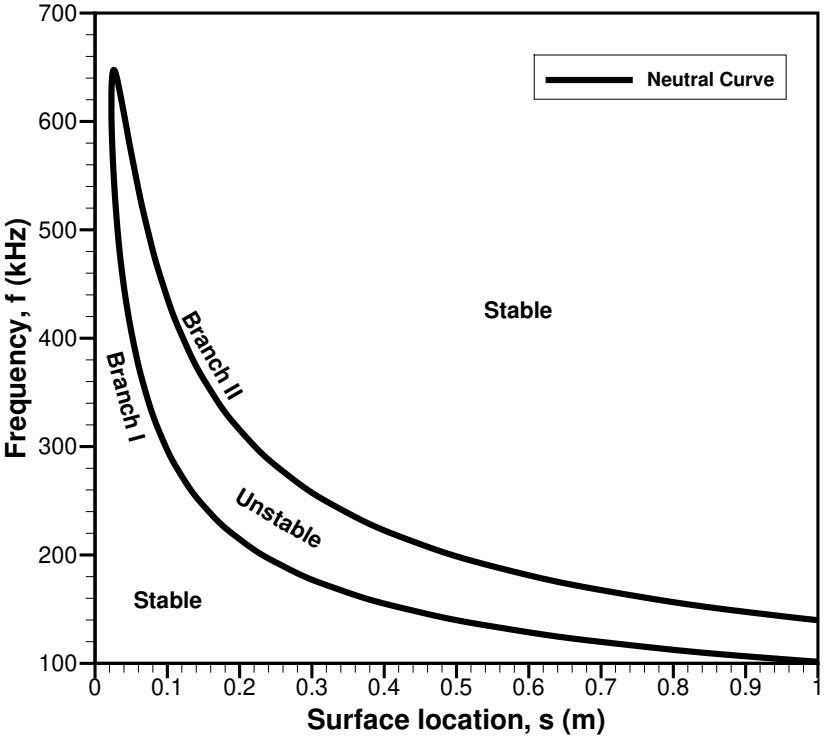

Figure 6.3: Neutral curve for mode S exhibiting Mack's second mode instability on mode S.

because they can cause transition if the roughness control strategy does not attenuate them.

The longer cone means the N-factor analysis can be extended to include the complete range of unstable frequencies. Figure 6.4 contains the N-factor values for unstable frequencies from 140 to 420 kHz in increments of 20 kHz. In case C.1, the half-meter-long cone reached a maximum N value of 7.3 for a frequency of 200 kHz. By comparison, the extended simulation has a maximum N value of 10.6 for a frequency of 140 kHz, a 45.2% increase. Due to the narrow frequency range and large width of the lower neutral curve, the last 0.5 meters of the N-factor plot is dominated by just a few frequencies. Intermittent turbulence is known to occur at these flow conditions around 0.34 m, corresponding to an N value of 5.75. For the passive roughness control strategy, this means that any unattenuated frequency that can potentially reach an N-factor value above 5.75 could destabilize the boundary layer and lead to transition.

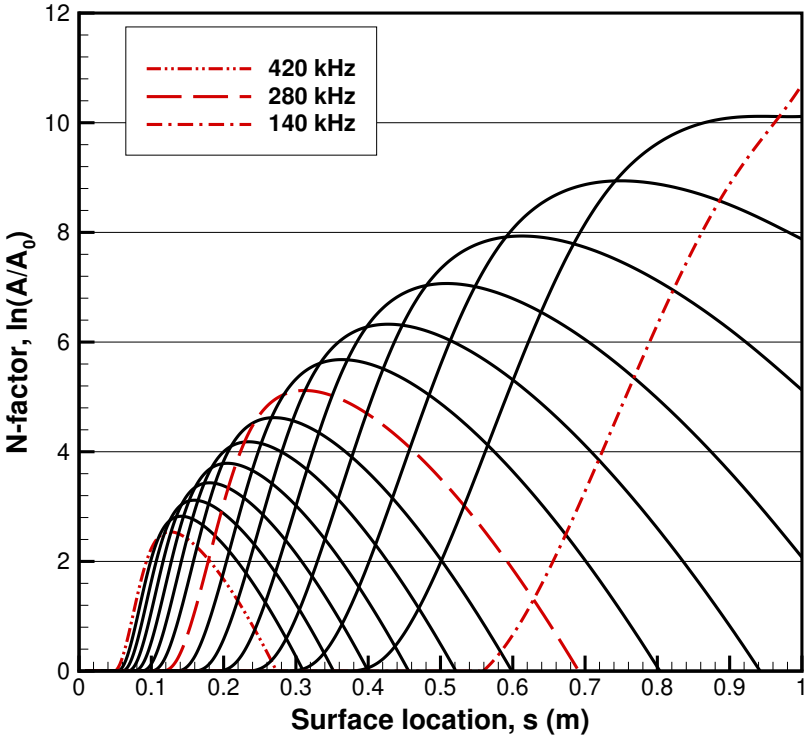

Figure 6.4: N-factor values for Mack's second mode instability on mode S. Fixed frequencies go from 140 to 420 kHz in increments of $\Delta f = 20$ kHz.

The last parts of the stability analysis to address for case C.1-Ext are the phase speed and growth rate for the roughness synchronization frequency of 208 kHz. The phase speeds for modes F1+, F1-, and S (Fig. 6.5) are largely unchanged from the half-meter simulation. Mode F1-'s phase speed continues to decrease to a value of 0.62. Meanwhile, mode S maintains a slightly increasing phase speed between the continuous and slow acoustic speeds. The only addition to the phase speed diagram is mode F2+, which emerges from the fast acoustic spectrum near $s = 0.756$ m. However, the phase speed of mode F2+ does not decrease much before reaching the end of the cone frustum. If the cone were longer, or if the fixed frequency were higher, mode F2+ would reach the branch point near the vorticity/entropy spectrum, and mode F2- would emerge. Mode F2- would then couple with mode S at some point downstream, and Mack's third mode instability would appear.

Moving on to the growth rate plot in Fig. 6.6, again, the growth rate result for modes F1+, F1-, and S are identical to the half-meter cone. The extended length frustum shows

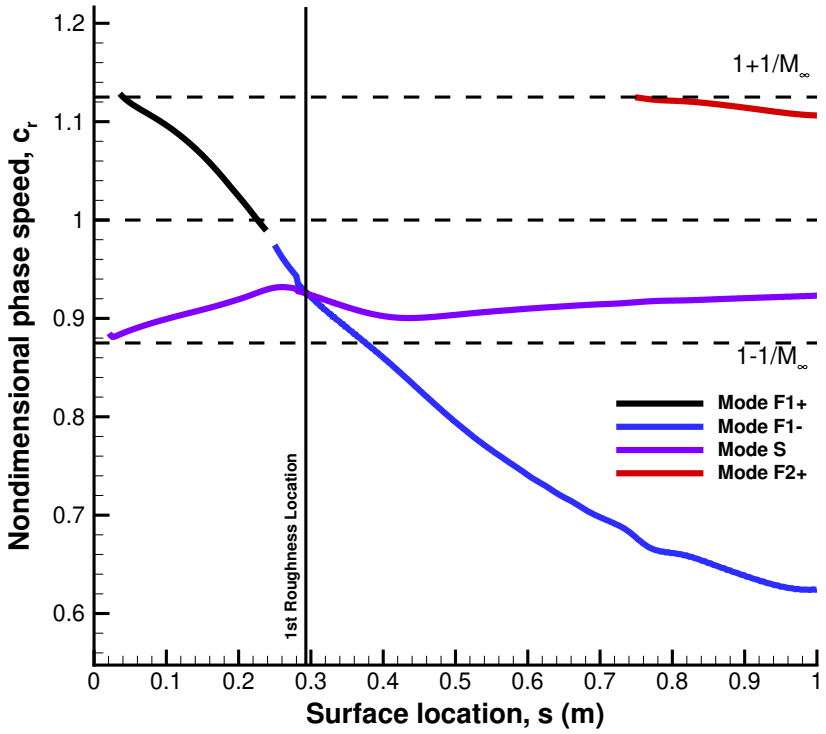

Figure 6.5: Phase velocity for modes F and mode S at the roughness synchronization frequency of 208 kHz.

that mode F1-, after decoupling with mode S, keeps a steady growth rate near -100 m^{-1}. Mode S also reaches its branch II neutral point at $s = 0.662$ m where the growth rate becomes stable. Mode F2+'s growth rate is shown overlapping mode S at the end of the cone. Although this is unusual to see in the context of mode F1 and mode S, the result is anticipated for higher Fast modes from a simplified model of mode coupling. The simplified model posits that the imaginary wavenumber terms for a pair of coupled modes will be zero unless they are in the vicinity of where the modes intersect (e.g., the synchronization point), at which point the wavenumbers will become complex conjugates of one another [FT11]. To some degree, this is what we see when mode S becomes unstable and mode F1- mirrors it by dipping. The reason these two modes do not have the same growth rate before the second mode instability appears is because of their proximity to the nose tip and a separate first mode instability mechanism.

To summarize the extended cone results briefly, by lengthening the frustum 0.5 meters,

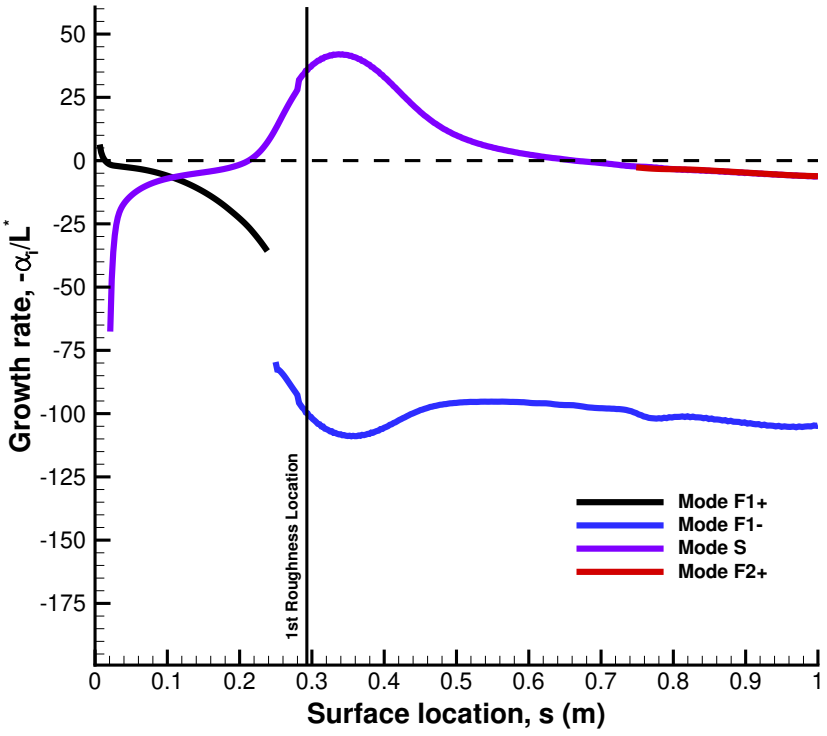

Figure 6.6: Growth rate for modes F and mode S at the roughness synchronization frequency of 208 kHz.

the range of unstable frequencies has increased, and so has the potential for destabilizing the boundary layer. Thus any transition-delaying roughness array must account for this. It is already known that frequencies below the synchronization frequency are amplified by surface roughness. In order to delay transition, any roughness configuration should be carried out to the end of the cone.

6.3 Unsteady Roughness Results

This section presents the unsteady results for a single roughness strip and the roughness array. The results include x-t diagrams of the unsteady disturbances as they propagate downstream, time traces of the disturbances at different time intervals, Fourier decomposition of the unsteady data into pressure spectra, and comparisons of the maximum disturbance amplitudes as a function of frequency and cone location. These results, along with the extended

cone frustum, provide a detailed insight into the long-term ability of surface roughness to attenuate second mode frequencies.

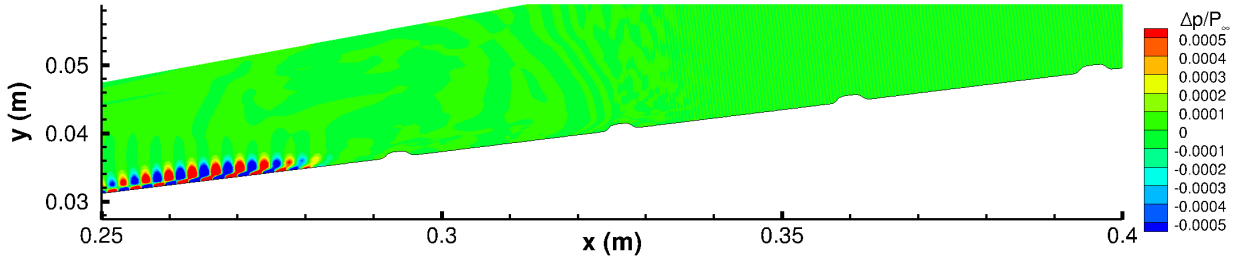

(a)

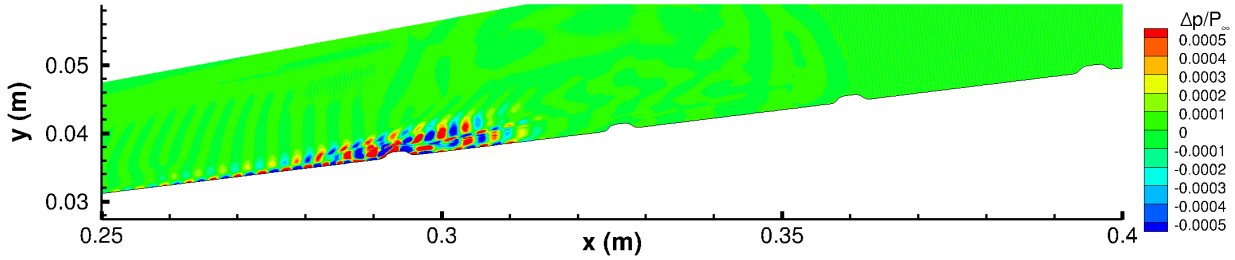

(b)

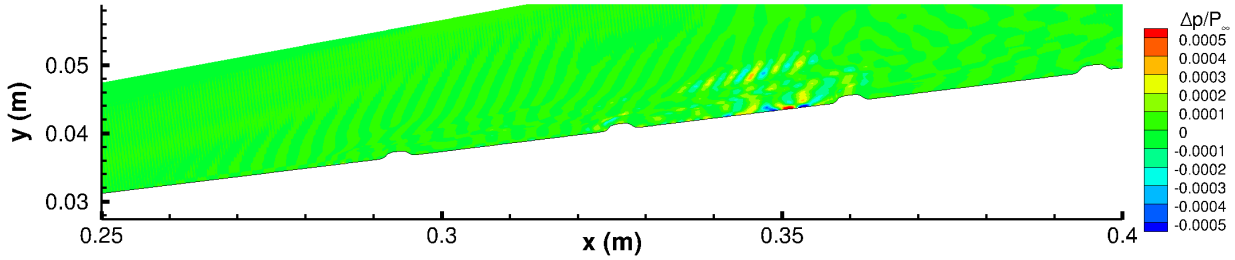

(c)

Figure 6.7: (a) Unsteady disturbance as it approaches the first four strips of the roughness array. (b) As the disturbance traverses the first strip, parts of it are pushed into flow behind the shock. (c) By the second strip the disturbance is significantly weakened and the parts swept into the flow are dissipating. Contour levels are clipped to emphasize the disturbance.

For the unsteady DNS simulations of the roughness array, the blowing-suction actuator is added to the steady-state simulation upstream of the array. The pulse is defined by Eq. (2.26) and the parameters in Table 2.1. The actuator wraps circumferentially around the cone and produces a 2-D instability wave. Figure 6.7a shows the axisymmetric view of the disturbance

as it approaches the roughness array. The disturbance is fully formed and contains the rope-like structures indicative of Mack's second mode instability. As the disturbance passes over the first strip in the array (Fig. 6.7b), part of the disturbance is swept into the flow behind the shock. This flow behavior is consistent with the single roughness unsteady results in Chapter 5. The part of the disturbance that remains in the boundary layer is left visibly weaker by the roughness strip. By the second and third strip (Fig. 6.7c), the disturbance within the boundary layer is hardly visible. Meanwhile, the oscillations in the inviscid flow behind the shock proceed to dissipate. Thus far, the disturbance pressure results in Fig. 6.7 show that the first half of the roughness array is effective at damping the second mode.

The disturbance's propagation over the remaining strips in the array continues in Fig. 6.8. By the fourth strip (third to last), the weakened disturbance is spread out over the array (Fig. 6.8a), with part of the disturbance passing over the fourth strip and another part in between the fourth and fifth strip. The disturbance shows signs of amplification as it approaches the roughness strip. The same disturbance behavior can be seen near the fifth and sixth strips (Fig. 6.8b), where the disturbance is wider than the distances between the strips. Causing different segments of the disturbance to be amplified, attenuated, and amplified again simultaneously. Meanwhile, parts of the disturbance are transported away into the inviscid layer as it passes over each roughness strip. The sixth and last strip in the array (Fig. 6.8c) shows upstream amplification near the strip and downstream attenuation. Unlike the upstream roughness strips, the oscillations pushed into the inviscid layer appear stronger. Downstream of the last element, the oscillations appear weaker but are already growing in amplitude. Overall, the roughness array successfully damps the second mode, but in doing so, it undergoes cycles of amplification and damping along with the shedding of disturbance energy into the flow behind the shock.

Focusing now on the long-term downstream disturbance behavior afforded by case C.1-Ext, Fig. 6.9a shows the disturbance as it propagates away from the roughness array. The disturbance is clearly damped and barely visible within the boundary layer; likewise, the oscillations in the flow behind the shock appear to dissipate. As the disturbance propagates downstream, it quickly grows in amplitude (Fig. 6.9b). By Fig. 6.9c, the disturbance is

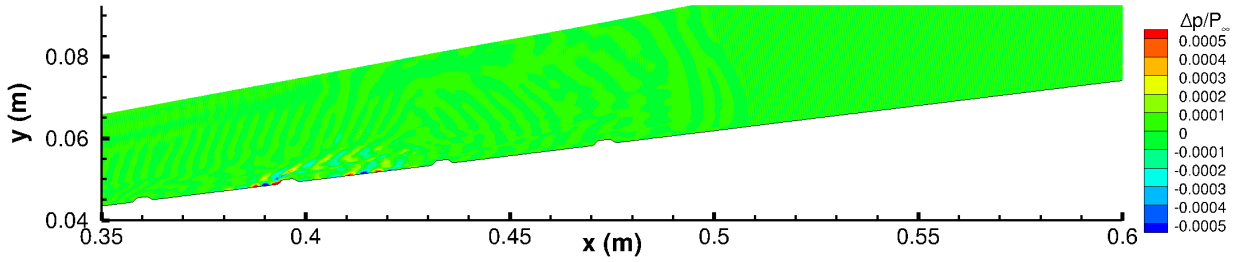

(a)

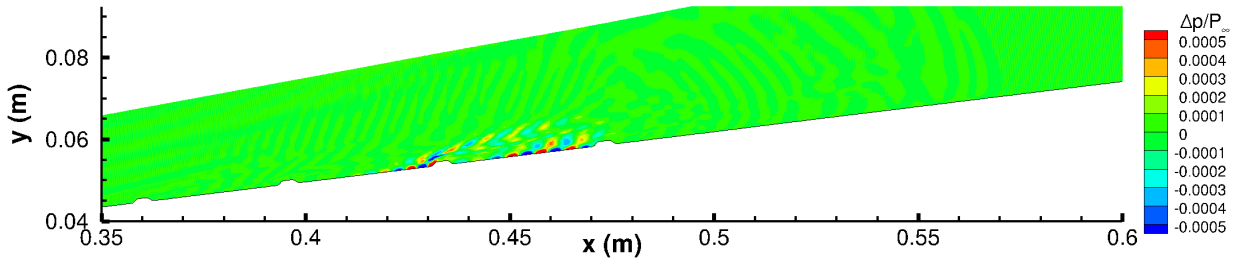

(b)

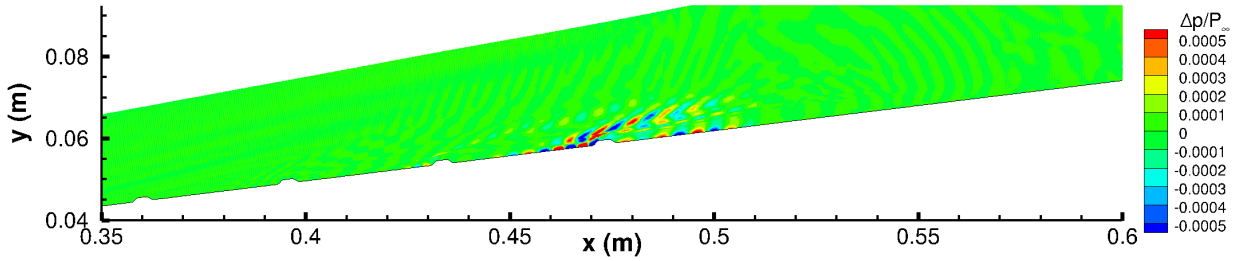

(c)

Figure 6.8: (a) The disturbance appears significantly weakened by the third to last roughness strip. (b) The disturbance structure is spread across several strips and appears to grow in strength. (c) By the last strip the disturbance is growing but is still weaker than its initial strength. Contour levels are clipped to emphasize the disturbance.

proportionally as strong as it was upstream of the roughness array and continues to grow further downstream. This downstream evolution is eye-opening; research on the roughness effect has already established that roughness elements amplify the lower downstream frequencies. The sudden regrowth of the disturbance shows that, although the roughness array delayed transition, it also destabilized the boundary layer. This result means that passive boundary layer control strategy needs to be applied to the whole length of the cone to keep

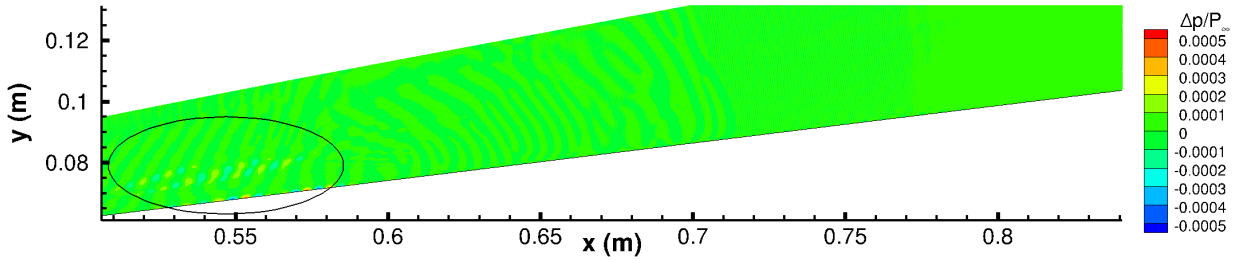

(a)

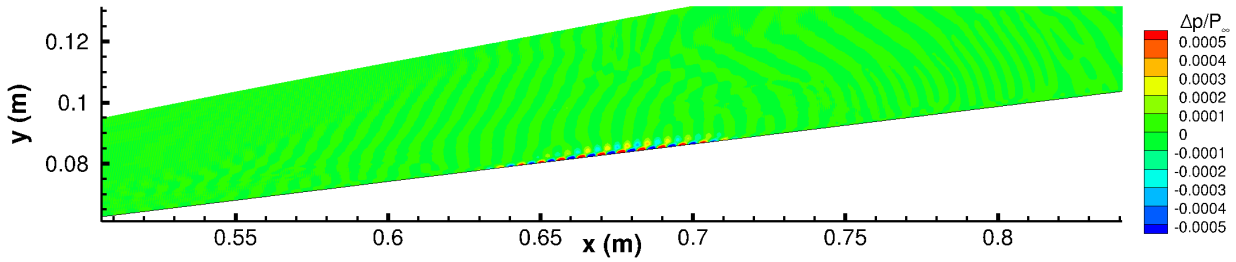

(b)

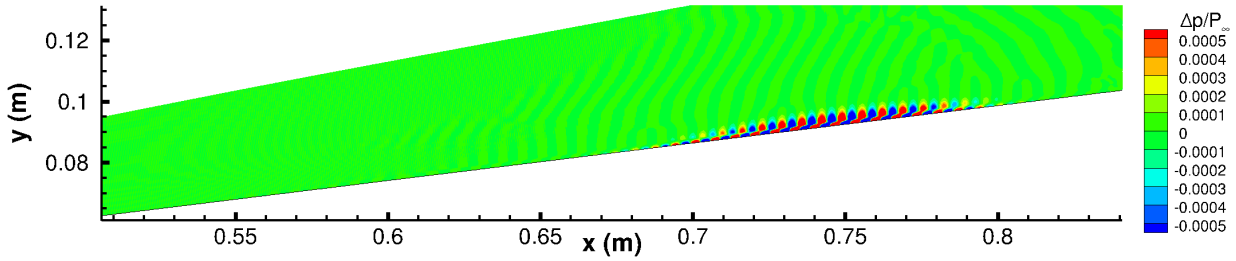

(c)

Figure 6.9: (a) Downstream of the roughness array the disturbance is damped significantly and barely visible (ellipse) in the flow. (b) Slightly further downstream the disturbance begins to grow. (c) The disturbance grows quickly, comparable to its initial strength, and continues to grow downstream. Contour levels are clipped to emphasize the disturbance.

transition delayed.

An x-t diagram of an unsteady pulse on a cone with a single roughness strip is presented in Fig. 6.10. The single roughness strip is placed at the synchronization location for the 208 kHz frequency intended to attenuate the 240 kHz frequency responsible for intermittent turbulence, and the actuator is located at $s = 0.1$ m. The figure shows the pressure

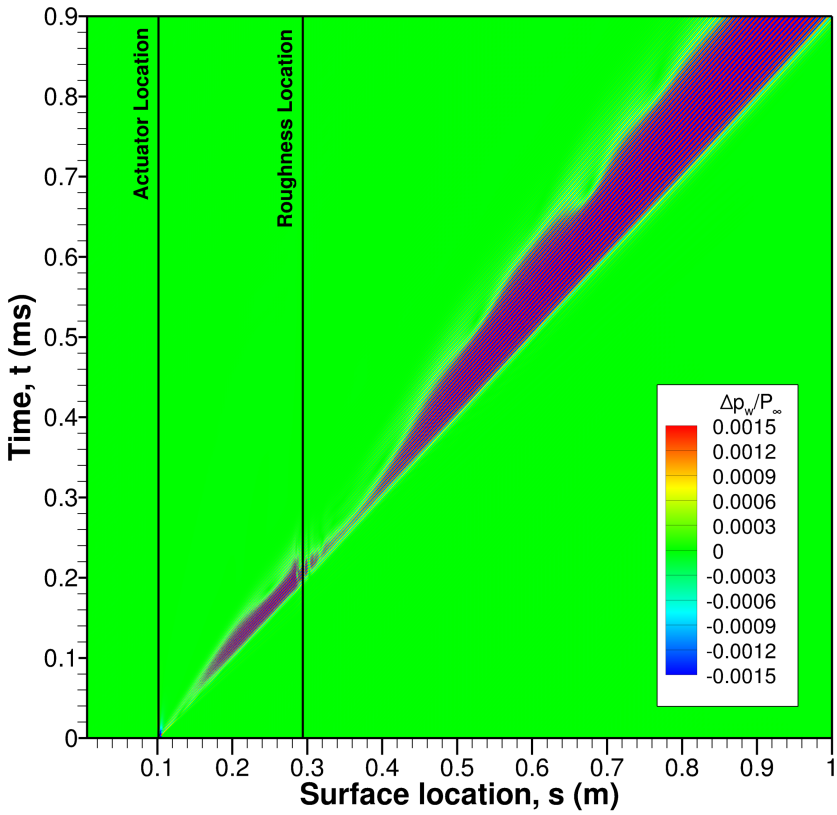

Figure 6.10: Single roughness strip x-t diagram showing the individual wave trajectories of the disturbance. Contours are clipped to show weaker satellite wave; $\max|\Delta p_{wall}/P_\infty| = 0.0262$.

perturbation as it propagates along the cone's surface over time.

The diagram makes it possible to view the disturbance as individual wave trajectories as they fan out from the actuator. The results in Fig. 6.10 clearly show the single roughness strip damps those wave trajectories. Amongst the collection of trajectories, the wavefront is visible throughout the unsteady simulation and does not change the angle of its trajectory. This constant angle means that the roughness strip does not impede the disturbances speed of propagation. However, the trailing wave trajectory takes on most of the amplitude attenuation. As time progresses, these amplitudes begin to grow again as expected reaching a maximum disturbance pressure ratio of 0.0262. Overall, the single roughness strip manages to attenuate the disturbance for a distance of 0.1 to 0.15 m.

The x-t diagram of an unsteady disturbance on a cone with the roughness array is pre-

sented in Fig. 6.11. The roughness array is intended to attenuate a broad range of second

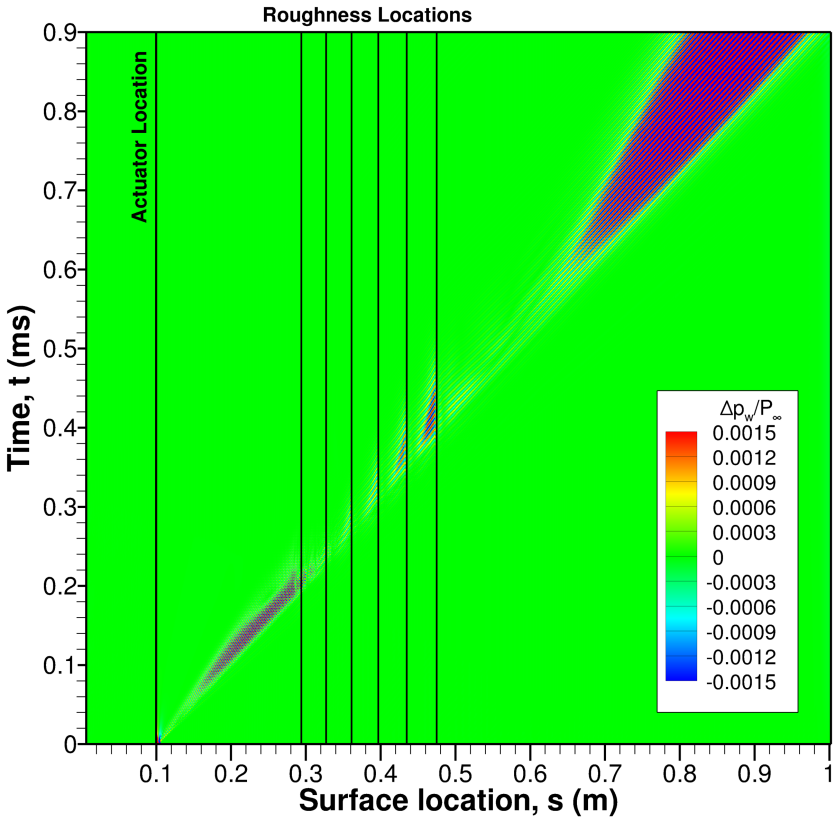

Figure 6.11: Roughness array x-t diagram showing the individual wave trajectories of the disturbance. Contours are clipped to show weaker satellite wave; $\max|\Delta p_{wall}/P_\infty| = 0.105$.

mode frequencies. The actuator is again located at $s = 0.1$ m. The diagram clearly shows that the roughness array is attenuating the disturbance. Except for of a few patched between roughness strips, the waves are damped to the point where they are no longer visible. Downstream, the wave trajectories reappear and begin to grow again, this time reaching a much higher maximum disturbance pressure ratio of 0.105. Overall, the roughness array manages to attenuate the disturbance for a distance of 0.4 to 0.45 m; however, the increased maximum pressure ratio clearly shows that the array is destabilizing to the boundary layer long term.

Although the x-t diagram provides an entire overview of the unsteady disturbance, it is difficult to discern its structure. Figure 6.12 features time traces along the surface taken

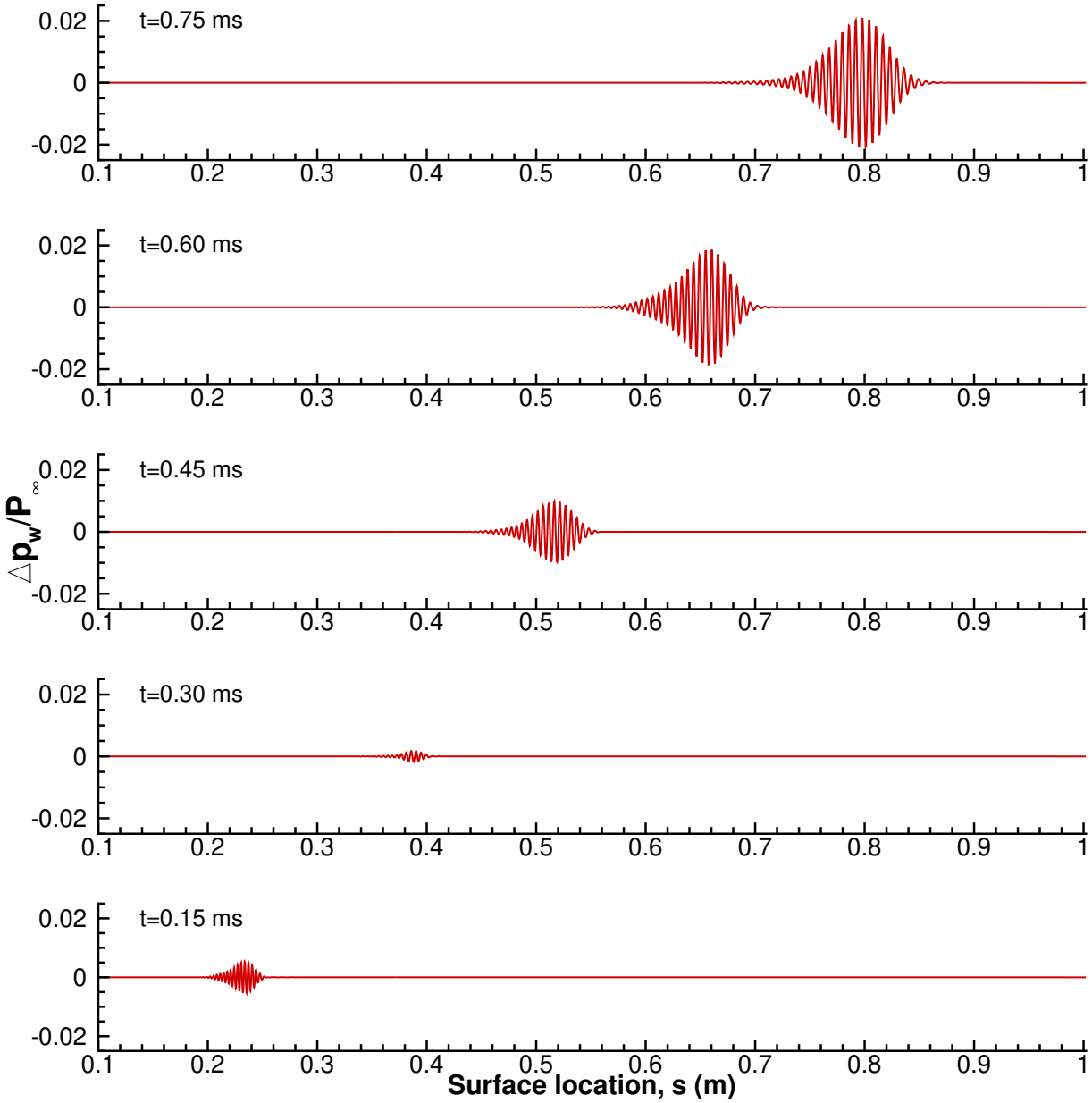

Figure 6.12: Propagation of disturbance along the cone surface with a single roughness strip. The instantaneous pressure is plotted at five equal time intervals of $\Delta t = 0.15$ ms.

at regular intervals of 0.15 ms for the single roughness strip simulation. At $t = 0.15$ ms ,the disturbance is upstream of the roughness strip and appears as a single wave packet. At $t = 0.30$ ms, the disturbance is just downstream of the roughness strip and is significantly reduced in amplitude as expected. Advancing further in time, the disturbance grows in amplitude from its attenuated state. This behavior is expected since mode S is unstable. The disturbance also maintains its appearance as a coherent wave packet with no additional modulation.

Time traces for the roughness array are presented in Fig. 6.13. The time traces are taken at the same 0.15 ms intervals as before. Like in Fig. 6.13, at $t = 0.15$ ms, the wave packet is upstream of the roughness strip and identical in appearance. The six roughness strips in the array then attenuate the disturbance significantly at $t = 0.30$, 0.45, and 0.60 ms. In general, the wave packet is attenuated by a factor of three or more. By $t = 0.60$ ms the wave packet is downstream of the last roughness strip and already starting to grow. At $t = 0.75$ ms the wave packet has grown significantly over a short distance. The wave is two-thirds the amplitude of the wave packet in Fig. 6.12 at the same time instant. So even though the wave packet is attenuated for longer with a roughness array than a single strip, the array could ultimately act to destabilize the boundary layer.

Since the disturbance is comprised of many different waves, it is possible to use Fourier decomposition to obtain its frequency spectrum. The decomposition is important because it provides insight into the growth and decay of individual frequencies and is more readily compared with LST results. The unsteady wall pressure data featured in Figs. 6.10 and 6.11 are used to obtain the disturbance's frequency spectrum for both roughness configurations. The resulting spectrum is normalized by the initial Gaussian pulse in order to compare the growth and decay of individual frequencies together, irrespective of their initial strength. The resulting normalized frequency spectra for both roughness configurations are featured in Fig. 6.14 along with the spectra for cone with no surface roughness. The smooth surface spectra in Fig. 6.14a provides a base case for comparison with the roughness spectra to see which frequencies are attenuated or amplified by the surface roughness.

Along with the spectra the neutral stability curve for mode S, obtained from LST analysis,

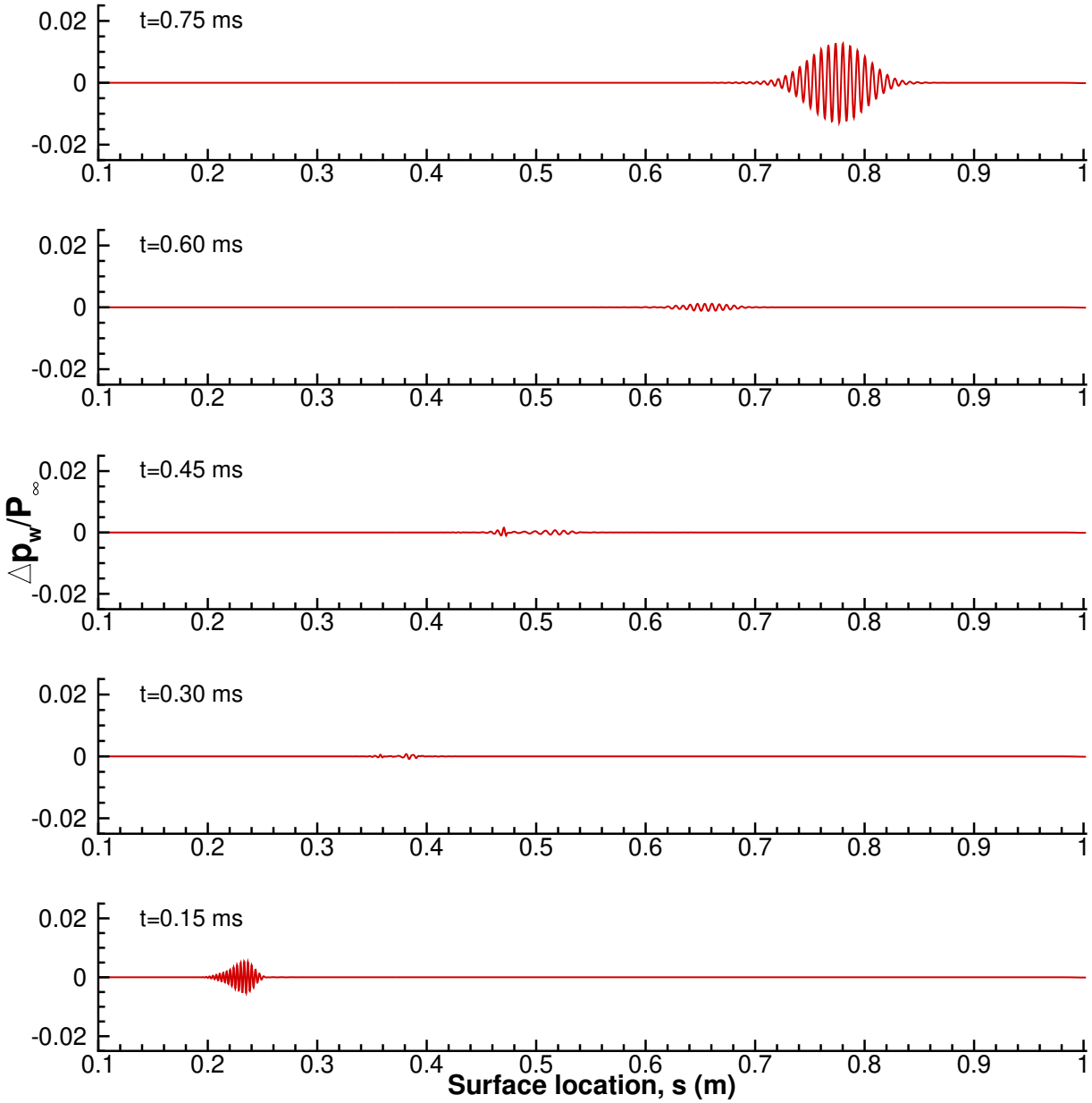

Figure 6.13: Propagation of disturbance along the cone surface with roughness array. The instantaneous pressure ratio is plotted at five equal time intervals of $\Delta t = 0.15$ ms.

is plotted in each subfigure. There is excellent agreement between each spectra and branch II of the neutral stability curve. Since growth rates are unstable between branch I and branch II, and stable everywhere else, amplitudes are expected to grow inside the neutral stability curve and decay outside of it. As Fig. 6.14a illustrates really well, the amplitude grows to the left of the branch II neutral stability curve for a fixed frequency and begins to dampen immediately to the right as expected. This result is notable because it shows good agreement between two separate and distinct methods: Fourier decomposition and LST analysis.

The frequency content of the second mode instability varies as it propagates, as evidenced by the spectrum contours in Fig. 6.14a. Higher frequencies increase in amplitude before dampening out, while lower frequencies, which have no amplitude at first, gradually increase downstream. This research reveals that the instability comprises only a small range of frequencies at any given location, with the frequency content shifting to lower frequencies downstream. Lower unstable frequencies also have longer residency in the boundary layer than higher unstable frequencies that grow and decay over short intervals, which illustrates why lower frequencies are more dangerous for laminar-turbulent transition.

Moving on to the Fourier analysis of the time histories with roughness, Fig. 6.14b is the spectrum for the cone with a single roughness strip. Using the neutral stability curve for reference and comparing Fig. 6.14b with Fig. 6.14a, the roughness strip has altered the spectrum significantly. Frequencies between 206 and 249 kHz, covering a range between 0.298 and 0.432 m, are significantly attenuated. While unstable frequencies lower than 206 kHz see an increase in magnitude. The amplifed frequencies are notably lower than the roughness synchronization location frequency of 208 kHz. The remaining contours follow the smooth surface spectrum's general shape, which grow and decay with respect to the neutral curve. For case C.1-Ext, the N-factor analysis and prior empirical results indicate that a frequency of 240 kHz is expected to cause intermittent turbulence around 0.340 m. Figure 6.14b shows that the 240 kHz frequency is sufficiently attenuated, and although there is no way to determine how far transition has been delayed accurately, from relative contour values between the smooth cone and single roughness strip, it can be estimated that transition has been delayed by at least 9.2 cm to $s = 0.432$ m. Downstream of this point, however, it is

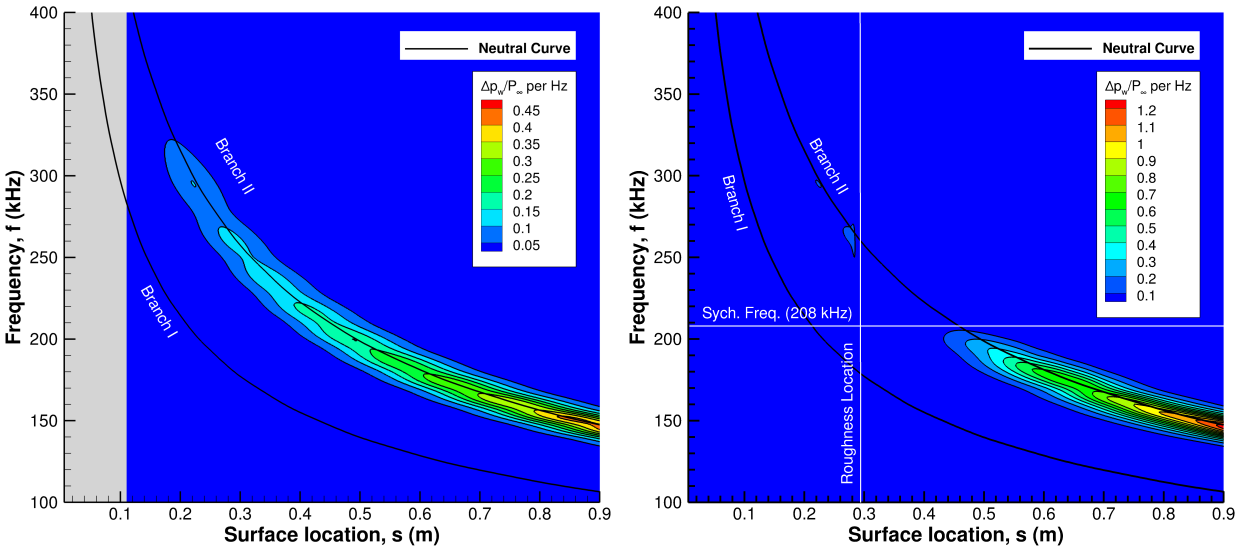

(a) No Roughness

(b) Single Strip

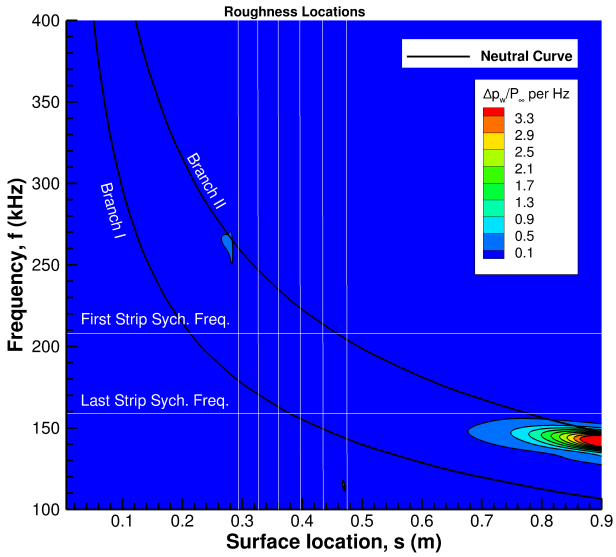

(c) Roughness Array

Figure 6.14: Normalized frequency spectra of unsteady DNS pressure results for a (a) smooth surface, (b) single roughness strip, and (c) roughness array.

clear from the amplified spectrum that the roughness strip destabilizes the boundary layer, which guarantees inevitable transition. The extended cone provides clear evidence that the single roughness strip can delay the growth of the second mode for some time but ultimately destabilizes the boundary layer.

The unavoidable destabilization of the boundary layer can be remedied by using multiple roughness strips. The frequency spectrum in Fig. 6.14c shows that the roughness array has altered the spectrum even further than the single roughness strip. Frequencies between 156 and 249 kHz are attenuated, while unstable frequencies lower than 156 kHz see an increase in strength. The cone surface between 0.298 and 0.677 m has also been cleared of the second mode instability. As with the single roughness strip, the array has sufficiently attenuated the 240 kHz frequency responsible for transition, and with the use of multiple strips, it can be estimated that transition has been delayed by at least 33.7 cm to $s = 0.677$ m. This is clear evidence that the roughness array can delay boundary transition downstream over longer distances. However, once the array ends, frequencies lower than the synchronization frequency of the last strip are greatly amplified, making transition inevitable. The long-term downstream behavior of the second mode instability on the extended cone clearly shows that the roughness effect is ultimately destabilizing to the boundary layer.

Figure 6.15 takes a closer look at the FFT results for fixed frequencies for both the single roughness element and the roughness array. Plotting select frequencies reveals data about the FFT results that are otherwise obscured by discrete contour levels. For instance, the frequencies 275 and 250 kHz in Fig. 6.15a show growth upstream of the roughness strip and then attenuation downstream of it, but not before undergoing some damped oscillations. The 225 kHz disturbance pressure shows some growth downstream of the strip but is mostly attenuated. This frequency is followed by the disturbance pressures for 200, 175, and 150 kHz, and all exhibit increased growth. This growth is expected as these frequencies are less than the roughness strip synchronization frequency of 208 kHz.

Figure 6.15b looks at the same fixed frequencies for the roughness array FFT results plus the frequency exhibiting the maximum downstream amplification. The frequencies 275 and 250 kHz are relatively unchanged showing the same initial upstream growth, downstream

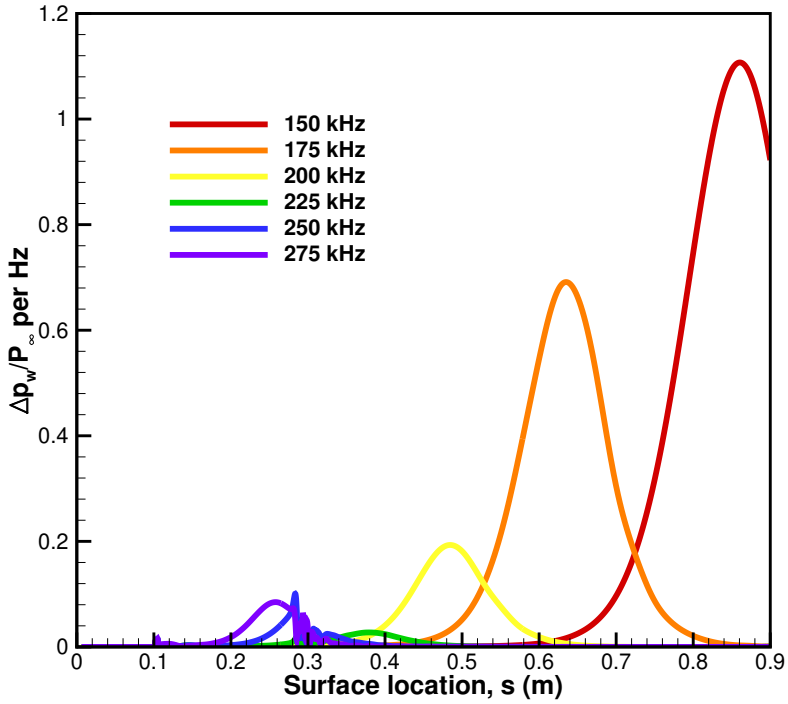

(a) Single Strip

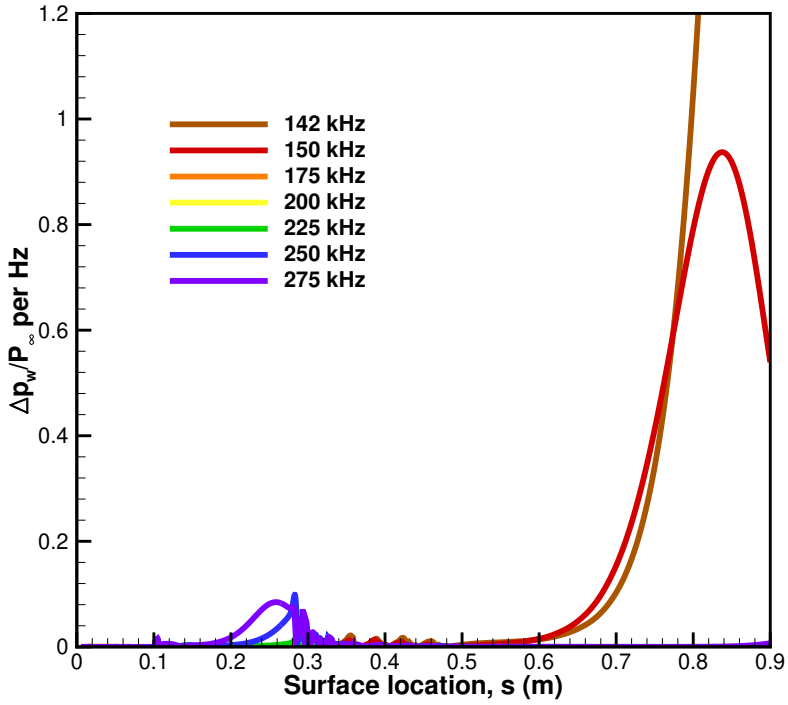

(b) Roughness Array

Figure 6.15: Spatial evolution of wall pressure perturbation at fixed frequency FFT results for (a) a single roughness strip and (b) roughness array.

attenuation, and damped oscillations. However, the frequencies 225, 200, and 175 kHz differ from Fig. 6.15a and undergo complete attenuation with minor amplification at each roughness strip in the array. Only the last two frequencies, 150 and 142 kHz show significant growth. This growth is expected as these frequencies are lower than the synchronization frequency of 164 kHz for the last strip in the array.

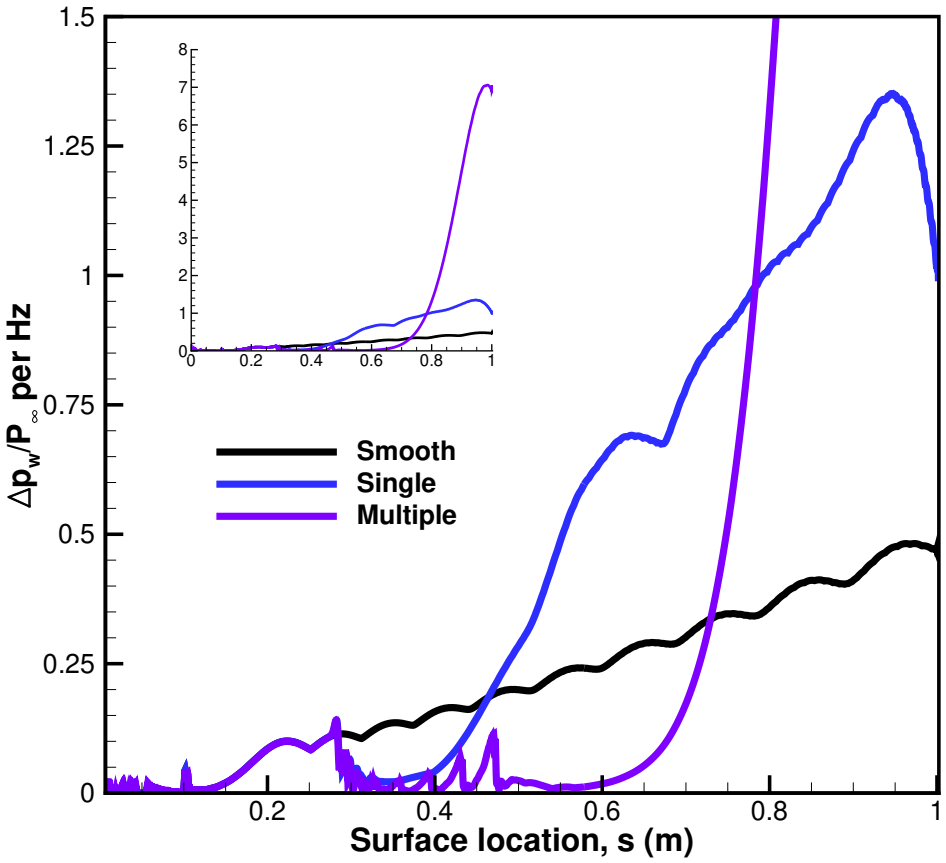

Figure 6.16: Maximum pressure disturbance spectra, $\Delta p_w/P_\infty$ per Hz, as a function of streamwise loction.

Since the objective of the passive boundary layer control strategy is to attenuate the second mode instability, it is advantageous to examine and compare the maximum disturbance pressure FFT across the smooth and roughness configurations. Figure 6.16 compares the maximum disturbance pressure as a function of streamwise location. This figure makes the extent of the attenuation and amplification abundantly clear. For instance, both roughness configurations have the same Max $\Delta p_w/P_\infty$ per Hz as the smooth cone between the

actuator at $s = 0.101$ m and the first roughness location at $s = 0.294$ m. This shows that the roughness strips have very little upstream influence. Downstream of the single roughness, the roughness effect has effectively attenuated the maximum disturbance pressure up to $s = 0.464$ m, where the single roughness plot intersects the plot for the smooth cone. Beyond this point, the Max $\Delta p_w/P_\infty$ per Hz increases rapidly with a tremendous growth rate over the base flow, reaching a peak that is 2.8 times larger in magnitude. Likewise, the max disturbance pressure for the roughness array is effectively attenuated up $s = 0.731$ m. At which point, the growth rate for the roughness array max disturbance pressure explodes and reaches a peak 14.7 times higher than the smooth surface base flow. Figure 6.16 communicates quite effectively that the roughness effect can delay transition but ultimately destabilizes the boundary layer.

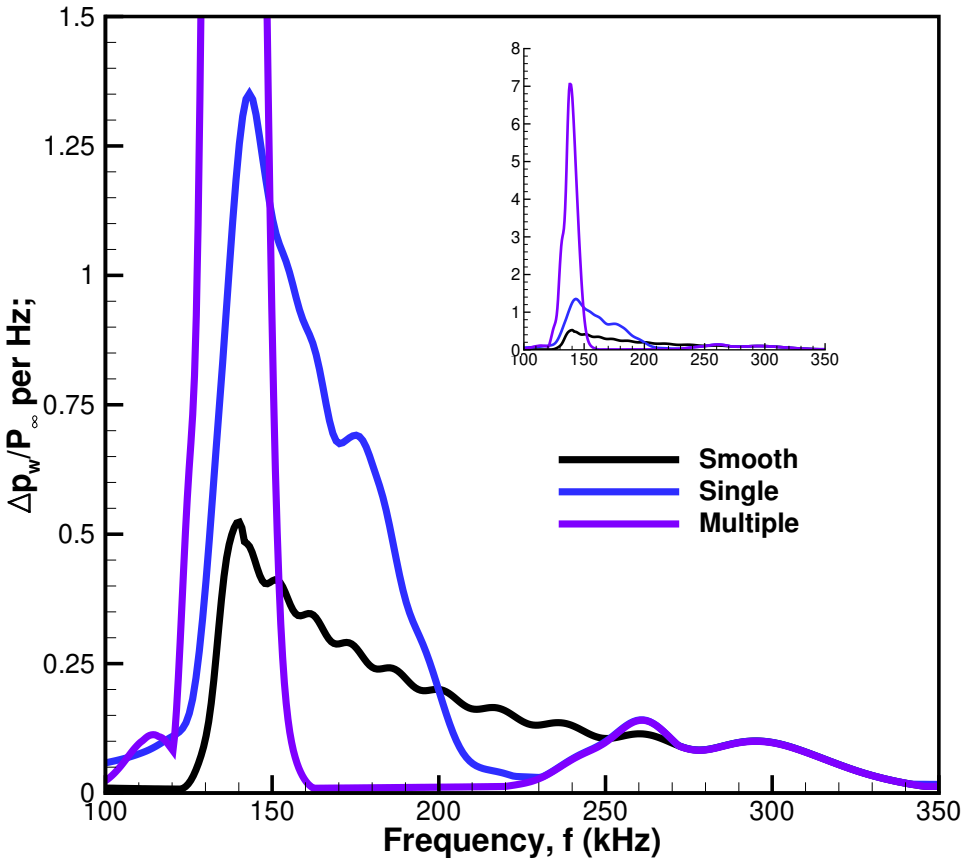

Figure 6.17: Maximum pressure disturbance spectra, $\Delta p_w/P_\infty$ per Hz, as a function of frequency.

Figure 6.17 compares the maximum disturbance pressure FFT as a function of frequency. The figure clearly shows which frequencies are being attenuated and amplified. For frequencies higher than 272 kHz, no attenuation or amplification has taken place. A narrow band between 251 and 272 kHz sees some slight amplification; this can be attributed to the decaying oscillations behind the first roughness location seen in Fig. 6.15. For the single roughness strip, the range between 200 and 251 kHz is effectively attenuated. This range is the target range identified by the N-factor analysis to contain the 240 kHz frequency most likely to cause intermittent turbulence. The successful attenuation of this range shows that the roughness strip fulfilled its intended design. Frequencies below 200 kHz are amplified significantly, peaking around 142 kHz. The drop-off in amplitude is due to the finite length of the cone. The results for the roughness array show that frequencies between 152 and 251 kHz are effectively attenuated; in fact most of the range is essentially flat, which is the goal of the control strategy. However, around 161 kHz amplitudes grow tremendously fast, reaching a peak around 138 kHz.

Both roughness configurations show an interesting behavior of the roughness effect. It would appear that the surface roughness does not dampen or dissipate the second mode as initially thought but instead transfers the disturbance energy from higher frequencies to an increasingly narrow band of lower frequencies.

An interesting detail of the smooth cone disturbance pressure FFT is the undulations in both the positional and frequency plots. Presumable linear growth of the instability would cause the plot to be smooth. This issue is addressed in great detail in Section 8.3. In brief, it is the result of primary and secondary wave interference brought on by forcing by the blowing-suction actuator and its proximity to the neutral curve.

CHAPTER 7

Experimental Validation

This chapter presents the experimental results done in collaboration with Dr. Katya Casper at Sandia National Laboratories and the accompanying linear stability analyses. Experimental results include pressure spectra at two transducer locations on the cone with and without roughness and Schlieren images of the boundary layer. The pressure spectra show which unstable frequencies are growing or attenuated and when the boundary layer becomes turbulent. The Schlieren images show the physical structures present in the boundary layers during transition, such as laminar and turbulent boundary layers and the second mode's rope-like waves.

The roughness array designed in Chapter 6 was tested under two experimental conditions: Mach 8 and Mach 5. The Mach 8 experiment (case C.2) followed the flow conditions used to design the roughness array except that the test article had a smaller nose radius. In general, sharper blunt nose radii decrease the stability of the boundary layer, making the experiment a more rigorous test of the roughness array—however, changes in boundary layer thickness, roughness cut-off frequency, synchronization location, and transition locations could make the roughness array ineffective. Linear stability results of the sharper cone's boundary layer are provided to show that the roughness can adequately attenuate the second mode instability as designed.

The Mach 5 experiment (case C.3) examines what happens when the roughness array is in off-design flow conditions. The Mach 5 flow brings with it a different boundary layer with new synchronization locations and new transition mechanisms like Mack's first mode instability. Linear stability analysis of the Mach 5 boundary layer is performed to understand its stability characteristics thoroughly. N-factor calculations are performed to gauge the

relative strength of the second mode instability, and growth rate maps of the first and second mode are computed to identify the frequency ranges of the instabilities and where they are located on the cone.

To summarize the experimental results briefly, the Mach 8 results show that the roughness array did indeed stabilize the boundary layer and attenuated the target frequencies. This result is validation that the surface roughness control strategy works on a cone with a growing boundary layer with a range of unstable frequencies. Contrastingly, the Mach 5 experiment shows that the surface roughness was ineffective at attenuating the second mode or the first mode and destabilized the boundary layer. The broad takeaway here is that the control strategy may not work in off-design conditions.

7.1 Case C.2: Experimental Validation and Sharp Nose Effects

The purpose of case C.2 is for experimental validation with CFD simulations of the transition-delaying roughness designed using the steady-state results of case C.1. As mentioned in Section 1.2, the nose tip radius of the experiment was 0.05 mm instead of 0.5 mm, for which the transition-delaying roughness was designed. Thus, to see if the as-designed roughness array also satisfied the passive boundary layer control strategy in the new flow field, case C.2 was computed.

7.1.1 Smooth Cone Steady-state Results

The steady-state pressure and temperature results for the frustum of the C.2 cone are featured in Fig. 7.1. The results are typical of a straight blunt cone. The pressure results on the top half of the cone show a moderate change in pressure ratio along the frustum. In the bottom half of Fig. 7.1, the temperature ratio contours show a warm-wall thermal boundary layer, which is expected since the simulation assumes a constant wall temperature that is higher than the freestream temperature. The flow behind the shock maintains a nearly uniform temperature ratio until it reaches the edge of the thermal boundary layer. Overall, there is very little change in the streamwise gradient along the cone.

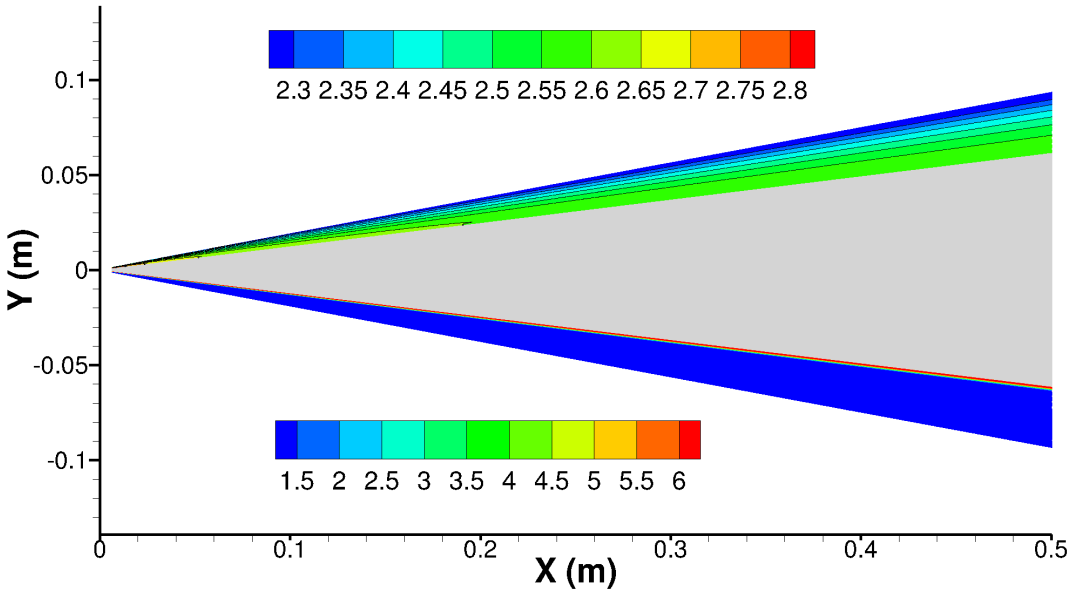

Figure 7.1: Pressure and temperature contours along the cone frustum. The figure is split with pressure plotted on the top half of the cone and temperature plotted on the bottom.

Taking a closer look at just the blunt nose tip in Fig. 7.2, the steady-state pressure and temperature results are presented together. The pressure contours show an increasing maximum pressure ratio toward the nose tip followed by a favorable pressure gradient downstream. Because of its much smaller radius, the gradients in the pressure field are concentrated near the nose tip. Similarly, the temperature contours also show an increasing maximum temperature towards the nose tip. Unlike the cone frustum, the sharp nose radius imparts a temperature gradient over the entire flow between the wall. The sharp nose's area of influence extends approximately six radii downstream for pressure and twelve radii for temperature. Beyond these distances, the pressure and temperature ratios take on the appearance of the frustum in Fig. 7.1. This lack of downstream influence is noteworthy because it means that the different nose radii between cases C.1 and C.2 do not significantly affect the frustum where the roughness array is located.

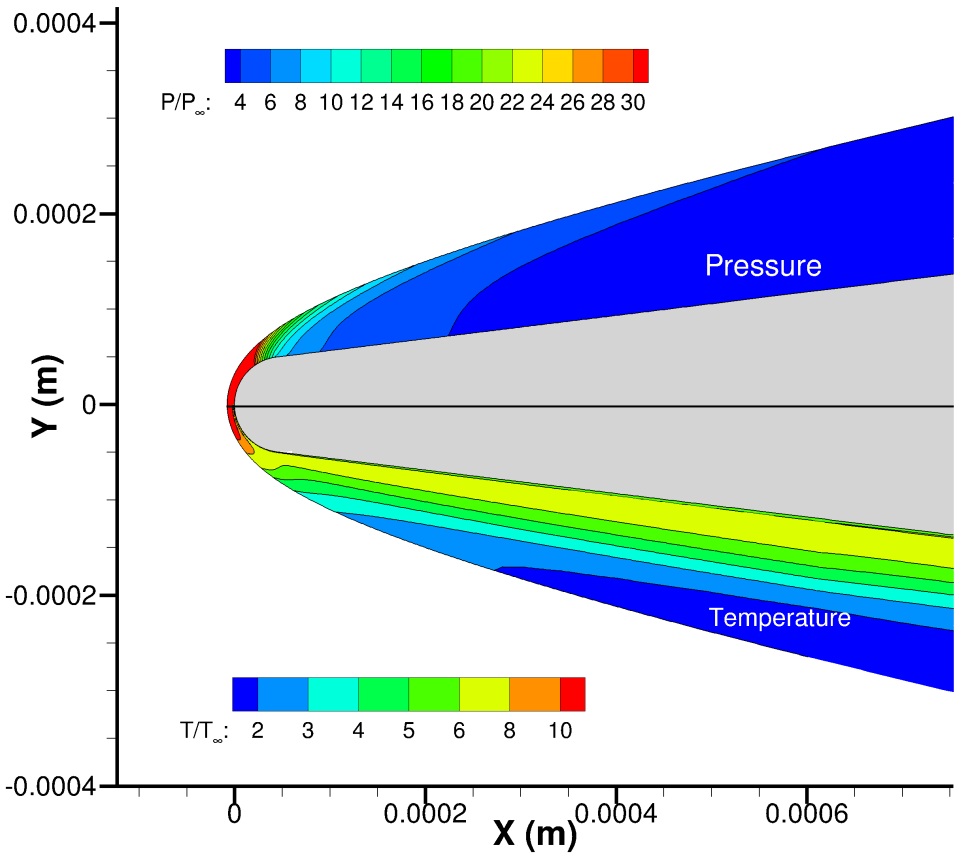

Figure 7.2: Pressure & temperature contours at the blunt nose tip. The figure is split with pressure plotted on the top half of the cone and temperature plotted on the bottom half.

7.1.2 Linear Stability Analysis of Steady-state

In Casper et al. [CBH16], the $r_n = 0.5$ mm blunt cone was known from experiment to undergo intermittent turbulence at approximately 0.34 m. In Chapter 6, which details the design of the roughness, the N-factor analysis of the $r_n = 0.5$ mm blunt cone shows that the intermittent turbulence location corresponded with an instability frequency of 240 kHz. For the $r_n = 0.05$ mm simulation currently in question the same location corresponds to a peak instability frequency of approximately 260 kHz as seen in Fig. 7.3. The onset of turbulence on the sharper cone is slightly upstream of the 0.34 m location.

This 260 kHz frequency, however, is not the cut-off frequency of the roughness array.

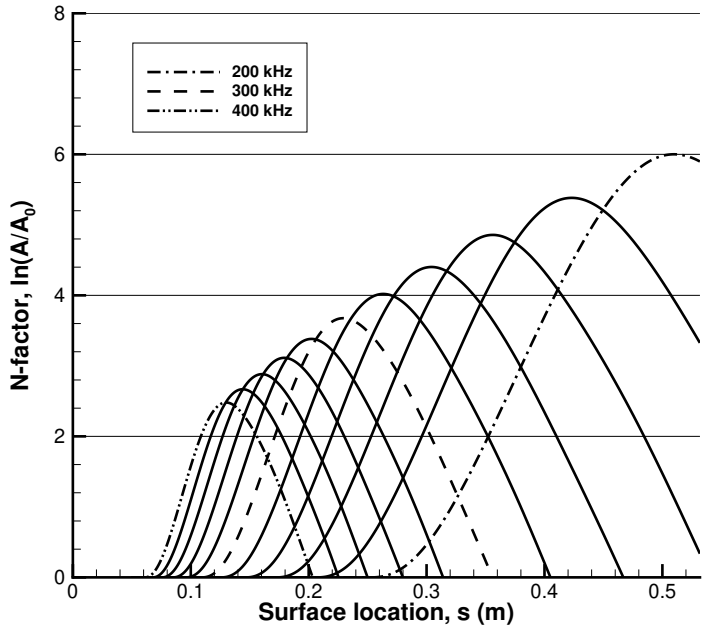

Figure 7.3: N-factor of Mack's second mode growth rate. Fixed frequencies go from 200 to 400 kHz in increments of $\Delta f = 20kHz$.

The cut-off frequency is 228 kHz, which is determined by identifying the frequency of the synchronization point corresponding to the first roughness strip in the array at $s = 0.2936$ m. The synchronization point is determined from the phase speed plot for 228 kHz given in Figure 7.4. Due to the branch cut between mode F+ and mode F- the synchronization point could not be resolved. Instead, the synchronization point was determined by connecting the ends of mode F+ and mode F- as illustrated by the red dashed line in Fig. 7.4a and noting where it intersects with mode S. This interpolation is reasonable since the phase speed for mode F is approximately linear between the vorticity/entropy and slow acoustic phase speeds. For 228 kHz, this intersection occurs at $s = 0.2936$ m. For a single roughness strip at this location, frequencies higher than 228 kHz are expected to be attenuated, while lower frequencies are expected to be amplified. Thus, the roughness array is expected to attenuate the 260 kHz frequency associated with intermittent turbulence on the sharper cone. The additional downstream roughness strips will ensure the amplified lower frequencies are attenuated.

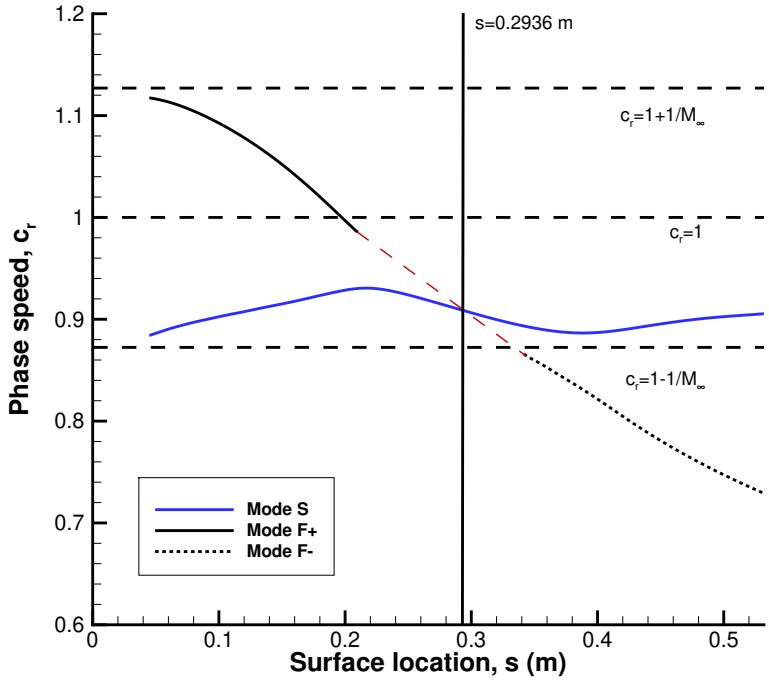

(a) Phase speed

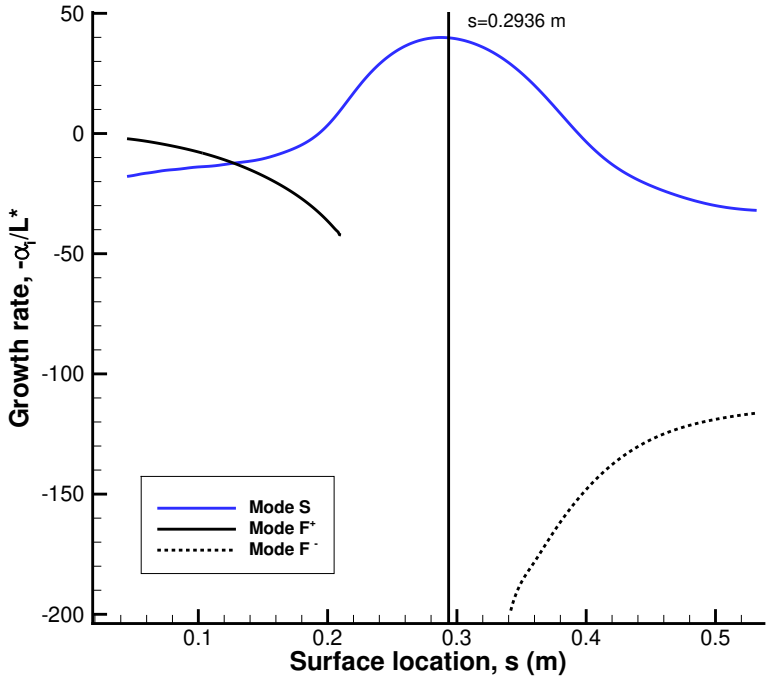

(b) Growth rate

Figure 7.4: Phase speed and growth rate for mode F and mode S at 228 kHz.

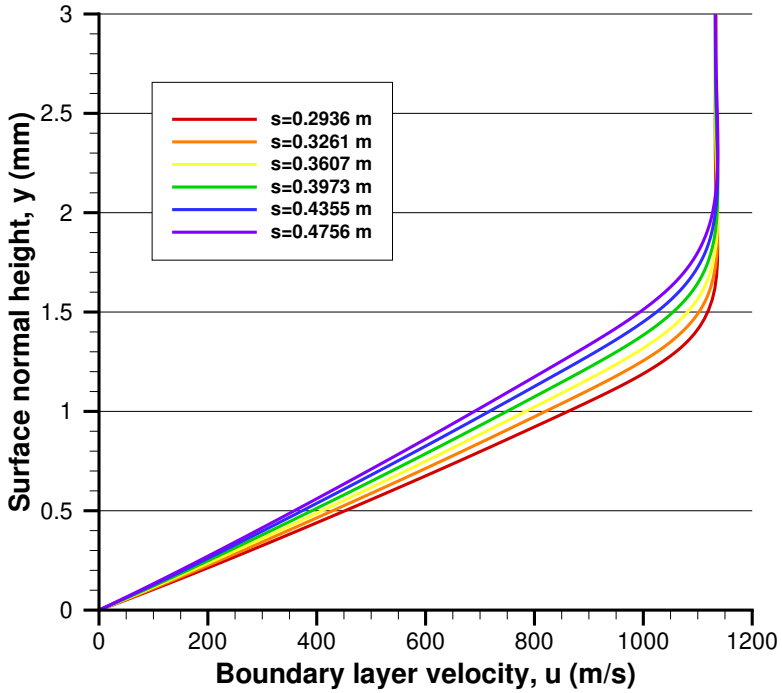

Figure 7.5: Boundary layer profile at each of the roughness strip locations.

Strictly speaking, mode S and mode F are not fully synchronized in that they do not have the same wavenumber, α, and angular frequency, ω, at the synchronization point, but instead are coupled over a range of wavenumbers for a given frequency. The appearance of Mack's second mode instability in Fig. 7.4b is indicative of this coupling, which forces mode S to become unstable and mode F to become more stable. Coincidentally, the roughness location nominally corresponds to mode S's peak unsteady growth rate.

Since the experiment has a sharper 0.05 mm nose radius than the 0.5 mm designed for in case C.1, it is important to know if the difference in nose radii significantly modified the boundary layer. The roughness array design called for the strips to be half the boundary layer thickness in height and twice its thickness in width. Any difference in the boundary layer thickness could significantly change the ratio of the roughness height to the boundary layer. The dimensional boundary layer profiles at each of the six roughness locations are plotted in Fig. 7.5. Their thicknesses are tabulated in Table 7.1, along with the heights of the simulated and experimental roughness strips. The roughness strips are manufactured

by adhering thermal tape to the test article. The tape has a nominal height of 0.2 mm with taller heights approximated by layering the tape. Table 7.1 shows that the ratios of experimental roughness to boundary layer height are close to the designed ratio of 0.5. As the roughness strips are immersed within the boundary layer, they should attenuate Mack's second mode instability [FWZ15].

Table 7.1: Ratio of roughness strip heights to boundary layer thickness for case C.2

Surface, s (m)	BL Height (mm)	Sim. Height (mm)	Ratio	Exp. Height (mm)	Ratio
0.2936	1.649	0.813	0.493	0.8	0.485
0.3261	1.738	0.864	0.497	0.8	0.460
0.3607	1.828	0.916	0.501	0.8	0.438
0.3973	1.918	0.955	0.498	1.0	0.521
0.4355	2.051	1.001	0.488	1.0	0.488
0.4756	2.067	1.053	0.509	1.0	0.484

Now that it has been established that the roughness array is adequately designed to attenuate Mack's second mode within the context of the smooth surface steady-state and linear stability theory, the steady-state with the roughness-array can be simulated. The pressure and temperature contours for the cone with surface roughness are featured in Fig. 7.6. Figure 7.6a shows that the Mach waves produced by the leading edge of each roughness strip merge within the shock layer. From the pressure contours, it appears that these merged Mach waves will not reach the shock boundary. This merging is contrasted with a single roughness strip that will produce a distinct Mach wave that will intersect with the shock boundary [HZ17]. The temperature contours in Fig. 7.6b show a significant increase in temperature ratio over the smooth cone simulation in Fig. 7.1. The increased temperature ratio is highly localized to the upstream corner of each roughness strip. This heating indicates that, while the purpose of the roughness array is to delay transition and thus reduce the heat flux to the surface due to turbulence, the strips themselves are subject to increased localized heating. Moreover, the presence of the roughness has caused the thermal boundary layer to

thicken; thus, the thermal gradient is more visible within the shock layer.

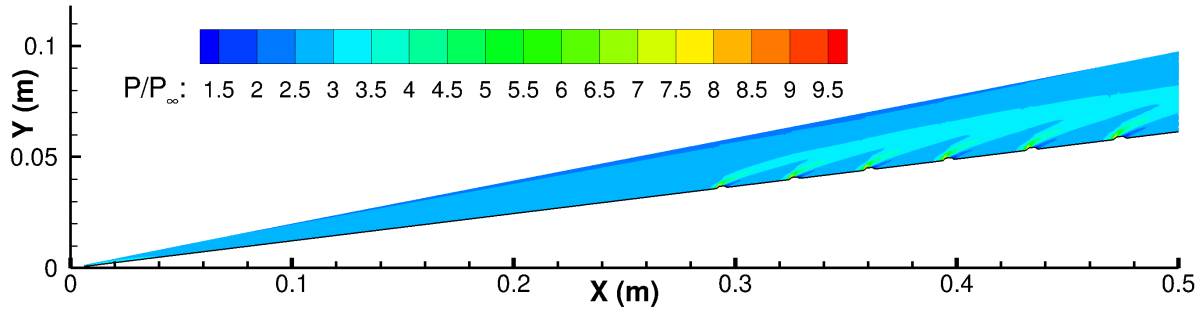

(a)

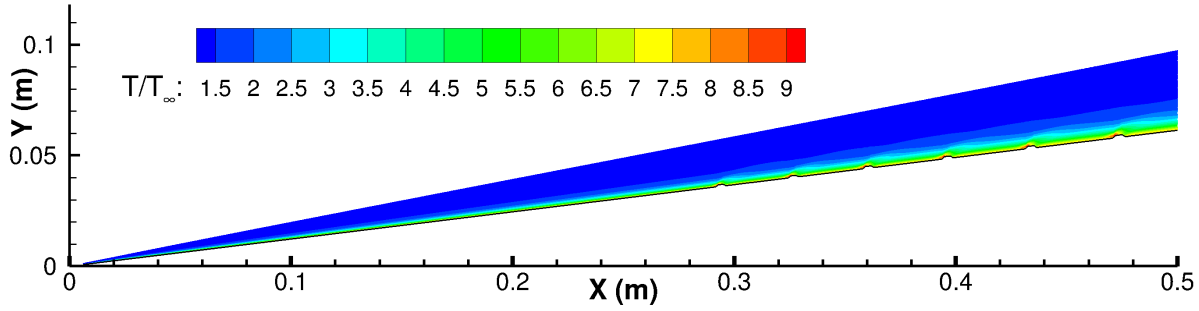

(b)

Figure 7.6: Steady-state (a) pressure and (b) temperature contours over roughness array.

A closer look at the pressure field around several of the roughness strips in Fig. 7.7 shows that while the compression region on the leading edge of the roughness is significantly higher than its surroundings, it too is relatively localized. The same is also true of the expansion area behind the roughness. It is suspected that this localization is due to the roughness strips being in an array. By contrast, on a single roughness strip, these compression and expansion regions lend themselves to creating a clearly defined Mach wave and expansion fan that extends downstream and into the shock layer [HZ17].

Moreover, the streamtraces in Fig. 7.7 evince a flowfield in which the roughness strips significantly influence the boundary layer. Wherein the streamtraces are pushed away from the cone surface. Simultaneously, streamtraces closer to the shock boundary are unperturbed, which is to be expected in a supersonic flow. One feature that is missing from the flow is

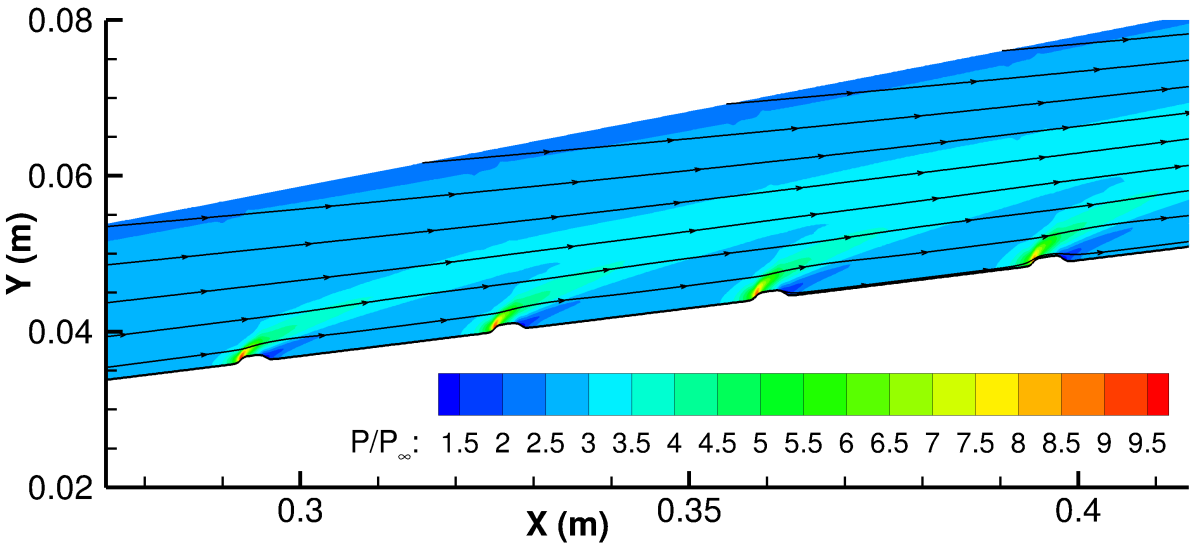

Figure 7.7: Streamtraces over the four leading roughness strips on a pressure contour.

the separation regions on either side of the roughness strip as seen in Fig. 7.8. Separation regions are present on isolated roughness strips with the same height, width, and smooth edges as the first strip in the array [HZ17]. They are also present on flat plates with a half-ellipse roughness [FWZ14b]. The reason for the separation regions' absence here is unclear; however, it may be related to how localized the compression and expansion regions are to the roughness.

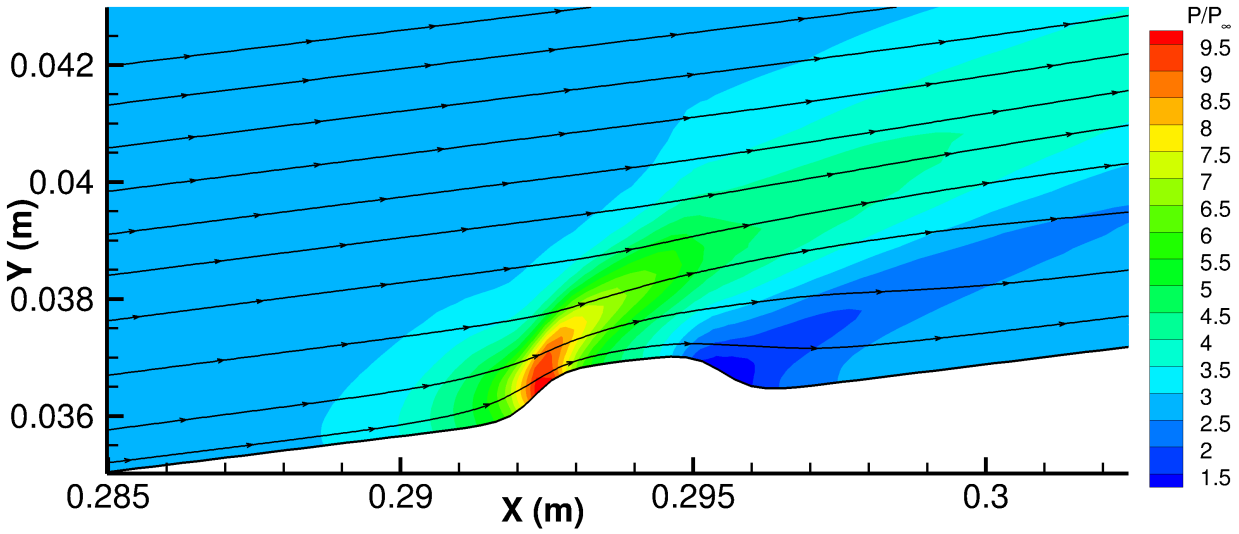

Figure 7.8: Streamtraces over the first strip in the roughness array on a pressure contour.

7.1.3 HWT-8 Experimental Results

Mach 8 experimental results show that the roughness strips successfully delayed transition. Fig. 7.9 shows a comparison of the pressure spectra with and without the roughness elements at two different freestream conditions. At a Re near $7.0 \times 10^6/m$, large second mode waves near 200 kHz develop without the presence of roughness. These waves are also clearly visible as rope-like waves in the boundary layer in schlieren images (Fig. 7.10a). When the roughness is added, much smaller second mode waves are measured. Also, because the boundary layer thickens with the presence of roughness, the frequency of the waves shifts to lower frequencies near 120 kHz. The corresponding schlieren image (Fig. 7.10b) indicates a thicker boundary layer and very faint rope waves are visible.

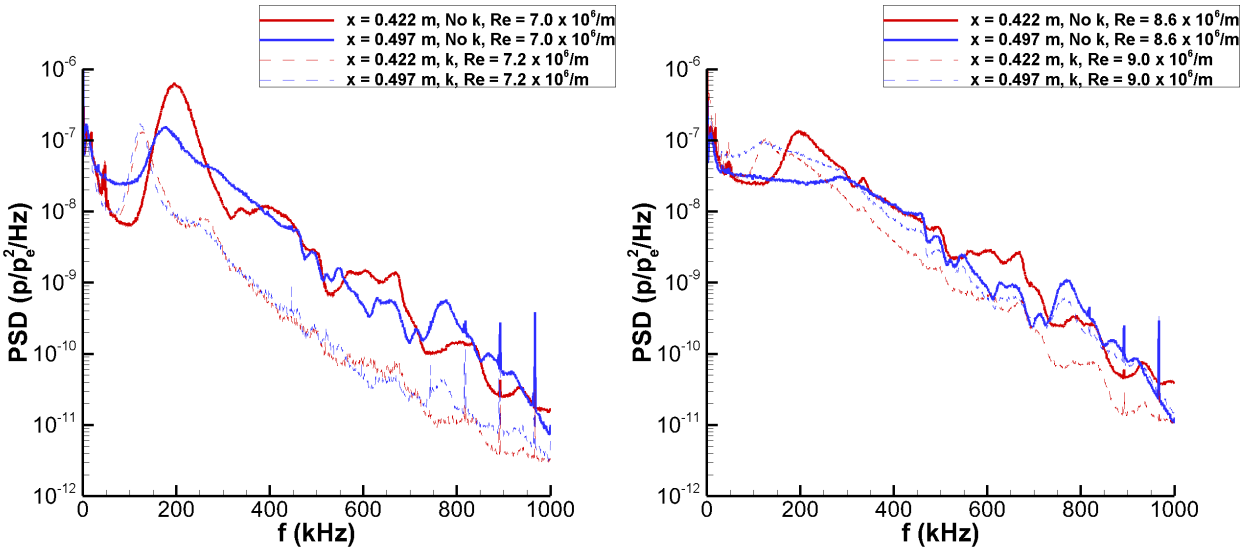

(a) Re near $7.0 \times 10^6/m$.

(b) Re near $9.0 \times 10^6/m$.

Figure 7.9: Case C.2 comparison of pressure spectra at x = 0.422 and 0.497 m.

At a higher freestream Re near $9.0 \times 10^6/m$, transition again seems to be delayed, though the results are less clear because the boundary layer is mostly turbulent at this condition. The pressure spectra without roughness show an intermittently turbulent boundary layer by x = 0.422 m. The remnants of second mode waves near 200 kHz are seen, but the broadband frequency content indicates a predominately turbulent boundary layer. Further downstream at x = 0.497 m, the spectra look mostly turbulent. This turbulence is also observed in the

schlieren images (Fig. 7.10c) without roughness.

With roughness on the cone at this higher Re, the pressure spectra look qualitatively similar. At x= 0.422 m, remnants of second mode waves can again be seen, but at a lower frequency near 120 kHz. Broadband frequency content is at a lower level than observed with the roughness, suggesting a transition delay. Further downstream at x = 0.497 m, the spectra are relatively broadband, but remnants of the waves still exist (while the spectra appeared fully turbulent without roughness). Therefore, qualitatively, the spectra again appear less turbulent. Schlieren images with the roughness (Fig. 7.10d) also appear less turbulent, and the snapshot that is shown indicates the presence of second mode waves as opposed to a fully turbulent boundary layer as in Fig. 7.10c.

(a) No roughness, $Re = 6.8 \times 10^6/m$.

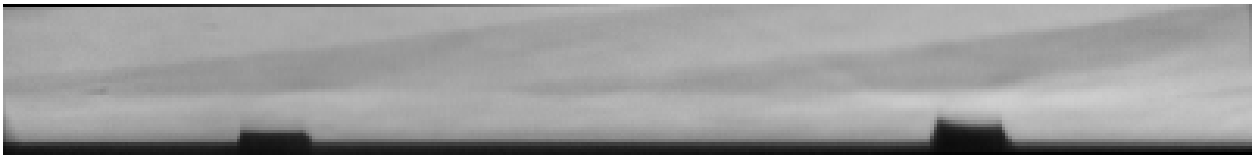

(b) Roughness, $Re = 7.0 \times 10^6/m$.

(c) No roughness, $Re = 8.6 \times 10^6/m$.

(d) Roughness, $Re = 9.0 \times 10^6/m$.

Figure 7.10: Case C.2 schlieren images of the cone boundary layer between x = 0.422 and 0.497 m.

7.2 Case C.3: Off-design Mach 5 Experiment

Case C.3 investigates the experimental results of the transition-delaying roughness under off-design conditions and investigates the effect of transition-delaying roughness on the first mode instability. During the Mach 8 experiment, the option became available to run the roughness array in a Mach 5 flow. A lingering question about transition-delaying roughness is, "how will it perform in off-design flow conditions?" The roughness design process is highly dependent on flow-specific features such as boundary layer height, synchronization location, and transition location. Furthermore, laminar-turbulent transition itself is highly dependent on flow conditions, making the question a prudent one. The answer could have significant implications on the practical application of transition-delaying surface roughness.

The Mach 5 flow also presents the opportunity to investigate how the first mode instability interacts with the roughness array. The first mode instability, more commonly identified as T-S waves, is often found in supersonic flows below Mach 5 before ceding to the second mode instability at higher Mach numbers. However, around Mach 5, both modal instabilities can be present if conditions allow. The experiment and subsequent numerical investigation are important because it is unknown if the first mode instability can be attenuated in the same manner as the second mode. The instability does not arise from the synchronization of two discrete modes like the second mode. Also, the first mode instability is most unstable as an oblique wave, unlike the second mode instability, which is most unstable as a planer wave. Thus, case C.3 provides the chance to investigate transition-delaying roughness on the first mode instability, albeit with a roughness array not designed with the first mode in mind.

7.2.1 Smooth Cone Steady-state Results

The steady-state pressure and temperature results for the cone frustum are contained in Fig. 7.11. The results are typical of a straight blunt cone. The pressure results on the top half of the cone show a moderate pressure ratio along most of the frustum far away from the nose tip. The temperature ratio in the bottom half of Fig. 7.11 is also typical of a straight blunt cone. The contours show a warm-wall thermal boundary-layer produced

by the constant wall temperature and a low-temperature ratio within the shock layer. The nearly uniform temperature extends over the majority of the cone.

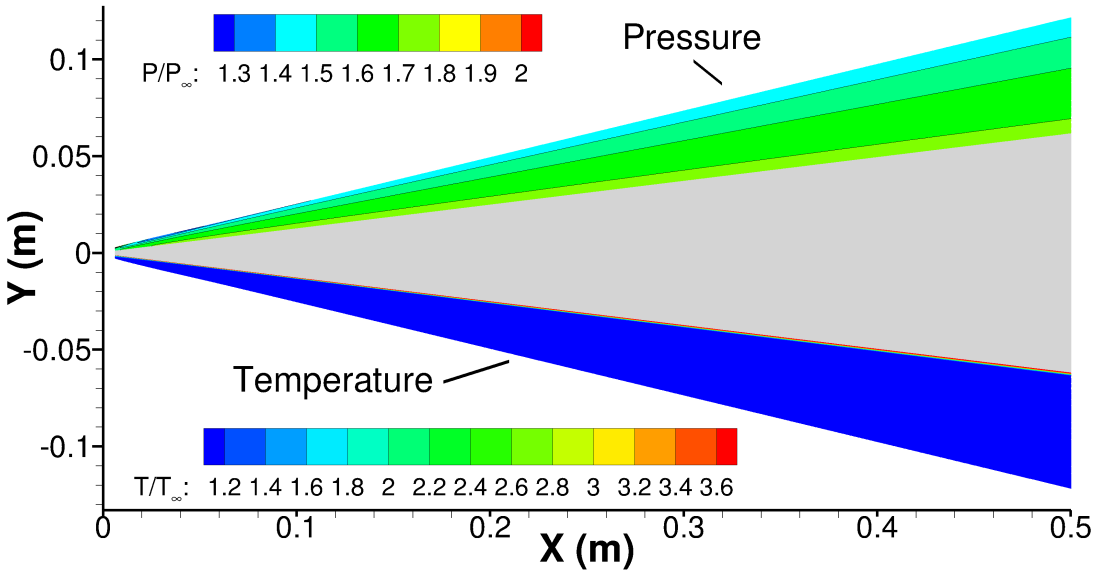

Figure 7.11: Pressure and temperature contours along the cone frustum. The figure is split with pressure plotted on the top half of the cone and temperature plotted on the bottom.

Looking just at the blunt nose tip in Fig. 7.12, the steady-state pressure and temperature results are presented together. The pressure contours show an increasing maximum pressure ratio toward the nose tip followed by a favorable pressure gradient downstream. Unlike the majority of the cone, a steep pressure gradient is located near the nose tip. Likewise, the temperature contours also show an increasing maximum temperature towards the nose tip. These higher gradients are because the bow shock is increasingly perpendicular to the flow and close to the stagnation point. The pressure and temperature gradients occupy the entire shock layer. The nose's area of influence extends approximately three radii downstream for pressure and six radii for temperature. Beyond these distances, the pressure and temperature take on the ratios seen on the frustum in Fig. 7.11.

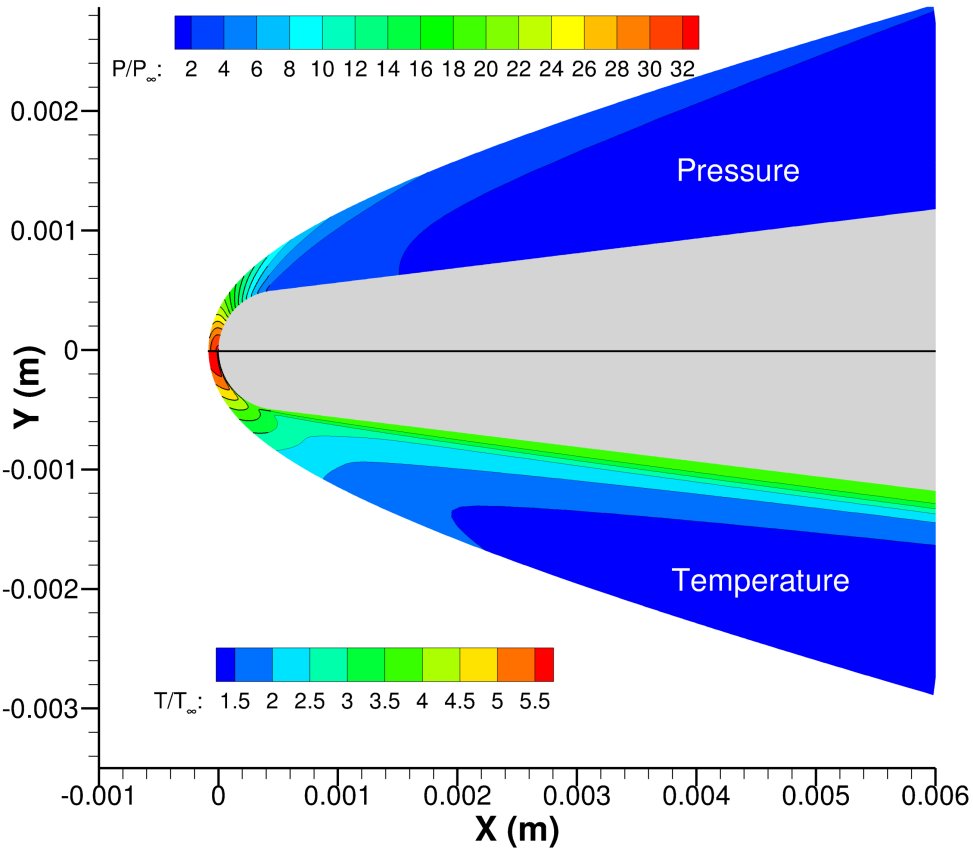

Figure 7.12: Pressure and temperature contours at the blunt nose tip. The figure is split with pressure plotted on the top half and temperature plotted on the bottom.

7.2.2 Linear Stability Analysis of Steady-state

The N-factor for mode S is computed from the smooth cone steady-state data. Using the e^N method, the unsteady growth rates of boundary-layer disturbances are integrated downstream at a fixed frequency. The amplitude growth comes from LST analysis using the steady simulation boundary layer profiles. The N-factor plot in Fig. 7.13 contains a frequency range from 275 to 625 kHz and reaches a maximum N-factor of three at the end of the cone. This result is considerably different from case C.1, which has a narrower range of frequencies over the same distance and also reaches a maximum N-factor of 6.4. Even though the maximum N-factor is quite low within a noisy wind tunnel like HWT-5, it may be sufficient to cause

transition. However, the second mode is not the dominant transition mechanism in HWT-5 [ACB10].

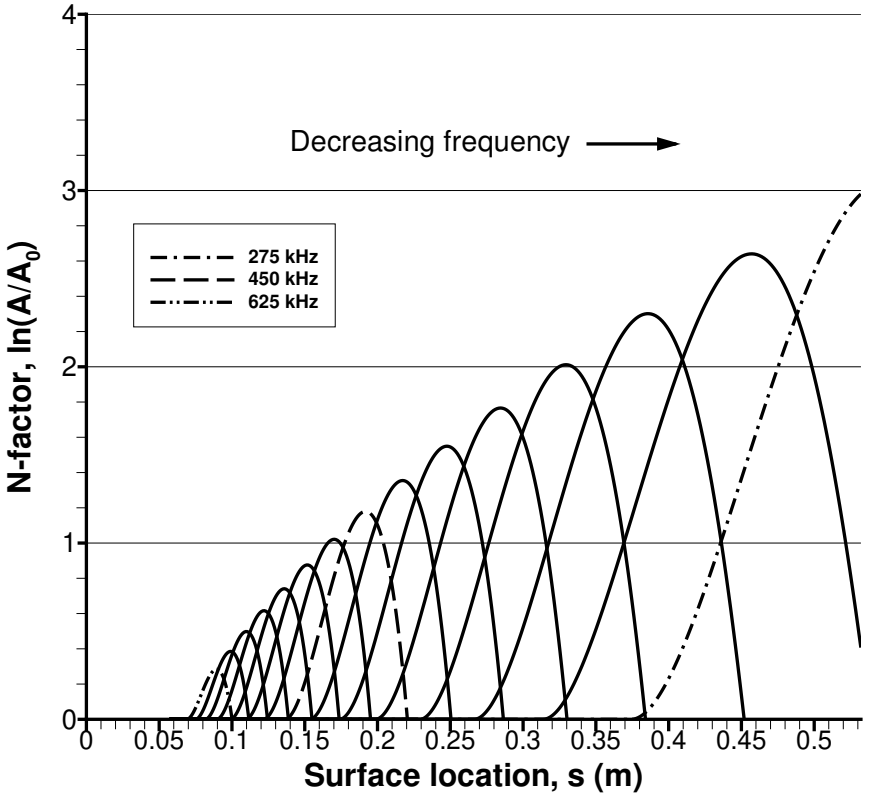

Figure 7.13: N-factor of second mode growth rate for $\beta_r = 0.0$. Fixed frequencies go from 275 to 625 kHz in increments of $\Delta f = 25kHz$.

It should be noted the N-factor plot does not provide insight into which frequencies will cause transition, only a value that can be used to reference empirical data on transition. The notion is that at a certain frequency of the instability will grow to such an extent that non-linearities will begin to dominate, and breakdown will occur. These eventual non-linearities are assumed to be negligible in the derivation of the LST equations and thus do not account for them.

In addition to the N-factor, another useful result from stability analysis is the neutral curve. Figure 7.14 contains the neutral curve for a planar wave when the second mode is most unstable. Overall, the instability region is relatively narrow, meaning the high-frequency growth rates do not remain unstable for long. But since the region is curved,

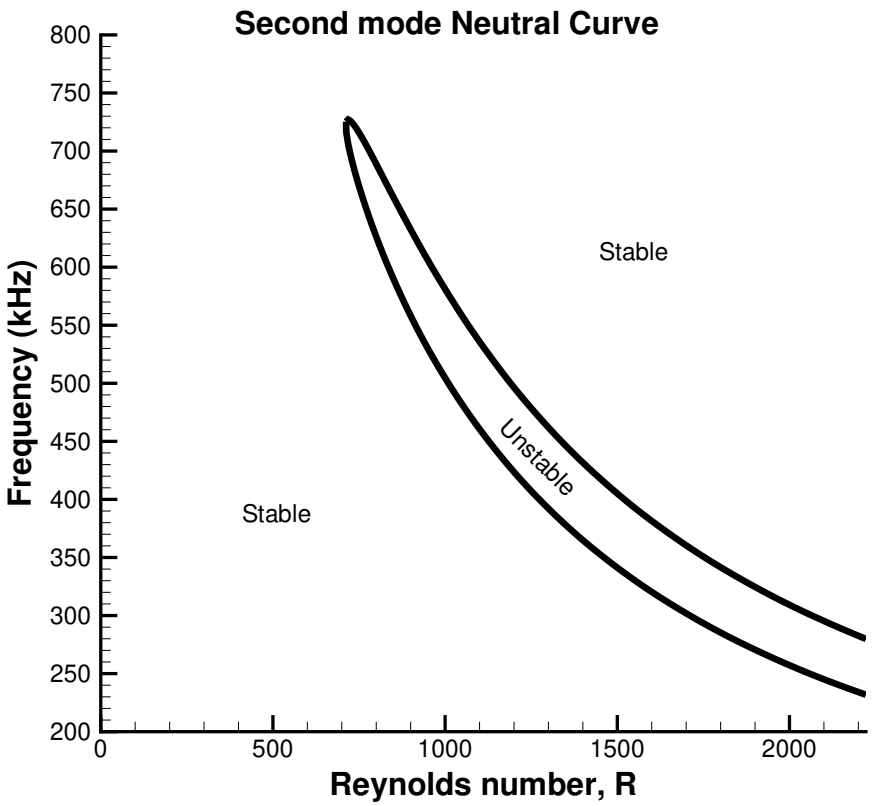

Figure 7.14: Neutral stability curve surrounding second-mode instability for $\beta_r = 0.0$.

lower unstable frequencies can grow more slowly over the longer distance. This long growth enables these unstable frequencies to reach high N-factor values.

In addition to the neutral curve, the growth rate map over the cone for frequencies up to 1 MHz is plotted in Fig. 7.15. This map is for a planar wave where $\beta_r = 0$. The neutral curve is visible within the map as the first solid contour at $-\alpha/L^* = 0$. The growth rate map provides information on the strength of the growth rate; for example, while the lower frequencies have the largest N-factors, it is the middle frequency range that have the highest growth rates by value. This variation in growth rates shows that a weak instability allowed to grow over some distance is more destabilizing to the boundary layer than a strong instability growing over a short distance. Furthermore, comparing the relative magnitudes of the growth rates, it is clear that stable growth rates are many times larger than unstable growth rates. This means the amplitudes of stable mode S frequencies are minuscule with

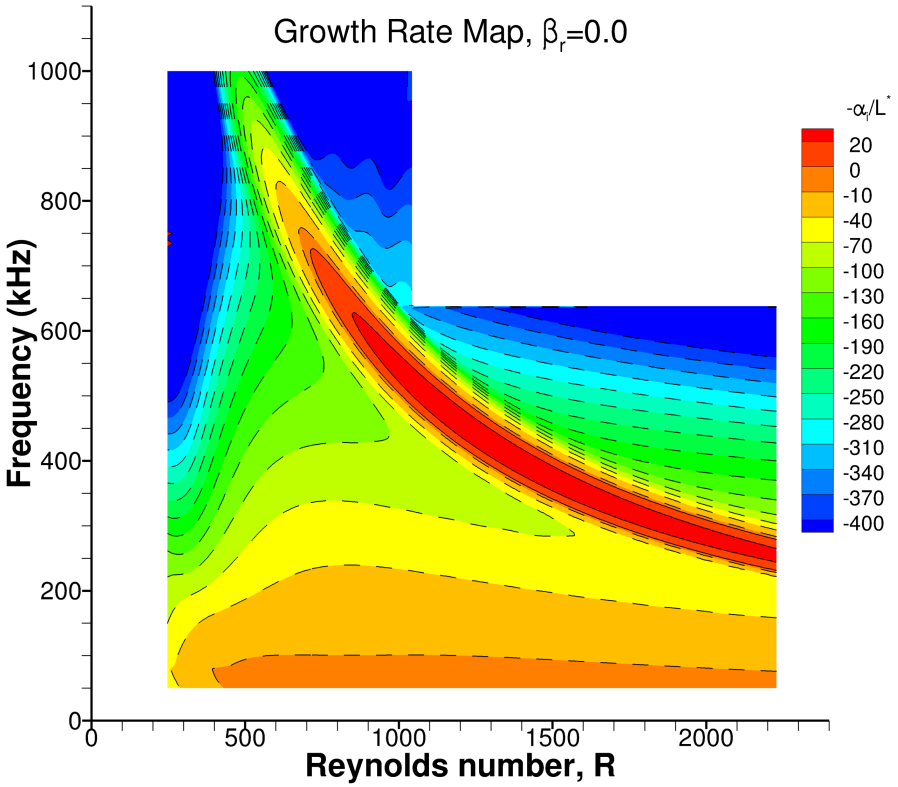

Figure 7.15: Growth rate map of mode S at $\beta_r = 0.0$. Solid contours (—) denote unstable growth rates, dashed contours (- - -) denote stable growth rates.

respect to a broadband disturbance within the boundary-layer.

Another noteworthy feature of Fig. 7.15 is the stable contour of the first mode taking shape at the bottom of the map. If β_r is increased and the growth rate map is recomputed, LST analysis essentially solves for an oblique wave imposed on the boundary-layer profile. The results for $\beta_r = 0.1$ and 0.2 are presented in Fig. 7.16. The plots differ in several minor but important ways from Fig. 7.15. For one, the higher frequencies of the unstable second mode have stabilized, and the growth rates for the remaining unstable frequencies have decreased in magnitude. This result is expected since the second mode is most unstable for $\beta_r = 0.1$. Secondly, the previously stable first mode is now unstable. The range of unstable frequencies is narrow, but the prolonged instability region means those unstable modes can grow to the point where they cause transition. A closer view of the unstable first-mode

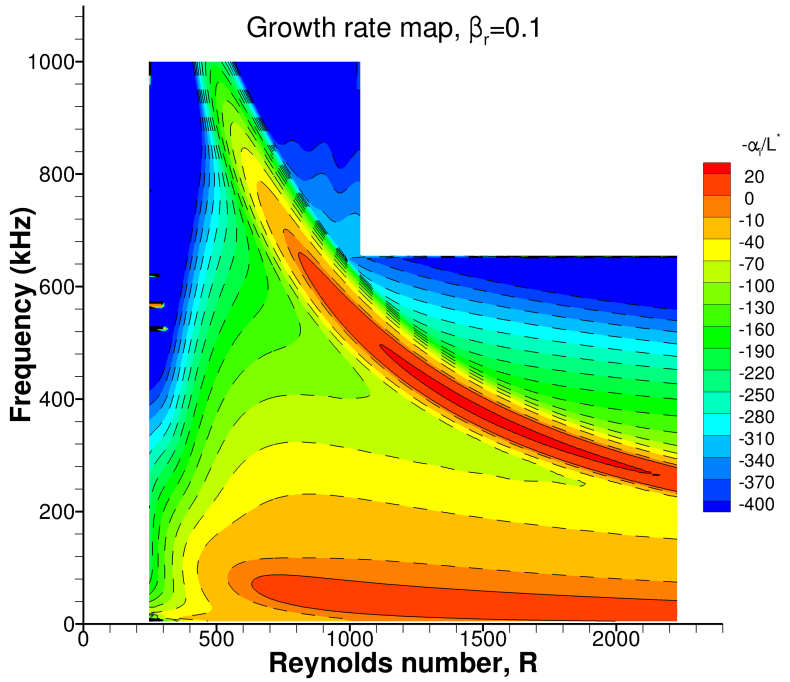

(a)

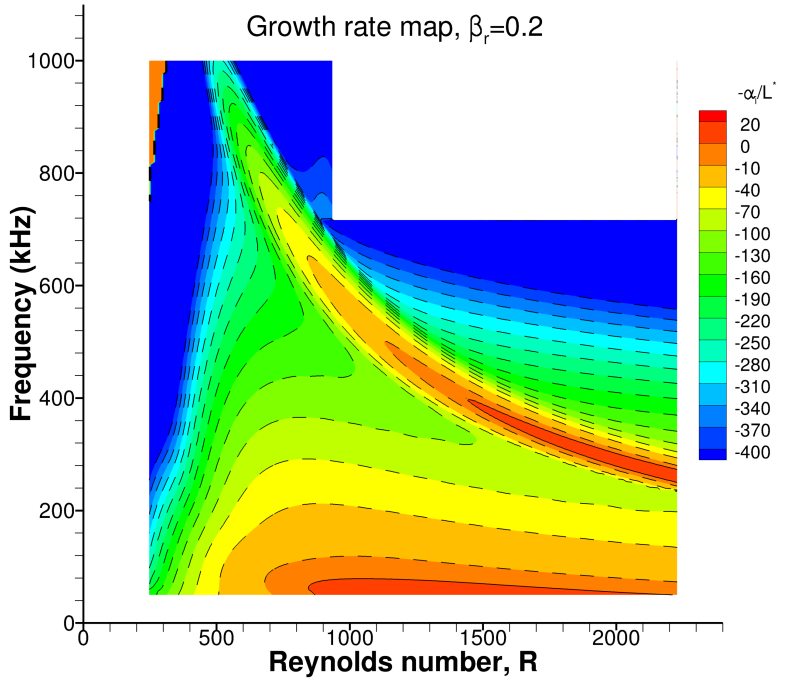

(b)

Figure 7.16: Growth rate map of mode S for $\beta_r = 0.1$ and 0.2. Solid contours (—) denote unstable growth rates, dashed contours (- - -) denote stable growth rates.

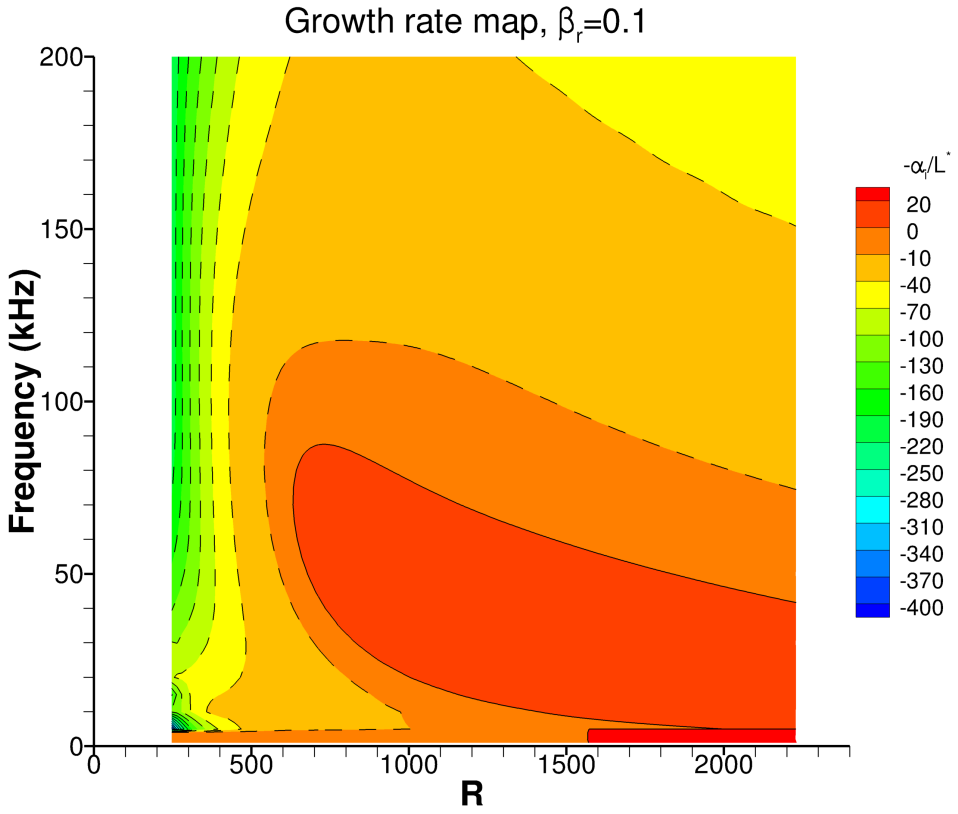

Figure 7.17: Growth rate of 1st-mode for $\beta_r = 0.1$. Solid contours (—) denote unstable growth rates, dashed contours (- - -) denote stable growth rates.

region for $\beta_r = 0.1$ is provided in Fig. 7.17.

Moreover, looking at the relative position of the unstable second mode region on top of the unstable first mode region in Fig. 7.16, it is clear that both modes will be unstable at nearly the same locations on the cone. Two simultaneous unstable modes and their possible interactions serve as the motivation to research first mode/second mode interaction.

Lastly, oblique wave LST analysis comes with a big caveat: it assumes that β_i is 0. In other words, any spanwise waves are neutral. The reason for this assumption is that there is no easy way of determining β_i. In early LST literature, it is noted that β_i is a free parameter but offered no means of determining it [Mac84]. Some schemes have been devised to link β_i with α_i, but strictly speaking, there is no physical reason to assume α_i and β_i are dependent.

7.2.3 HWT-5 Experimental Results

Unfortunately, experimental results at Mach 5 indicated that the roughness strips did not delay transition. This result is likely because, at Mach 5, both first and second mode waves show significant growth [CBH16]. Therefore, the delay mechanism used at Mach 8 to delay second mode transition may promote the growth of first mode waves at Mach 5. Moreover, the roughness array was not designed to attenuate the second mode in a Mach 5 flow.

Figure 7.18 compares the pressure spectra measured with and without the roughness elements. Without roughness, large second mode waves are observed near 250 kHz at x = 0.422 m. The boundary layer also appears intermittently turbulent, as indicated by the rise of broadband frequency content. Further downstream at x = 0.497 m, the boundary layer has transitioned to turbulence. With the roughness array, the boundary layer is already turbulent by x = 0.422 m. Further downstream, broadband turbulence is still observed, but with an additional peak near 100 kHz. These may be additional disturbances introduced by the presence of the roughness array.

Schlieren movies, both with and without the roughness, verify the pressure spectra results. Figure 7.19a shows the boundary layer without roughness. The boundary layer is mostly laminar with a second mode instability wave packet on the left of the image. By the right of the image, the boundary layer is turbulent. The whole movie shows that the boundary layer on the left side of the cone is intermittently turbulent, while it remains fully turbulent downstream. The presence of roughness (Fig. 7.19b) modifies the boundary layer and makes it thicker, however, the boundary layer continues to appear turbulent throughout the entire movie, again indicating no delay of transition with roughness strips at Mach 5.

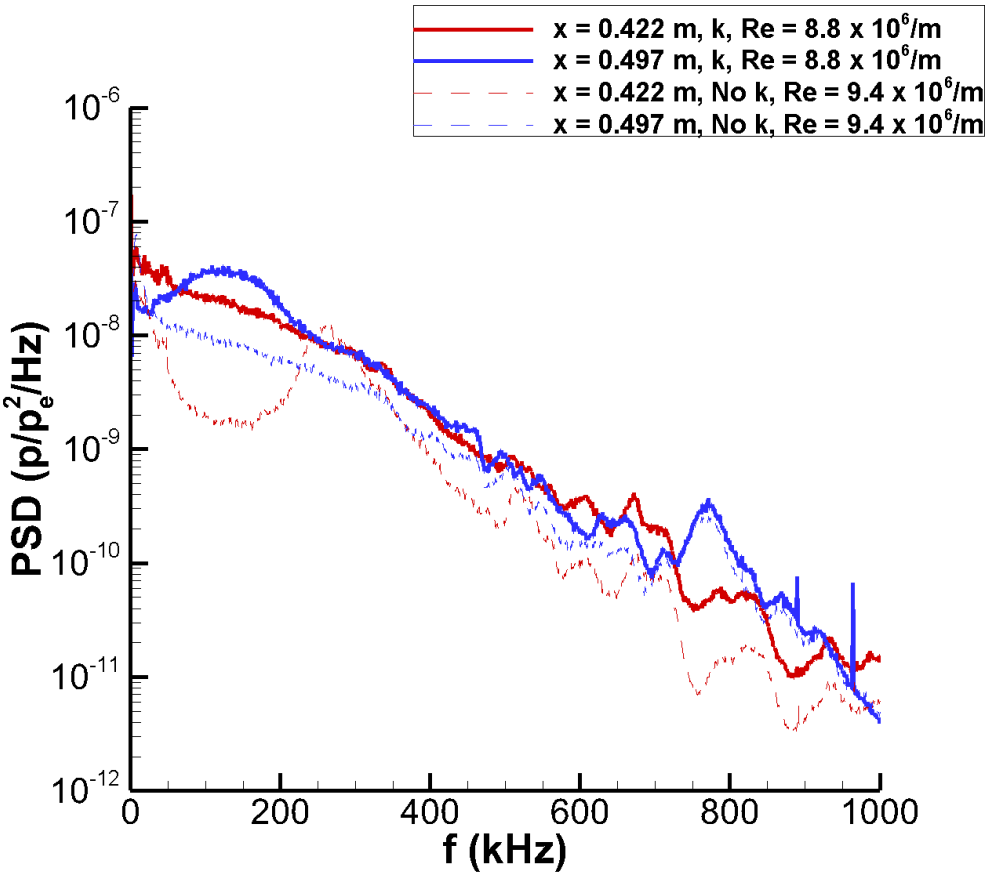

Figure 7.18: Mach 5: comparison of pressure spectra at x = 0.422 and 0.497 m. Re near $9.0 \times 10^6/m$.

(a) No roughness, $Re = 9.4 \times 10^6/m$.

(b) Roughness, $Re = 8.8 \times 10^6/m$.

Figure 7.19: Case C.3: Schlieren images of the cone boundary layer between x = 0.422 and 0.497 m.

CHAPTER 8

Supersonic Mode in Warm Wall Conditions

This chapter investigates acoustic-like emissions from the boundary layer of a low-enthalpy flow over a Mach 8 cone with a warm wall condition and an associated wave packet interference pattern between primary and satellite waves. While performing the computational study for Case C.1-Ext, the acoustic-like waves seen in Fig. 8.1 were observed emitting from the boundary layer in an unsteady simulation without roughness. These acoustic-like waves are qualitatively similar to those seen by Chuvakhov and Fedorov [CF16], and Knisely and Zhong [KZ19a, KZ19b, KZ19c, KZ20] in their DNS investigation of supersonic modes. Despite the similarities between the observed phenomena, the simulation conditions are very different; the supersonic mode reliably appears in flows with cooled walls, making its appearance in a warm wall flow unexpected.

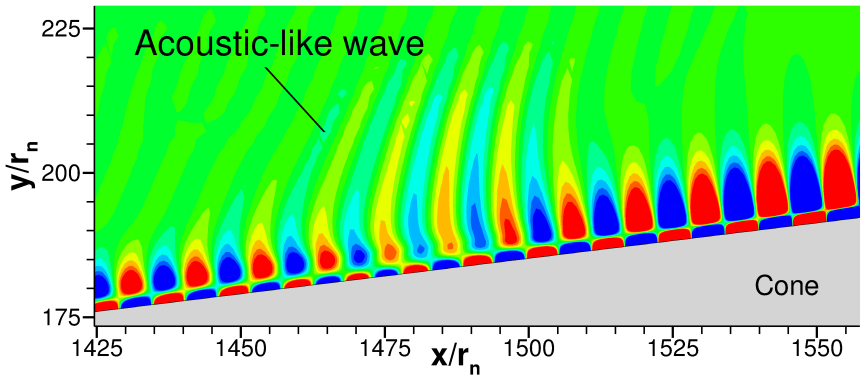

Figure 8.1: Weak acoustic-like waves emitting from the boundary layer. The waves are similar in appearance to those emitted by the supersonic mode.

The investigation is far removed from recent supersonic mode investigations, which makes this in-depth analysis of a low-enthalpy flow with warm wall condition unique in the litera-

ture. The case parameters in this investigation occupy a previously unexamined space that has been otherwise dismissed because the unstable mode did not have supersonic mode attributes, leaving stable supersonic modes investigated. This research seeks to understand an unexpected numerical result and to shed light on the supersonic mode in low freestream enthalpy flows with a warm wall condition.

The simulation approach in this chapter is to use the shock-fitting DNS code to obtain the steady state solution around a cone. The solution is used as the boundary layer profiles for LST analysis and as the base flow for unsteady DNS simulations. LST provides a theoretical analysis of the discrete boundary layer modes and provides the data required to compute modal phase speeds, growth rates, and eigenfunctions. The unsteady DNS simulation provides a time-accurate evolution of a boundary layer disturbance which can be analyzed with Fourier decomposition.

The cone geometry in this chapter is the same as case C.1-Ext: a slender straight blunt cone at zero angle-of-attack with a half-angle of 7°, a nose radius of 0.5 mm, and a total length of 1.0 m measured from the nose tip. The flow conditions are also the same as C.1-Ext which were taken from a previous experiment performed in Sandia National Laboratories' HWT-8 [CBH16] for the same cone geometry and are listed in Table 8.1.

Table 8.1: Freestream flow conditions for supersonic mode simulation

Parameter	Value	Parameter	Value
M_∞	8.0	T_w/T_∞	6.21
ρ_∞	0.024803 kg/m^3	T_w/T_{ad}	0.52
p_∞	330.743 Pa	T_w	279.0 K
$h_{0,\infty}$	1.174 MJ/kg	Re_∞/l	9,584,257 m^{-1}
U_∞	1093.07 m/s		

The freestream conditions are assumed fixed upstream of the bow shock and an isothermal wall is assumed along the cone surface from the nose tip to the end of the cone frustum. The isothermal boundary condition neglects surface heating by the flow. Of significance to

the current supersonic mode investigation is the wall-to-recovery temperature ratio, T_w/T_{ad}, in Table 8.1, which is indicative of a warm wall, especially when compared to the ratios of other supersonic mode investigations as seen in Fig. 1.7.

8.1 Steady-state Solution

The steady state pressure and temperature contours for the blunt nose and frustum of the cone are presented together in Fig. 8.2. Overall, the steady state solution is typical for a straight blunt cone. Looking at the blunt nose tip in Fig. 8.2a, the pressure contours show a maximum pressure ratio at the very tip of the cone followed by a favorable pressure gradient moving downstream. This favorable pressure gradient quickly gives way to the moderate pressure ratios seen on the frustum in Fig. 8.2b. The temperature contours also show a maximum temperature ratio at the nose tip, however, it is offset from the stagnation point due to the isothermal wall boundary condition.

Moving to the frustum of the cone in Fig. 8.2b, the pressure results on the top half of the figure show a moderate pressure ratio, and a mild favorable pressure gradient moving downstream along the extent of the cone. In the bottom half of Fig. 8.2b, the temperature ratio contours show a high thermal gradient between the boundary layer and the flow behind the shock, which extends over the entire frustum. This high thermal gradient is expected due to the isothermal wall condition, which is considerably higher than the temperature behind the shock and subsequently the freestream temperature.

8.2 Linear Stability Analysis of Steady-state.

In this chapter LST is used to obtain the dispersion relations for the discrete boundary layer modes F and S at select frequencies. The phase speed and growth rate of the discrete modes are computed from these LST results. The nondimensional phase speed is defined as

$$c_r = \frac{\omega}{\alpha_r}, \tag{8.1}$$

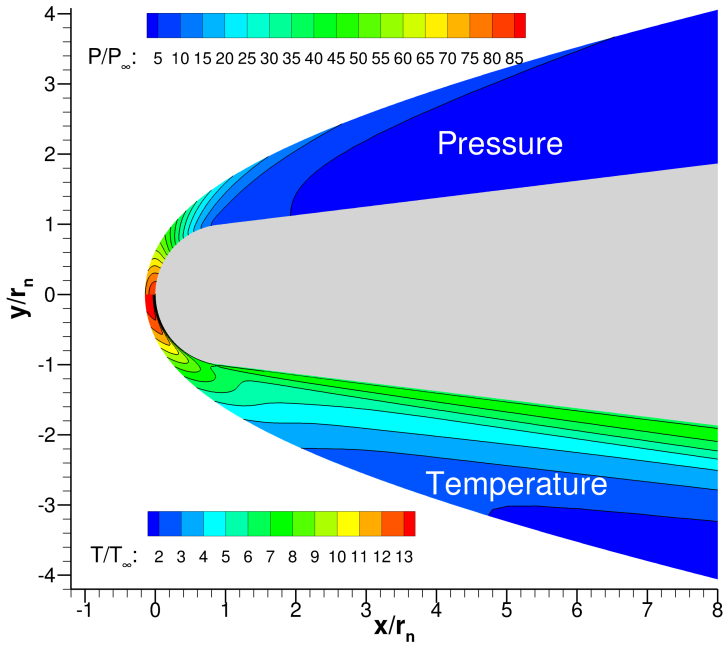

(a)

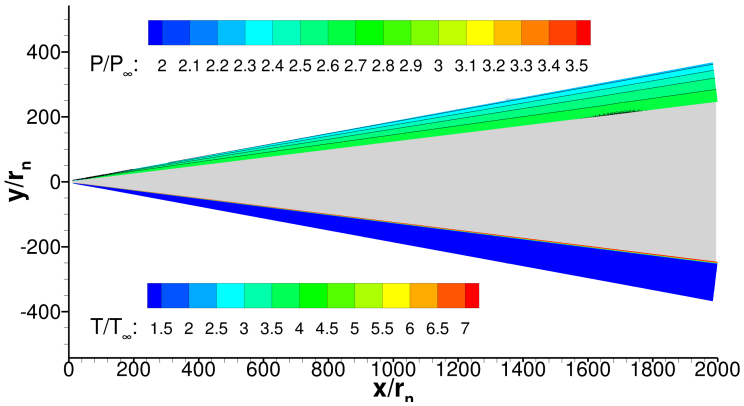

(b)

Figure 8.2: Pressure and temperature contours at the (a) blunt nose tip, and on the (b) cone frustum. The subfigures are split with pressure ratio plotted on the top half and temperature ratio plotted on the bottom half.

where α_r is the real part of the nondimensional wave number. The nondimensional phase speed is used to identify the discrete modes based on where they originate amongst the continuous spectra, and in order to interpret their behavior. Likewise, the dimensional growth rate, $-\alpha_i/L^*$, is the negative of the imaginary part of the complex wavenumber over

the boundary layer length scale, L^*, where $L^* = \sqrt{s\mu_{\infty/\rho_\infty U_\infty}}$. The growth rate is used to identify when modes are stable and unstable: positive growth rates for unstable modes and negative growth rates for stable modes.

To study the boundary layer's stability characteristics, LST is used with the steady state solution to obtain the discrete boundary layer modes F and S. For this particular spatial stability analysis, 160kHz and 260kHz are chosen as representative frequencies. As will be seen in Section 8.3, 160kHz is close to where the constructive/destructive interference behavior occurs, and 260kHz is in the vicinity of blowing-suction actuators.

Before proceeding, a discussion on discrete mode terminology is in order. In general, this investigation follows the modal naming conventions put forth by Fedorov and Tumin [FT11]. Mode F describes the discrete modes that originate from the fast acoustic spectrum where $c_r = 1 + 1/M_\infty$, and mode S describes the discrete mode that originates from the slow acoustic spectrum where $c_r = 1 - 1/M_\infty$. If more than one discrete mode appears from either acoustic spectrum, the modes are numbered in order of appearance by increasing ω. Occasionally, a discrete mode may undergo a branch cut or bifurcation when crossing one of the continuous spectra, such as the entropy/vorticity spectrum ($c_r = 1$). In such a case, as ω is increased, the mode approaching the branch cut is given a "+", and the mode departing the branch cut is given a "-". In this investigation mode F undergoes a branch cut when crossing the entropy/vorticity spectrum. In Refs. [KZ19b], [BS15], and [Tum20], however, mode F both crosses a branch cut and bifurcates when crossing the entropy/vorticity spectrum and slow acoustic spectrum, respectively, and "+/-" usage is redefined. These references and the current investigation use very similar but incongruous discrete mode terminology, so it is important to note that identically named modes may not describe the same physical mode.

The phase speeds and growth rates of modes F and S for each frequency are contained in Fig. 8.3. Figures 8.3a and 8.3c show how mode F1+ originates in the fast acoustic spectrum and steadily slows down until it reaches the vorticity/entropy branch cut where F1- emerges on the other side. As mode F1-'s phase speed continues to decrease, it couples with mode S, as seen by the mirrored modal growth rate curves in Figs. 8.3b and 8.3d. After coupling, mode F1- slows to the slow acoustic wave speed and passes it without coalescing

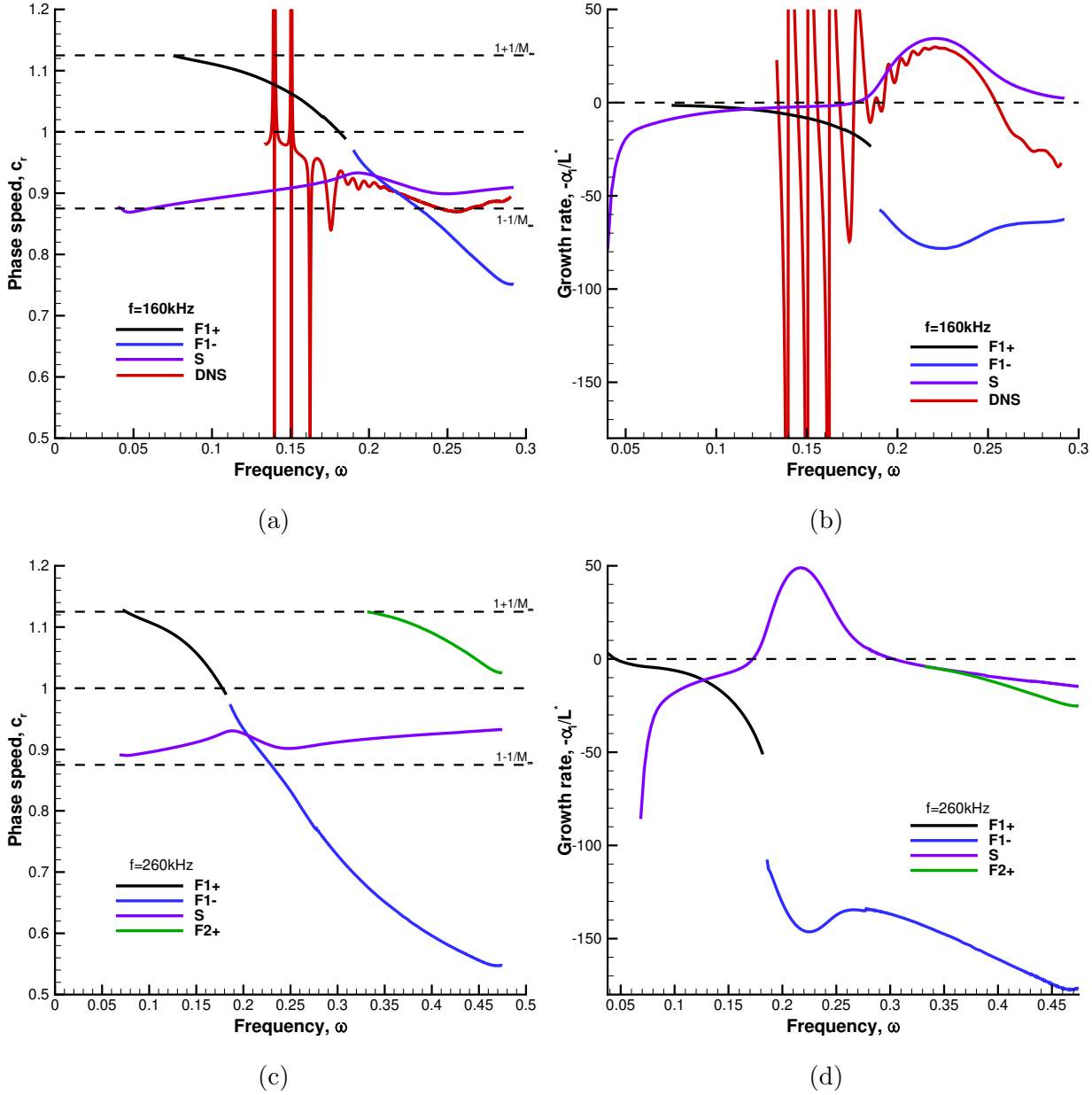

Figure 8.3: Nondimensional phase speed and growth rate results obtained from LST for discrete modes F and S at 160kHz and 260kHz. 160kHz frequency includes phase speed and growth rate results obtained from unsteady DNS

or bifurcating with the slow acoustic branch cut.

Conversely, mode S originates from the slow acoustic spectrum and takes on a phase speed between $c_r = 1$ and $c_r = 1 - 1/M_\infty$. The coupling of mode F1- and mode S, causes mode S to become unstable. This is the well-known second mode instability and is the only unstable mode found in the LST analysis. Furthermore, mode F1- is stable as a consequence of coupling.

Of primary interest to the investigation is when any discrete modes become supersonic. This is because the acoustic-like waves seen in Fig. 8.1 are indicative of a supersonic mode. In addition to the supersonic region within the boundary layer, where the relative Mach number is less than negative one, $\overline{M} < -1$, there is a second region of relative supersonic flow above it where $\overline{M} > 1$. In order for $\overline{M}$ to be greater than one, the nondimensional phase speed must be less than $1 - 1/M_\infty$. Thus a discrete mode will be supersonic when $c_r < 1 - 1/M_\infty$.

Of the modes in Fig. 8.3 only mode F1- is slower than the slow acoustic and becomes supersonic at $\omega = 0.23$. When the phase speed of a discrete mode is supersonic, it is possible for acoustic-like waves to emit into the inviscid region outside of the boundary layer. However, mode F1- is very stable, and any acoustic-like waves are likely to be weak and not sustained without forcing.

By contrast, the supersonic mode in Knisley and Zhong [KZ19b, KZ19c] and Chuvakhov and Fedorov [CF16] was an attribute of an unstable F1 mode. Because the mode was unstable, they saw very a strong supersonic response with acoustic-like waves propagating farther outside the boundary layer (see Fig. 9 of Ref. [KZ19c] and Fig. 14 and 15 of Ref. [CF16]). Moreover, the unstable supersonic mode F1 had to cross the slow acoustic continuous spectrum branch cut, resulting in a bifurcation of the mode (see Fig. 16 of Ref. [KZ19b] and Fig. 4a of Ref. [CF16]). There is no similar bifurcation of mode F1- in the present study since its stability keeps it away from the slow acoustic continuous spectrum branch cut as seen in Fig. 8.4. Thus any acoustic-like waves produced by the supersonic mode F1- are likely to be damped.

In addition to the LST results, Figs. 8.3a and 8.3b contain phase speed and growth rate results obtained from DNS. The complex wavenumber components needed to compute the phase speed and growth rate are obtained from the amplitude and phase angle of the Fourier decomposed pressure fluctuations at the wall. The wavenumber's real and imaginary parts are computed using the following equations,

$$\alpha_r = \frac{d}{ds}\psi(f), \tag{8.2}$$

$$\alpha_i = -\frac{1}{\Delta\phi(f)}\frac{d}{ds}\Delta\phi(f), \tag{8.3}$$

where $\Delta\phi(f)$ is the pressure amplitude-frequency at the wall, and $\psi(f)$ is the phase angle at frequency f. The resulting phase speed and growth rate results consist of the combined discrete and continuous modes. Bi-orthogonal decomposition can be used to extract the discrete modes from the combined signal [Tum03], but the decomposition is out of scope of the current research. In the meantime, it is possible to gain some insight and comparison between LST and DNS without decomposing the signal further, assuming that the more dominant mode has a more significant influence on the combined signal.

The large oscillations seen in the DNS results in both Figs. 8.3a and 8.3b around $\omega = 0.15$ are attributed to the proximity of the disturbance to the actuator and are attributed to forcing. In general, the DNS phase speed in Fig. 8.3a follows the LST result for mode S, however, it appears translated downward slightly, which could be attributed to influences by mode F1-. It is also important to note that the phase speed dips below $c_r < 1 - 1/M_\infty$ around $\omega = 0.255$, indicating the phase speed becomes supersonic. This supports the idea that the acoustic-like waves seen Fig. 8.1 and in the unsteady results in section 8.3 result from a supersonic mode. The DNS growth rate in Fig. 8.3b also follows, albeit slightly below, the LST result for mode S, before trending towards the stable growth rate for mode F1-. The DNS phase speed and growth rate trends agree reasonably well with the LST results. The DNS results also support the presence of a supersonic mode.

To better understand how discrete modes can interact with the continuous spectra, the discrete modes featured in Fig. 8.3 are plotted with the continuous spectra branch cuts in the complex phase speed plane in Fig. 8.4. The mode's complex phase speed is computed by

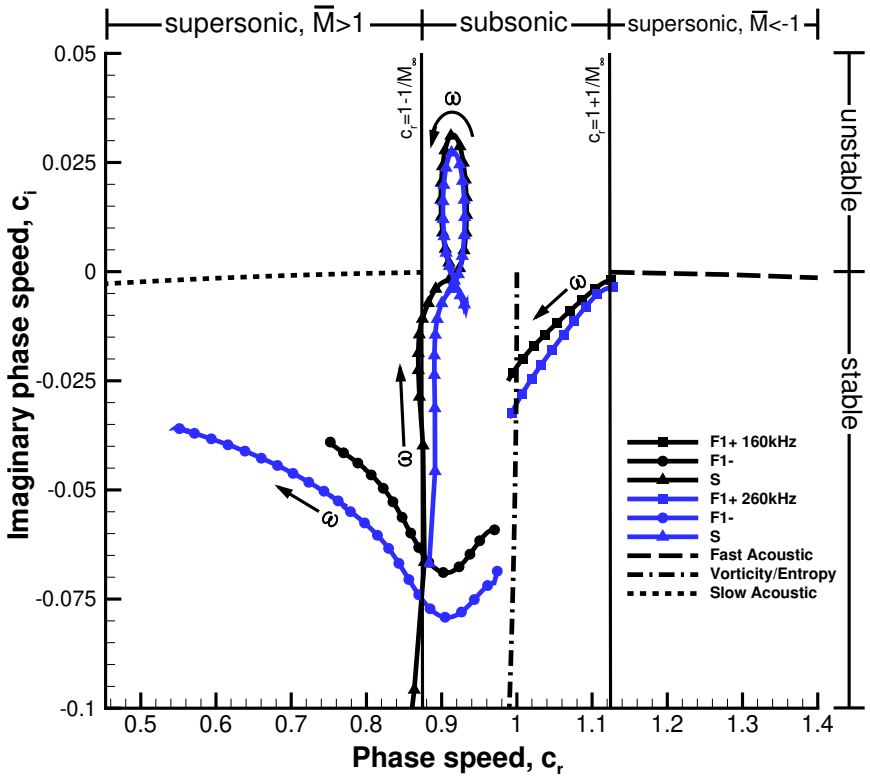

Figure 8.4: Discrete modes F and S in the complex phase speed plane for f=160 and 260kHz.

dividing the mode's frequency by its complex wave number. The real part of the complex phase speed is plotted along the x-axis and the imaginary part along the y-axis. Demarcations along the top of Fig. 8.4 denote where discrete modes become supersonic and subsonic based on their nondimensional phase speed. Likewise, divisions along the right side denote where the discrete modes become stable and unstable. In addition to the discrete modes, the figure also includes the branch cuts for the fast acoustic, vorticity/entropy, and slow acoustic continuous spectra. The branch cut locations are calculated using the methods developed by Balakumar and Malik[BM92].

Concerning the discrete modes, Fig. 8.4 shows F1+ originating near the fast acoustic spectrum branch cut on the right side of the figure and then moving left to the vorticity/entropy spectrum branch cut with increasing ω where it stops. From the other side of the vorticity/entropy spectrum branch cut, mode F1- emerges and moves to the left with increasing ω, at one point crossing from a subsonic to supersonic phase speed. Note that both F1+ and F1- are in the stable region of Fig. 8.4. Mode S originates from the bottom of the figure near the slow acoustic phase speed line and moves upwards towards the unstable region with increasing ω before looping back to the stable region. Unlike mode F, mode S is confined to the subsonic phase speed region.

Similar complex phase speed figures have been plotted by Refs. [CF16], [KZ19a], [BS15], and [Tum20] in their supersonic mode investigations (see Figs. 4, 16, 10, and 4 of Refs. respectively). In those investigations, the emergence of a separate discrete supersonic mode was synonymous with a discrete mode coalescing with the slow acoustic spectrum branch cut from above and a separate discrete supersonic mode emerging from below. Thus, the coalescing discrete mode had to have a phase velocity less than $1 - 1/M_\infty$, and an imaginary phase velocity greater than the slow acoustic branch cut, meaning it was both supersonic and unstable. For visual reference, this puts the mode in the upper-left region of Fig. 8.4. None of the discrete modes in this investigation appear in the phase speed plane's upper-left region. LST predicts that the supersonic mode behavior seen in this investigation does not appear to result from coalescing or emerging discrete modes. Instead, it results from a stable mode F1-'s decreasing phase speed. By contrast, the coalescing discrete mode in the literature cited

above was an unstable mode F1- (according to this investigations mode naming convention). The cited literature also had a very strong acoustic-like wave response, likely due to the mode's instability. However, this is not the case here, where the mode's stability makes the acoustic-like wave response comparatively weak, as seen in the propagating disturbance in Fig. 8.8. To summarize, the supersonic mode F1- observed in this investigation lacks the instability and coalescence with the slow acoustic spectrum branch cut seen in the References mentioned above. These differences provide a new view of how supersonic discrete modes behave in low-enthalpy flows with warm wall conditions.

Moreover, the unstable mode S does not appear to play a role in the observed supersonic behavior unlike the unstable mode in the investigations mentioned above. The loop seen in Fig. 8.4 is because mode S is multi-valued in c_r due to coupling with F1- (which is monotonic in c_r). Moreover, since mode S generally increases in c_r with increasing ω, it is not likely to cross the slow acoustic wave speed and is therefore not susceptible to supersonic behavior.

Further insight into modes F and S's behavior can be gained by examining the real part of their pressure eigenfunction. In Ref. [KZ19b], the supersonic mode's eigenfunction has a strong oscillatory feature that extends outside of the boundary layer. To investigate similar features, this study looks at both mode F1- and S before and after mode F1-'s phase speed crosses the slow acoustic wave speed. Figure 8.5 contains the eigenfunctions at $\omega = 0.23$, right before mode F1- becomes supersonic, for both modes F1- and S at 160 and 260kHz. In general, the eigenfunctions' shapes are very similar for both frequencies when accounting for the growth in the boundary layer and grid stretching in the wall normal direction introduced by normalizing the vertical coordinate, y_n, by the shock height, H_s. The boundary layer edge δ_{99}/H_s is denoted by red x's in each plot; for both mode F1- and mode S, the eigenfunction extends above the boundary layer and does not deviate away from $\hat{p}_r = 0$ once reaching that value in the inviscid layer. Since $\omega = 0.23$ is just before mode F1- becomes supersonic, oscillations into the area behind the shock are not expected for either discrete mode.

Continuing downstream to $\omega = 0.26$ where mode F1-'s phase speed is now supersonic, Fig. 8.6 contains the plots of the real part of the pressure eigenfunction for both discrete modes at the same frequencies as before. While mode F1-'s phase speed is supersonic, mode

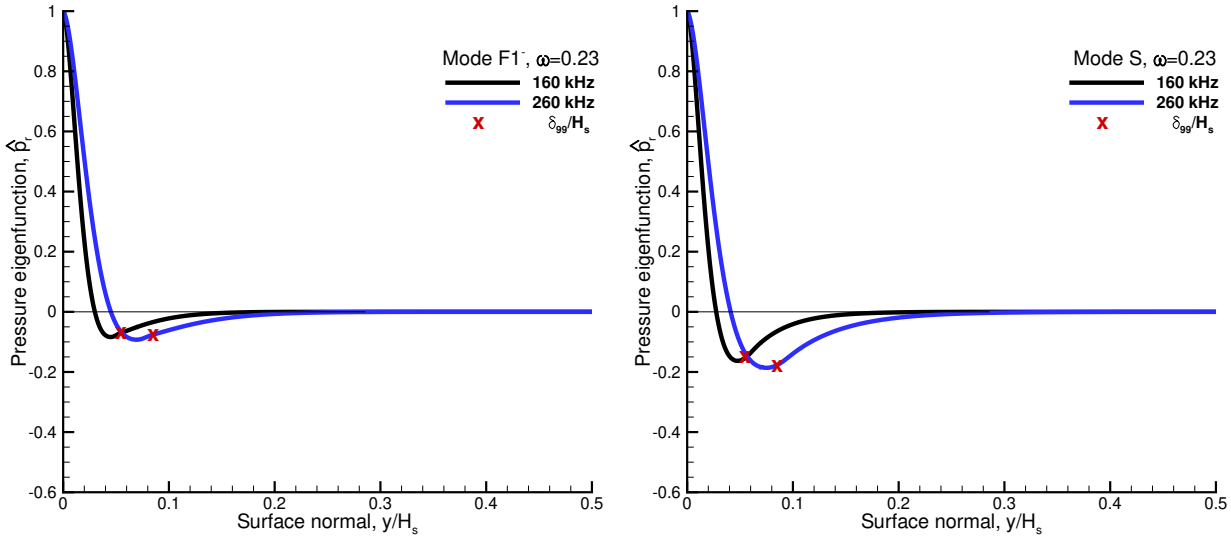

(a) (b)

Figure 8.5: Comparison of (a) mode F1- and (b) mode S pressure eigenfunctions at $\omega = 0.23$, after synchronization and in the vicinity of the slow acoustic phase speed.

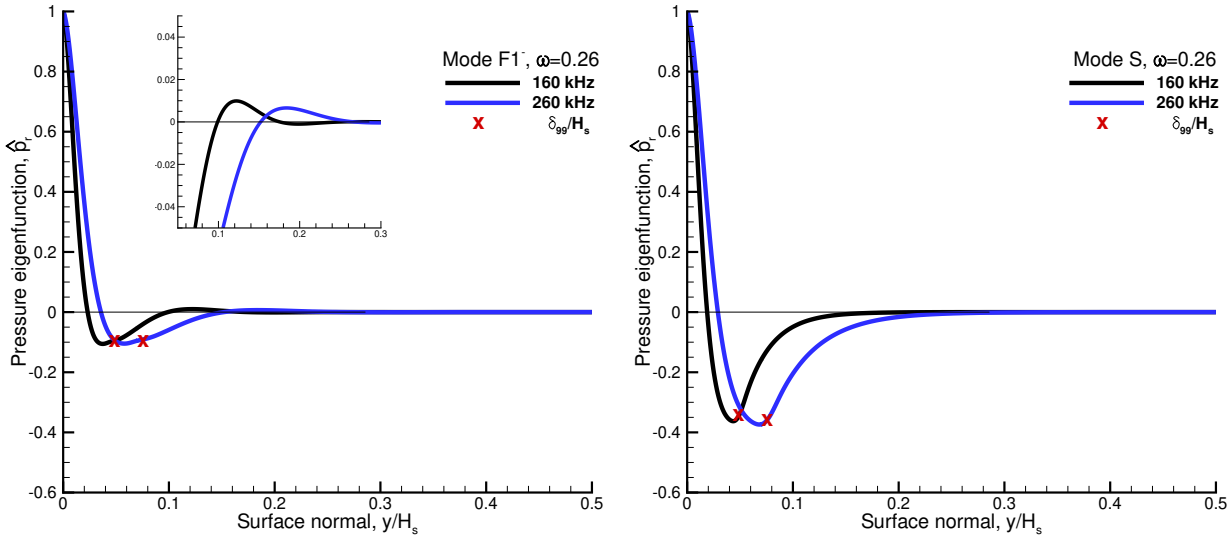

(a) (b)

Figure 8.6: Comparison of (a) mode F1- and (b) mode S pressure eigenfunctions at $\omega = 0.26$, downstream where mode F1-'s phase speed is less than that of a slow acoustic wave.

S's phase speed is not, thus any oscillations beyond the boundary layer are expected to appear for mode F1- and not mode S. The eigenfunctions are again similar across frequency when controlling for vertical stretching. As before, the profiles extend above the boundary layer edge, however, their shape is slightly different from that seen at $\omega = 0.23$. The mode S profiles are similar, as they do not move away from $\hat{p}_r = 0$ in the inviscid layer. However, the profiles for mode F1- oscillate once about $\hat{p}_r = 0$ above the boundary layer edge before returning to zero, as seen in the inset plot of Fig. 8.6a. This oscillation, although weak, is significant because it provides a mechanism for acoustic-like waves to appear in the flow behind the shock. Similarly, unstable supersonic modes produce more persistent oscillations beyond the boundary layer edge (see Fig. 15 of Ref. [KZ19b]), resulting in the acoustic-like waves seen in the inviscid layer. Furthermore, mode S does not exhibit any oscillations on account of its subsonic phase speed. Thus it is reasonable to conclude that since mode F1-'s eigenfunction has no oscillations when subsonic and a weak oscillation when supersonic, that mode F1- is responsible for the acoustic-like waves seen in the DNS results.

An effective way to visualize the supersonic mode using the LST framework is to expand the pressure eigenfunction to produce a contour plot of the pressure fluctuations. An approximate 2-D representation of the discrete modes can be obtained using the real part of the normal mode equation used to derive the LST equations,

$$p'(y) = Re\{\hat{p}(y)e^{(i(\alpha s - \omega t))}\}, \tag{8.4}$$

which simplifies to,

$$p'(y) = (\hat{p}_r(y)cos(\alpha_r s - \omega t) - \hat{p}_i(y)sin(\alpha_r s - \omega t))\, e^{-\alpha_i s}. \tag{8.5}$$

By substituting the pressure eigenfunction, $\hat{p}$, into Eq. (8.5), along with its wavenumber, α, and frequency, ω, the pressure perturbation, p', can be obtained at its streamwise location, s. A contour plot of the perturbation is then generated by varying s slightly upstream and downstream, as seen in Fig. 8.7. The contour levels are normalized by the growth rate term $e^{-\alpha_i s}$ and clipped to better visualize the mode better.

The resulting contour plots in Fig. 8.7 are the normalized pressure fluctuations for modes F1- and S at 160kHz and $\omega = 0.26$. The local relative Mach number, computed with respect

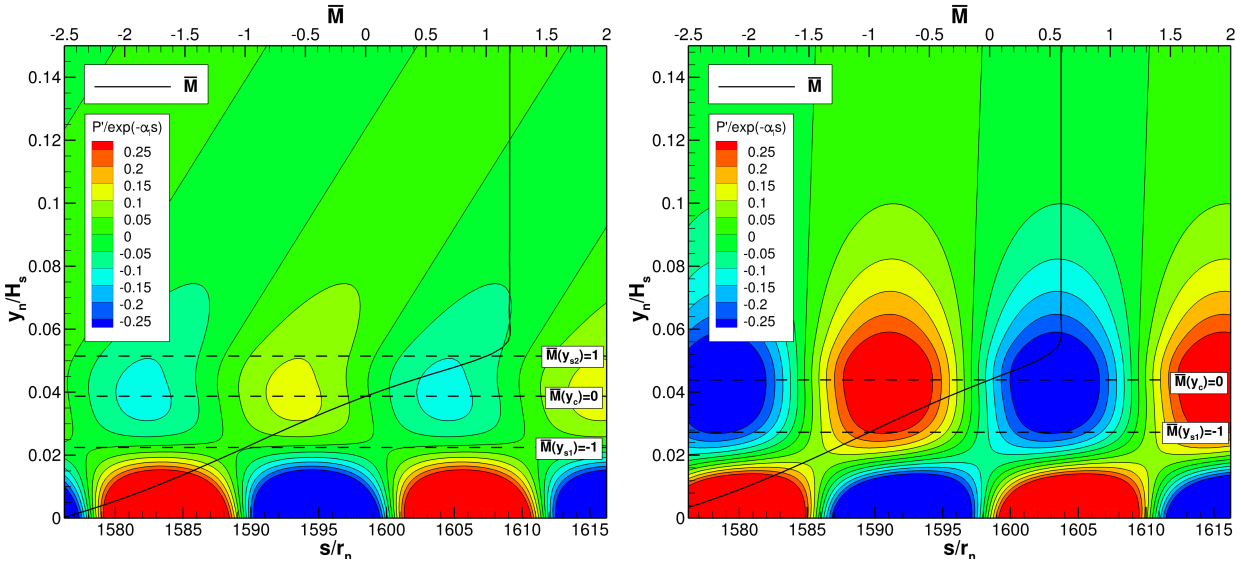

(a) (b)

Figure 8.7: Normalized pressure fluctuation contours for (a) mode F1- and (b) mode S overlaid with local relative Mach number. Contours are constructed from pressure eigenfunction results obtained from LST at 160kHz and $\omega = 0.26$. The locations of the first (y_{s2}) and second (y_{s1}) sonic lines and critical layer (y_c) are demarcated by relative Mach number.

to its discrete mode's phase speed, is plotted on top of the pressure fluctuations as a function of boundary layer height. Dashed lines in each figure demark relative Mach numbers of interest, such as the first sonic line ($\overline{M}(y_{s1}) = -1$), the critical layer ($\overline{M}(y_c) = 0$), and the second sonic line ($\overline{M}(y_{s2}) = 1$). The dashed lines also effectively denote regions in the boundary layer where the relative Mach number is subsonic ($-1 < \overline{M}(y) < 1$) and supersonic ($\overline{M}(y) > 1$ and $\overline{M}(y) < -1$).

The pressure fluctuation for mode F1- in Fig. 8.7a produces a unique asymmetric repeating pattern. The small oscillation seen in the real part of the eigenfunction in Fig. 8.6a, when paired with its imaginary component, actually reveals decaying Mach waves. These Mach waves have a similar appearance to the acoustic-like waves emanating from the boundary layer seen in Fig. 8.1, albeit smaller in size. Most importantly, these Mach waves also appear above the second sonic line where the relative Mach number is supersonic. When the

relative Mach number is greater than 1, the flow is supersonic with respect to the mode's phase speed, signifying that the mode is propagating upstream supersonically in the flow's inertial frame; this is why the Mach waves are angled downstream. Moreover, the Mach waves and second sonic line are consistent with the supersonic mode diagram prepared by Knisely and Zhong for a neutral supersonic mode in the large wave number limit (see Fig. 2 in Ref. [KZ19b]). Thus the appearance of Mach waves above the second sonic line provides further justification that mode F1- is the supersonic mode responsible for the acoustic-like waves.

Unlike mode F1-, the contour of mode S in Fig. 8.7b produces a symmetric repeating pattern of perturbations without decaying Mach waves and has no second sonic line. The absence of these two features is expected because, as shown in Fig. 8.3a, mode S is subsonic at $\omega = 0.26$. The relative Mach number profile in Fig. 8.7b confirms this because at no point in the boundary layer is the relative Mach number greater than 1. This is because mode S has a faster wave speed relative to the meanflow than mode F1-. As such, mode S cannot produce Mach waves. Therefore, any supersonic mode behavior observed in the DNS results is due to mode F1- and not mode S.

To summarize, the LST analysis for mode F1- shows that it takes on a supersonic phase speed downstream, has an upper sonic line in the boundary layer when supersonic, and that its eigenfunction produces acoustic-like waves. Therefore, if there exists a supersonic mode in the unsteady simulation, it is likely the result of mode F1-. Similarly, mode S is expected to be subsonic and unstable and not responsible for the observed supersonic behavior.

8.3 DNS Results on a Smooth Cone

Two unsteady cases are considered in this investigation that differ only in the blowing-suction actuator's location. In Case I, the actuator is located at the surface location, $s_c/r_n = 400$, measured from the nose tip, and in Case II at $s_c/r_n = 200$. Initially, the appearance of the primary and satellite waves and acoustic-like waves were observed in Case I. Since the appearance of the acoustic-like waves was unexpected for the present flow conditions, Case

II was run to investigate if the actuator's location was a cause for the unexpected result. The same steady base flow and pulse parameters are used for both DNS cases.

The disturbance generated by Gaussian pulse which introduces a broad spectrum of frequencies into the flow field. After the disturbance has propagated along the cone and fully exited the domain, the unsteady data is analysed with Fourier decomposition. The decomposition of the unsteady disturbance into its constituent frequencies makes it possible to observe how individual frequencies are growing and decaying in space.

8.3.1 Case I: Upstream Actuator Location

Case I contains the unsteady results that motivated this investigation: the acoustic-like waves emanating from a traveling disturbance. Figure 8.8 shows acoustic-like waves emanating from the boundary layer as the disturbance develops features of the supersonic mode as it propagates downstream. The acoustic-like waves are relatively weak compared to the overall disturbance strength and do not extend very far into the flow field behind the shock. However, they resemble the supersonic mode and are inconsistent with a pure second mode instability. The acoustic-like waves are also positioned between a downstream and an upstream portion of the disturbance. As will be shown in Fig. 8.11, the two portions of the disturbance consists of a primary and satellite wave packet. This brings us to another peculiar aspect of this unsteady disturbance: the periodic constructive/destructive interference between these two packets. As seen in Fig. 8.8b, destructive interference creates a "hole" in the oscillation beneath the acoustic-like waves. The hole originates near the surface and does not propagate with the pulse, eventually exiting the disturbance altogether as it propagates downstream. A more detailed look at the interference phenomenon is described in Fig. 8.9.

The acoustic-like wave emissions and constructive/destructive interference are evident in Fig. 8.9a. The downstream angle of the emissions is indicative of their supersonic phase speed as they are propagating supersonically upstream relative to the base flow (albeit translating downstream with the disturbance). The emissions, however, are very weak compared to the much stronger primary wave to its right and the satellite wave to its left. Figure 8.9a shows

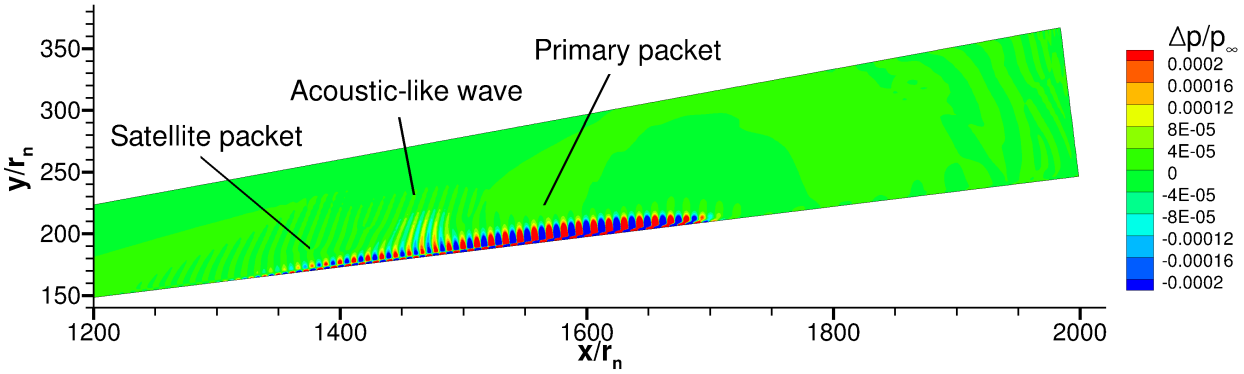

(a)

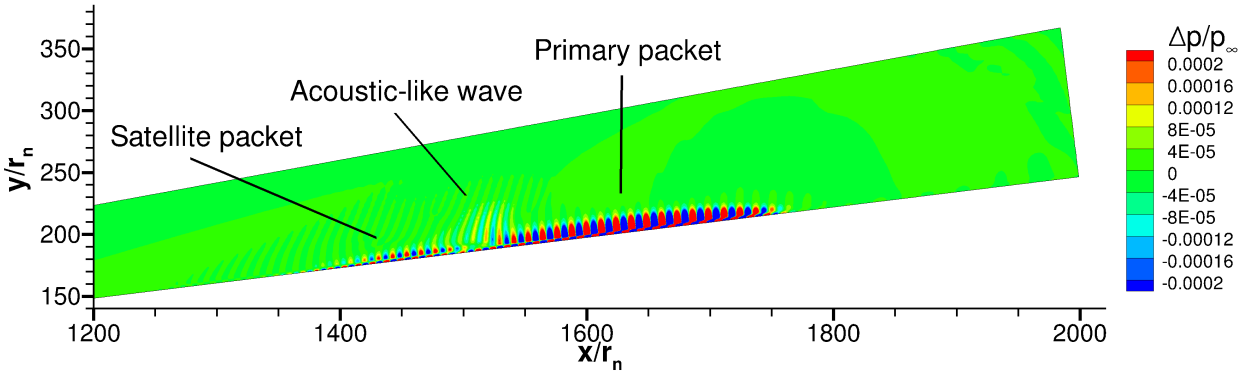

(b)

Figure 8.8: (a) The acoustic-like waves seen in context of the entire disturbance. (b) A hole in the oscillations develop in the boundary layer beneath the acoustic-like waves due to the destructive interference between the primary and satellite wave packets. The contour levels are clipped to make the pressure perturbations more visible.

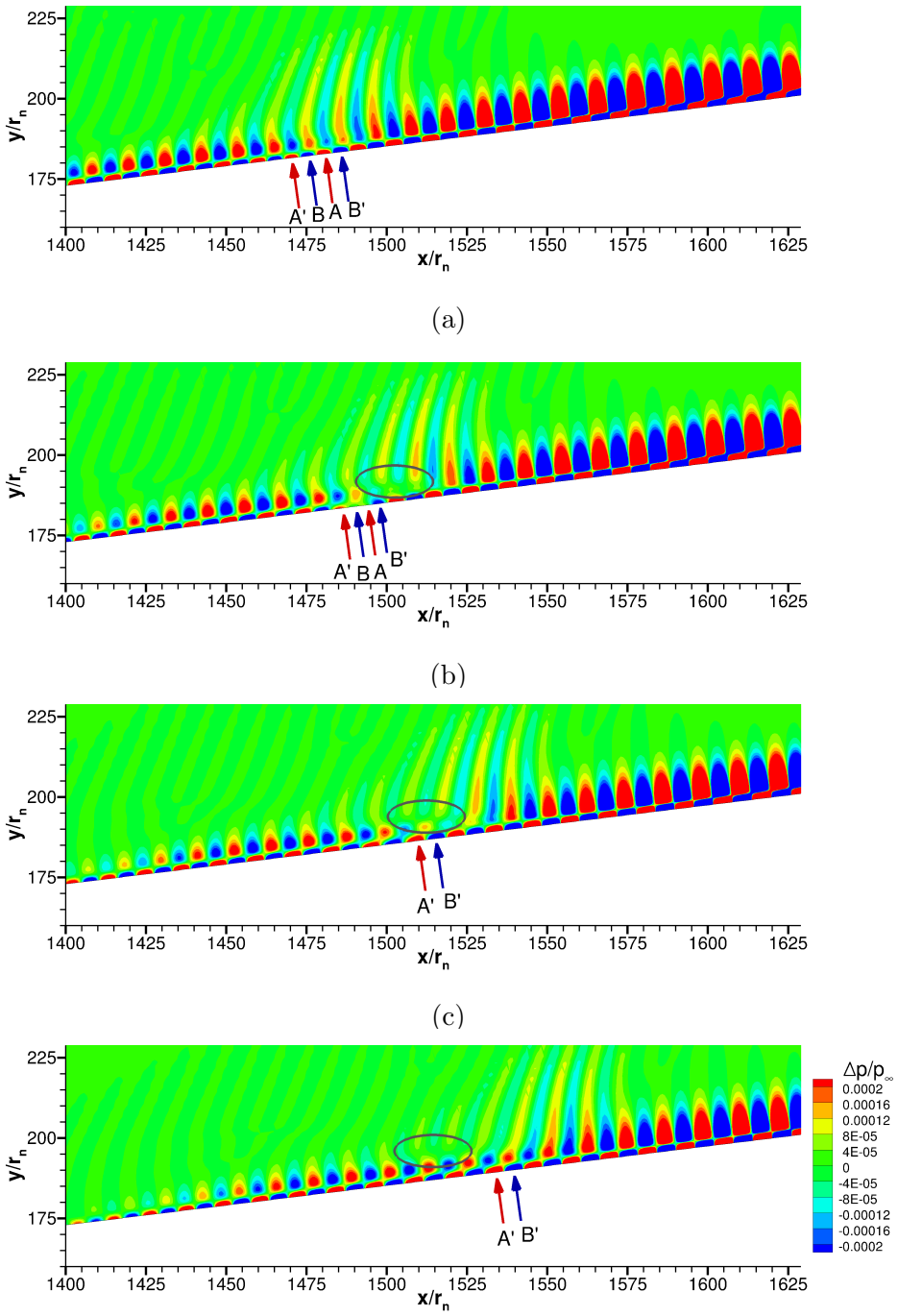

Figure 8.9: Progression of pulse interference patterns: (a) wave train prior to interference, (b) interference between oscillations becomes apparent above (ellipse) and below (arrows) the first sonic line, (c) above the sonic line a hole in the oscillations persists into the shock layer, below the sonic line surface oscillations cancel out (arrows A & B), (d) wave train returns to its previous appearance.

the disturbance's initial state before any wave interference occurs. In Fig. 8.9b, oscillations below the first sonic line, denoted by the arrows A and B, weaken in strength as they start to cancel. Above the first sonic line, the oscillations around $x/r_n = 1500$ to 1510 begin to interfere, creating a hole with no pressure oscillations. By Fig. 8.9c, the weakening oscillations below the sonic line, A and B, have canceled out completely, leaving the oscillations originally to their right and left, A' and B', adjacent to one another. Moreover, the hole appears to exit the disturbance and merge with the disturbance-free pressure field. By Fig. 8.9d, the pulse assumes the same appearance as it did in Fig. 8.9a before the wave interference began. In total, the interference pattern appears six times along the cone's length, as the acoustic-like waves emanate uninterrupted from the disturbance.

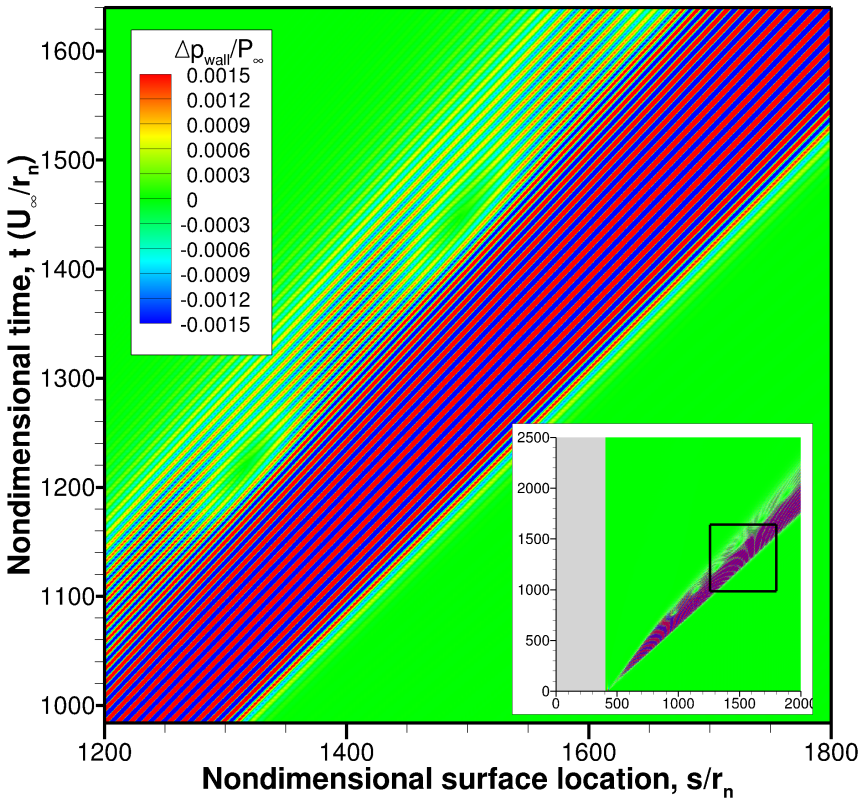

Figure 8.10: Case I x-t diagram of unsteady pulse showing the individual wave trajectories. Contours are clipped to show weaker satellite wave; $\max|\Delta p_{wall}/P_\infty| = 0.0291$.

One way to view the propagation of the disturbance is to plot it as an x-t diagram, such

as in Fig. 8.10, which shows the pressure perturbation along the cone's surface over time. An inset plot features the entire unsteady simulation starting from the actuator location at $s_c/r_n = 400$, while the enlarged view features the wave trajectories of the disturbance and several instances of constructive/destructive interference on the cone surface.

The x-t diagram makes it possible to view the individual wave trajectories that make up the disturbance. From Fig. 8.10, the leading wave trajectory that comprises the wavefront is present and consistently the same throughout the unsteady simulation—that is, no new wave trajectories appear ahead of it as time progresses, meaning the wavefront propagates steadily downstream. The trailing wave trajectory, however, is not the same throughout the simulation. As time progresses, slower wave trajectories appear behind the trailing trajectory, thus becoming the new trailing trajectory and adding to the overall width of the disturbance.

Figure 8.10 shows that as the wave trajectories fan out from the actuator, the primary wave packet comprises the faster shallower trajectories. In contrast, the satellite wave packet, which appears just before the first interference patch, comprises slower, steeper trajectories. As a result of the slower trajectories, the relative Mach number increases across the disturbance from the primary to satellite wave. This is noteworthy because if the relative Mach number across the disturbance becomes greater than one, given appropriate values for flow velocity and speed of sound within the boundary layer, it is possible for the supersonic mode to exist.

Although the x-t diagram provides an entire overview of the unsteady disturbance, it is difficult to discern the disturbance's structure. Figure 8.11 features time traces along the surface taken at regular nondimensional time intervals, where t has been nondimensionalized by the ratio of the freestream velocity to nose radius, U_∞/r_n. At $t = 328$ the disturbance appears as a single wave packet—this is typical of previous unsteady simulations containing supersonic modes after the actuator's initial forcing [KZ19b]. Between $t = 328$ and 682 the disturbance nearly doubles in amplitude. Growth of the disturbance is expected because, as the LST analysis shows, mode S is unstable. However, its sudden attenuation by $t = 1038$ is atypical and will be discussed at the end of this section. By $t = 682$, however, a satellite

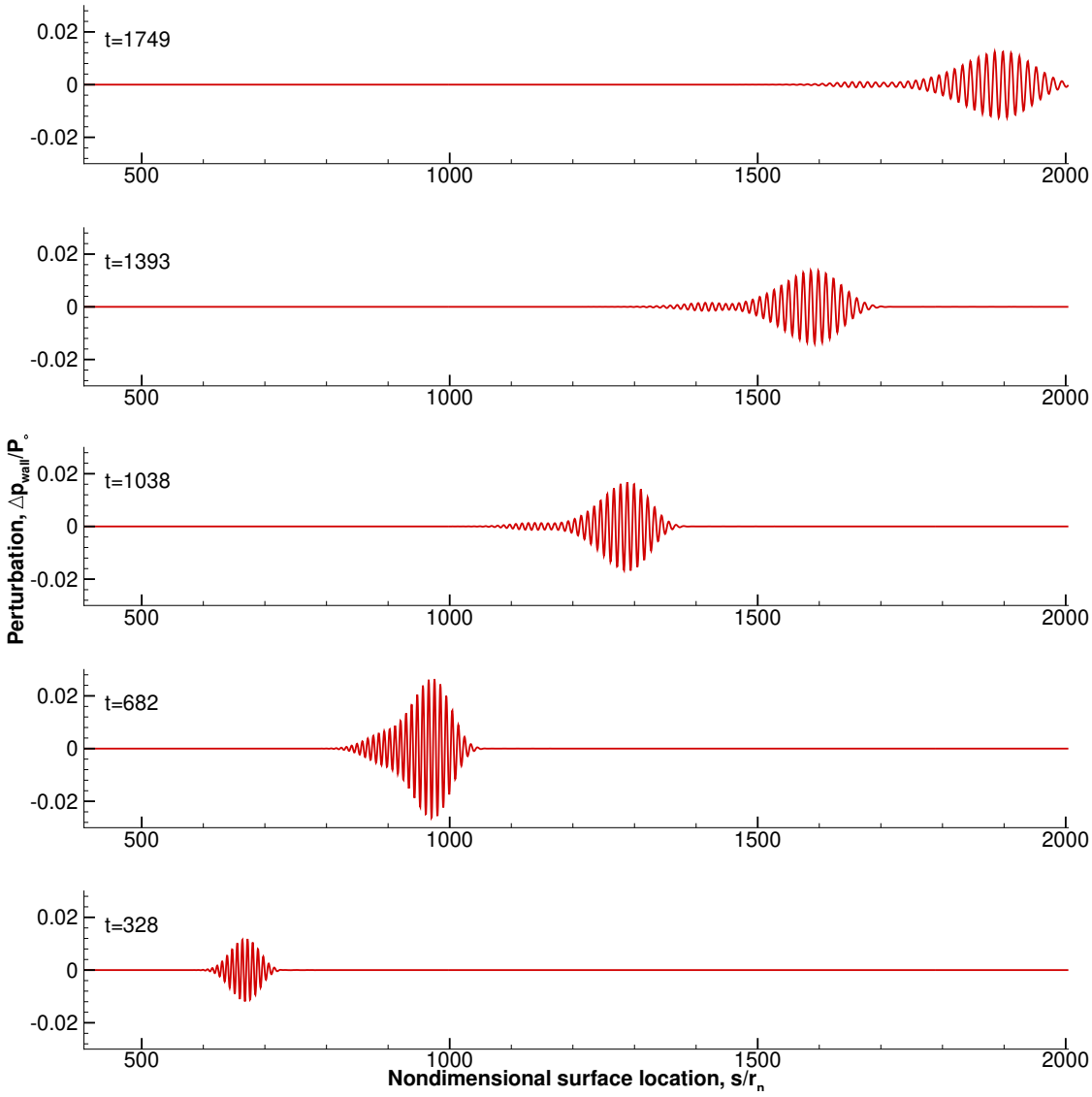

Figure 8.11: Propagation of disturbance along the cone surface for Case I with actuator located at $s_c/r_n = 400$. The instantaneous pressure is plotted at five equal nondimensional time intervals of 356.

wave packet appears as a lower amplitude tail on the main packet. In general, the satellite wave packet can be identified as the packet following the primary wave and by its lower amplitude. When undergoing destructive interference, the two wave packets appear separate from one another, otherwise, the satellite wave packet appears as a long tail connected to the primary wave packet. By $t = 1038$ the satellite wave packet is fully formed, although it is considerably weaker, with $max|\Delta p_{wall}/P_\infty| = 1.33\text{x}10^{-3}$ compared to the primary waves at $1.66\text{x}10^{-2}$. For the intervals between $t = 1038$ and 1749, the satellite wave packet is clearly present and separate from the primary wave.

A closer look at the interference between the primary and satellite waves is examined in Fig. 8.12. Whereas Fig. 8.11 shows the instantaneous propagation of the disturbance over most of the cone, Fig. 8.12 shows in detail the evolution of the primary and satellite wave packets over a shorter interval. In particular the interval from $t = 874$ and 1312 includes the second and third patches seen in the inset plot of Fig. 8.10. The satellite wave packet is clearly visible and separate from the primary wave packet at $t = 984$ and 1202, whereas at $t = 874$, 1093, and 1312, the satellite wave appears as a tail on the primary wave packet.

As the disturbance propagates downstream, it spreads in length due to wave dispersion, as seen in Fig. 8.10. Since the primary and satellite wave packets are also dispersive, any spreading of the wave packets will cause the waves to interact with one another resulting in either constructive or destructive interference. Constructive and destructive interference occurs when the superposition of two waves form a resultant wave of greater or lower amplitude. The patches in Fig. 8.10 and the holes seen in Fig. 8.9 are likely caused by destructive interference. Likewise, what causes the primary wave and satellite wave to appear attached at $t = 874$, 1093, and 1312 in Fig. 8.12 results from constructive interference. As was specified previously, the actuator pulse is kept intentionally weak to maintain the disturbance's linear growth and is therefore unlikely to exhibit nonlinear behavior. As such, superposition is a linear process that can account for the repeating pattern of constructive/destructive interference.

How the primary and satellite wave packets relate to the acoustic-like waves is unclear at this point. Except to say that the wave packets are probably the result of forcing by the

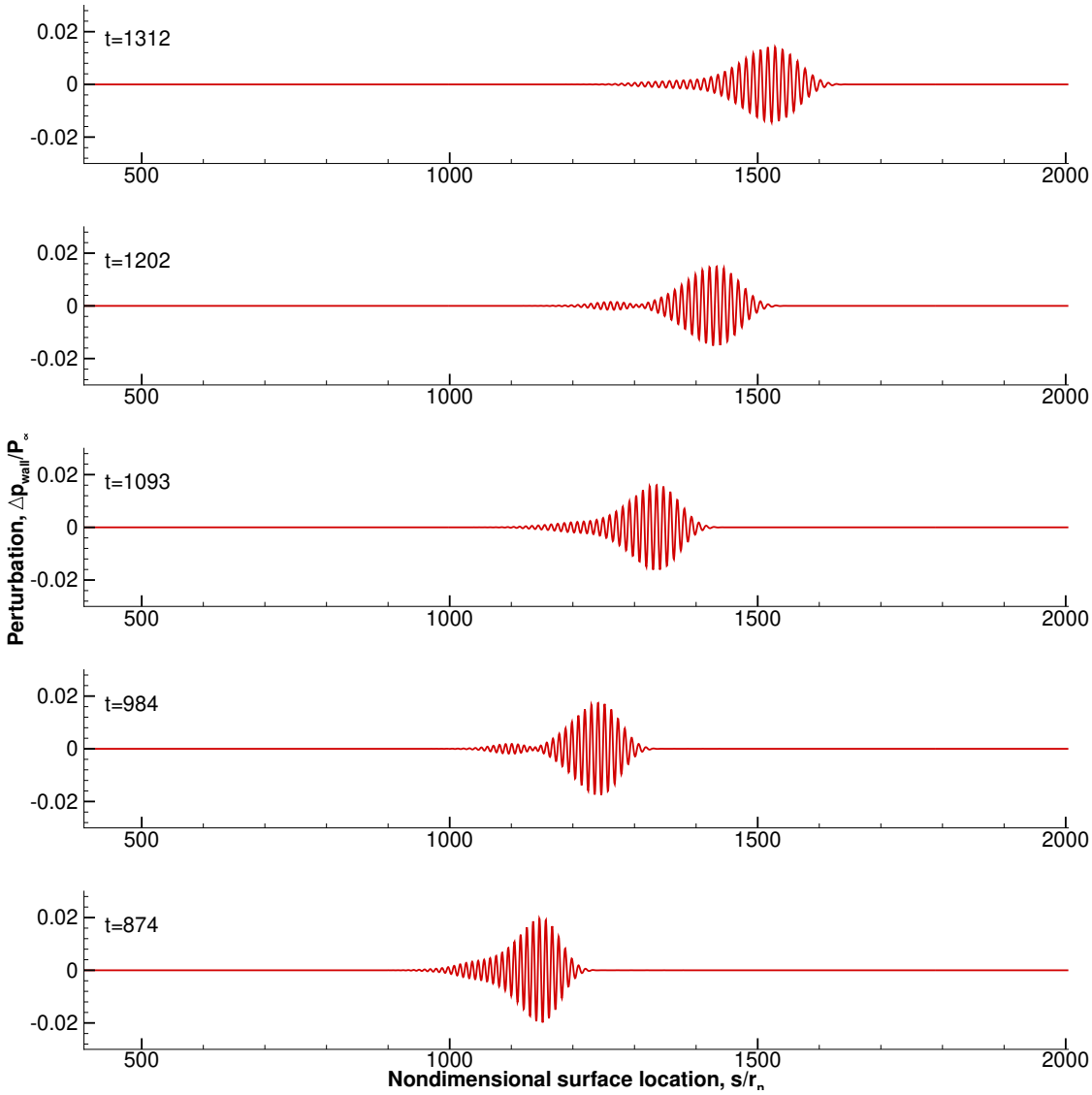

Figure 8.12: Case I primary and satellite waves packet evolution over a select time interval. At $t = 984$ and 1202 both wave packets are distinct from one another due to interference between packets. All other instances show the satellite wave packet as a tail on the primary wave packet. Actuator located at $s_c/r_n = 400$.

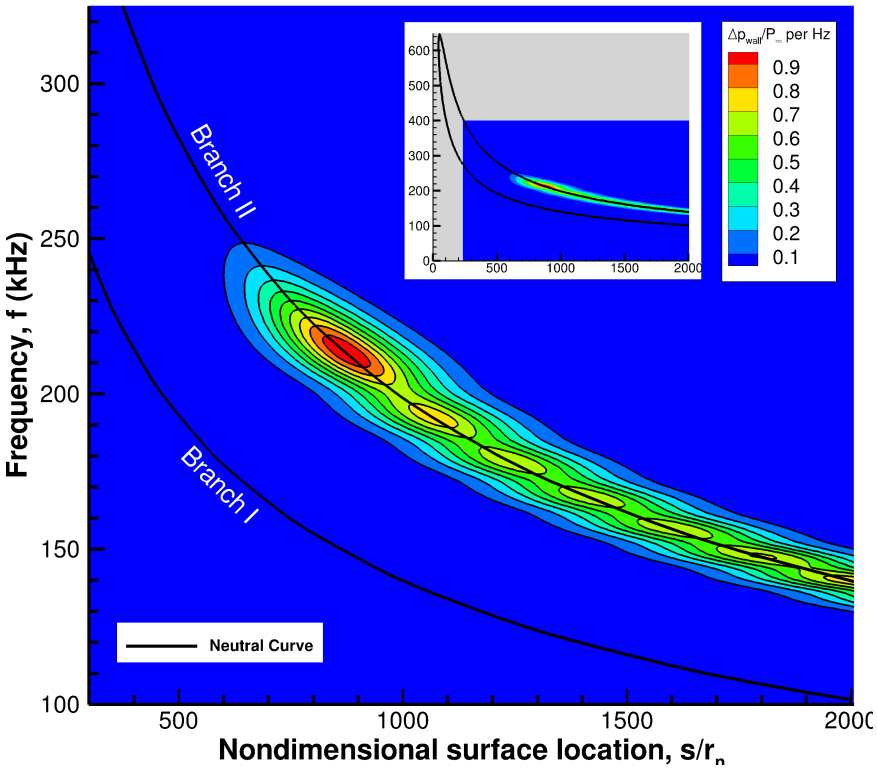

Figure 8.13: Case I normalized frequency spectrum of unsteady DNS pressure results combined with unstable mode S neutral stability curve. Actuator located at $s_c/r_n = 400$.

actuator and that the acoustic-like emissions appear at the interface between primary and satellite wave packets, as seen in Fig. 8.9.

Since the disturbance is comprised of many different waves, it is possible to use Fourier decomposition to obtain its frequency spectrum. The decomposition is important because it provides insight into the growth and decay of individual frequencies and is more readily compared with LST results. The unsteady wall pressure data featured in Fig. 8.10 is used to obtain the disturbance's frequency spectrum. The resulting spectrum is normalized by the initial Gaussian pulse in order to compare the growth and decay of individual frequencies together, irrespective of their initial strength. The resulting normalized frequency spectrum is featured in Fig. 8.13 along with the neutral stability curve for mode S, obtained from LST analysis. There is really good agreement between the spectrum and branch II of the neutral curve. Since growth rates are unstable between branch I and branch II, and stable

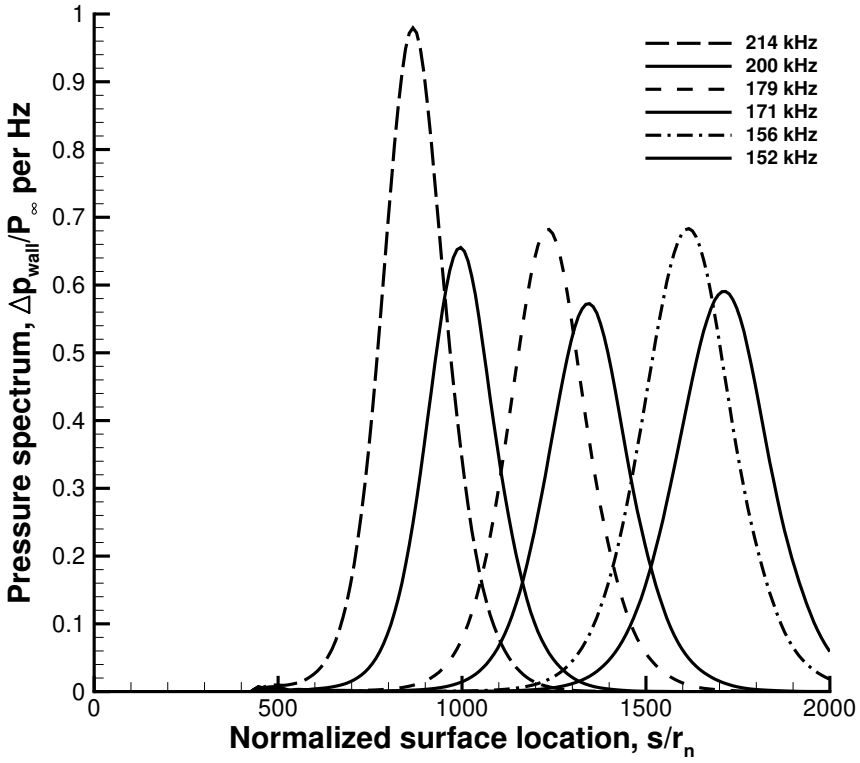

Figure 8.14: Case I selected frequencies of the normalized spectrum showing typical growth and decay. Actuator located at $s_c/r_n = 400$.

everywhere else, amplitudes are expected to grow inside the neutral stability curve and decay outside of it. As Fig. 8.13 shows, the amplitude grows to the left of the branch II neutral stability curve for a fixed frequency and begins to dampen immediately to the right as expected. This result is notable because it shows good agreement between two separate and distinct methods: Fourier decomposition and LST analysis.

An important feature of Fig. 8.13 is its notable array of peaks and saddles along the perturbed spectrum aligning with the branch II neutral curve. To investigate these peaks and saddles further, fixed frequency slices of the spectrum are plotted in Fig. 8.14, corresponding to three pairs of peaks and saddles along the perturbed spectrum. Despite the undulations in the frequency spectrum, each frequency still grows and decays in the expected manner—in that there is no modulation within a fixed frequency, only a single peak. Indicating that the amplitude curves of individual frequencies are more typical than they first appear

The six patches in Fig. 8.10, correspond spatially to the six saddles points in Fig. 8.13, suggesting that the frequencies that undergo destructive interference in the unsteady data are 200kHz, 184kHz, 171kHz, 161kHz, 152kHz, and 143kHz. As a result of the interference, these frequencies' respective amplitudes are damped. This lends more support to the explanation that the patches and holes result from wave superposition, as explained earlier in the research.

Lastly, a note on the atypical growth and attenuation seen in Fig. 8.11 around $s/r = 863$. The atypical growth can be attributed to the boundary layer's receptivity at the actuator's location. As seen in Fig. 8.13, the maximum pressure perturbation corresponds to a frequency of $214kHz$ and has neutral stability points at $s/r_n = 403$ and 863. Likewise, the actuator's center, located at $s_c/r_n = 400$, is close to the frequency's branch I neutral point, indicating the boundary layer at the actuator location is highly susceptible to disturbances of $214kHz$. As a result, the atypical growth would appear to be a consequence of the actuator's location and branch I neutral curve. However, the sudden attenuation does not appear to have an apparent cause. As has been suggested in the preceding discussion, destructive interference does provide a means to dampen individual frequencies. Moreover, Tumin's work found that the supersonic mode is a means for redistributing energy from the boundary layer to the inviscid layer [Tum20]. The inference implying that the stable supersonic mode can attenuate boundary layer perturbations; however, detailed analysis is needed to determine the cause of the attenuation.

8.3.2 Case II: Upstream Actuator Location

In addition to Case I, a second unsteady case with a different actuator location is computed. With the unanticipated interference pattern and the unexpected appearance of acoustic-like waves in the first case, it is prudent to investigate if the actuator's location had any unanticipated forcing on the unsteady results. Undoubtedly, the unsteady results will not be identical to the previous case because moving the actuator's location changes its relationship with the neutral stability curve and its receptivity with the boundary layer. The purpose of this second case is to see if the same primary and satellite wave packets and the supersonic

acoustic-like waves are present. Thus, the actuator is moved upstream to $s_c/r_n = 200$ and run with identical Gaussian pulse parameters as Case I.

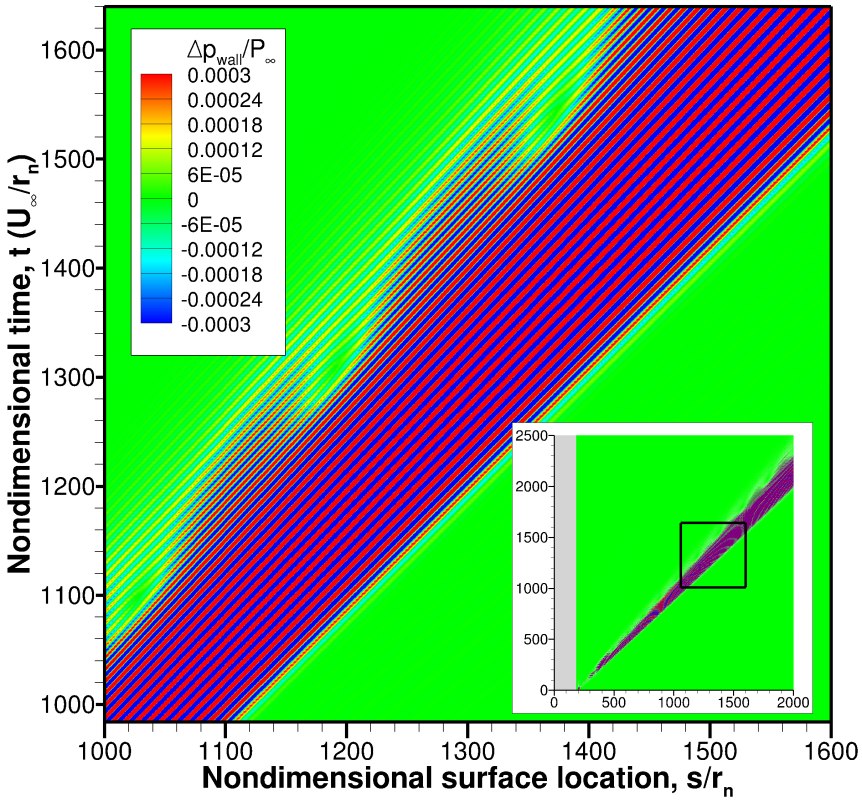

Figure 8.15: Case II x-t diagram of unsteady pulse showing individual wave trajectories. Contours are clipped to show weaker satellite wave; $\max|\Delta p_{wall}/P_\infty| = 9.37\text{x}10^{-3}$.

Figure 8.15, like the previous x-t diagram, features the wave trajectories of the complete unsteady disturbance along the cone's surface. An inset plot features the entire unsteady simulation starting from the actuator location at $s_c/r_n = 200$, and the main plot features the wave trajectories of the disturbance and several instances of destructive interference. As in Case I, the leading wave trajectory is the same throughout the unsteady simulation. Moreover, the trailing wave trajectory is also not the same throughout the simulation, with slower wave trajectories appearing behind the trailing trajectory, resulting in an increased disturbance width. The main plot in Fig. 8.15 also contains the conspicuous interference patches seen in Case I, this time forming a sawtooth-like pattern with the interference patches. These

patches are also the result of destructive interference between primary and satellite waves; however, the satellite wave is weaker in this Case.

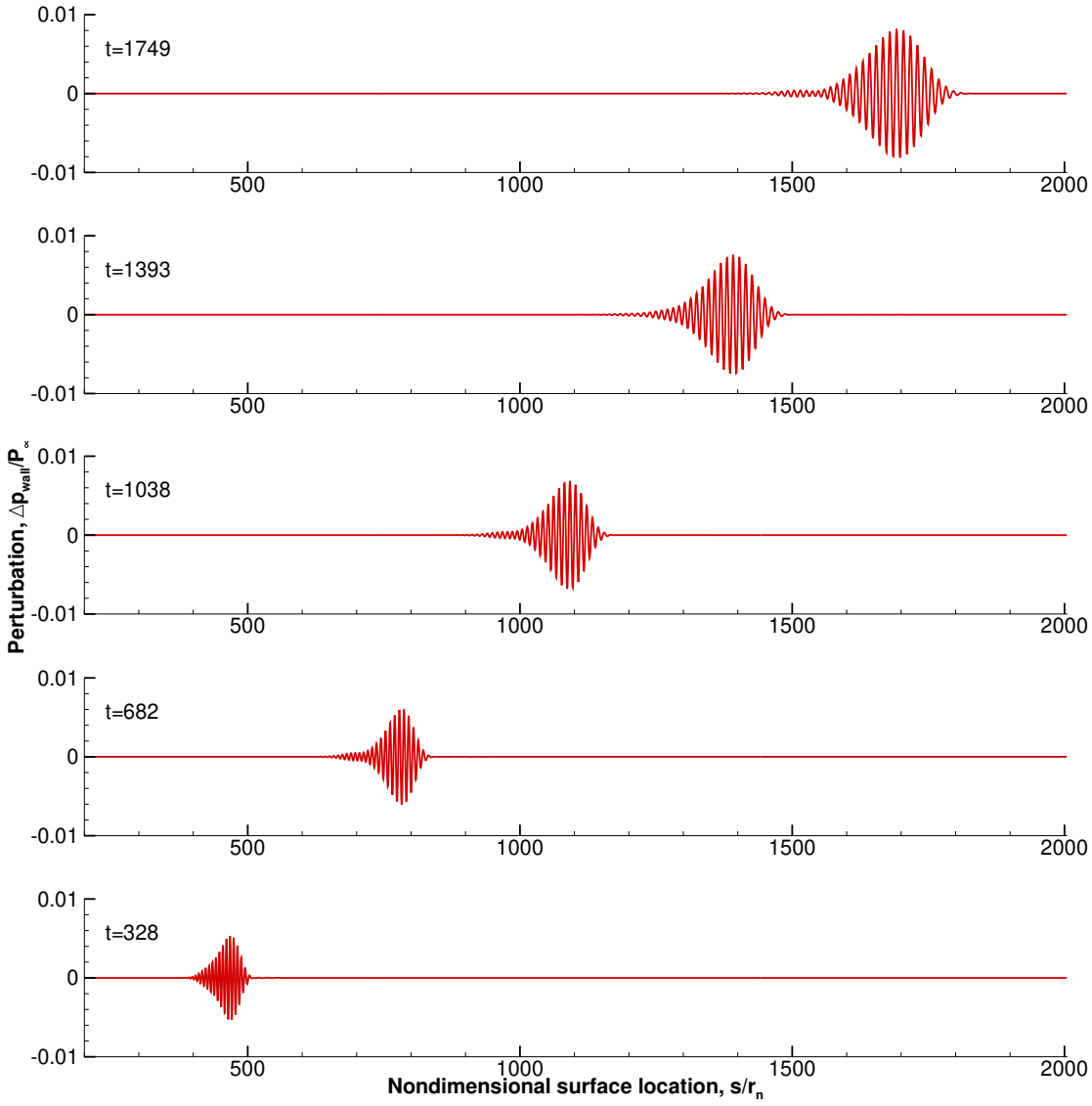

Figure 8.16: Case II propagation of disturbance along the cone surface with actuator located at $s_c/r_n = 200$. The instantaneous pressure is plotted at five equal nondimensional time intervals of 355.

Examining individual time traces, like those in Fig. 8.16, reveals that the disturbance's structure is more typical for an unsteady surface pulse: the disturbance grows steadily downstream with little atypical growth and attenuation. From $t = 328$ to 1749, the maximum amplitude grows 59%, from $\max|\Delta p_{wall}/P_\infty| = 5.25\text{x}10^{-3}$ to $8.18\text{x}10^{-3}$. The growth is very

mild compared to Case I, which, although having the same initial pulse strength, saw a larger disturbance amplitude. This is likely because the upstream actuator is aligned with the narrower, high-frequency portion of the neutral stability curve, as seen in Fig. 8.17. This

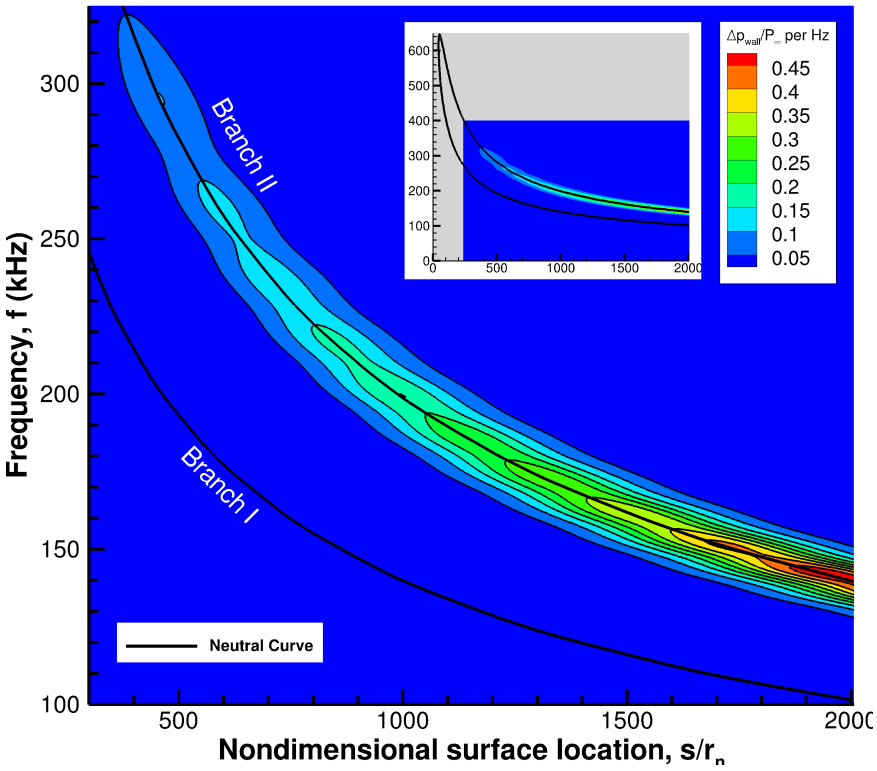

Figure 8.17: Case II normalized pressure frequency spectrum of unsteady DNS results combined with unstable mode S neutral stability curve. Actuator located at $s_c/r_n = 200$.

means that there will be more damping of the lower frequencies before reaching the neutral curve's unstable region. Regardless of the reduced growth, a satellite wave is present as a tail on the primary wave and is even less prominent than the satellite wave in Fig. 8.11. This verifies in part that the primary and satellite wave packets and any resulting interference are independent of actuator location.

As before, a Fourier decomposition of the temporal data is used to compute its frequency spectrum. Figure 8.17 contains both the frequency spectrum and neutral curve for the upstream actuator. Once again, the DNS frequency spectrum agrees very well with the LST neutral curve. Overall, the spectrum increases downstream with decreasing frequency as

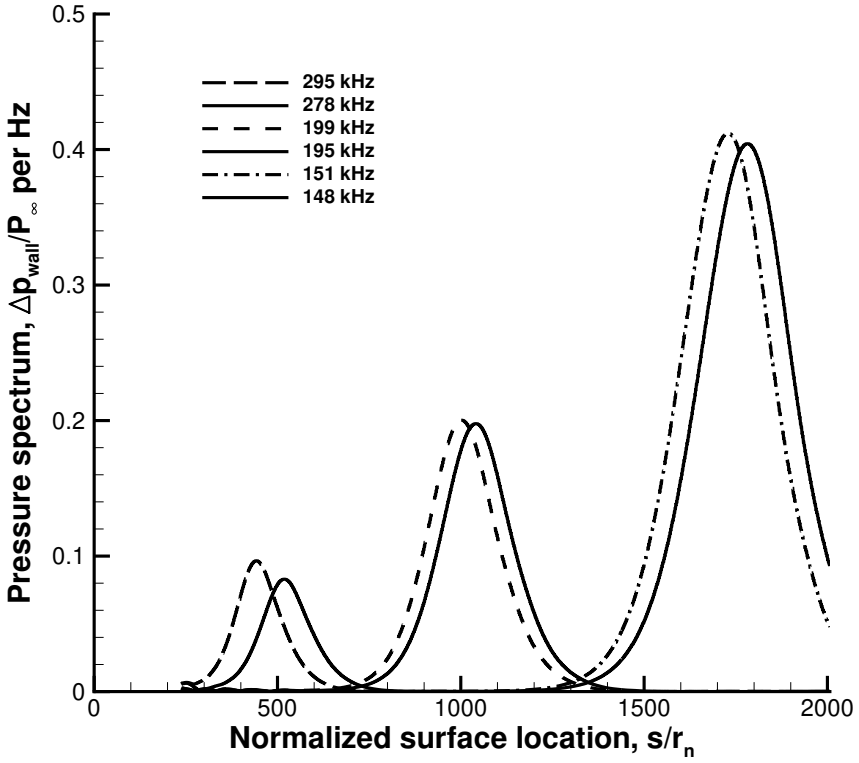

Figure 8.18: Case II selected frequencies of the normalized spectrum showing typical growth and decay. Dashed lines correspond to peak frequencies and solid lines correspond to the nearest saddle point frequency. Actuator located at $s_c/r_n = 200$.

expected. There is, however, an obvious meandering of the contours. This appears to be a result of the constructive/destructive interference seen in Fig. 8.15; however, because the satellite wave is much weaker, the same peaks and saddles do not appear in the contour plot as they do in Fig. 8.13.

Close inspection of the frequency spectrum data, however, does reveal that the meandering contours in Fig. 8.17 are the result of the same peaks and saddles. Three pairs of fixed frequency peaks and saddles along the perturbed spectrum are plotted in Fig. 8.18. Like Case I, each frequency grows to a maximum amplitude and decays as anticipated. However, unlike Case I, the perturbed spectrum appears to grow steadily downstream: successive peaks growing higher in amplitude, despite the interspersed saddles. Moreover, the destructive interference between wave packets also appears to have a slight damping effect on the

saddle point frequencies, as seen in Case I.

Overall, the Case II unsteady results better resemble the linear disturbance growth expected when using a surface blowing-suction actuator. Even so, the same primary and satellite wave packets, the same acoustic-like emissions, and the same peaks and saddles that appeared in Case I also appear here. Therefore, it is reasonable to conclude that, while the unsteady results did differ, the observed phenomenon of supersonic acoustic-like waves and interference patterns is not solely due to the actuator's placement.

8.4 Group Velocity Analysis of Primary and Satellite Modes

Thus far the identity of the primary and satellite wave packet has been inferred from their relative positions and appearance: a low amplitude packet following a stronger mode S dominate packet. A better way to determine the mode content of each packet is to compute their group velocity. When studying a packet composed of many waves with different frequencies and wavenumbers, each with its own phase velocity, it is useful to compute the group velocity of the overall packet. The group velocity tells us the velocity of the overall packet shape and the speed at which the energy of the packet propagates. Unlike phase speed, which is the ratio of a wave's frequency over its wavenumber, the group velocity is the derivative of the frequency with respect to wavenumber. Thus the group velocity of a disturbance may contain separate peaks, which is useful for identifying the existence of multiple wave packets. Thus the appearance of primary and satellite wave packets should be supported by at least two peak group velocities. Similar group velocity calculations a have been carried out by Tumin while studying the supersonic mode [Tum20].

In temporal LST, where ω is complex, and α is real, the group velocity is understood as the real part of its derivative with respect to α for a two-dimensional wave ($\beta = 0$). In spatial theory, where ω is real, and α is complex, the derivative is taken with respect to α_r; thus it is important to form the correct derivative with α_i held constant. The group velocities for

each discrete modes were computed using the following formula taken from Mack[Mac77],

$$v_g = \left(\frac{\partial \omega}{\partial \alpha_r}\right)_{\alpha_i} = \left(\frac{\partial \omega}{\partial \alpha_r}\right)_{\omega_{i=0}} \left[1 + \left(\frac{\partial \alpha_i}{\partial \alpha_r}\right)^2_{\omega_{i=0}}\right]^{-1}. \tag{8.6}$$

Figure 8.19 contains the group velocities for modes F1+, F1-, and S computed from the spatial LST results plotted against ω. Recall thatω is the non-dimensional frequency and is equal to the product of the local Blasius Reynolds number and non-dimensional frequency, RF, which in turn makes it a function of location, s, and circular frequency f. Thus, the range of group velocities can be interpreted as being present at all locations for a fixed frequency or at a fixed location over many frequencies. Figure 8.19 also includes the horizontal lines demarcating the fast acoustic, vorticity/entropy, and slow acoustic non-dimensional phase speeds for reference—group velocity and phase speed should not be construed as synonymous, however.

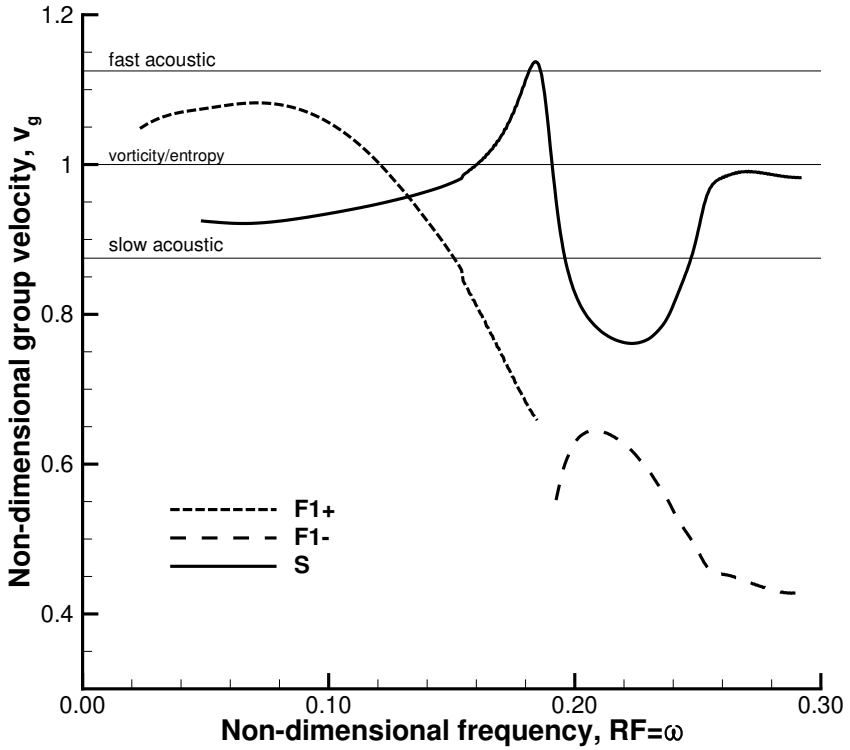

Figure 8.19: Group velocities of mode S and F from LST results.

For a start, mode S has two discernible peak group velocities. The first peak is quite clear and is located at $\omega = 0.184$, with v_g equal to 1.13. The second peak is much broader and

is located at $\omega = 0.271$, with v_g equal to 0.98. An astute eye may notice that these group velocities are faster than the mode S phase speeds in Figs. 8.3a and 8.3c, this is because group velocity relates to the propagation speed of the wave packet envelope and need not be the same as the waves it contains. The large dip between the two peaks occurs in the vicinity where modes F1- and S couple. During this coupling, the mode F1- group velocity has a broad peak around $\omega = 0.21$, with v_g equal to 0.632. In this instance, the group velocity is slower than slow acoustic and is slower than the phase speed of mode F1-. Again, the wave packet envelope need not propagate at the same speed as the waves it contains. Mode F1+ also has its own broad peak around $\omega = 0.073$, but since it was not observed in the unsteady DNS, it has not played a significant role in our analysis.

In regards to the primary and satellite wave packets, the first peak in mode S presents a viable candidate for the group velocity of the primary wave packet. As for the satellite wave packet, the second peak in mode S also seems like a viable candidate. This is because the group velocities are close in value and could create the environment where dispersion causes constructive/destructive interference. Suffice it to say there are multiple group velocities present in this flow field, two of which are clearly present in the unsteady data. For our purposes the group velocity is useful for identifying packets using theory, but is secondary to the main focus of this investigation which is to study individual supersonic modes at a given frequency.

Lastly, LST analysis can compute the e^N transition criterion, which is typically used to correlate N with transition onset in different environments such as flight tests and wind tunnel facilities [Mal03]. The e^N criterion is included in the analysis because it shows how an unstable fixed frequency mode grows in amplitude downstream within the LST framework. With this understanding, one may assume that the disturbance in the unsteady DNS should grow downstream. The criterion is defined as follows:

$$e^N = \frac{A(s)}{A_0} = \exp\left(\int_{s_0}^{s} -\alpha_i(s,\omega)ds\right), \tag{8.7}$$

where $A(s)$ is the integrated disturbance amplitude, A_0 is the initial disturbance amplitude, s is the surface location, s_0 is the location where the mode first becomes unstable. The

integration is performed for a constant frequency. The often-cited N-factor value is the exponent of Eq. (8.7). The e^N criterion provides the normalized disturbance amplitude but provides no information on the amplitude of the incoming disturbance, which is necessary for better transition prediction.

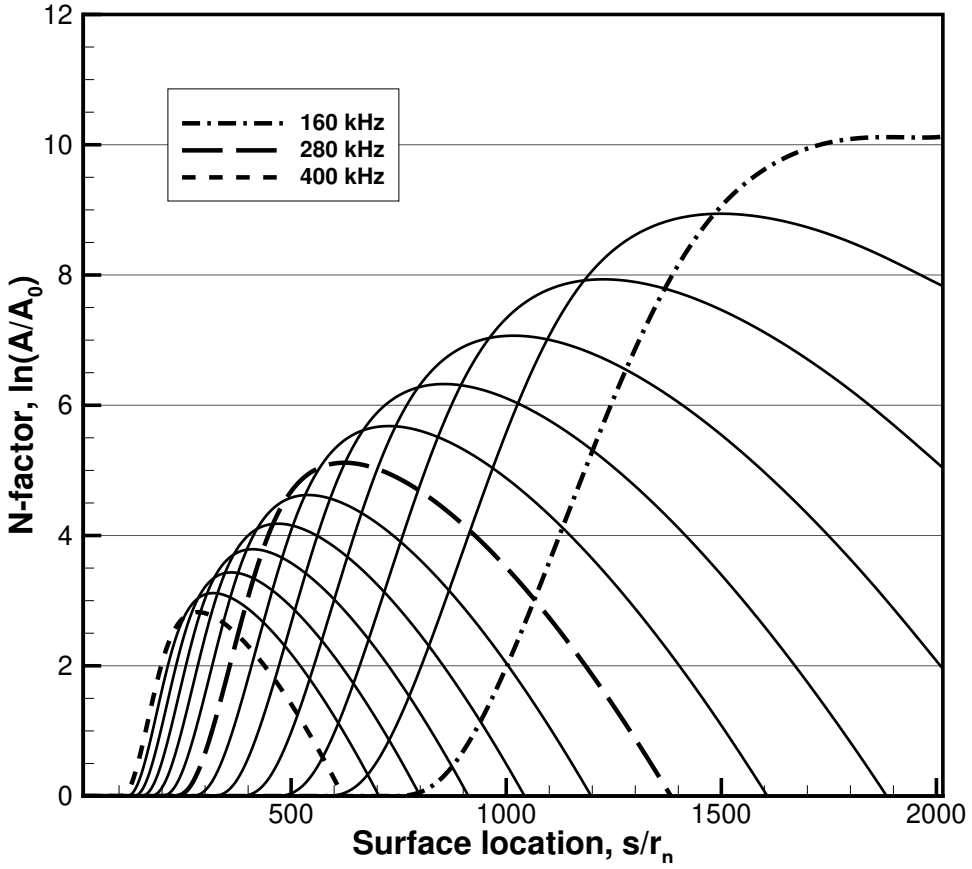

Figure 8.20: N-factor values for Mack's second mode instability on mode S. Fixed frequencies go from 160 to 400 kHz in increments of $\Delta f = 20kHz$.

The N-factors in Fig. 8.20 are of Mack's second mode instability, computed from the imaginary component of the mode S wavenumber obtained from LST. The results show that disturbances will grow downstream and become increasingly unstable with decreasing frequency. However, this LST based result is contrary to the unsteady DNS results obtained for the downstream actuator in Case I and much of the upstream actuator in Case II as well. The disturbance produced by the downstream actuator in Fig. 8.11, as previously discussed, undergoes very little growth downstream and is even attenuated from an upstream peak

amplitude. Moreover, the frequency spectrum in Fig. 8.13 contains many repeating peaks and saddles. The disturbance produced by the upstream actuator also shows similar peaks and saddles in its frequency spectrum, but its downstream growth is more consistent with the N-factor trend. These differences constitute a significant discrepancy between the LST and DNS results, but the discrepancy is justifiable because LST cannot capture the interference pattern results. LST analysis requires solving the dispersion relation using steady boundary layer data at fixed locations and repeating the solution procedure at many locations across the domain. As such, it cannot capture flow field behaviors that evolve over space and time. By contrast, unsteady DNS can capture the evolution of a pulse downstream and all of the 2-D phenomena that accompany it. To summarize, LST analysis provides crucial theoretical results such as phase speed, growth rate, and mode shape but is limited in describing the evolution of phenomena like the unsteady interference pattern.

CHAPTER 9

Summary

The purpose of this dissertation is to investigate new questions and unknown aspects of the roughness effect. These aspects can be generally organized into five topics: novel conical geometries, downstream implications of second mode attenuation, empirical evidence of second mode attenuation over a range of unstable frequencies, consequences of the roughness effect in off-design flow conditions, and further our fundamental understanding of supersonic modes in low-enthalpy warm wall flows.

This dissertation uses a DNS code to simulate the effect of surface roughness on the transition process on a hypersonic cone. The code solves the three-dimensional Navier-Stokes equations under a perfect gas assumption. The axisymmetric roughness strip is replicated using a body-fitted grid over an analytical shape. This approach, along with shock-fitting allows for a uniform 5^{th}-order global accuracy throughout the domain. Unsteady results are produced using a blowing-suction actuator, introducing a Gaussian pulse into the boundary layer to stimulate the second mode instability.

The code is used to investigate the transition delaying properties of the roughness effect in a series of numerical simulations on straight blunt cones. The investigations revolve around the application of the passive boundary layer control strategy patented by Zhong and Fong [ZFW14] for attenuating the hypersonic second mode instability. The strategy entails using LST to compute the N-factor for a range of frequencies, identifying the target frequency to be attenuated, finding its synchronization location, and then scaling a roughness strip to the boundary layer's proportions at that location. A single roughness strip is designed to investigate the validity of the roughness effect on straight blunt cone and then extended into a roughness array to attenuate a range of unstable second mode frequencies.

This roughness array was implemented on a hypersonic test article in a computational/ experimental collaboration with Dr. Katya Casper at Sandia National Laboratories. The experiments not only validated the DNS results but also the transition-delaying roughness design methodology.

Overall, the results of cases C.1, C.1-Ext, C.2 and Mach 8 experiment confirm that the passive transition-delaying control strategy works on a straight blunt cone, and that the roughness effects behavior is consistent with what is observed on a flat plate. For a single roughness strip, frequencies higher than the synchronization frequency of the roughness location are attenuated, and lower frequencies are amplified. Furthermore, an array of roughness strips can attenuate a broader range of frequencies over longer distances on the cone frustum. Thus, the roughness effect phenomenon has been shown to exist in conical flow fields.

9.1 Straight Blunt Cone Geometries

Where test article geometry is concerned, all of the simulations in this dissertation are on a straight blunt cone. The majority of the prior in-depth computational research on the roughness effect focused entirely on 2-D flat plates. While flat plates are a standard test article, it is not a geometry often used by hypersonic experimentalists whose cylindrical shock tubes and blow-down tunnels are better suited for axisymmetric geometries like straight blunt cones. The straight blunt cone geometry makes research on the roughness effect more relevant to real world applications.

Conical flow fields, however, are notably different from flat plates. For instance, their prominent bow shock, entropy layer swallowing, conical surface, and flow relief angle. These differences make it necessary to study the nuances of the flow field. One such difference is the flow around the roughness element. The steady-state results from case C.1 show that the separation zones immediately upstream and downstream of the roughness are larger and smaller, respectively, compared to flat plate results. This result is notable because the downstream separation zone has been suggested as a possible damping mechanism [TZC15, HS64, Fuj06]. The mechanism posited by Tang et al. that a vortex sheet between the

separation zone and the rest of the boundary layer prevents the second mode from penetrating into the zone, thus reflecting it back in to the boundary layer towards the sonic line [TZC15]. This reflection incurs an amplitude reduction via Miles' law, thus suppressing the second mode. The extent of the vortex sheet downstream would suggest that the amount of damping is dependent on the size of the separation zone. Thus, minimal attenuation would be expected with a smaller separation zone, which is not the case in this simulation. If the hypothesized mechanism's ability to dampen is in any way proportional to the extent of the separated region, then weaker attenuation would be expected on a cone, but that is not the case in this simulation. Instead, the attenuation of the second mode on a cone is comparable with the attenuation of a flat plate. The existence of separation zones does not appear to play a role as an attenuation mechanism.

The investigation also confirmed that the second mode's attenuation is a result of the element's proximity to the synchronization location and not due to its proximity with the branch I/II neutral points. A criticism of the roughness effect is that it is the coincidence of the roughness's location and the local branch I neutral frequency that determines the cut-off between which frequencies are attenuated and which are amplified. However, Fourier decomposition of the unsteady disturbance for the single roughness strip shows that branch I neutral frequency, which is lower than the synchronization frequency, is contained in the range of amplified frequencies. This amplification indicates that the branch I neutral frequency is not the cut-off frequency for the roughness effect.

Another difference between a straight cone and a flat plate is in the LST analysis. Flat plate LST results are similar to those obtained using a similarity solution. Discrepancies between the two are often a result of including the bow shock in flat plate simulations. However, flat plate results can be reasonably nondimensionalized; such that phase speed and growth rate plots can be known for all frequencies instead of computed individually. This nondimensionalization means that it is simpler to compute the synchronization location for a desired frequency. This is not the case for straight cones, which cannot be accurately nondimensionalized because of their blunt nose radius, cone half-angle, and conical shape. Moreover, the conical flow field starts to break the LST parallel flow assumption. Consequently, LST

analysis at the desired synchronization frequency needs to be computed in order to find the synchronization location; likewise, if the location of a surface element is known, a process of guess-and-check needs to be conducted to find the associated synchronization frequency.

The simulation cases in this research offer a variation in Mach number, nose radius, and cone length. Previous computational studies on the roughness effect focused on a Mach 5.92 flow regime. This regime is close to where hypersonic flow is generally agreed to start and contains both first and second mode instabilities. Cases C.1 and C.1-Ext with its Mach 8 flow extends roughness effect research to more relevant Mach numbers where second mode instabilities dominate. Moreover, the sharper nose radius of case C.2 increases the strength of the second mode instability. The ability of the roughness array to attenuate the instability in the Mach 8 experiment demonstrates how effective the roughness effect is in attenuating the second mode. Not only does the roughness effect work in higher Mach flows but it is also insensitive to the strength of the instability.

The one-meter-long cone in case C.1-Ext provides new insight into the roughness effect and the long-term feasibility of the transition-delaying control strategy. The single roughness strip and roughness array configurations both looked at the long-term downstream growth of unattenuated second mode frequencies. Prior to the investigation, it was unknown if the unattenuated frequencies would resume growth at their normal rate or if it would be accelerated, and if the accelerated growth would be enough to cause transition. The results are eye-opening, the maximum disturbance pressure PSD as a function of cone surface location shows that the PSD is many times larger for the simulations with surface roughness than the base simulation without roughness. The PSD for a single roughness reaches a peak $\Delta p_w/P_\infty$ per Hz that is 2.8 times larger than the base case. Likewise, the PSD for the roughness array reaches an astounding peak $\Delta p_w/P_\infty$ per Hz that is 14.7 times higher than the base case. These same results show that the transition-delaying control strategy is very effective at attenuating their targeted frequencies, but if the strategy is not carried out to the end of the cone, the unattenuated frequencies will grow and likely cause transition. Thus, for the control strategy to be effective, it must be applied to the entire length of the cone.

Furthermore, when looking at the max disturbance pressure PSD as a function of fre-

quency, we see that the control strategy concentrates the disturbance into a narrowing band of amplified frequencies. This narrowing suggests that the roughness effect or control strategy does not necessarily dampen or dissipate the second mode instability but instead transfers disturbance energy from higher frequencies to lower frequencies. This transfer is reflected in the pressure spectra for the Mach 8 experimental results, where a lower frequency peak emerges after successfully attenuating the target frequency range. The result is also consistent with the experimental observation that the roughness strips increase the boundary layer thickness. Since the wavelength of the second mode is proportional to the boundary layer thickness, and frequency is inversely proportional to the wavelength through phase velocity, then an increase in boundary layer thickness should be accompanied by a decrease in second mode frequency. Moreover, while there is some dissipation into the inviscid layer as the disturbance travels over the roughness strip, it appears most of the energy is transferred into these lower frequencies. Again the results indicate that the control strategy needs to be judiciously applied to the entire cone frustum to be effective.

9.2 Joint Numerical and Experimental Conclusions

Numerical simulations are undertaken to design a surface roughness array that would attenuate Mack's second mode instability and maintain laminar flow over a Mach 8 hypersonic blunt cone. Multiple experimental runs at the Mach 8 condition with different Reynolds numbers are performed, as well as an off-design Mach 5 condition. The roughness array successfully delays transition in the Mach 8 case as intended but does not delay transition in the Mach 5 case. For validation and further analysis, numerical cases C.2 and C.3 were computed using the Mach 8 and Mach 5 experimental flow conditions. Linear stability analysis is applied to the simulations to determine their boundary layer stability characteristics. Stability analysis of case C.2 shows that the roughness array is adequately designed to attenuate the second mode. Whereas, analysis of case C.3 reveals the Mach 5 boundary layer is dominated by Mack first mode instability and it cannot be attenuated by the the roughness array.

The joint numerical and experimental investigation of the roughness effect has two main takeaways. The first is that a roughness array designed to attenuate Mack's second mode instability was implemented on a test article and transition was successfully delayed. Not only was transition delayed but PSD results show that the frequencies targeted for attenuation were in fact the frequencies attenuated. Not only does this result bolster the empirical evidence for the roughness effect, it also shows that the phenomenon exists in boundary layers that grow downstream and contain a range of unstable frequencies.

The second important result is that the roughness arrays are not effective when applied to off-design flow fields. It appears that slight changes in geometry are permissible, such as the nose radius, but significant changes to the flow conditions, such as Mach number, are detrimental. The experimental results show that the roughness array not only did not delay transition in the Mach 5 case but may have also interacted with Mack's first mode and promoted transition.

This result points to the hypothesis that roughness arrays may not be able to attenuate first mode transition as it does the second mode. The hypothesis is the first mode cannot be suppressed in the same manner because, the instability does not arise from mode coupling. To extend this hypothesis further, one could predict that the other Mack mode instabilities (e.g. 3rd, 4th, etc.) can be attenuated because they are the result of discrete mode coupling.

9.3 Supersonic Mode Discussion and Conclusions

During the current roughness effect study, an unsteady disturbance on a smooth cone surface in case C.1-Ext exhibited weak acoustic-like waves emanating from the boundary layer and a peculiar constructive/destructive interference pattern. The acoustic-like waves are reminiscent of supersonic discrete modes, which are not expected in the low-enthalpy, warm wall flow of case C.1-Ext . Because of this, the unsteady results merited further investigation.

The origin of the acoustic-like waves appears to result from a supersonic mode as initially predicted. The discrete modes' phase speeds show that modes F1+, and S are both subsonic; only mode F1- acquires a supersonic phase speed after initially being subsonic. A comparison

of mode F1-'s eigenfunction before and after becoming supersonic shows the eigenfunction does acquire an additional oscillation when supersonic. A contour plot of the pressure fluctuation generated from the eigenfunction result shows that mode F1- does have angled Mach waves similar to those found in the unsteady simulation. The F1- growth rate results show that the mode is also very stable, resulting in acoustic-like waves that are much weaker than the overall disturbance. Mode F1-'s complex phase speed also shows that it behaves quite differently from other unstable supersonic modes investigated in the literature due to its stability. Where other modes might start unstable, become supersonic, eventually coalesce with the slow acoustic continuous spectrum, and then bifurcate into a separate stable supersonic mode; the supersonic mode in this study starts and remains stable, and becomes supersonic due to decreasing phase speed, never approaching the slow acoustic continuous spectrum. Thus, this study has shown that there is more than one supersonic mode evolution.

In addition to the LST analysis supporting mode F1- as the supersonic mode, the phase speed of the disturbance computed from DNS data does become momentarily supersonic, further supporting the conclusion that the acoustic-like waves initially motivating this investigation are due to a supersonic mode.

Regarding the unsteady interference pattern, wave trajectories and time traces of unsteady pressure data show clear evidence of constructive/destructive interference between primary and secondary wave packets inside the unsteady disturbance. Fourier decomposition of the unsteady pressure data also shows repeating peaks and saddles in the frequency spectrum that align spatially with the unsteady data's destructive interference pattern. DNS analysis of the results supports the explanation that the pattern results from wave packets trailing one another, while wave dispersion causes them to spread and superimpose with one another resulting in interference. The destructive interference also causes narrow bands of frequencies to dampen in amplitude.

On a methodological note, the reason for using a Gaussian pulse in unsteady simulations is to perturb the boundary layer to a wide range of frequencies and to study the resulting linear modal growth and decay. Understanding what caused the primary and secondary

wave packets and peculiar disturbance behavior is vital because it presents an obstacle to researchers whose DNS studies require a coherent wave packet to study linear modal growth. The present investigation supposes this behavior is due to the actuator's location and its proximity to the second mode neutral curve.

In conclusion, supersonic modes are not limited to high-enthalpy, cold wall flows. Previous studies focused almost exclusively on cool walled flows for their ability to produce an unstable supersonic discrete mode. This research demonstrates with LST analysis and DNS results that stable supersonic discrete modes can also exist in warm walled flows. The LST results show a stable supersonic mode that produces weak Mach waves outside the boundary layer. Likewise, the DNS results show that the supersonic mode can appear in unsteady disturbances with forcing. These new findings indicate that a stable supersonic discrete mode can exist in low-enthalpy, warm wall flows. This new result contributes to our fundamental knowledge of the supersonic modes' properties and behaviors.

9.4 Suggestions for Future Work

The roughness effects' ability to attenuate oblique wave instabilities such as Mack's first mode has not been adequately studied. The Mach 5 experimental results show that the roughness array as designed has no effect on the first mode and may destabilize the boundary layer. However, it is quite possible that the roughness effect cannot attenuate the first mode because it does not have a synchronization location. The synchronization location is a consequence of mode coupling between mode F and mode S, and the first mode does not arise due to mode coupling. An in-depth study of 2-D roughness on a flat plate in Mach 5 flow subjected to oblique waves should be carried out.

On the topic of surface roughness, no numerical simulations have been undertaken to investigate the roughness effect as it pertains to fully isolated roughness. Holloway and Sterrett's early experiment and Fujii's experiment included fully isolated roughness and showed that they are capable of delaying transition, but it is unknown how this is accomplished [HS64, Fuj06]. Does the principle of synchronization location still apply? Is the instability

only suppressed directly behind the roughness? Is it suppressed in its wake? If so, how is this accomplished? Is isolated roughness better or worse at attenuating the second mode instability than 2-D or axisymmetric roughness? These are all valid questions that can be answered by numerical simulation of isolated roughness on a flat plate.

Regarding the stable supersonic mode investigation, numerous research questions can be pursued. For instance, where is the upper temperature bound for the unstable supersonic mode? Is mode F1 the only supersonic discrete mode? Can mode S become supersonic as well? Is forcing of the stable supersonic mode able to attenuate boundary layer disturbances? These are lines of possible research that come from this investigation and could be of interest to other researchers.

REFERENCES

[ACB10] Christopher Alba, Katya Casper, Steven Beresh, and Steven Schneider. "Comparison of Experimentally Measured and Computed Second-Mode Disturbances in Hypersonic Boundary-Layers." *48th AIAA Aerospace Sciences Meeting Including the New Horizons Forum and Aerospace Exposition*, 2010.

[BM92] P. Balakumar and M. R. Malik. "Discrete modes and continuous spectra in supersonic boundary layers." *Journal of Fluid Mechanics*, **239**:631–656, 1992.

[BS15] N. P. Bitter and J. E. Shepherd. "Stability of highly cooled hypervelocity boundary layers." *Journal of Fluid Mechanics*, **778**:586–620, 2015.

[Cas09] K. M. Casper. *"Hypersonic Wind-Tunnel Measurements of Boundary-Layer Pressure Fluctuations."*. Master's thesis, Purdue University, School of Aeronautics & Astronautics, August 2009.

[CBH16] Katya M. Casper, Steven J. Beresh, John F. Henfling, Russell W. Spillers, Brian O. M. Pruett, and Steven P. Schneider. "Hypersonic Wind-Tunnel Measurements of Boundary-Layer Transition on a Slender Cone." *AIAA Journal*, **54**(4):1250–1263, 2016.

[CF16] Pavel V. Chuvakhov and Alexander V. Fedorov. "Spontaneous radiation of sound by instability of a highly cooled hypersonic boundary layer." *Journal of Fluid Mechanics*, **805**:188–206, 2016.

[DWZ10] Le Duan, Xiaowen Wang, and Xiaolin Zhong. "A high-order cut-cell method for numerical simulation of hypersonic boundary-layer instability with surface roughness." *Journal of Computational Physics*, **229**(19):7207–7237, 2010.

[Fed11] A.V. Fedorov. "Transition and Stability of High-Speed Boundary Layers." *Annual Review of Fluid Mechanics*, **43**:79–95, 2011.

[FT11] Alexander Fedorov and Anatoli Tumin. "High-Speed Boundary-Layer Instability: Old Terminology and a New Framework." *AIAA J.*, **49**(8):1647–1657, 2011.

[Fuj06] Keisuke Fujii. "Experiment of the Two-Dimensional Roughness Effect on Hypersonic Boundary-Layer Transition." *Journal of Spacecraft and Rockets*, **43**(4):731–738, 2006.

[FWH15] Kahei Danny Fong, Xiaowen Wang, Yuet Huang, Xiaolin Zhong, Gregory R. McKiernan, Roy A. Fisher, and Steven P. Schneider. "Second Mode Suppression in Hypersonic Boundary Layer by Roughness: Design and Experiments." *Aiaa J.*, **53**(10):1–6, 2015.

[FWZ12] Danny Fong, Xiaowen Wang, and Xiaolin Zhong. "Finite roughness effect on modal growth of a hypersonic boundary layer." *50th AIAA Aerospace Sciences Meeting including the New Horizons Forum and Aerospace Exposition*, (January):1–27, 2012.

[FWZ14a] K D Fong, X Wang, and X Zhong. "Numerical simulation of roughness effect on the stability of a hypersonic boundary layer." In *Comput. Fluids*, volume 96, pp. 350–367, Big Island, Hawaii, 2014.

[FWZ14b] Kahei Danny Fong, Xiaowen Wang, and Xiaolin Zhong. "Numerical simulation of roughness effect on the stability of a hypersonic boundary layer." *Computers and Fluids*, **96**:350–367, 2014.

[FWZ15] Kahei Danny Fong, Xiaowen Wang, and Xiaolin Zhong. "Parametric Study on Stabilization of hypersonic boundary layer waves using 2-D surface roughness." (January):1–20, 2015.

[HCZ19] Christopher L. Haley, Katya M. Casper, and Xiaolin Zhong. "Joint Numerical and Experimental Investigation of Roughness Effect on Hypersonic 2nd Mode Instability and Transition." *AIAA Scitech 2019 Forum*, pp. 1–19, 2019.

[Hol12] B.R. Hollis. "Blunt-body entry vehicle aerothermodynamic: transition and turbulent heating." *Journal Spacecraft and Rockets*, **49**(3):435–449, 2012.

[HS64] Paul F Holloway and James R Sterrett. "Effect of Controlled Surface Roughness on Boundary Layer Transition and Heat Transfer at Mach Numbers of 4.8 and 6.0." *Nasa Tn D-2054*, (April), 1964.

[HZ14] Yuet Huang and Xiaolin Zhong. "Numerical Study of Hypersonic Boundary-Layer Receptivity with Freestream Hotspot Perturbations." *Aiaa J.*, **52**(12):1–21, 2014.

[HZ17] Christopher L. Haley and Xiaolin Zhong. "Direct Numerical Simulation of Hypersonic Flow over a Blunt Cone with Axisymmetric Isolated Roughness." *47th AIAA Fluid Dynamics Conference*, pp. 1–27, 2017.

[Jam59] Carlton S. James. "Boundary-Layer Transition on Hollow Cylinders in Supersonic Free Flight as Affected by Mach Number and a Screwthread type of Surface Roughness." Technical report, 1959.

[KZ19a] Carleton P Knisely and Xiaolin Zhong. "Significant Supersonic Modes and the Wall Temperature Effect in Hypersonic Boundary Layers." *AIAA Journal*, **57**(4):1552–1566, 2019.

[KZ19b] Carleton P Knisely and Xiaolin Zhong. "Sound radiation by supersonic unstable modes in hypersonic blunt cone boundary layers. I. Linear stability theory." *Physics of Fluids*, **31**(2), 2019.

[KZ19c] Carleton P Knisely and Xiaolin Zhong. "Sound radiation by supersonic unstable modes in hypersonic blunt cone boundary layers. II. Direct numerical simulation." *Physics of Fluids*, **31**(2), 2019.

[KZ20] Carleton P. Knisely and Xiaolin Zhong. "Impact of Vibrational Nonequilibrium on the Supersonic Mode in Hypersonic Boundary Layers." *AIAA Journal*, **58**(4):1704–1714, 2020.

[LZ12] J. Lei and X. Zhong. "Linear stability analysis of nose bluntness effects on hypersonic boundary layer transition." *Journal of Spacecraft and Rockets*, **49**(1):24–37, 2012.

[Mac69] L. M. Mack. "Boundary layer stability theory." Technical Report 900-277, JPL Report, 1969.

[Mac77] L. M. Mack. "Transition Prediction and Linear Stability Theory." Technical report, AGARD Laminar-Turbulent Transition 22, Oct 1977.

[Mac84] Leslie M. Mack. "Boundary Layer Linear Stability Theory." Technical report, 1984.

[Mac87] L.M. Mack. "Review of Linear Compressible Stability Theory." In D.L. Dwoyer and M.Y. Hussaini, editors, *Stability of Time Dependent and Spatially Varying Flows*, pp. 164–187. Springer-Verlag, 1987.

[Mac90] L. M. Mack. "On the Inviscid Acoustic-Mode Instability of Supersonic Shear Flows Part 1: Two-Dimensional Waves." *Theoretical Computational Fluid Dynamics*, **2**:97–123, 1990.

[Mal90] M R Malik. "Numerical methods for hypersonic boundary layer stability." *J. Comput. Phys.*, **86**(2):376–413, 1990.

[Mal03] M R Malik. "Hypersonic flight transition data analysis using parabolized stability equations with chemistry effects." *Journal of Spacecraft and Rockets*, **40**(3):332–344, 2003.

[Mor88] M. V. Morovin. "Recent insights into instability and transition to turbulence in open-flow systems." Technical Report ICASE-88-44, NASA Langley Research Center, 1988.

[Mor18] C.M. Mortensen. "Toward and understanding of supersonic modes in boundary-layer transition for hypersonic flow over blunt cones." *Journal of Fluid Mechanics*, **846**:789–814, 2018.

[MRH94] M. V. Morkovin, E. Reshotko, and T. Herbert. "Transition in open flow systems–A reassessment." *Bulletin of American Physical Society*, **39**:1882, 1994.

[MZ03] Yanbao Ma and Xiaolin Zhong. "Receptivity of a supersonic boundary layer over a flat plate. Part 1. Wave structures and interactions." *Journal of Fluid Mechanics*, **488**:31–78, 2003.

[In AGARD Rep. 709.]

[MZ16] Clifton H. Mortensen and Xiaolin Zhong. "Real-Gas and Surface-Ablation Effects on Hypersonic Boundary-Layer Instability over a Blunt Cone." *AIAA Journal*, **54**(3):1–19, 2016.

[Res91] E. Reshotko. "Hypersonic Stability and Transition." *Hypersonic flows for reentry problems*, **1**(A93-42576 17-02):18–34, 1991.

[Res08a] E. Reshotko. "Paths to Transition in Wall Layers." Technical Report RTO-EN-AVT-151, NATO OTAN, 2008.

[Res08b] E. Reshotko. "Transition Issues for Atmospheric Entry." *Journal of Spacecraft and Rockets*, **45**(2):161–164, 2008.

[Sch08] Steven P. Schneider. "Summary of Hypersonic Boundary-Layer Transition Experiments on Blunt Bodies with Roughness." *Journal of Spacecraft and Rockets*, **45**(6):1090–1105, 2008.

[SSS17] Adrian Sescu, Jeremy Sawaya, Vasileios Sassanis, and Miguel R. Visbal. "Study of the Effect of Two-dimensional Wall Non-uniformities on High-speed Boundary Layers." *47th AIAA Fluid Dynamics Conference*, (June):1–20, 2017.

[Sut93] William Sutherland. "LII. The viscosity of gases and molecular force." *The London, Edinburgh, and Dublin Philosophical Magazine and Journal of Science*, **36**(223):507–531, 1893.

[Tum03] Anatoli Tumin. "Multimode decomposition of spatially growing perturbations in a two-dimensional boundary layer." *Physics of Fluids*, **15**(9), 2003.

[Tum20] Anatoli Tumin. "Wave Packets and Supersonic Second Modes in a High-Speed Boundary Layer." In *AIAA Scitech 2020 Forum*, number AIAA 2020-0106, pp. 1–13, 2020.

[TZC15] Qing Tang, Yiding Zhu, Xi Chen, and Cunbiao Lee. "Development of second-mode instability in a Mach 6 flat plate boundary layer with two-dimensional roughness." *Physics of Fluids*, **27**(6), 2015.

[Whi05] F.M. White. *Viscous Fluid Flow*. McGraw-Hill, 3rd edition, 2005.

[Wil80] J. Williamson. "Low-Storage Runge-Kutta Schemes." *Journal of Computational Physics*, **35**(1):48–56, 1980.

[Wu05] Xuesong Wu. "Mach wave Radiation of nonlinearly evolving supersonic instability modes in shear layers." *Journal of Fluid Mechanics*, **523**:121–159, 2005.

[WZ19] Xuesong Wu and Zhongyu Zhang. "First-principle description of acoustic radiation of shear flows." *Philosophical Transactions of the Royal Society A: Mathematical, Physical and Engineering Sciences*, **377**:20190077, 12 2019.

[ZFW14] Xiaolin Zhong, Kahei Danny Fong, and Xiaowen Wang. "Hypersonic laminar flow control.", 2014.

[WO Patent App. PCT/US2013/070,798.]

[Zho98] Xiaolin Zhong. "High-Order Finite-Difference Schemes for Numerical Simulation of Hypersonic Boundary-Layer Transition." *Journal of Computational Physics*, **144**(2):662–709, 1998.

[ZKM20] Ludovico Zanus, Carleton P. Knisely, Fernando Miro Miro, and Fabio Pinna. "Multiple-Tool Stability Analysis of Supersonic Modes in Thermo-Chemical Nonequilibrium Boundary Layers." In *AIAA Aviation 2020 Forum*, number AIAA 2020-3067, pp. 1–20, 2020.

[ZW12] Xiaolin Zhong and Xiaowen Wang. "Direct Numerical Simulation on the Receptivity, Instability, and Transition of Hypersonic Boundary Layers." *Annual Review of Fluid Mechanics*, **44**(1):527–561, 2012.